学位論文

X-ray substructure in clusters of galaxies and its implications for the physics of the intergalactic plasma

(銀河団内の X 線構造の研究と銀河間プラズマ物理への示唆)

平成 27 年 12 月博士（理学）申請

東京大学大学院理学系研究科
物理学専攻

一戸　悠人

Abstract

The majority of the baryons in the Universe are in the form of diffuse plasma, i.e. intergalactic medium (IGM), which permeates the space between galaxies. Most of the IGM that is currently observable resides in clusters of galaxies, where it is referred to as intracluster medium (ICM). The fundamental microphysical properties of the IGM/ICM, such as viscosity, magnetic fields, and turbulence, however, still remain poorly constrained, despite their importance for both astrophysics and cosmology.

In order to investigate the microphysics of the ICM observationally, we focus on X-ray substructure in galaxy clusters, especially on "cold front"s, which are the interface between a lower temperature, denser gas parcel and a more rarefied, hotter ambient medium. Although studies of X-ray substructures have been routinely done so far, most of them have focused only on the substructure itself. In this thesis, we have extended the point of view to both "higher-order substructure", i.e., substructures in the substructure, and "lower-order substructure", i.e., the relation between multiple substructures, and attempted to draw new constraints on the ICM microphysics. We have selected three systems; Abell 85, the Perseus cluster, and Abell 3667, all of which are among the brightest, and host prominent X-ray substructures.

In Abell 85, we have found a huge spiral pattern in the main cluster, as well as a smooth edge and a peculiar bent morphology in the subcluster currently falling in. We suggest that the spiral is due to gas sloshing induced by a previous merger, and the morphology of the subcluster is likely to result from the interaction between the subcluster and the main cluster gas sloshing. We suggest that this observation demonstrates the interaction between multiple X-ray substructures, so far an overlooked point of view, which provides us with information about the configuration of magnetic fields and their dynamical impact.

We have found that Abell 85 also hosts a long stripped tail of the subcluster, while the subcluster's cool core is located at the leading edge of the subcluster. The length of the stripped tail may imply its long life time, and thus the suppression of strong turbulence and diffusion. The core at the leading edge indicates that the subcluster gas has been almost completely stripped during its infall, which poses a challenge to recent simulations which find that the core usually survives major mergers, indicating the insufficiency of the simple hydrodynamic approximation employed by the models.

In the Perseus cluster, we have found a significant double-layered structure in the eastern cold front. Through thermodynamic studies, we have revealed that the double-layered structure is consistent with being a Kelvin-Helmholtz instability (KHI) layer on the sloshing cold front. This is the first case where a KHI layer candidate itself is examined thermodynamically, resulting in stronger evidence for the existence of such an instability layer. In addition, we have found a pressure deficit in the KHI layer with respect to the ambient medium, which could be supported by magnetic fields or turbulence. We have found that the turbulent heating resulting from the collapse of KHI may balance radiative cooling, and that the estimated

turbulent heating rate agrees within an order of magnitude with the previous estimate performed with a completely different method. Our results therefore stress the importance of the turbulent heating in the context of the cooling problem in the cores of galaxy clusters, and indicate that the turbulence triggered by sloshing-induced KHIs may have nonnegligible contributions to the ICM turbulence, which has not been considered extensively.

Also in the Perseus cluster, we have found feather-like structures below the western cold front. We suggest that this is due to gas depletion resulting from magnetic field amplification associated with the sloshing motion of the ICM. Based on the scenario, we have estimated the ambient magnetic field strength using such an X-ray substructure through thermodynamic properties for the first time.

In Abell 3667, we have found that the cold front is not monotonically smooth but fluctuating. This indicates that KHIs are not completely suppressed on the cold front as opposed to the previous interpretations of the complete suppression of the KHI. This is the first observational indication of developing KHIs on a merger cold front. Based on this argument, we have presented the value of the ICM effective viscosity for the first time. The viscosity value is consistent with the previous observational upper and lower limits, possibly indicating the intriguing universality of the ICM effective viscosity.

All of our results can be discussed from one underlying aspect, i.e., the insufficiency of the simple hydro*static* description of the ICM. Our studies have offered some of the first quantitative estimates of the fundamental microphysical properties of the ICM, stressing the necessity for a hydro*dynamic*, or *magnetohydrodynamic* treatment of the ICM. We think it is observations with these points of view that are essential for the quantitative understanding of the most dominant baryons in our Universe.

Contents

Chapter 1

Introduction

The growth of cosmic structure is driven by the gravity of dark matter, which is invisible, and the most dominant mass component in the Universe. Baryonic matter represents only a small fraction of the entire mass component ($\sim$15%, Allen et al., 2011; Komatsu et al., 2011; Planck Collaboration et al., 2013), and the majority of the baryonic component is thought to be in the form of a diffuse medium that fills the space between galaxies (intergalactic medium, IGM), following the cosmic structure.

Among gravitationally collapsed structures, clusters of galaxies are the largest and most recently formed (and still forming). They evolve to the typical mass of $10^{14\text{-}15} M_{\odot}$ via accretion of smaller structures and successive mergers of smaller clusters or groups (Sarazin, 2002). Most of the IGM currently observable resides in galaxy clusters where it is referred to as intracluster medium (ICM).

Due to the very deep gravitational potential and merger shocks, the ICM has been heated to extremely high temperatures ($10^{7\text{-}8}$ K), and shines brightly at X-ray wavelengths. Indeed, galaxy clusters are one of the most luminous classes of objects in the X-ray sky, and thus have been among the main targets in the field of X-ray astrophysics since the first extragalactic X-ray detection of M87 in the Virgo cluster (Byram et al., 1966).

Although most of the baryons reside in the IGM/ICM, many questions remain about the physics of this diffuse plasma. The most fundamental and important open issues regard the basic microphysical properties of the IGM, such as its effective viscosity, thermal conductivity, geometry and strength of the magnetic fields, turbulence, mixing timescale, and heating-cooling balance.

The ICM microphysics naturally plays an important role in studies of astrophysical phenomena. For example, cluster mergers are the most energetic events in the Universe, where a tremendous amount of gravitational energy ($\sim 10^{64}$ erg) is released in the ICM (Sarazin, 2002); the gravitational energy dissipates into other forms of energy such as heat, turbulence or particle acceleration. In the cluster cores, on the other hand, active galactic nuclei (AGN) inject mechanical energy into the surrounding ICM, quenching the star formation by heating or pushing out the gas, and preventing the runaway cooling of the ICM around the core (McNamara & Nulsen, 2007). The problems of how efficiently the energy dissipation happens, what fraction of the energy is channeled into each form, and how the energy is transported through the ICM, all highly depend on the microphysics of the ICM, and still remain uncertain.

Another area where microphysics plays an important role is cosmology. As galaxy clusters

are the largest virialized structures, their mass function is very sensitive to the underlying cosmology (Allen et al., 2011). Since the cluster mass and its X-ray observables are tightly correlated, X-ray observations of galaxy clusters are one of the most important cosmological probes. However, X-ray mass estimations of galaxy clusters are usually made under the assumption of hydrostatic equilibrium, and thus any deviation from the equilibrium, such as electron-ion nonequilibrium, non-thermal pressure support, or inhomogeneity of the ICM, may cause biases and preclude accurate measurements (Reiprich et al., 2013).

As shown above, it is essential to understand the physical properties of ICM from many points of view. However, the ICM is difficult to model because of its complex magnetohydrodynamic nature (Kitayama et al., 2014) and, therefore, as the extreme conditions in the ICM cannot be reproduced in a laboratory, we need to investigate these microphysical properties observationally.

When a dynamical or thermodynamic disturbance, such as a merger or an outburst of the central AGN, occurs in a system, the ICM therein must respond to the disturbance. The complex morphology of the resulting X-ray substructures provides indirect clues about the ICM microphysics.

Previous studies of X-ray substructures have been routinely done so far, but most of them have focused only on the substructure itself. In this thesis, we extend the point of view to both "higher-order" (i.e., substructures in the substructure) and "lower-order" (i.e., the relation between multiple substructures), and examine the constraints that can be placed on the plasma properties, such as viscosity, magnetic fields and the survivability of gas structures. We mainly focus on "cold front"s, which are the interface between a lower temperature, denser gas parcel and a more rarefied, hotter ambient medium, typically resulting from a merger of two systems. We selected three systems, each of which provides advantages over any other targets in certain aspects and all of which are among the brightest galaxy clusters showing a given type of substructure.

The first target is Abell 85, which is one of the most complexly interacting systems in the X-ray sky, and thus the most suitable system to study various substructures associated with the interaction, including cold fronts and shocks. We combine the data from all the three latest X-ray observatories and study the complex system comprehensively.

The second target is the Perseus cluster, which is the X-ray brightest, and one of the most deeply observed targets with *Chandra*. By exploiting the highest-quality *Chandra* data currently available, we studied the thermodynamic aspects of fine substructures which emerge in connection with cold fronts for the first time.

The last target is Abell 3667, which hosts the most prominent cold front. We investigate the front from an overlooked point of view, i.e., the azimuthal variation, and investigate the hydrodynamic aspects of the ICM in unprecedented detail.

This thesis is organized as follows; in Chapter 2, we briefly review observational aspects and important physical properties of galaxy clusters and ICM. In Chapter 3, we introduce the three latest X-ray satellites, whose data we used, and each of which has its advantages depending on the situation. In Chapter 4, we summarize the analysis techniques which are important in the subsequent chapters. In Chapters 5, 6, and 7, we present our analysis and results obtained for Abell 85, the Perseus cluster, and Abell 3667, respectively. In Chapter 8, the conclusions are presented with future prospects.

Chapter 2

Review: galaxy clusters and intracluster plasma

2.1 The Universe and galaxy clusters

The current widely-accepted picture of the Universe is that it is well described with the Λ-CDM cosmological model with its curvature being flat, consisting of ∼70% of dark energy, ∼25% of dark matter, and ∼5% of baryonic matter (Planck Collaboration et al., 2014). The large-scale structure of the Universe, in which we see filamentary overdensities as well as voids, is called "cosmic web".

Clusters of galaxies are currently known to be the largest gravitationally bound objects in the Universe. The masses of galaxy clusters are typically in the range of $10^{14\text{-}15}$ $M_{\odot}$, and the systems have typical sizes of ∼2 Mpc. A galaxy cluster typically consists of ∼85% dark matter, ∼12% diffuse hot plasma, and ∼3% galaxies and stars (Sarazin, 2011). They are located at the knots of the cosmic web, continuously growing because of the accretion flow along the cosmic web.

A galaxy cluster typically contains several tens to hundreds of bright galaxies, and more fainter galaxies (Sarazin, 2011). Indeed, clusters of galaxies were initially identified as regions of galaxy overdensities. The first systematic survey of these galaxy overdensities was performed by Abell (1958) in the optical wavelength, resulting in the so-called "Abell catalogue", which is still one of the most important galaxy cluster catalogs.

2.1.1 X-ray observational history of galaxy clusters

The first extragalactic X-ray detection of M87 in the Virgo cluster (Byram et al., 1966) with a rocket experiment was followed by X-ray detections of the Coma cluster and the Perseus cluster (Kellogg et al., 1971). Cavaliere et al. (1971) suggested a hypothesis that galaxy clusters are generally X-ray emitters. This hypothesis was confirmed by the first X-ray satellite *Uhuru* (Forman et al., 1978), which observed X-rays from 16 Abell clusters (Kellogg et al., 1973). Since then, galaxy cluster studies have been a major class of X-ray astrophysics.

Initially, the X-ray emission mechanism from galaxy clusters was a matter of debate, where the two major candidates were (1) inverse Compton scattering of CMB photons and (2) thermal bremsstrahlung radiation (Brecher & Burbidge, 1972). The discovery of an emission

feature which coincides with the line emission due to Fexxv and Fexxvi transitions by Mitchell et al. (1976) from the Perseus cluster through the *Ariel 5* rocket experiment strongly supported the scenario of X-ray emission from galaxy clusters being predominantly due to thermal bremsstrahlung.

Successive X-ray satellites such as *HEAO-1* (Peterson, 1975), *Einstein* (Giacconi et al., 1979), *ROSAT* (Aschenbach et al., 1981), *ASCA* (Tanaka et al., 1994), *Chandra* (Weisskopf et al., 2000), *XMM-Newton* (Jansen et al., 2001) and *Suzaku* (Mitsuda et al., 2007) have been extending our knowledge on galaxy clusters (Bradt et al., 1992). *Einstein*, which is the first satellite equipped with an X-ray telescope (Wolter Type I), enabled us for the first time to regularly study extended gas in galaxy clusters with dramatically improved sensitivity compared to previous missions (Helfand et al., 1980), and revealed that the morphology of X-ray emitting gas in galaxy clusters shows a remarkable variety (Murray, 1980; Forman & Jones, 1982).

ROSAT is known for the X-ray all-sky survey in the soft X-ray energy range (0.1-2 keV), using the Position Sensitive Proportional Counter (PSPC), which has a large field of view of $\sim 2^\circ$ diameter, a relatively high on-axis angular resolution of $\sim$25 arcsec, and a large effective area of $\sim$300 cm^2 at 1 keV. The all-sky survey results are still referred to as the highest-sensitivity, highest-angular-resolution soft X-ray all-sky survey to date.

Apart from the all-sky survey, it also provided many suggestive results on gas structure in galaxy clusters. For example, Huang & Sarazin (1996) observed the Hercules cluster using the *ROSAT* High Resolution Imager (HRI), and revealed the cluster to have various scales of substructures, and Boehringer et al. (1993) found X-ray cavities corresponding to the radio lobes in the center of the Perseus cluster, which showed clear evidence of the interaction between relativistic particles and ICM for the first time.

ASCA was the first X-ray satellite to employ CCD technology as a focal plane detector. Its Solid-state Imaging Spectrometer (SIS) offered for the first time opportunities of simultaneous imaging and spectroscopy in a relatively wide (0.4-10 keV) energy range. Temperature mapping, and thus the studies based on associating substructure with thermodynamics, became available. The *ASCA* observations revealed that most of the clusters are far from isothermal, and have significant temperature substructure such as merger shocks, even when the surface brightness is nearly symmetric (e.g., Henriksen & Markevitch, 1996; Markevitch et al., 1998; Churazov et al., 1999).

Another topic in which *ASCA* made breakthroughs is elemental abundance studies. Thanks to the CCD technology, measurements of the abundances of the elements other than iron became possible for the first time. For example, Fukazawa et al. (1998) measured the abundances of silicon and iron, and found that while the iron abundances depend weakly on the temperature of the ICM, the silicon abundances seem higher in the hotter clusters than in the cooler clusters, suggesting the difference in the fractions of type-Ia and type-II SNe contributing to the metal enrichment process, depending on the cluster richness.

Thanks to the largest effective area and the refined CCDs with a good angular resolution, *XMM-Newton* has been one of the most important recent X-ray missions. Werner et al. (2008) found the first observational evidence of X-ray emission from cosmic filaments between Abell 222 and Abell 223. With the Reflection Grating Spectrometer, Peterson et al. (2003) found the severe deficit of emission lines predicted from the cooling-flow model, strongly suggesting the non-existence of strong cooling flows in cluster cores, while Pinto et al. (2014) discovered Ovii emission lines for the first time, which however suggests the existence of a certain amount of cool gas. Sanders et al. (2010) put direct limits on turbulent broadening

of emission lines from ICM for the first time.

Chandra's unprecedented angular resolution revealed surprising substructures, e.g., bubbles of a variety of sizes (Fabian et al., 2000, 2006, 2011a), filaments (Fabian et al., 2008, 2011b), ripples (Fabian et al., 2006), and cold fronts (Markevitch et al., 2000; Vikhlinin et al., 2001a). It also enabled us to study substructures within a substructure, e.g., in X-ray tails (Randall et al., 2008; Sun et al., 2010) and around cold fronts (Mazzotta et al., 2002; Werner et al., 2016). In some cases, the length scale resolved with *Chandra* is comparable to the collisional length scale, and thus studies regarding the plasma physics of the ICM were made possible for the first time (Ettori & Fabian, 2000; Vikhlinin & Markevitch, 2002; Markevitch & Vikhlinin, 2007). Markevitch et al. (2002) found a first clear example of a shock front in a galaxy cluster, and the result in combination with weak lensing mass data led to one of the most important evidences for the existence of dark matter (Markevitch et al., 2004).

With the low and stable background of *Suzaku*, our knowledge on galaxy clusters has been extended out to the virial radii, where the cluster emission is very faint (Reiprich et al., 2009; George et al., 2009; Simionescu et al., 2011; Werner et al., 2013b). The entropy profiles were found to deviate from the theoretical expectation (George et al., 2009; Kawaharada et al., 2010; Simionescu et al., 2011; Walker et al., 2013), indicating the presence of some mechanisms which cause biases of the measurement, e.g., accretion shock, nonthermal pressure, or gas inhomogenieties. Studies of merger shocks associated with radio relics have been established (Akamatsu et al., 2012a,b; Akamatsu & Kawahara, 2013). Metal abundance profiles suggest the early enrichment of the elements before the cluster formation (Werner et al., 2013b; Sasaki et al., 2014; Simionescu et al., 2015).

Despite these continuous progresses of X-ray studies, a number of questions are still to be answered. One of the most important but still insufficiently revealed aspects of galaxy clusters is the microphysical properties of the ICM. Although they are gradually becoming accessible with the advent of latest X-ray missions, especially *Chandra*, the physical properties of the ICM are still investigated in rather qualitative manner. The main reason for this situation is that we virtually lack dynamical information of the ICM.

ASTRO-H and future missions

ASTRO-H (Takahashi et al., 2014), which is the sixth Japanese X-ray satellite and is planned to be launched in 2016, is equipped with four instruments; Soft X-ray Spectrometer (SXS, Mitsuda et al., 2010), Soft X-ray Imager (SXI, Tsunemi et al., 2010), Hard X-ray Imager (HXI, Kokubun et al., 2010) and Soft Gamma-ray Detector (SGD, Tajima et al., 2010; Ichinohe et al., 2016). Among the instruments, SXS is most expected to make a breakthrough, enabling turbulent strength and gas bulk motions of galaxy clusters to be measured for the first time (Kitayama et al., 2014). Measurements of gas motion also complement the high angular resolution observations by reducing the uncertainties due to the lack of dynamical information, and thus it is also expected that the studies of the ICM microphysics become more accurate and quantitative.

There are some other planned missions; *eROSITA* (Predehl et al., 2014), which is scheduled to be launched in 2017, is the first mission which will perform an X-ray all sky survey after *ROSAT*. With the sensitivity of $\sim$30 times that of *ROSAT*, it will certainly increase both the quality and quantity of the X-ray cluster data especially for cosmological use. *Athena* (Barcons et al., 2015) is the largest X-ray observatory in the 2020s. Although the planned launch year of 2028 is not a very near future, its large effective area (15 times that of *XMM-*

Newton), high grasp (a few times that of *eROSITA*), high angular resolution (5-10 arcsec, uniformly within $r = 30$ arcmin), and high spectral resolution (better than *ASTRO-H* SXS) are worth waiting for.

2.1.2 Cluster merger

Galaxy clusters grow via accretion of and mergers with smaller systems (Sarazin, 2002). Cluster mergers with the mass ratio of ~ 1 are called "major merger"s and they are the most energetic events in the Universe, where a tremendous amount of gravitational energy of $\sim 10^{65}$ erg is released.

The impact of a merger on the systems should depend on the properties of the ICM (e.g., the initial temperature structure, the magnetic field configuration, and the degree of relaxation) as well as the parameters of the merger (e.g., the impact parameter and the mass ratio). Cluster mergers are thus expected to be highly complex phenomena, and indeed there have been observations of merging clusters of various X-ray morphology (e.g., Abell 3667, Vikhlinin & Markevitch 2002; the bullet cluster, Markevitch et al. 2002; Abell 85, Ichinohe et al. 2015).

2.1.3 Galaxy clusters as a cosmological probe

As galaxy clusters are the largest gravitationally bound objects, their constituents are thought to be fair samples of the matter content in the Universe. Zwicky (1937) applied the virial theorem to the Coma cluster, and revealed that the gravitational potential of the system is much larger than one can expect from the optical luminosity, suggesting the presence of dark matter.

At present, there is a lot of observational evidence for the existence of dark matter, from e.g. galactic rotation curves, (e.g. Begeman et al., 1991), gravitational weak lensing (e.g. Clowe et al., 2006) or the observation of the cosmic microwave background (CMB, e.g. Komatsu et al., 2011; Planck Collaboration et al., 2014). However, the physical properties of dark matter remain one of the fundamental mysteries in the field of physics, except that the dark matter is thought to consist of cold, almost collisionless particles (Jenkins et al., 1998; Markevitch et al., 2004; Garrett & Dūda, 2011).

Since the indication of dark matter, galaxy clusters have been one of the most fruitful cosmological probes (Allen et al., 2011). The *ROSAT* observation of the Coma cluster showed that the cosmic baryon fraction is $\Omega_b \sim 0.05$ for the first time (White et al., 1993). The weak-lensing mass map of the Bullet Cluster clearly showed the existence of dark matter, and its collisionless nature (Markevitch et al., 2004). Examining the mass function of galaxy clusters to test the cosmological model is also a powerful tool (e.g., Burenin et al., 2007; Vikhlinin et al., 2009a,b).

Hydrostatic equilibrium

Assuming the ICM is in hydrostatic equilibrium in the cluster gravitational potential Φ, the pressure p and the mass density ρ of the ICM should satisfy the hydrostatic equation,

$$\nabla p = -\rho \nabla \Phi. \tag{2.1}$$

Assuming spherical symmetry and the ICM to be an ideal gas, the radial mass profile of the cluster $M(r)$ is calculated using

$$M(r) = -\frac{kT(r)r}{\mu m_p G}\left(\frac{d\ln\rho(r)}{d\ln r} + \frac{d\ln kT(r)}{d\ln r}\right), \tag{2.2}$$

where kT is the radial temperature profile, $\mu = 0.6$ is the mean atomic weight, m_p is the proton mass and G is the gravitational constant (Markevitch & Vikhlinin, 2007). Both $\rho(r)$ and $kT(r)$ are X-ray observables, and thus one can measure the mass of the cluster from the X-ray radial thermodynamic profiles.

One important caveat is that the assumption of hydrostatic equilibrium is probably inaccurate, especially at the outskirts of clusters (Reiprich et al., 2013). Deviations from hydrostatic equilibrium such as electron-ion nonequilibrium (e.g. Hoshino, 2012), non-thermal pressure support (Lau et al., 2009; Kawaharada et al., 2010, e.g.,), or inhomogeneity of the ICM (e.g., Nagai et al., 2007b; Simionescu et al., 2011), may cause biases in the estimation of the true mass of galaxy clusters. An improved understanding of the microphysical properties of this plasma (see also Section 2.2.1) can help us to better gauge the impact of these biases.

Self-gravitating system and beta model

When particles are bound together by their own gravity, it is called a self-gravitating system. Assuming that a system consists of a single species of collisionless particles of mass m, velocity dispersion σ^2, and number density n, the equation of state is given by $p = \sigma^2 mn$. From the hydrostatic equation, the radial density profile is calculated using

$$n(r) = n_0 \exp\left[-\frac{\Phi(r)}{\sigma^2}\right]. \tag{2.3}$$

Combining the relation above with the Poisson equation $\Delta^2\Phi(r) = 4\pi G m n(r)$, the density profile approximately follows the King model;

$$n(r) = n_0(1 + (r/r_c)^2)^{-3/2}, \tag{2.4}$$

where r_c is the characteristic radius called "core radius" (King, 1962).

Where gas and collisionless particles coexist in the same gravitational potential, two hydrostatic equations lead to an equation

$$-\frac{kT_g}{\mu m_p}\frac{d}{dr}\ln(n_g T_g) = -\sigma^2\frac{d}{dr}\ln n, \tag{2.5}$$

where the subscript g denotes the physical values of gas. Assuming that the gas is isothermal and the collisionless particles follow the King profile, the gas density is given by

$$n_g(r) = n_0\left(1 + (r/r_c)^2\right)^{-3\beta/2}, \tag{2.6}$$

where $\beta = \mu m_p \sigma^2/kT_g$ and called "beta model". The beta model describes well the observations of outer radii of clusters, but deviates from the observation of cluster cores (Sarazin, 2011).

2.2 Intracluster plasma

The tremendous amount of gravitational energy ($\sim 10^{65}$ erg) released during cluster mergers dissipates into other forms of energy, such as particle acceleration, turbulence or heat. Currently it is not understood in detail how this energy is distributed into the different channels, but most of the energy is converted into heat via merger shocks propagating through the ICM.

Heated by the merger shocks, the ICM temperature reaches $T \sim 10^{7\text{-}8}$ K, corresponding to the thermal energy of $kT \sim$ keV, and the ICM is almost completely ionized. On the other hand, the ICM density is extremely rarefied, with the typical electron number density being $n_e \sim 10^{-4\text{--}2}\mathrm{cm}^{-3}$. These extreme conditions, which cannot be reproduced in laboratory experiments, make the ICM an interesting target also from the point of view of plasma physics.

2.2.1 Microphysical properties

Coulomb collision

Because of its high temperature, the ICM is almost completely ionized. In this case, energy transport takes place mostly through Coulomb collisions. Assuming the Maxwellian energy distribution of electrons, the Coulomb mean free path of electrons is expressed as

$$\lambda_e = \frac{3^{3/2}(kT)^2}{4\pi^{1/2} n_e e^4 \ln\Lambda} \sim 15 \text{ kpc} \left(\frac{kT}{7 \text{ keV}}\right)^2 \left(\frac{n_e}{10^{-3} \text{ cm}^{-3}}\right)^{-1}, \tag{2.7}$$

where kT is the electron temperature, n_e is the electron density, e is the elementary charge and $\ln\Lambda \sim 40$ is the Coulomb logarithm (Sarazin, 2011; Markevitch & Vikhlinin, 2007). The Coulomb mean free path of protons is same as that of electrons ($\lambda_e = \lambda_p$) because the collisional timescale is proportional to the square root of the particle mass, while the kinematic velocity is proportional to the inverse of the particle mass.

Since the Coulomb mean free path is shorter than most of the length scales in clusters, generally the ICM can be treated as a collisional fluid, which follows the hydrodynamic equations. However, in several cases where the length scale of a structure is shorter than or comparable to the ICM Coulomb mean free paths (e.g. interaction between a galaxy and the ICM), the ICM may need to be treated as a collisionless fluid.

Equilibration timescale

When a population of plasma particles is in a non-Maxwellian distribution, the population gradually relaxes into the Maxwellian distribution. The equilibration timescale of such electrons $\tau_{\mathrm{eq}}(e,e)$ is expressed by

$$\tau_{\mathrm{eq}}(e,e) \sim 9.8 \times 10^4 \text{ yr} \left(\frac{kT + kT_f}{8 \text{ keV}}\right)^{3/2} \left(\frac{n + n_f}{10^{-3} \text{ cm}^{-3}}\right)^{-1}, \tag{2.8}$$

where kT and n are temperature and density of electrons, and kT_f and n_f are temperature and density of field particles (Spitzer, 1965; Sarazin, 2011), with the Coulomb logarithm $\ln\Lambda = 40$ assumed (Petrosian et al., 2008). The equilibration timescale between electrons

and protons is longer: $\tau_{\rm eq}(e,p) = (m_p/m_e)^{1/2}\tau_{\rm eq}(p,p) = (m_p/m_e)\tau_{\rm eq}(e,e) \sim 1836\tau_{\rm eq}(e,e)$, where m_p and m_e are the masses of protons and electrons respectively.

The electrons are quickly relaxed into a Maxwellian distribution of temperature T_e with the timescale of $\tau_{\rm eq}(e,e)$, then the ions are subsequently relaxed into the distribution of temperature T_i. T_e and T_i are usually different, and these two Maxwellian distributions are relaxed into a Maxwellian with a timescale of $\tau_{\rm eq}(e,p)$.

Since these $\tau_{\rm eq}$s are smaller than the typical cluster age of 10^9 yr, the ICM particles are expected to be in kinetic equilibrium with a single kinetic temperature. However, in some cases where a deviation from the equilibrium has taken place recently (e.g. cluster outskirts or just behind shock fronts), the particle population may still remain out of equilibrium, or at least the temperatures may be different between the electrons and the ions.

Radiative cooling

The ICM radiatively loses its energy by emitting X-ray photons, which is called "radiative cooling". As the most dominant radiative process of the ICM is thermal bremsstrahlung, which roughly scales as the product of electron density and ion density $n_i n_e$, the cooling function Λ (energy loss rate per unit volume; erg/s/cm^3) is usually normalized by the densities; $\Lambda = \Lambda_N n_i n_e$, where Λ_N is the normalized cooling function.

The internal energy per unit volume u, divided by the cooling function characterizes the timescale with which the gas loses its energy significantly. This timescale is called "cooling timescale" and expressed as

$$\tau_{\rm cool} = \frac{u}{\Lambda} = \frac{3}{2}\frac{n_e + n_i}{n_e n_i}\frac{kT}{\Lambda_N}. \tag{2.9}$$

Using $\Lambda_N \sim 10^{22.75}$ erg cm^3 s^{-1} for the solar-metal-abundance gas with the temperature of several keV (Sutherland & Dopita, 1993), the cooling time is ~ 2 Gyr$(kT/5\,{\rm keV})(n_e/10^{-2}\,{\rm cm}^{-3})^{-1}$, where $n_e = 1.2 n_i$ is assumed.

Generally the density of the ICM is $10^{-2\text{-}-4}$ cm^{-3}, and thus the cooling time is longer than the typical cluster age of order Gyr, which means that the ICM virtually does not cool. However, around the cluster core ($r \lesssim 100$ kpc), the density is $\sim 10^{-1}$ cm^{-3} and thus the cooling time is shorter than the cluster age. This may cause a "cooling catastrophe", a cooling instability where the cluster core loses its energy, is cooled down, shrinks, and loses the energy more rapidly, probably resulting in a very rapid complete energy consumption.

The first idea proposed to solve the problem was that a significant amount of gas is streaming to the core to support the energy loss, and called "cooling flow" (e.g. Fabian & Nulsen, 1977; Fabian, 1994). The cooling flow scenario has been tested by many observations; Edge (2001) measured the cold molecular gas mass for 16 central cluster galaxies, and found that the estimated cold gas mass represents only 5-10% of the previous estimations of the mass deposited by the cooling flows. Based on *ASCA*'s CCD imaging spectroscopy in a wide energy range, Makishima et al. (2001) pointed out that the cooling flow rates are significantly lower than the previous estimates. Using the Reflection Grating Spectrometer on *XMM-Newton*, Peterson et al. (2003) found that many of the spectral lines characteristic of low temperature X-ray gas do not exist in the spectra of the cluster cooling flow regions. Pinto et al. (2014) found O VII emission lines for the first time from individual objects, suggesting the presence of a certain amount of cool gas, but far below cooling flow rate predictions.

The absence of strong cooling flow is now widely accepted, and mechanisms suppressing the cooling are broadly examined. As the heating source, Takahara & Takahara (1981) proposed

the heat conduction from the periphery of the core, while Tucker & Rosner (1983) proposed the the energy input from the central AGN (Active Galactic Nucleus). Totani (2004) proposed that relativistic particles produced by neutralino annihilation may provide heat, and Fujita et al. (2004) proposed that the fluid instability may cause "tsunami"s and help heat to be transported from the periphery of the core. As the mechanism which transport the heat from the source to the cool core, Fabian et al. (2006) proposed sound waves and weak shocks, while Zhuravleva et al. (2014) suggested the turbulent energy dissipation.

Magnetic field

The ICM is in a plasma state, and thus is inevitably permeated by magnetic fields. Although it is difficult to determine the magnetic field strength directly, there have been a variety of attempts to constrain the magnetic field strength in clusters of galaxies. Most of the observations suggest that the ICM is significantly magnetized, with the ambient magnetic field strength of order of μG, while in some special cases, magnetic fields can be stronger to several tens of μG (Carilli & Taylor, 2002; Clarke, 2004).

When polarized radio emission from a celestial source passes through the magnetized plasma, the plane of polarization will be rotated. As the two polarization modes have different phase velocities, the overall position angle will be also rotated. The intensity of the rotation is expressed by the Rotation Measure (RM);

$$\mathrm{RM} = 811.9 \int_0^L n_e B_{||} dl \ \mathrm{rad/m^2}, \tag{2.10}$$

where the integration is performed along the line-of-sight length of the volume of the magnetized plasma L, n_e is the electron density in cm^{-3}, and $B_{||}$ is the line-of-sight magnetic field strength in μG (Clarke, 2004). The change in the position angle is expressed as $\Delta\chi = \mathrm{RM}\lambda^2$ rad, where λ is the radio wavelength, and thus the magnetic field strength can be measured by selecting several observational wavelengths appropriately.

Dreher et al. (1987) measured the rotation measure of the Cygnus A radio galaxy, and estimated the magnetic field strength in the Cygnus A cluster at 2-10 μG. Since this observation, Faraday rotation measurement has been a standard tool for measuring the cluster magnetic fields, in the cases where radio sources exist (e.g., $\sim 30\mu$ G for the tangled component in Hydra A, Taylor & Perley 1993; 3.9-5.4μG in the Coma cluster, Bonafede et al. 2010).

Another method with which we are in principle able to measure the magnetic field strength, is to incorporate radio data. Diffuse radio emission has been extensively observed in galaxy clusters. The radio emission in clusters is roughly classified into two categories; one is radio haloes, which have a relatively symmetric shape and are often found around cluster cores. The other one is radio relics, which have a more irregular shape and are often found in the cluster periphery. The diffuse radio emission is thought to originate from the synchrotron emission from relativistic electrons. The mechanism of producing such relativistic electrons has long been a matter of debate, and several hypotheses have been proposed (e.g., turbulent acceleration of electrons for the origin of radio haloes, Brunetti et al. 2001; shock acceleration of particles for the origin of radio relics, Akamatsu et al. 2012a,b; Akamatsu & Kawahara 2013).

The population of relativistic electrons attributed to the synchrotron emission can scatter the CMB (Cosmic Microwave Background) photons via inverse Compton scattering. The

emissivity of inverse Compton emission is proportional to the energy density of the CMB, while that of the synchrotron emission is proportional to the energy density of the magnetic field. Usually, synchrotron emission emerges in the radio band while the corresponding inverse Compton emission does in the X-ray band. The power-law indices α of these two spectra are same and assuming $\alpha = -1$, the magnetic field strength is calculated using

$$B = 1.7(1+z)^2 \left(\frac{S_r \nu_r}{S_X \nu_X} \right)^{1/2} \ \mu\mathrm{G}, \tag{2.11}$$

where z is the redshift of the cluster, S_r and S_X are the radio and X-ray flux densities measured at the frequencies of ν_r and ν_X (Carilli & Taylor, 2002). Therefore, when both emission components exist in a single spectrum, one can estimate the magnetic field strength by comparing the flux density of the synchrotron radiation with that of inverse Compton emission.

Because of the absence of the exponential cutoff in the spectra, inverse Compton emission is expected to be comparable to or to overwhelm the thermal bremsstrahlung emission in the hard X-ray band. Hard X-ray emission has been detected in several targets (e.g., the Coma cluster, Wik et al. 2009; Gastaldello et al. 2015; Abell 3667, Nakazawa et al. 2009; the bullet cluster, Wik et al. 2014). However, all of the hard X-ray detections are basically consistent with the hot thermal bremsstrahlung, and thus estimating the magnetic field strength using inverse Compton emission has not been successful until now. Instead, using the upper limits on the inverse Compton emission strength, several lower limits on the magnetic field strength have been placed, typically in the range of $0.1 - 1\mu$G.

In the presence of such magnetic fields, charged particles gyrate around the magnetic field lines. The typical gyroradius of a thermal electron or proton is expressed as

$$r_g = \frac{\sqrt{3mkT}}{|q|B} c_0 = 10^{-10\text{-}-9} \ \mathrm{kpc} \left(\frac{kT}{4.0 \ \mathrm{keV}} \right)^{1/2} \left(\frac{B}{\mathrm{nG}} \right)^{-1}, \tag{2.12}$$

where m is the particle mass, kT is the temperature of the particle distribution, $|q|$ is the absolute value of the charge of the particle, B is the magnetic field strength, and c_0 is the speed of light. The gyroradius is far shorter than any scales of interest in galaxy clusters, and thus transport processes across magnetic lines are generally negligible in clusters of galaxies.

Viscosity

In the existence of shear flow, the fluid viscosity is important at the interface. The force F exerted on a unit volume of the fluid at the interface is expressed as

$$F = \mu \left(\nabla^2 \mathbf{v} + \frac{1}{3} \nabla (\nabla \mathbf{v}) \right), \tag{2.13}$$

where μ is the dynamic viscosity of the fluid, and $\mathbf{v}$ is the fluid velocity, where the volume viscosity is assumed to be zero. In the absence of magnetic fields, the fiducial dynamic viscosity of a plasma is expressed by the temperature dependent isotropic Spitzer-like viscosity;

$$\mu = \frac{0.406 \sqrt{m_i} (kT)^{5/2}}{Z^4 e^4 \ln \Lambda} \sim 8000 \mathrm{g/cm/s} \left(\frac{kT}{10 \ \mathrm{keV}} \right)^{5/2}, \tag{2.14}$$

where m_i is the ion mass, kT is the plasma temperature, Ze is the charge of the ion, and $\ln\Lambda = 40$ is assumed (Spitzer, 1965; Sarazin, 1986; Roediger et al., 2013a). This viscosity value does not depend on the density, while strongly depends on the temperature.

When magnetic fields exist, the viscosity depends both on the direction of the magnetic field lines and the velocity. However, in the case that the ratio of the gyrofrequency ω to the collisional frequency $1/\tau$ is smaller than unity $\omega\tau \ll 1$, the trajectories of the particles are almost straight, and thus the effect of the magnetic fields is still small. In the existence of strong magnetic fields $\omega\tau \gg 1$, the viscosity for the velocity gradient parallel to the magnetic field is same as the Spitzer value, while the viscosity for the velocity gradient perpendicular to the magnetic field is smaller by $\sim 1/(\omega\tau)^2$ (Spitzer, 1965; Braginskii, 1958).

Viscosity may contribute to heating the ICM via friction or drag force between the member galaxies and ICM (Hunt, 1971; Sarazin, 1986). Viscosity can suppress fluid instabilities and slow down the energy transport at the interface of two gas phases e.g. the ICM and interstellar medium in a galaxy, or bubble blown by the central AGN and the ICM (Sarazin, 1986; Sijacki & Springel, 2006). Although the effect of viscosity on the ICM substructures has not been widely studied theoretically due to numerical limitations, recent numerical simulations have shown the importance of the effect of physical viscosity regarding e.g. the morphology and the survival time of substructure, or entropy generation in clusters (e.g., Sijacki & Springel, 2006; Roediger et al., 2013b, 2015b).

Observationally, the effective value of the ICM viscosity has not been extensively studied. Fabian et al. (2003) associated the structure of a filament in the Perseus cluster with a buoyant bubble and inferred the lower limit of the dynamic viscosity $\nu = \mu/\rho > 4 \times 10^{27}$ cm^2/s, while Schuecker et al. (2004) set an upper limit $\nu < 3 \times 10^{29}$ cm^2/s from the pressure power spectrum of the Coma cluster. Recently, by comparing the observational morphology of X-ray substructure with numerical simulation results, it has been suggested that the effective viscosity appears to be reduced by a factor of $\lesssim$0.1 from the Spitzer value (e.g., Roediger et al., 2013a, 2015b; Werner et al., 2016; ZuHone et al., 2015).

Thermal conductivity

In the presence of a temperature gradient, heat is conducted down the temperature gradient. When the typical scale height of the temperature gradient $T/|\nabla T|$ is longer than the Coulomb mean path of the particles and thus the ICM can be treated as a fluid, the heat flux is expressed by

$$\mathbf{Q} = -\kappa \nabla T, \tag{2.15}$$

where κ is the thermal conductivity of the ICM. For a Lorentz gas, the thermal conductivity κ_L is given by;

$$\kappa_L = 20 \left(\frac{2}{\pi}\right)^{3/2} \frac{(kT_e)^{5/2} k}{\sqrt{m_e} e^4 Z \ln\Lambda}, \tag{2.16}$$

where kT_e is the electron temperature, k is the Boltzmann constant, m_e is the electron mass, e is the elementary charge, Z is the atomic number of the ion. For an actual gas, the heat conductivity κ is reduced by a factor of order unity δ_T; $\kappa = \delta_T \kappa_L$ (Spitzer, 1965; Sarazin, 1986).

According to Cowie & McKee (1977), when the mean free path is comparable to or larger

than the temperature scale height, the heat flux is saturated to the value

$$Q_{\rm sat} = 0.4 \left(\frac{2kT_e}{\pi m_e} \right)^{1/2} n_e k T_e. \tag{2.17}$$

In the existence of magnetic fields, the thermal conductivity also varies depending on the direction with respect to the magnetic field lines, similarly to the case of viscosity.

ICM thermal conductivity has been investigated/measured in some systems, by using the sharp temperature gradients of the cold fronts (e.g., Abell 3667, Vikhlinin & Markevitch 2002; Xiang et al. 2007; Datta et al. 2014; Abell 2142, Ettori & Fabian 2000). It has been suggested that the heat conduction is suppressed by a factor of order 0.001-0.01, which is also a similar case to the case of viscosity.

Turbulence

As mentioned in Section 2.2.1, the ICM viscosity has been estimated to be suppressed significantly. In this case, the Reynolds number of the system $\mathrm{Re} = \rho U L/\mu$, where ρ is the number density of the fluid, and U and L are the characteristic velocity and length scale, is expected to be high, leading to the emergence of turbulent flows.

The turbulent energy is transferred from a certain injection scale to smaller scales (so-called "inertial scale") and eventually dissipates into heat. Assuming the turbulent properties during the inertial scale are universal, spatially isotropic and homogeneous, the kinetic energy spectrum of hydrodynamic turbulence is expressed by the Kolmogorov spectrum;

$$E(k_1) = C_K \epsilon^{2/3} k_1^{-5/3}, \tag{2.18}$$

where k_1 is the wavenumber corresponding to the length scale of the turbulence, $C_K \sim 1.65$ is the Kolmogorov constant, and ϵ is the density-normalized dissipation rate (Schekochihin et al., 2009; Brandenburg & Nordlund, 2011; Zhuravleva et al., 2014).

Turbulent motion contributes to the total pressure as a nonthermal pressure component, and thus affects the mass estimation of galaxy clusters (Evrard, 1990; Rasia et al., 2004; Brüggen & Vazza, 2015). From numerical simulations, the turbulent pressure support has been estimated at 5-20% of the total pressure, depending on the situation (Faltenbacher et al., 2005; Lau et al., 2009). Also, the turbulent cascade is one of the candidates which transports the kinetic energy of the gas to the thermal energy, balancing the radiative cooling of the ICM (Zhuravleva et al., 2014).

There have been several observations that support the existence of turbulence in the ICM. Churazov et al. (2004) found the lack of evidence for the effect of resonant scattering in the Perseus cluster, and suggested the presence of gas motion with a range in velocities of at least half of the sound speed. Schuecker et al. (2004) investigated the pressure fluctuation power spectrum of the Coma cluster and found the spectrum to be consistent with the prediction of Kolmogorov-type turbulent spectrum. Churazov et al. (2008) compared the gravitational potential profile inferred using X-ray and optical data, and suggested that the contribution of the non-thermal pressure is $\sim$10% of the thermal pressure. Recently Zhuravleva et al. (2014) have inferred the turbulent velocity power spectra of the Perseus cluster and the Virgo cluster directly for the first time, and shown that the observed power spectra are consistent with the Kolmogorov-type spectrum.

As turbulence is random motion of the fluid particles, the turbulent strength manifests itself as the broadening of the X-ray spectral lines. However, until now, X-ray high resolution

spectroscopy has been exploiting the technique of dispersive spectrometers, which is not the most suitable technique for spatially extended objects like clusters. Despite that, using the Reflection Grating Spectrometer of *XMM-Newton*, Sanders et al. (2010) performed a high-resolution X-ray spectroscopic study of the core of Abell 1835, which is a luminous, relatively high-redshift ($z = 0.2523$) cluster, and set an upper limit on the line broadening by line-of-sight velocity to be 274 km/s, and deduced that the ratio of turbulent energy density to the thermal energy density is $< 13\%$. Through resonance scattering, the relative intensity of the X-ray spectral lines also provides information about the turbulent strength (Churazov et al., 2004; Werner et al., 2009; de Plaa et al., 2012; Zhuravleva et al., 2013).

This kind of direct measurement of fine spectroscopic features will arrive at the next stage with the microcalorimeter (Soft X-ray Spectrometer, SXS; Mitsuda et al., 2010), onboard the *ASTRO-H* satellite (Takahashi et al., 2014), which is being launched in 2016. SXS is not a dispersive spectrometer and thus enables the velocity broadening to be measured without the restriction from the spatial extension of the target (Kitayama et al., 2014).

2.2.2 Radiation from hot diffuse ICM

Thermal bremsstrahlung

Because of its low density, the ICM is generally assumed to be optically thin except for the energies corresponding to the resonance lines (Böhringer & Werner, 2010). In consequence, the radiation from the ICM is mainly due to thermal bremsstrahlung. The emissivity of thermal bremsstrahlung ϵ_ν^{ff} is

$$\epsilon_\nu^{ff} = \frac{2^5\pi e^6}{3mc^3}\left(\frac{2\pi}{3km}\right)^{1/2} T^{-1/2} Z^2 n_e n_i e^{-h\nu/kT} \tilde{g}_{ff}, \tag{2.19}$$

where m is the electron mass, T is the temperature, Z is the atomic number of the ions, n_e and n_i are the number densities of electrons and ions, and $\tilde{g}_{ff}$ is a velocity averaged Gaunt factor, which depends on the temperature and the spectral frequency ν but is generally of order unity (Rybicki & Lightman, 1979). Except for the weak energy dependence of the Gaunt factor $\bar{g}_{ff} \sim E^{-0.4}$, the functional form depends on the energy only through the exponential. As a consequence, the spectrum continuum is flat and simply shows a cut off around the corresponding energy (see also Figure 2.1). By integrating ϵ_ν^{ff} over the spectral frequency, we obtain the bolometric emissivity $\epsilon^{ff} \propto n_e n_i T^{1/2} Z^2 \bar{g}_B$, where $\bar{g}_B \sim 1.2$ is a frequency average of the velocity averaged Gaunt factor.

Line emission

On top of the bremsstrahlung continuum, we also see many emission lines, which reflect the elemental composition of the ICM. For the typical cluster temperature of $2 - 8$keV, the strongest line feature is Kα emission around 6.4-6.9 keV, mainly from helium-like and hydrogen-like iron atoms. There are plenty of other lines at lower energies from other lighter species such as carbon, nitrogen, oxygen, neon, magnesium, silicon, sulfur, argon, or calcium, as well as L lines of iron and nickel. Generally these lines become more prominent at lower temperatures.

The main ionization mechanism of the ICM atoms is collisional ionization;

$$e + X^i \rightarrow e + e + X^{i+1}, \tag{2.20}$$

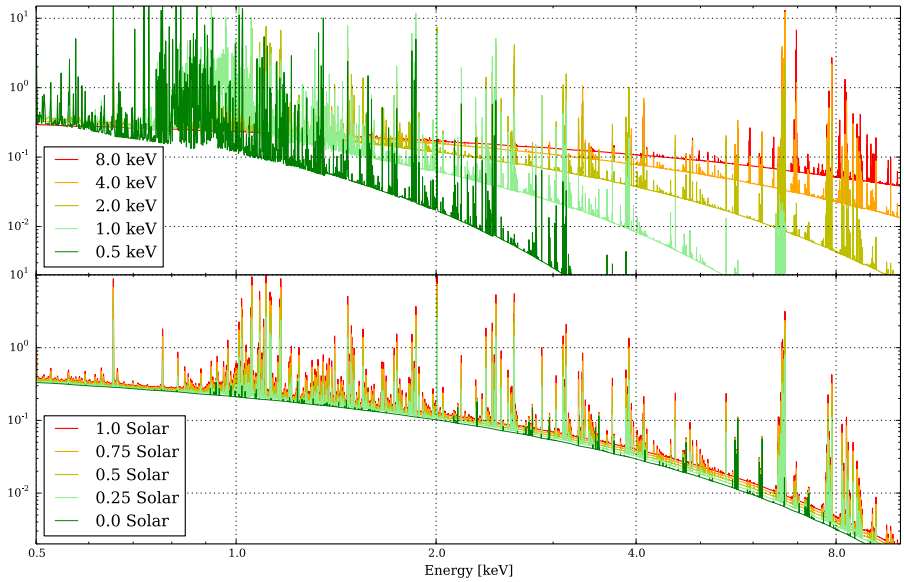

Figure 2.1 ICM energy spectra for different ICM properties. *Top:* different temperature, where the metal abundance is fixed to 0.75 Solar (Lodders, 2003). *Bottom:* different metal abundance, where the temperature is fixed to 2.0 keV. The y-axis is arbitrary, but proportional to erg/s/cm^2/keV.

where e is an electron and X^i is an atom X having been ionized i times. The main recombination mechanisms are radiative and dielectronic recombination;

$$e + X^{i+1} \left(\rightarrow X^{i**}\right) \rightarrow X^i + \gamma(\mathrm{s}), \tag{2.21}$$

where γ denotes a photon and $**$ denotes the doubly excited state.

As the above processes are not the inversion of each other, the ionization state of the ICM is not the one which is achieved in thermodynamic equilibrium with Saha's equation, but the one which is achieved in collisional ionization equilibrium. In this case, the ionization state does not depend on the particle density, but only on the temperature and the metal abundance. Figure 2.1 shows the ICM energy spectra in various setups of the ICM properties. It is clearly seen that the strength of each line is determined by the ICM temperature and the abundance of each element.

2.3 X-ray substructure

We observe various morphological features associated with dynamical/thermodynamic disturbances in the ICM, with various scales ranging from kpc to Mpc. Here we introduce X-ray substructures which are often found in galaxy clusters. Figure 2.2 shows examples of such X-ray substructure in the literature.

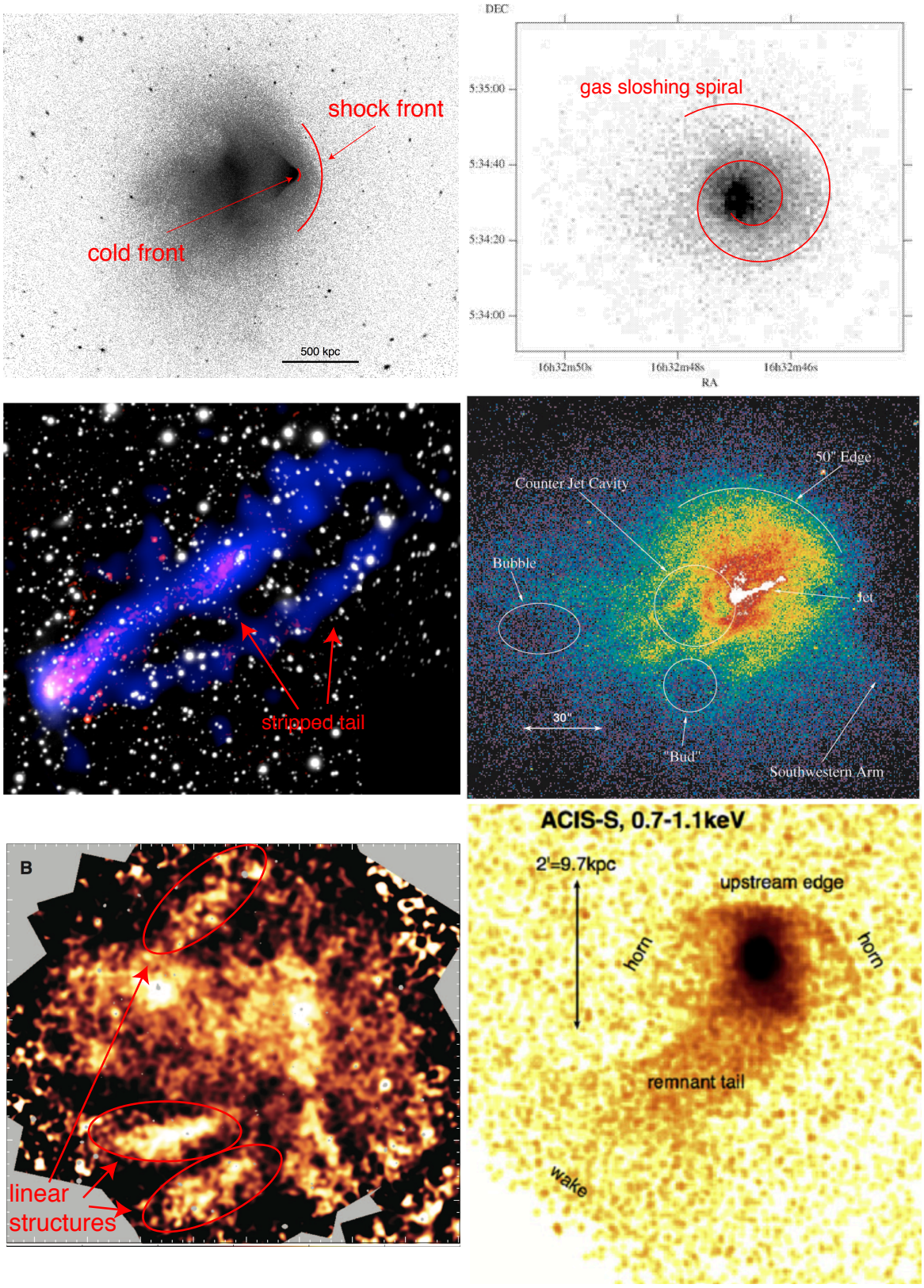

Figure 2.2 *Top left:* shock front and cold front in the Bullet Cluster, taken from Markevitch (2006). *Top right:* gas sloshing in Abell 2204, taken from Sanders et al. (2005). *Middle left:* stripped tail in Abell 3627, taken from Sun et al. (2010). *Middle right:* AGN-related substructures around M87 in the Virgo cluster, taken from Forman et al. (2005). *Bottom left:* linear structures in the Coma cluster, taken from Sanders et al. (2013). *Bottom right:* stripped tail and developing instabilities ("horn"s) around M89 in the Virgo cluster, taken from Roediger et al. (2015b).

2.3.1 Shock fronts

Supersonic motion in the ICM drives shock fronts, which propagate through the ICM, heating and compressing the gas behind them. As a result, the shock front appears as a sharp jump of the surface brightness and thermodynamic properties. Shocks, especially merger shocks and accretion shocks in the cluster outskirts, release tremendous energy, and thus should be one of the most important processes for injecting gravitational energy into the ICM. Around the core of a cluster, bubbles blown by the central AGN may also produce shocks (Randall et al., 2015).

The Mach number $\mathscr{M}$ of the shock can be calculated using the Rankine-Hugoniot jump condition for monoatomic ($\gamma = 5/3$) gas,

$$\frac{T_1}{T_0} = \frac{(\mathscr{M}^2 + 3)(5\mathscr{M}^2 - 1)}{16\mathscr{M}} \tag{2.22}$$

where T_1 and T_0 are the temperature after and before the shock front (Landau & Lifshitz, 1959; Markevitch & Vikhlinin, 2007).

The most prominent shock front may be the merger-induced bow shock in the Bullet Cluster (1E 0657-56, Markevitch et al. 2002; see also Figure 2.2 top left), providing an estimate of the velocity of the infalling subcluster. This resulted in a sensitive and direct upper limit on the dark-matter self-collisional cross section by combining the velocity with the weak gravitational lensing observation of the system (Markevitch et al., 2004). Although shock-heated regions have been observed in many galaxy clusters (see the review by Markevitch & Vikhlinin, 2007), shock fronts exhibiting both sharp temperature and density jumps are rather rare (e.g., Abell 520, Markevitch et al. 2005; Abell 754, Macario et al. 2011; Abell 2146, Russell et al. 2010).

2.3.2 Cold fronts

Initially, surface brightness drops in X-ray images were usually thought to result from shock fronts (e.g. Markevitch et al., 1999). *Chandra* observations of Abell 2142 (Markevitch et al., 2000) and Abell 3667 (Vikhlinin et al., 2001a) surprisingly revealed that, although the systems host surface brightness edges, the outer and inner temperatures of these edges are in an opposite sense than expected in the situation where they were shocks. Rather, these surface brightness jumps are the interface between a dense, cooler subcluster core and ambient medium, and are called "cold front"s.

A cold front usually forms when a volume of dense cold gas is moving through rarefied hot ambient medium. Across the cold front, the density abruptly drops where the temperature and the entropy abruptly increase. As the temperature and the density change in an opposite sense, the pressure is almost continuous across the cold front, in contrast to shock fronts. Figure 2.3 schematically shows the difference between a shock front and a cold front.

One of the remarkable aspects of cold fronts is their sharpness. Indeed most of the cold fronts are sharp both in terms of the density jump and the temperature jump, which indicates that the transport processes such as diffusion and heat conduction are suppressed. The apparent smooth interfaces of the fronts indicate that fluid instabilities are also suppressed. These features are very suggestive regarding the underlying ICM microphysics, and actually many studies have been done in this respect (e.g., Ettori & Fabian, 2000; Vikhlinin et al., 2001b; Vikhlinin & Markevitch, 2002).

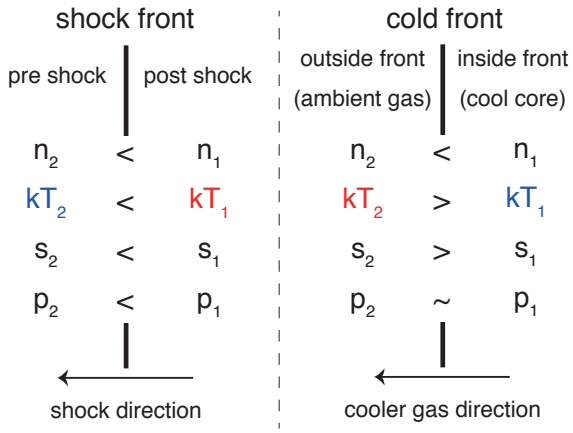

Figure 2.3 Comparison between a shock front and a cold front. n and kT are the gas density and the gas temperature. $p = nkT$ and $s = kTn^{-2/3}$ are the pressure and the entropy of the gas. The subscripts 1 and 2 denote the brighter part and the fainter part in X-ray images, respectively.

As the number of observations increase, cold fronts are found to be ubiquitous, actually more frequent than shock fronts (Owers et al. 2009b; Ghizzardi et al. 2010; see also the review by Markevitch & Vikhlinin 2007). Even a shock front accompanying a cold front has been observed (e.g., Markevitch et al. 2002; Macario et al. 2011; see also Figure 2.2 top left).

Cold fronts are generally classified into two categories. The first category are cold fronts formed directly because of a cold gas parcel flying through the ambient medium, referred to as "merger cold front"s. This type of cold fronts are found in several systems, especially in merging systems (e.g., Abell 3667, Vikhlinin et al. 2001a; the Bullet Cluster, Markevitch et al. 2002; M89 in the Virgo cluster, Machacek et al. 2006; Abell 754, Macario et al. 2011).

The other type of cold fronts are not directly related to mergers/infalls, but due to the motion of the ICM in the gravitational potential. They are called "sloshing cold front"s, and are often found around the cores of clusters which show no signs of recent mergers (e.g., Abell 2142, Markevitch et al. 2000; Abell 1795, Markevitch et al. 2001; RXJ1720.1+2638, Mazzotta et al. 2001). There are many mechanisms which can induce the motions of the ICM, but it has been shown numerically that a past merger event is an important mechanism (e.g., Ascasibar & Markevitch 2006; Roediger et al. 2011; ZuHone et al. 2011; see also the next section).

Fluid instabilities associated with cold fronts

Generally, at the interface between two fluid layers, instabilities may develop, among which two major types are Rayleigh-Taylor instability (RTI) and Kelvin-Helmholtz instability (KHI). In the presence of gravity, when the less dense gas layer is gravitationally below the denser gas layer, RTIs will develop. As cluster gravitational fields and the direction of increasing gas density are usually both toward the center, RTIs are not expected to be important (this is not necessarily the case for other kinds of substructure, e.g. AGN bubbles).

On the other hand, in the presence of finite shear flow, KHIs will emerge. Generally, shear flow of relative speed V between two inviscid, incompressible gas phases of different density

(ρ_1, ρ_2) induces exponentially developing KHIs on all length scales. The growth time of the perturbation of scale λ is

$$\tau_{\rm KHinvisc} = \sqrt{\Delta}\frac{\lambda}{2\pi V} = 10\ {\rm Myr}\sqrt{\Delta}\frac{\lambda}{45\ {\rm kpc}}\left(\frac{V}{700\ {\rm km\ s^{-1}}}\right)^{-1}, \tag{2.23}$$

where $\Delta = (\rho_1+\rho_2)^2/\rho_1\rho_2$, which means the perturbations on smaller scales grow faster than the larger scales do (Roediger et al., 2013b; Chandrasekhar, 1961).

Observationally, KHIs along sloshing cold fronts have been indicated in the literature mostly based on the morphological resemblance between X-ray images and numerical simulation results (e.g., Roediger et al., 2012, 2013a; Werner et al., 2016). On the other hand, KHIs along merger cold fronts have not been observed yet, while they have been occasionally found at their outermost azimuths (e.g., Mazzotta et al. 2002; Roediger et al. 2015a; see also Figure 2.2 bottom right).

2.3.3 Gas sloshing

When a merger occurs with a non-zero impact parameter, gravitational pull is exerted on both the ICM and the dark matter potential. During the merger, the dark matter particles, being collisionless, move toward the other cluster freely, while the ICM particles cannot because of collisional friction. As a result, the ICM distribution lags behind the dark matter potential, and gains angular momentum with respect to the dark matter potential.

Because of the angular momentum, the ICM starts to swirl in the potential. The swirling motion propagates subsonically, outward from the center of the cluster. In consequence, the ICM exhibits a characteristic morphology, namely, a spiral when the merger plane is perpendicular to the line-of-sight direction, or concentric arcs when the merger plane is parallel to the line-of-sight direction (for an example of sloshing spiral, see Figure 2.2 top right). Since the spiral arm is made of dense cold gas originating from the cluster core, the resulting radial thermodynamic profile is represented by alternating bright cold gas and dim hot gas. The spirals are often delineated by cold fronts.

Gas sloshing has been observed mainly around the core of galaxy clusters as shown in the previous section. However, recent observations have been revealing the existence of very large ($\gtrsim$500 kpc) scale gas sloshing (Simionescu et al., 2012; Paterno-Mahler et al., 2013; Rossetti et al., 2013; Walker et al., 2014; Ichinohe et al., 2015).

2.3.4 Gas stripping

When a gravitationally bound volume of gas is subjected to a flow of the ambient medium, the volume experiences ram pressure ρv^2, where ρ is the mass density of the ambient medium, and v is the flow speed. Ram pressure acts as another pressure component, and when the gravity is insufficient to hold the gas, the gas starts to be stripped off gradually, starting from the outer shell where the gravity is weak. This phenomenon is known as "ram pressure stripping" and has been observed widely from galaxy scales to cluster scales (e.g., M89 galaxy in the Virgo cluster, Machacek et al. 2006; ESO 137-001 galaxy in Abell 3627, Sun et al. 2010; Abell 2142, Eckert et al. 2014; Abell 85, Ichinohe et al. 2015; see also Figure 2.2 middle left).

2.3.5 AGN-related substructure

The AGN residing in the central elliptical galaxy in the cluster core launches powerful jets and injects mechanical energy into the ICM. The AGN-ICM interaction causes various X-ray substructure to emerge in the cluster centers (Figure 2.2 middle right).

Around cluster cores, roughly circular regions much fainter than the ambient gas have been observed widely. Many of these regions, also referred to as X-ray cavities, coincide with strong radio emission, suggesting these structures are bubbles inflated by the jets from the central AGN, filled with relativistic particles (e.g., McNamara & Nulsen, 2007; Fabian et al., 2006). X-ray cavities with no strong radio counterpart emission have also been observed (e.g., Fabian et al., 2006, 2011a), and are thought to be bubbles which are inflated by past AGN activities and where the relativistic particles can no longer be seen due to synchrotron losses. These bubbles can drive weak shocks and sound waves into the ICM (Fabian et al., 2006; Sanders & Fabian, 2007; Randall et al., 2015, e.g.,). The jet itself has also been observed (e.g. Forman et al., 2005).

When these bubbles of relativistic plasma detach from the jet and rise buoyantly through the cluster's atmosphere, they can displace and uplift the core gas (Churazov et al., 2001). Structures associated with this uplift have been observed (e.g., Forman et al., 2005); some of them are highly filamentary, indicating the importance of magnetic fields (e.g., Forman et al., 2007).

2.3.6 Linear structure

In addition to the above-mentioned filamentary structure associated with AGN outbursts, other types of coherent structures have been observed on larger scales.

Sanders et al. (2013) found linear structures in the Coma cluster (Figure 2.2 bottom left). These features probably originate from the stripped tail of merging subclusters. What is intriguing is the coherent length scale of the features, which implies a long lifetime of these features, and thus the suppression of the turbulence and conduction in the Coma cluster core, in spite of the apparent unrelaxed morphology of the Coma cluster. Werner et al. (2016) have found linear structures just below the cold front in the Virgo cluster. These features are qualitatively similar to the recent simulations of magnetized gas sloshing (e.g. ZuHone et al., 2011), and thus imply magnetic field amplification below the cold front.

2.3.7 Numerical simulations in the X-ray substructure studies

Observed X-ray substructures are usually too complex for simplified analytic modeling, and thus numerical simulations based on fluid equations are recently one of the major tools for studying ICM substructure. While numerical simulation codes had been available before, in-depth numerical studies of X-ray substructure have been developed relatively recently, driven both by the developments in computational capability and by the improvement in quality of X-ray imaging data after the launch of *Chandra* and *XMM-Newton*. Almost all kinds of X-ray substructure mentioned in the previous sections have been examined with the help of numerical simulations (e.g., AGN bubble, Churazov et al. 2001; Brüggen & Kaiser 2002; gas sloshing, Tittley & Henriksen 2005; ram-pressure stripping Roediger & Hensler 2005; mergers and shocks, Springel & Farrar 2007).

Numerical methods have also played a significant role in studies of cold fronts. A few years after the discoveries of cold fronts (Markevitch et al., 2000; Vikhlinin et al., 2001a), Heinz

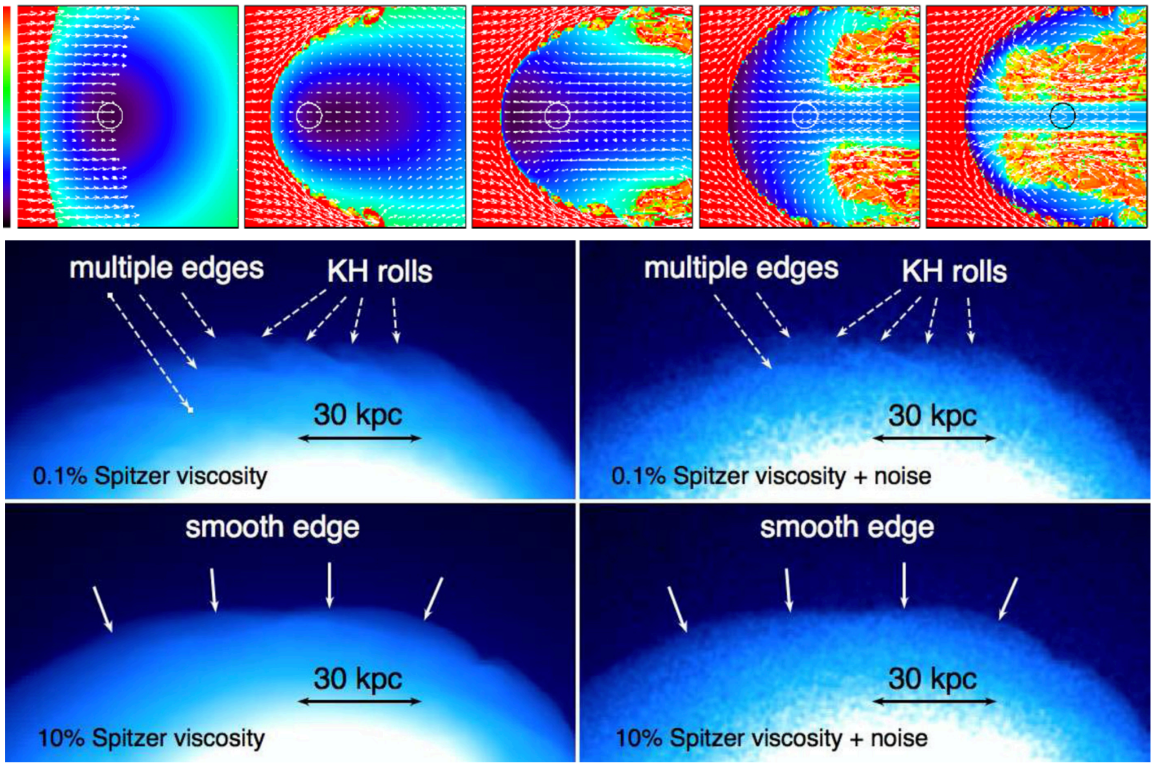

Figure 2.4 *Top:* numerical simulation of the formation of a merger cold front, reproduced from Heinz et al. (2003) and taken from Markevitch & Vikhlinin (2007). *Bottom:* numerical simulations of the development of KHIs along a sloshing cold front with different sets of microphysical parameters, taken from Roediger et al. (2013a).

et al. (2003) numerically simulated the formation of a merger cold front. They predicted that the low-entropy gas is uplifted during the formation of the cold front, and illustrated this scenario using the *XMM-Newton* data of Abell 3667. Ascasibar & Markevitch (2006) first showed that gas sloshing and the associated cold fronts can be easily induced even via minor mergers, which explains the reason of the ubiquity of cold fronts. Figure 2.4 shows examples of such numerical simulations of cold fronts.

Comparisons between the observed X-ray morphology, which represents the actual ICM physics, and the numerical simulation results, with which we can examine the effect of each ICM property, have been done in order to infer the underlying physics of the ICM. However, most of them have been rather qualitative until now. In this context, Roediger et al. (2011) comprehensively studied a cluster merger and the resulting sloshing cold fronts, and showed that the sloshing scenario can reproduce the observed morphology of the Virgo cluster quantitatively for the first time.

Recently, numerical simulations which incorporate the ICM microphysics such as magnetic field (ZuHone et al., 2011; Parrish et al., 2012; Shin & Ruszkowski, 2014; ZuHone et al., 2015), viscosity (Reynolds et al., 2005; Parrish et al., 2012; Roediger et al., 2013a, 2015b; ZuHone et al., 2015), and thermal conductivity (Parrish et al., 2009, 2012; ZuHone et al., 2013) have been a major topic. However, all of them have been performed in a parametric manner, that is, searching the parameter space varying the effective value of these microphysical properties to find the set of parameters that reproduces the X-ray morphology resembling the observed one best. Direct constraints of such parameters from observations are still an open problem, some of which the present thesis is going to address.

Chapter 3

Instruments

In this chapter, we summarize the basic information of the instruments whose data are used in subsequent chapters. Unless otherwise noted, the information is based on "The *Chandra* Proposers' Observatory Guide" (*Chandra* IPI Teams, 2014), "XMM-Newton Users Handbook" (XMM-Newton Community Support Team & XMM-Newton Science Operations Centre Team, 2014), or "The *Suzaku* Technical Description" (Pottschmidt et al., 2015).

3.1 Chandra

The *Chandra* X-ray observatory (CXO, Weisskopf et al., 2000) was launched in July 23, 1999, as one of NASA's great observatories satellite series. Figure 3.1 shows a schematic illustration of the entire satellite system, with some of the subsystems labeled. The most advantageous characteristic of *Chandra* compared to other satellites is its remarkable angular resolution, with a half-power diameter (HPD) of the on-axis point spread function (PSF) of below 0.5 arcsec, achieved by the Wolter Type-I X-ray telescope, High Resolution Mirror Assembly (HRMA, van Speybroeck et al., 1997).

In addition to the high angular resolution X-ray telescope (HRMA), it also employs two grating systems for high-resolution spectroscopy. The Low Energy Transmission Grating (LETG, Brinkman et al., 2000) and the High Energy Transmission Grating (HETG, Canizares et al., 2005) both offer resolving powers in excess of 500 in the energy range of 0.07-0.15 keV and 0.4-10.0 keV respectively.

Chandra employs two types of main focal plane detectors. The first type is CCD (Advanced CCD Imaging Spectrometer, ACIS; Garmire et al., 2003), which performs simultaneous imaging and spectroscopic observations. The other type is microchannel plate (High Resolution Camera, HRC; Murray et al., 2000), which is formally designed to be the focal plane detector of LETG, and which realizes wide-field and high-spatial-resolution observations, but without the spectral resolution comparable to CCDs. Note that, in the present thesis, we used the combination of the HRMA and the CCDs, for the purpose of imaging spectroscopy.

3.1.1 HRMA

The High Resolution Mirror Assembly (HRMA) is a logical successor of the X-ray telescopes utilized for the *Einstein* (Giacconi et al., 1979) and *ROSAT* (Aschenbach et al., 1981) missions. It consists of four pairs of concentric Wolter Type-I mirrors (Aschenbach, 1985), where four

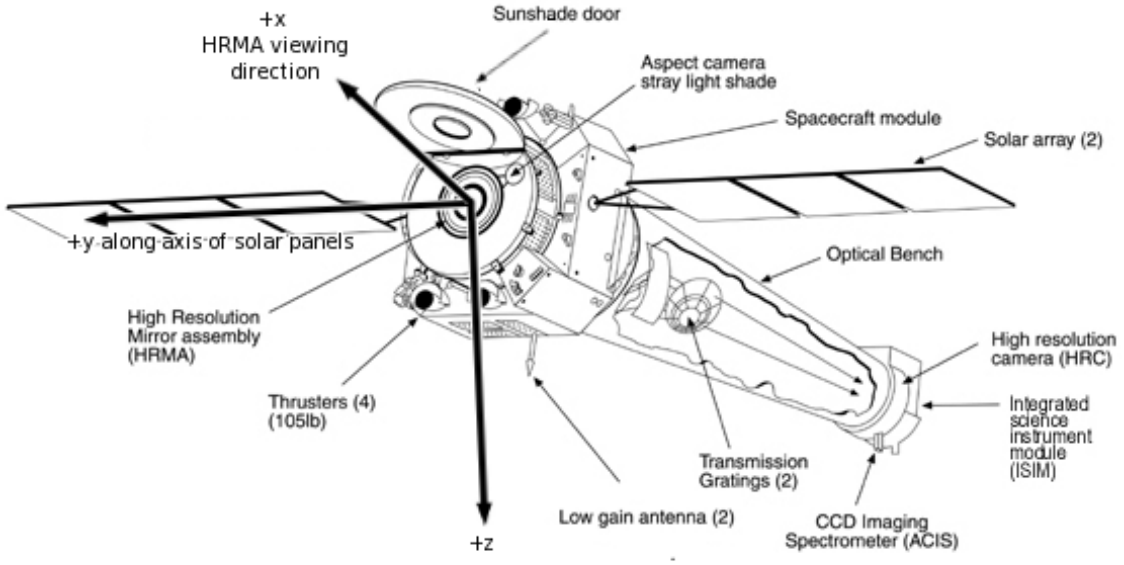

Figure 3.1 Schematic illustration of *Chandra*, taken from *Chandra* IPI Teams (2014).

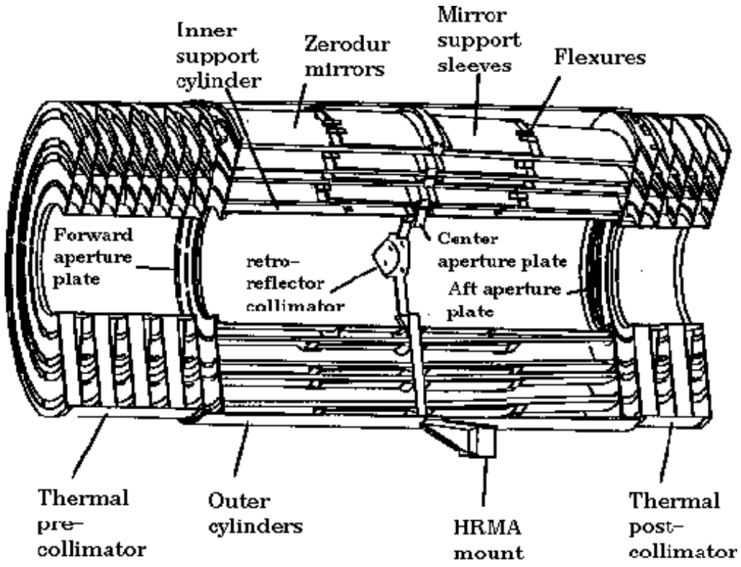

Figure 3.2 Illustration of the High Resolution Mirror Assembly (HRMA), taken from *Chandra* IPI Teams (2014).

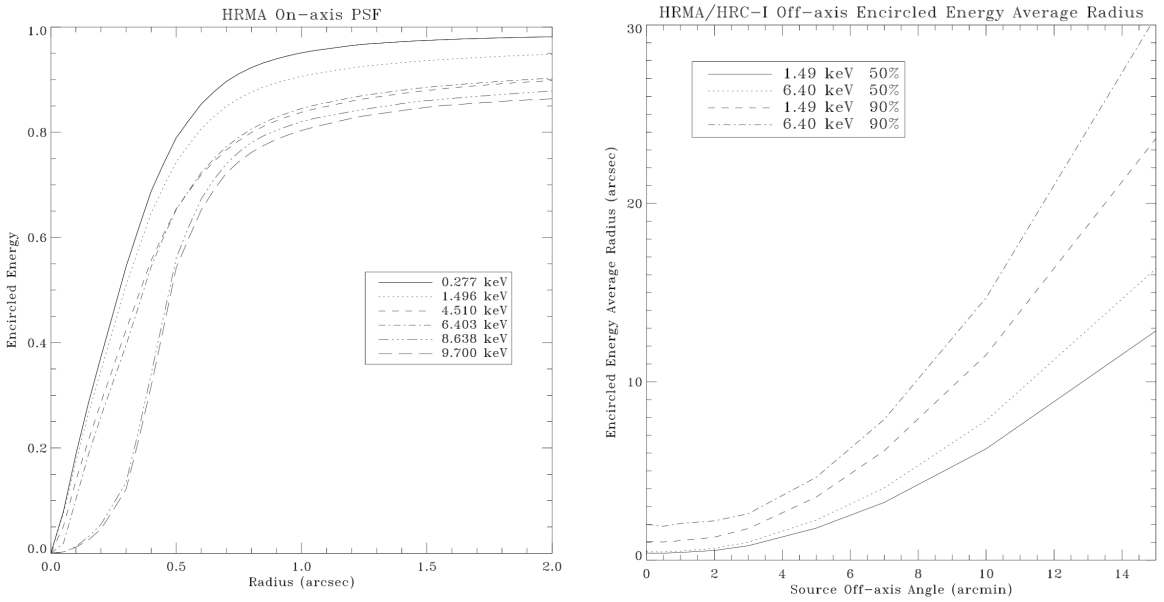

Figure 3.3 *Left:* on-axis point spread function (PSF) of HRMA. *Right:* off-axis encircled energy radii plotted against the source off-axis angle. Both figures are taken from *Chandra* IPI Teams (2014).

paraboloid mirrors and four hyperboloid mirrors, each of which is coated with iridium on a binding layer of chromium, are nested. Figure 3.2 shows the illustration of HRMA.

Figure 3.3 left shows the on-axis point spread function (PSF) of HRMA. The radius of the 50% enclosed-counts fraction aperture is less than 0.5 arcsec over most of the energy band, comparable to the ACIS pixel size of 0.492 arcsec. While the radius of the $\lesssim$ 75% enclosed-counts fraction aperture is relatively constant, that of $\gtrsim$ 80% highly depends on the energy, because the focal length of higher energies are different than the HRMA common focal length. Figure 3.3 right shows the off-axis point spread function (PSF) of HRMA. Although the PSF broadens toward the off-axis, the radius of the 90% enclosed-counts fraction aperture is less than 30 arcsec, which is better than the on-axis one of the telescope for *XMM-Newton* ($\sim$ 50 arcsec, see also Figure 3.8).

Figure 3.4 left shows the on-axis effective areas of HRMA. The geometrical effective area of HRMA is 1145 cm^2, while $<$ 10% of the geometrical area is obstructed by supporting structure. In combination with ACIS-S or ACIS-I, the on-axis effective area is $\gtrsim$ 50 cm^2 in the energy range of 0.6-7.5 keV. Figure 3.4 right shows the off-axis effective areas of HRMA. The effective area gradually decreases toward the off-axis, depending on the photon energy.

3.1.2 ACIS

The Advanced CCD Imaging Spectrometer (ACIS) consists of ten planar CCDs. Four of them are arranged in a square (2×2 array) and referred to as ACIS-I, while the other six are arranged in a 1×6 array and referred to as ACIS-S. Each CCD chip has 1024×1024 pixels, with the pixel size of 0.492 arcsec. The configuration of the ACIS is schematically shown in Figure 3.5. In addition to serving as the main focal plane detector of HRMA, ACIS-S can also serve as the main detector for the LETG or HETG. Two of the ACIS-S chips (S1 and

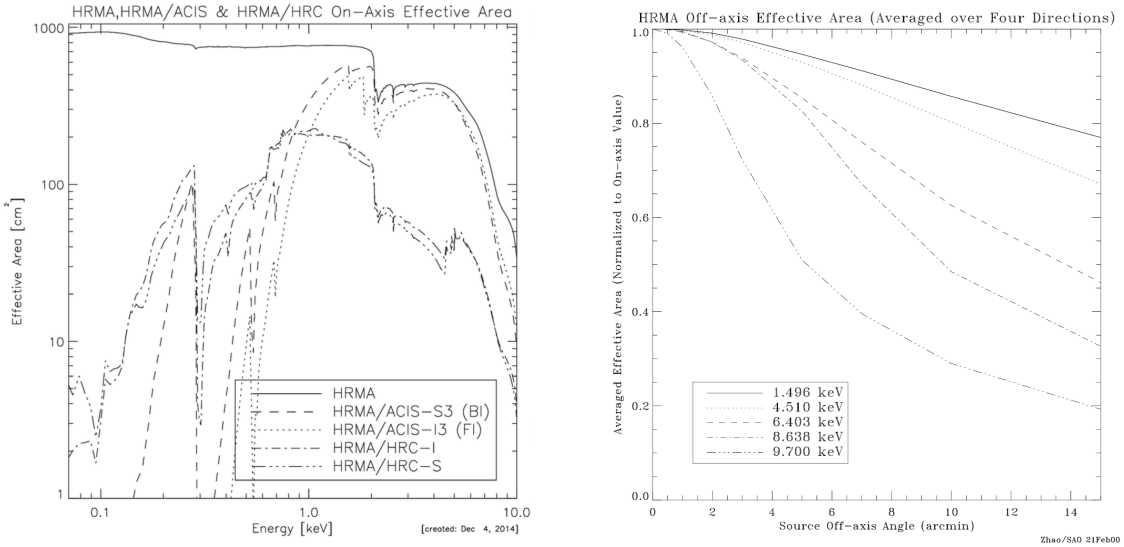

Figure 3.4 *Left:* on-axis effective areas for various combinations between optics and focal plane. *Right:* off-axis effective areas plotted against the source off-axis angle. Both figures are taken from *Chandra* IPI Teams (2014).

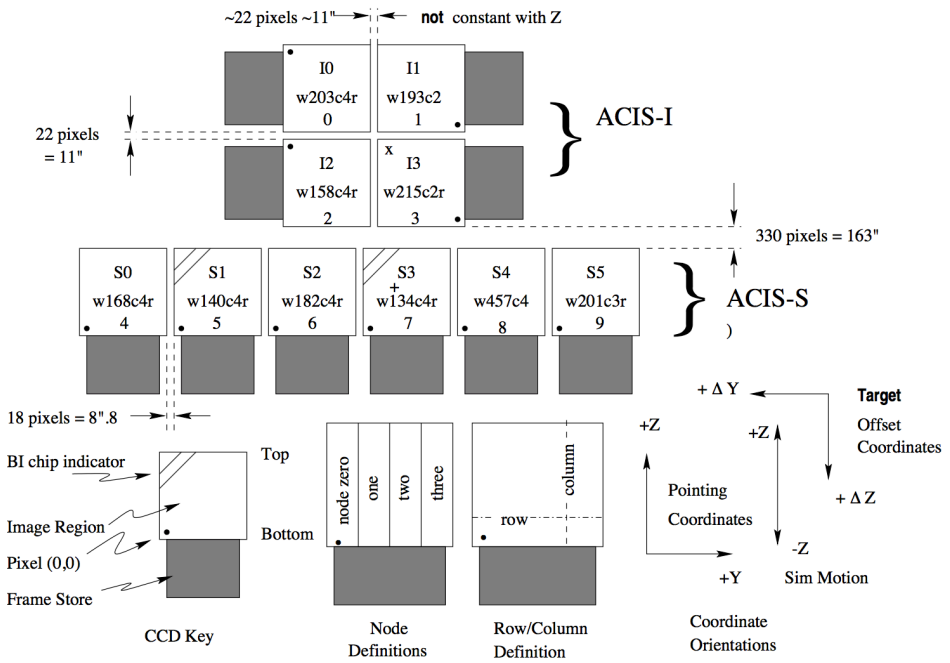

Figure 3.5 Schematic illustration of the configuration of the Advanced CCD Imaging Spectrometer (ACIS), taken from *Chandra* IPI Teams (2014).

S3) are back-illuminated (BI) chips, while the other eight chips (I0, I1, I2, I3, S0, S2, S4 and S5) are front-illuminated (FI) chips.

Figure 3.6 left shows the typical quantum efficiency of the ACIS-S chips. At higher energies, the quantum efficiency of the FI chips is better than that of the BI chips, while it is opposite at lower energies. The S3 chip is thicker than the S1 chip, thereby more efficient at higher energies. Figure 3.6 right shows the energy resolution of the ACIS chips during the pre-launch phase. The typical energy resolution (FWHM) is $\sim$ 100 eV and $\sim$200 eV for FI and BI chips, respectively.

3.2 XMM-Newton

XMM-Newton (Jansen et al., 2001) was launched on December 10, 1999, as one of ESA's four "cornerstone" missions in the Horizon 2000 Science Programme. Figure 3.7 shows a sketch of the payload of *XMM-Newton*. One of the most advantageous characteristics of *XMM-Newton* compared to other X-ray missions is the large effective area, provided by the three X-ray focusing telescopes (Aschenbach, 2002), each of which has a geometrical area of 1550 cm^2.

In addition to three CCD units (European Photon Imaging Camera (EPIC) MOS1, MOS2 and pn; Turner et al., 2001; Strüder et al., 2001), *XMM-Newton* is equipped with two essentially identical reflection grating spectrometers (Reflection Grating Spectrometer, RGS; den Herder et al., 2001), which provide a high-resolution spectroscopic capability with the resolving power in the range of 200-800, and also with an Optical Monitor (OM, Mason et al., 2001), which enables for the first time strictly simultaneous X-ray and optical/UV observations. All the six instruments can operate simultaneously, unlike *Chandra*, which requires one optics

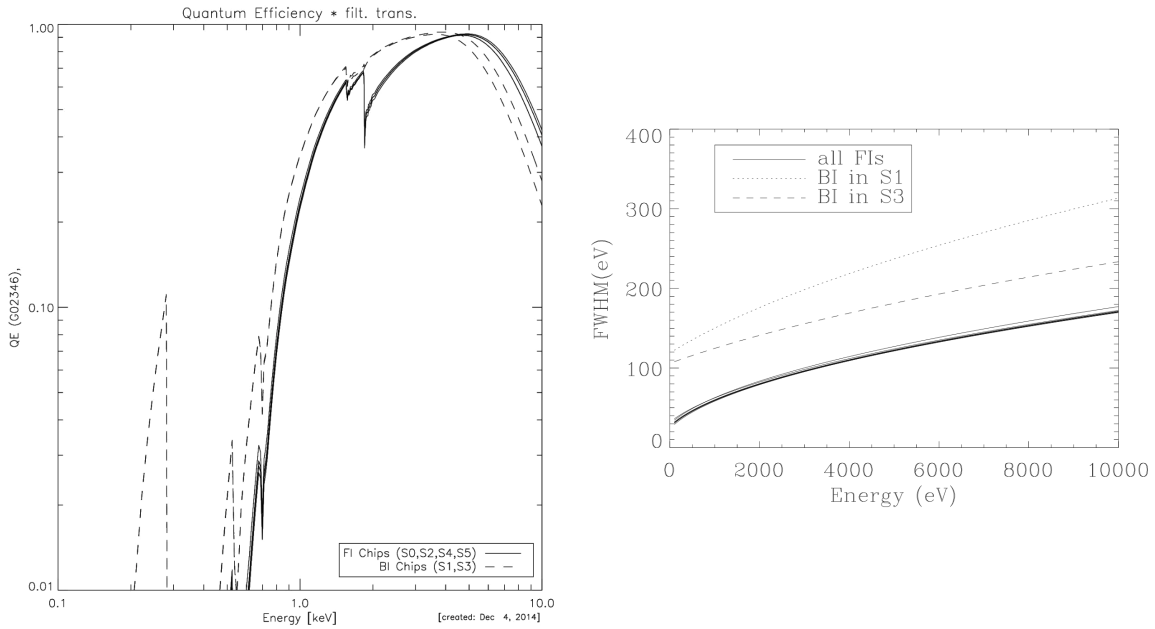

Figure 3.6 *Left:* on-axis effective areas for ACIS chips. *right:* pre-launch energy resolution of ACIS chips. Both figures are taken from *Chandra* IPI Teams (2014).

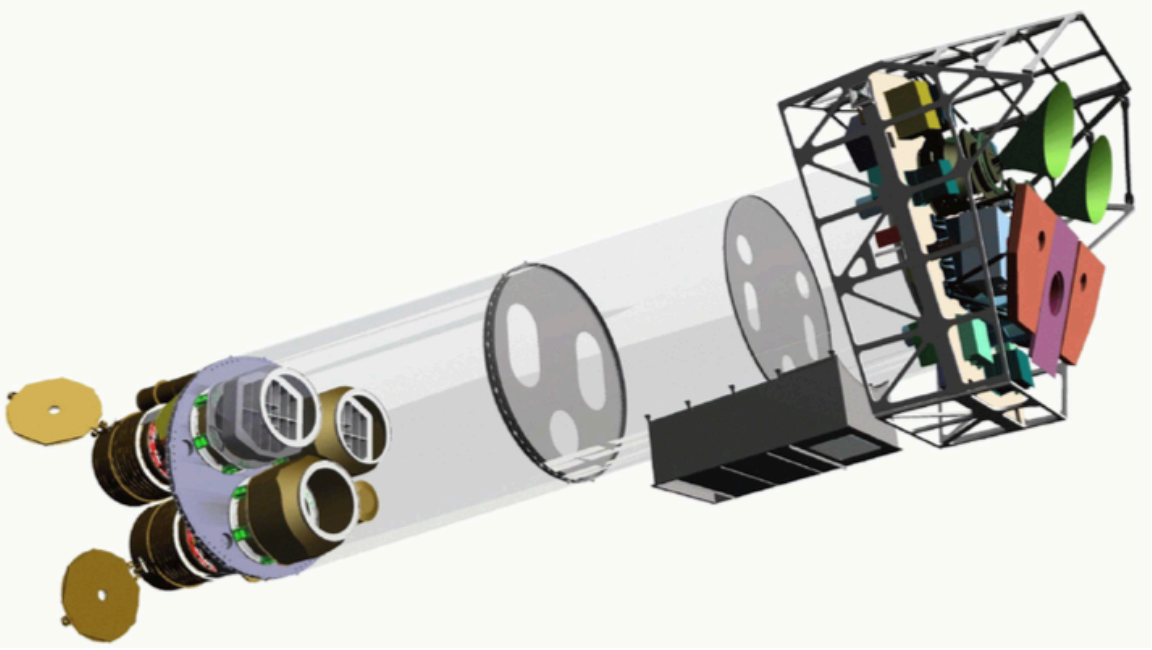

Figure 3.7 Sketch of *XMM-Newton*, taken from XMM-Newton Community Support Team & XMM-Newton Science Operations Centre Team (2014).

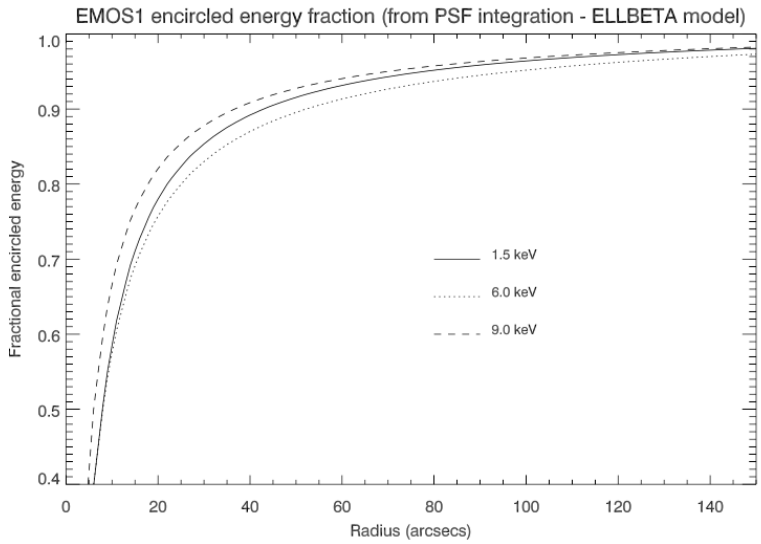

Figure 3.8 On-axis point spread function (PSF) of the X-ray telescope of EPIC MOS1, taken from XMM-Newton Community Support Team & XMM-Newton Science Operations Centre Team (2014).

and one focal plane detector module to be specified for each single observation.

3.2.1 X-ray Telescopes

XMM-Newton is equipped with three X-ray telescopes, each of which consists of fifty-eight co-axial Wolter Type-I X-ray mirrors. Two of them have grating assemblies in their light paths, in order to share the telescope between one CCD module (EPIC MOS1 or MOS2) and one RGS module. 44% of the incoming light is transmitted to the CCD module at the main focal plane (EPIC MOS1 or MOS2). The light path of the other telescope is not obstructed and thus all the photons are focused onto one of the CCD modules (EPIC pn).

Figure 3.8 shows the on-axis point spread function (PSF) of the MOS1 X-ray telescope. The half-power diameters (HPD) of the telescopes are $16.6 - 17.0$ arcsec for 1.5 keV photons, and degrade toward the larger off-axis angles. Note that the performances of the telescopes corresponding to the MOS1, MOS2 and pn detectors are different from each other, but generally show similar profiles.

Figure 3.9 left shows the on-axis net effective areas of the *XMM-Newton* X-ray telescopes, and Figure 3.9 right shows the off-axis vignetting effect. The telescopes are most efficient in the energy range of 0.2-10 keV, with the MOS+pn total effective area of $\gtrsim 100$ cm^2.

3.2.2 EPIC

The European Photon Imaging Camera (EPIC) consists of three CCD camera arrays for X-ray imaging spectroscopy. Two of the arrays are Metal Oxide Semiconductor (MOS) CCD arrays, and the other one is referred to as pn CCD array. Each MOS CCD array consists of seven independent front-illuminated CCDs with 600×600 pixels and the pixel size of 1.1 arcsec, whereas the pn CCD array consists of twelve independent back-illuminated CCDs with 200×64

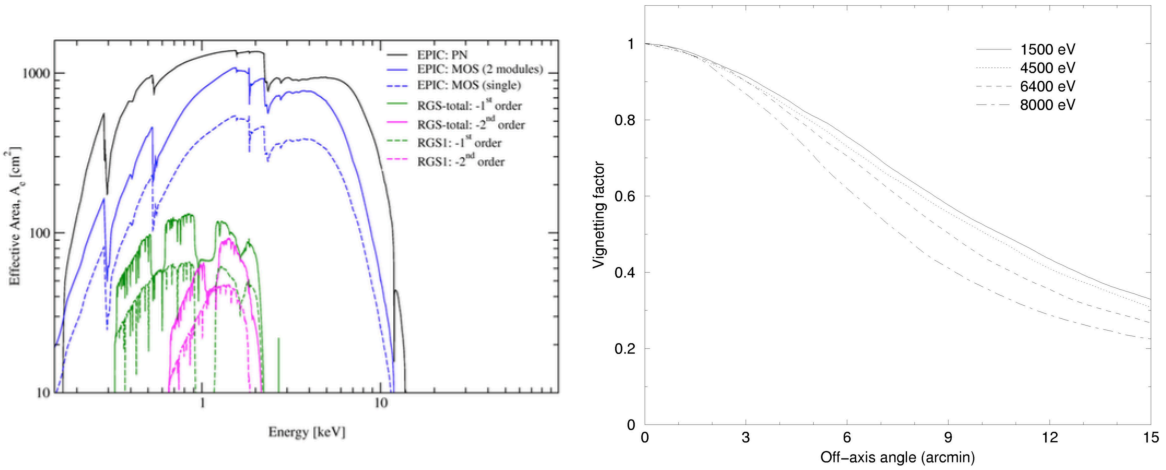

Figure 3.9 *Left:* on-axis net effective areas (including the effect of quantum efficiency). *Right:* off-axis vignetting factor plotted against the source off-axis angle. Both figures are taken from XMM-Newton Community Support Team & XMM-Newton Science Operations Centre Team (2014).

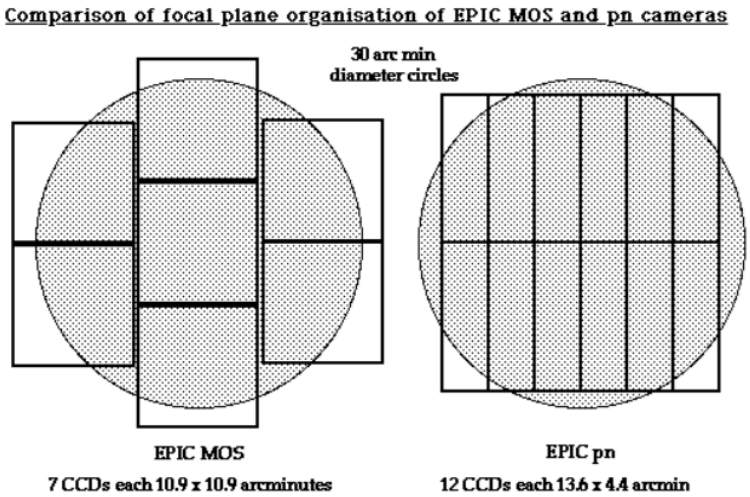

Figure 3.10 Schematic view of the arrangement of the MOS (left) and the pn (right) CCD arrays, taken from XMM-Newton Community Support Team & XMM-Newton Science Operations Centre Team (2014).

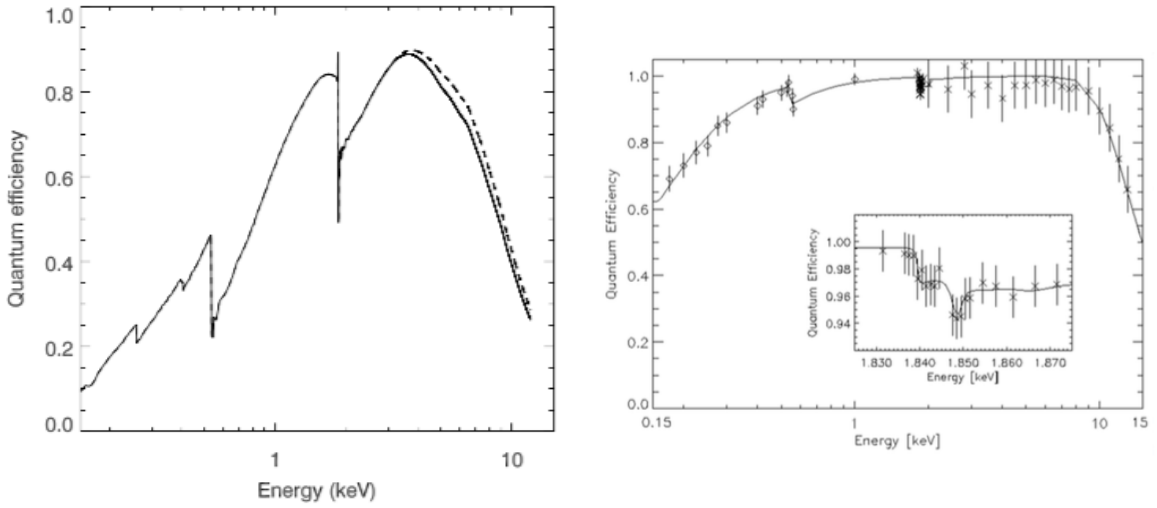

Figure 3.11 Quantum efficiency of the EPIC MOS1 (left solid line), the EPIC MOS2 (left dashed line) and the EPIC pn (right). Both figures are taken from XMM-Newton Community Support Team & XMM-Newton Science Operations Centre Team (2014).

pixels and the pixel size of 4.1 arcsec. Figure 3.10 shows the arrangement of the MOS and pn CCD arrays.

Figure 3.11 shows the quantum efficiency of both the MOS and pn CCD arrays. The quantum efficiencies of the pn CCDs are generally better than those of MOS CCDs. Figure 3.12 shows the energy resolution of both the MOS and pn CCD arrays. At the lower energies, the MOS energy resolution is better than that of pn, while it is similar to or slightly worse than that of pn above ~ 7 keV.

3.3 Suzaku

Suzaku (Mitsuda et al., 2007) is the fifth of the Japanese X-ray satellite series, launched in August 8, 2005. Figure 3.13 shows the schematic pictures of *Suzaku*. The most advantageous characteristic of *Suzaku* is its low and stable background thanks to its low earth orbit (∼550 km). *Suzaku* is equipped with four CCD modules (X-ray Imaging Spectrometer, XIS; Koyama et al., 2007) together with four corresponding X-ray telescopes (X-Ray Telescope, XRT; Serlemitsos et al., 2007), and a non-imaging Hard X-ray Detector (HXD, Takahashi et al., 2007), allowing wide-energy-band simultaneous (0.2-600 keV) observations. It is also equipped with an X-Ray Spectrometer (XRS, Kelley et al., 2007), which would have been the first soft X-ray calorimeter in orbit, but which is no longer operational because of the accidental leak of liquid helium.

3.3.1 XRT

Each of the four X-ray telescopes (XRT) consists of 175 nested reflectors made of aluminum, coated with gold. The total geometrical area per telescope is 873 cm^2. Figure 3.14 left shows the on-axis PSF of XRT. The HPD of XRT is 1.8-2.3 arcmin, which does not significantly vary within the *Suzaku* X-ray energy range of 0.2-12 keV.

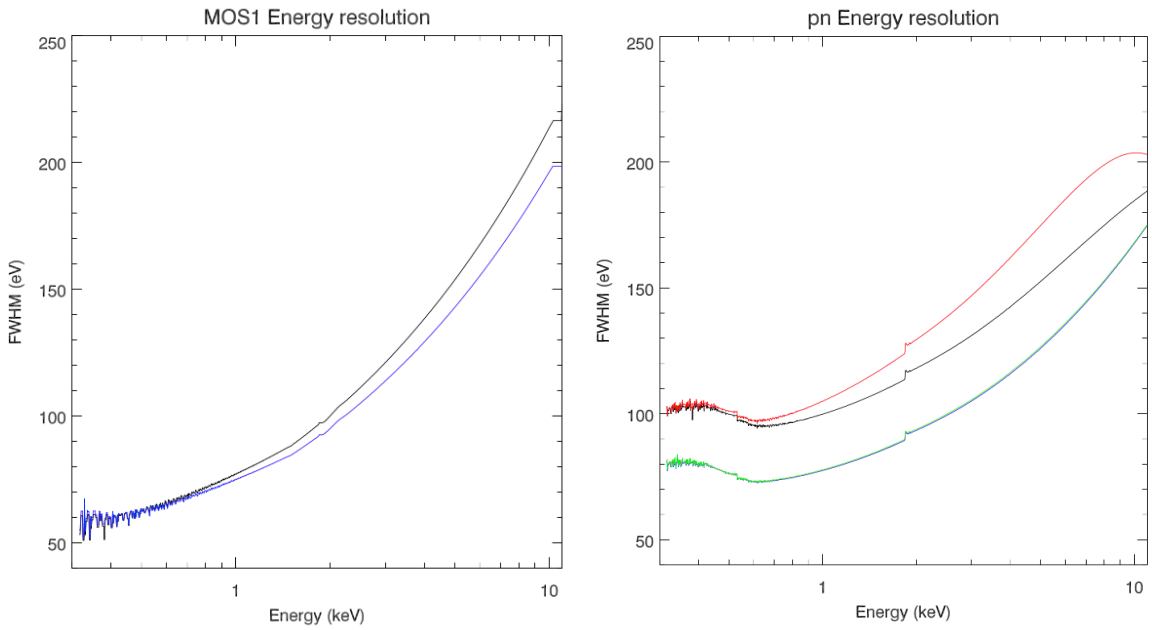

Figure 3.12 Energy resolution of the EPIC MOS1 (left) and the EPIC pn (right). The difference of the color reflects the distance from the readout nodes and event selection criteria. Both figures are taken from XMM-Newton Community Support Team & XMM-Newton Science Operations Centre Team (2014).

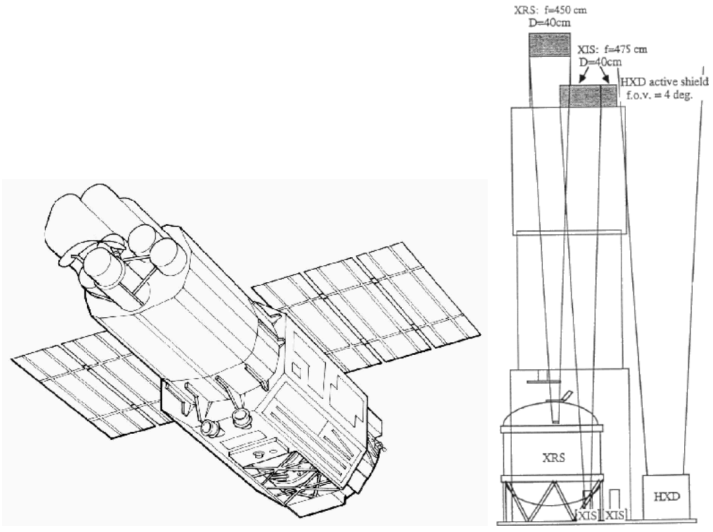

Figure 3.13 Schematic pictures of *Suzaku*, taken from Pottschmidt et al. (2015).

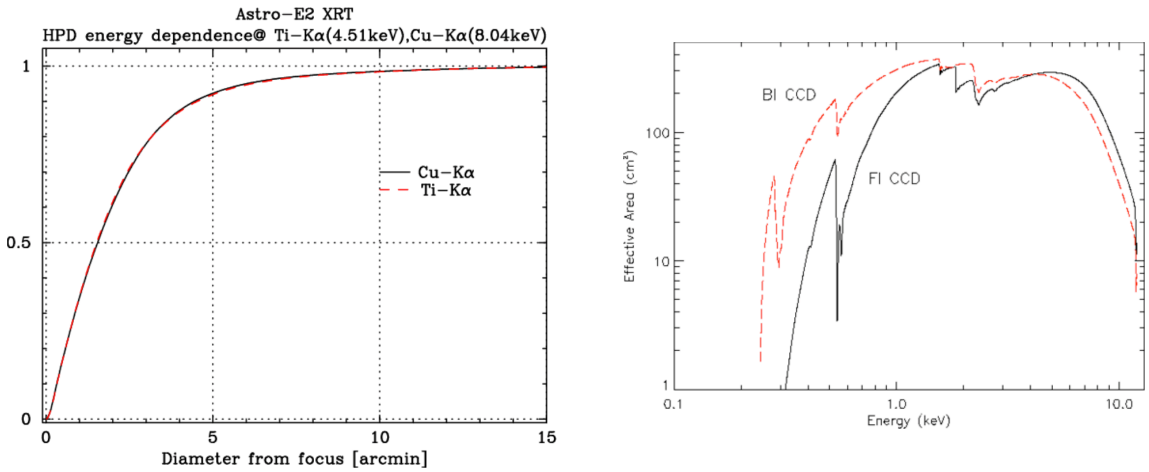

Figure 3.14 *Left:* on-axis point spread function (PSF) of XRT. *Right:* on-axis effective area of XRT, in combination with XIS CCD chips. Both figures are taken from Pottschmidt et al. (2015).

Figure 3.14 right shows the on-axis effective area of XRT. The geometrical effective area is 440 cm^2 at 1.5 keV and 250 cm^2 at 8 keV per telescope. In combination with the FI CCD chips, the net effective area per telescope is 340 cm^2 and 150 cm^2 at 1.5 keV and 8 keV, while it is 390 cm^2 and 100 cm^2 at 1.5 keV and 8 keV in combination with the BI CCD chip. The effective area decreases toward the off-axis, and becomes about a half at the chip edge.

3.3.2 XIS

The X-ray Imaging Spectrometer (XIS) consists of four CCDs, three of which are front-illuminated chips (XIS0, XIS2, XIS3), and the other one of which is a back-illuminated (XIS1) chip. Each chip has 1024×1024 pixels, with the pixel size of 1.04 arcsec, resulting in the chip field-of-view of 18 arcmin×18 arcmin. Figure 3.15 shows a photo of one of the four XIS modules. The XIS2 chip is entirely no longer operational after 2005 November due to micro-meteorite hits.

Figure 3.15 shows the energy resolutions of the XIS CCDs at 5.9 keV. The energy resolutions depend on time, but generally within the range of 150-200 eV. XIS employs the technology of Spaced-row Charge Injection (SCI), where electrons are injected periodically to fill up the charge traps occurring due to the space cosmic-ray radiation environment, which cause the degradation of the energy resolution. The break in the middle row in Figure 3.15 represents the change in the amount of SCI.

3.4 Comparison

Figure 3.16 shows a comparison of the X-ray background count rate between different X-ray satellites. Figure 3.17 shows the comparison of the effective area and the grasp. Table 3.1 shows a summary of the basic parameters of the CCD/Telescope combination of each satellite.

From the point of view of galaxy cluster observations, *Chandra* is the best satellite for investigating in detail the small-scale substructure of bright targets in detail thanks to its

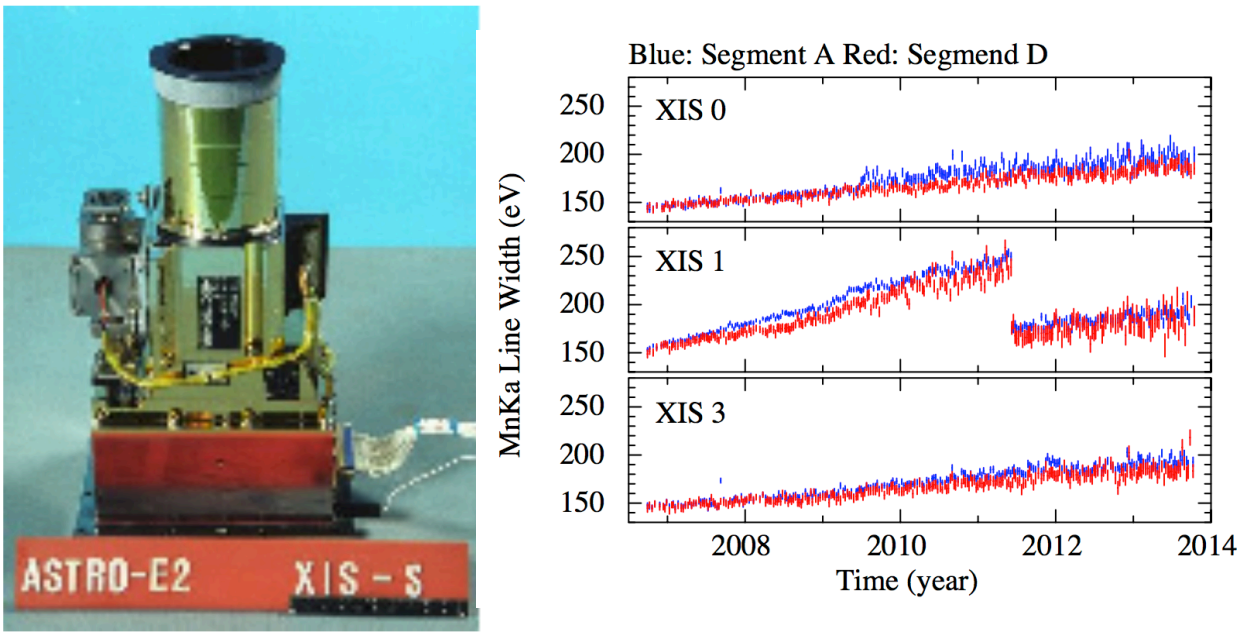

Figure 3.15 *Left:* photo of an XIS module. *Right: Suzaku* XIS energy resolutions at 5.9 keV (Mn Kα). The discontinuity in the middle row represents the change in the amount of Spaced-row Charge Injection (SCI). Both images are taken from Pottschmidt et al. (2015).

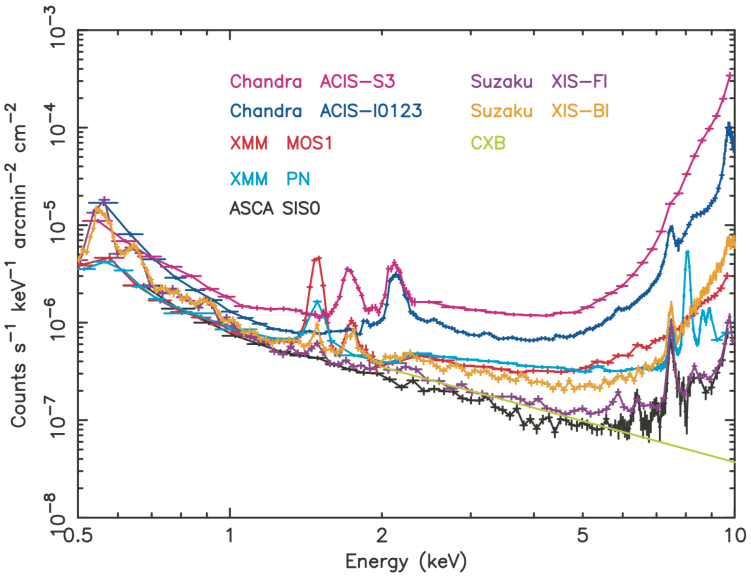

Figure 3.16 Comparison of X-ray background counting rate as a function of energy, taken from Mitsuda et al. (2007).

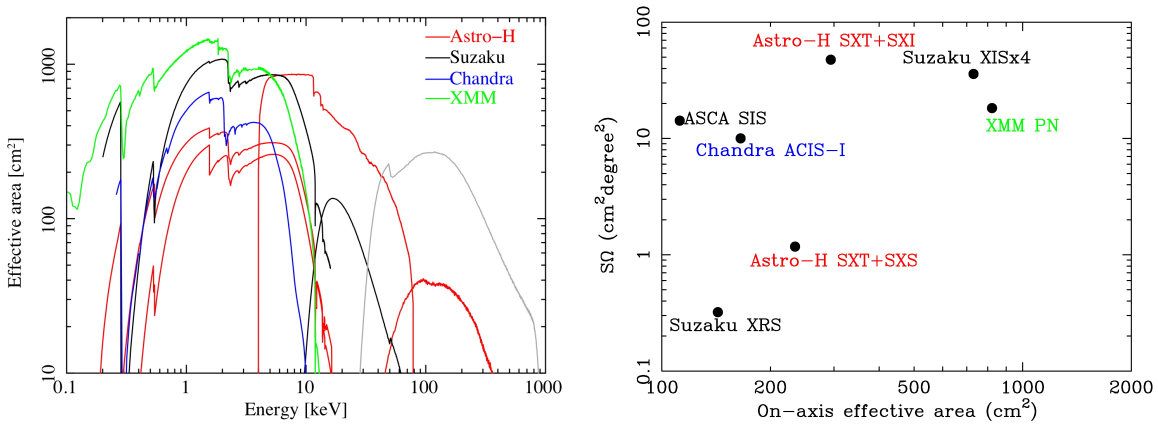

Figure 3.17 *Left:* comparison of the effective area. *Right:* comparison of the grasp. Both figures are taken from *ASTRO-H* official homepage (`http://astro-h.isas.jaxa.jp/researchers/sim/effective_area.html`).

Table 3.1. CCD/Telescope information

Parameter	*Chandra*	*XMM-Newton*	*Suzaku*
Mirror PSF (FWHM)	<0.5 arcsec	6 arcsec	1.8-2.3 arcmin
Energy range	0.1-10 keV	0.15-12 keV	0.2-12 keV
Effective area (1 keV)	555 cm^2 (ACIS-S)	4650 cm^2	1760 cm^2
Energy resolution	FI: ∼60 eV (1 keV) BI: ∼140 eV (1 keV)	MOS: ∼70 eV (1 keV) pn: ∼90 eV (1 keV)	50 eV (0.65 keV)
Single chip FOV	8.3′×8.3′	MOS: 10.9′×10.9′ pn: 13.6′×4.4′	18′×18′
Multiple chip FOV	ACIS-I: 17′×17′ ACIS-S: 51′×8.3′	∼30′ diameter	18′×18′

splendid angular resolution. *Suzaku* is the best instrument for investigating the faint outskirts of galaxy clusters thanks to its low and stable background as well as its relatively large effective area. *XMM-Newton* is the best instrument for performing spectroscopic studies of bright cluster centers thanks to the large effective area and the relatively good angular resolution. *Suzaku* and *XMM-Newton* are suitable for investigating the elemental composition thanks to their relatively high energy resolutions. With the large effective area and grasp, *XMM-Newton* is also suitable to collect large samples of galaxy clusters or survey a number of targets, where it is also an advantage that all the instruments onboard *XMM-Newton* can operate simultaneously including RGS and OM.

Chapter 4

Methods and techniques

In this chapter, we describe the data reduction/analysis methods and techniques which are common or important in the subsequent chapters.

4.1 General

Unless otherwise noted, the error bars correspond to 68% confidence level for one parameter. Throughout the thesis, we assume the standard ΛCDM cosmological model with the parameters of $(\Omega_m, \Omega_\Lambda, H_0) = (0.3, 0.7, 70$ km/s/Mpc).

4.1.1 Forward fitting

An X-ray photon emitted from celestial objects interacts with a detector not only via direct photoabsorption. It may interact with the detector via Compton scattering, resulting in a partial energy deposition. It is also possible that the photon first interacts with some other material, e.g., the frames of the detectors, then a part of its initial energy is absorbed by the detector.

In this case, the spectra which we observe are expressed as $D_i = \sum_j R_{ij} F_j$, where D_i is the data we obtain, F_j is the physical energy spectrum from the object, and R_{ij} is the response matrix which represents the probability that a photon of energy F_j is detected in the detector as energy D_i. As the unique inverse of the matrix R_{ij} does not always exist, the energy spectrum cannot be deduced directly and it is impossible to compare the data with the spectral model directly.

Thus, in order to compare a spectral model to the data at hand, the spectral model F'_j is first convolved with the response $D'_i = \sum_j R_{ij} F'_j$, and the convolved model is compared to the data D_i. This method is called forward fitting, and is the de-facto standard in X-ray astronomy.

4.2 Data reduction

4.2.1 *Chandra* data reduction

We reprocessed the archival standard level 1 event lists produced by the *Chandra* pipeline in the standard manner[1] using the CIAO software package and the CALDB to apply the appropriate gain maps and the latest calibration products.

We removed bad pixels and also applied the standard data grade selections. We examined the light curve of each observation in the 0.3-10 keV energy band with the standard time binning method recommended in the CIAO official analysis guides, to exclude periods of anomalously high background. Blank-sky background files provided by the *Chandra* team were processed in a similar manner and were scaled by the ratio of the photon counts in the data to those in the background in the high energy band (9.5-12 keV) where the effective area of the telescope is effectively zero.

4.3 Data analysis

4.3.1 *Chandra* flat-fielded image

We created the exposure and vignetting corrected, background subtracted *Chandra* images (flat-fielded image). To synthesize each full-band (0.6-7.5 keV) image, we first splitted the entire energy band into thirteen narrower energy bands (0.6-0.8, 0.8-1.0, 1.0-1.2, 1.2-1.5, 1.5-2.0, 2.0-2.5, 2.5-2.75, 2.75-3.0, 3.0-3.5, 3.5-4.0, 4.0-6.0, 6.0-7.0 and 7.0-7.5; all in keV), and generated the background subtracted image and the corresponding exposure map for each narrow energy band[2]. These narrow-band images are combined together to form a full-band image.

4.3.2 Unsharp-masking

Unsharp-masking is an imaging technique which is used to emphasize the edges in the image. In order to emphasize the low-contrast surface brightness structures, we created the unsharp-masked images by dividing the $\sigma = \sigma_1$ Gaussian smoothed flat-fielded image by the $\sigma = \sigma_2$ Gaussian smoothed one, where $\sigma_1 < \sigma_2$. In this case, roughly speaking, the edge features between the length scales of σ_1 and σ_2 are emphasized. The values of σ_1 and σ_2 are different for the different targets analyzed and given in the corresponding subsequent chapters.

4.3.3 Thermodynamic mapping

To explore the two-dimensional thermodynamic structure, we conducted (projected) thermodynamic mapping. We adopted the contour binning algorithm (Sanders, 2006), which divides the entire field of view into smaller regions, based on the statistical error of each bin calculated from the raw and the background counts, so that all the bins have similar statistical signal-to-noise (S/N) ratio.

For each of the bins, we extracted the spectra and fit them using a single-temperature thermal plasma model absorbed by the Galactic absorption (i.e. assuming that the spectra are represented by single-temperature thermal plasma). We translated the best-fitting

[1] CIAO 4.7 Homepage, Data Preparation; http://cxc.harvard.edu/ciao/threads/data.html
[2] CIAO 4.7 Homepage, Imaging; http://cxc.harvard.edu/ciao/threads/imag.html

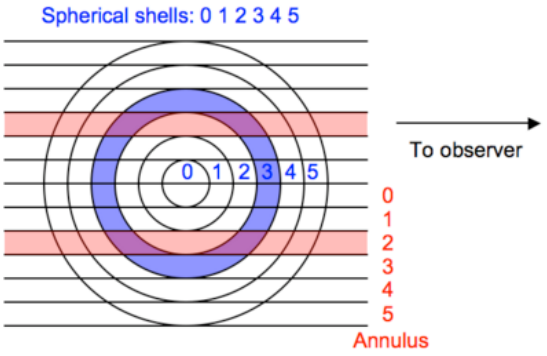

Figure 4.1 Conceptual illustration of deprojection, taken from "deproject v0.1.3 documentation"[3].

normalization value to the physical number density of the ICM, assuming that the ICM is uniform along the line-of-sight, that the line-of-sight depth of the ICM is also uniform over the entire field of view with the value of l, and that the electron density $n_{\rm e}$ and hydrogen ion density n_H satisfy a relation $n_{\rm e} = 1.2 n_H$. The calculated density n is combined with the best-fitting temperature value kT for the calculation of the pressure ($p = nkT$) and the entropy values ($s = kTn^{-2/3}$).

Note that, although the uniform line-of-sight depth assumption is arbitrary, it should not significantly bias conclusions based on the variations in the thermodynamic maps. On the other hand, because we observe emission measure weighted thermodynamic quantities, projection effects in the presence of multiphase gas may bias our quantitative measurements.

4.4 Techniques

4.4.1 Deprojection analysis

Clusters of galaxies are spatially extended not only in the sky plane, but also in the line-of-sight direction. Since the radiation from the ICM is optically thin, the energy spectrum $F_\nu(E)$ which we observe is the integral of the bremsstrahlung emission from each volume element along the line-of-sight;

$$F_\nu(E) \propto \int_V \epsilon_\nu^{ff} dV \sim \int_V \frac{n(V)^2}{\sqrt{kT(V)}} e^{-E/kT(V)} dV, \tag{4.1}$$

where $n(V)$ and $kT(V)$ are the ICM density and temperature, which depend on the position. It is clear that the actual spectrum that we observe does not have a form of $(kT)^{-1/2} n^2 e^{-E/kT}$, indicating that the temperature derived from the spectrum assuming the ICM being single-temperature thermal plasma is significantly biased unless the ICM is isothermal, which is unlikely especially when we observe near the cluster center. However, if the projected 3-dimensional geometry of the ICM is known, or by assuming it, we can mitigate the above-mentioned projection effect. This technique is called "deprojection", and is widely used in the study of diffuse objects.

[3] http://cxc.harvard.edu/contrib/deproject/

The conceptual illustration of deprojection is shown in Figure 4.1. In this case, assuming that the cluster is spherically symmetric and the ICM in each shell is isothermal, the observed spectrum in the annulus i is proportional to $\sum_{j=i}^{5} V_{ji}\epsilon_{\nu,j}^{ff}$, where V_{ji} is the line-of-sight volume of the spherical shell j, projected onto the annulus i, and $\epsilon_{\nu,j}^{ff}$ is the ICM emissivity in the spherical shell j. Since V_{ji} can be calculated analytically, the contribution from each shell can be decomposed.

Chapter 5

Substructures in Abell 85

Most of the contents in this chapter are taken from Y. Ichinohe, N. Werner, A. Simionescu, S. W. Allen, R. E. A. Canning, S. Ehlert, F. Mernier, T. Takahashi, "The growth of the galaxy cluster Abell 85: mergers, shocks, stripping, and seeding of clumping", Monthly Notices of the Royal Astronomical Society, Oxford Journals, 448(3), pp2971-2986, 2015 (Ichinohe et al., 2015). *XMM-Newton* data reduction is done by F. Mernier. *Suzaku* data reduction and analysis are done by A. Simionescu.

5.1 Overview

Abell 85 ($z = 0.055$, Oegerle & Hill, 2001) is the seventeenth brightest cluster of galaxies in the X-ray sky (Edge et al., 1990). It has been observed with various X-ray instruments, e.g. *Chandra* (Kempner et al., 2002), *XMM-Newton* (Durret et al., 2003, 2005a), *Suzaku* (Tanaka et al., 2010), and also in other wavelengths, e.g. radio (Slee et al., 2001; Schenck et al., 2014). The main cluster hosts an X-ray bright, metal rich, "cool core", and a recent optical study (López-Cruz et al., 2014) has shown its brightest central galaxy, Holm 15A, is the largest one known so far.

Abell 85 is also one of the most complex interacting systems known. Currently, at least two subclusters are falling into the main cluster: one from the south and the other from the southwest (Kempner et al., 2002; Durret et al., 2005a). Additionally, the ICM distribution shows an indication of sloshing (Laganá et al., 2010).

The subcluster falling in from the south (S subcluster) also has a bright central galaxy surrounded by cool X-ray gas. It has a clear tail structure, extending to the southeast, previously seen in both *Chandra* and *XMM-Newton* images. Previous *Suzaku* observations (Tanaka et al., 2010) detected a possible shock front in the northeast of the subcluster.

The second subcluster located towards the southwest (SW subcluster) has not previously been studied in detail, but Schenck et al. (2014) revealed the gas in the interface between the main cluster and this subcluster to have a high temperature. This region may be caused by a shock front induced by the SW subcluster merger, but associated radio emission has not been detected except for relic structures which are located at $\sim$150 kpc west of the interface region.

The above mentioned remarkable dynamical activities make Abell 85 an excellent system to investigate the X-ray substructure in galaxy clusters and its role with respect to the ambient medium or interaction between different substructures. We study the system comprehensively,

Table 5.1. Data

Satellite	Obs ID	Date	Detector	Net exposure time (ksec)[a]
Chandra	15173	2013-08-14	ACIS-S	39
Chandra	15174	2013-08-09	ACIS-S	36
Chandra	16263	2013-08-10	ACIS-S	37
Chandra	16264	2013-08-17	ACIS-S	34
Chandra	904	2000-08-19	ACIS-S	37
XMM-Newton	0065140101	2002-01-07	EPIC	12
XMM-Newton	0065140201	2002-01-07	EPIC	12
XMM-Newton	0723802101	2013-06-16	EPIC	97
XMM-Newton	0723802201	2013-06-18	EPIC	98
Suzaku	12025	2007-01-05	XIS	82
Suzaku	12033	2012-12-31	XIS	127
Suzaku	12036	2013-01-03	XIS	50

Note. — (*a*) The net exposure time is after the data screening.

by using all the latest X-ray satellites, namely, *Chandra*, *XMM-Newton*, and *Suzaku*. Four of the *Chandra* pointings, two of the *XMM-Newton* pointings, and two of the *Suzaku* are all taken recently, which enables us to study this system with an unprecedented detail.

Unless otherwise noted, we used SPEX (version 2.04.01, Kaastra et al., 1996) for the spectral fitting to minimize the modified C-statistic estimator (Cash, 1979; Nousek & Shue, 1989), which is the Poisson likelihood statistics, because some of the spectral bins contain very few counts. The error bars are calculated from the interval where the fit statistics increases by 1, which approximately corresponds to 1σ confidence interval (Cowan, 1997; Arnaud et al., 2011). We used the chemical abundance table determined by Grevesse & Sauval (1998).

5.2 Observations and data reduction

5.2.1 *Chandra* observations

We reprocessed the standard level 1 event lists of four newly observed pointings (ObsID 15173, 15174, 16263 and 16264) and one archival observation (ObsID 904) produced by the *Chandra* pipeline. The details of the data reduction are shown in Section 4.2.1. The software versions were CIAO 4.6, and CALDB 4.6.2. The net exposure times of each observation are summarized in Table 5.1.

Imaging analysis

We created the flat-fielded *Chandra* image as described in Section 4.3.1. Figure 5.1 shows the flat-fielded *Chandra* image (left, 0.6-7.5 keV). Also shown is the SDSS optical r-band image of

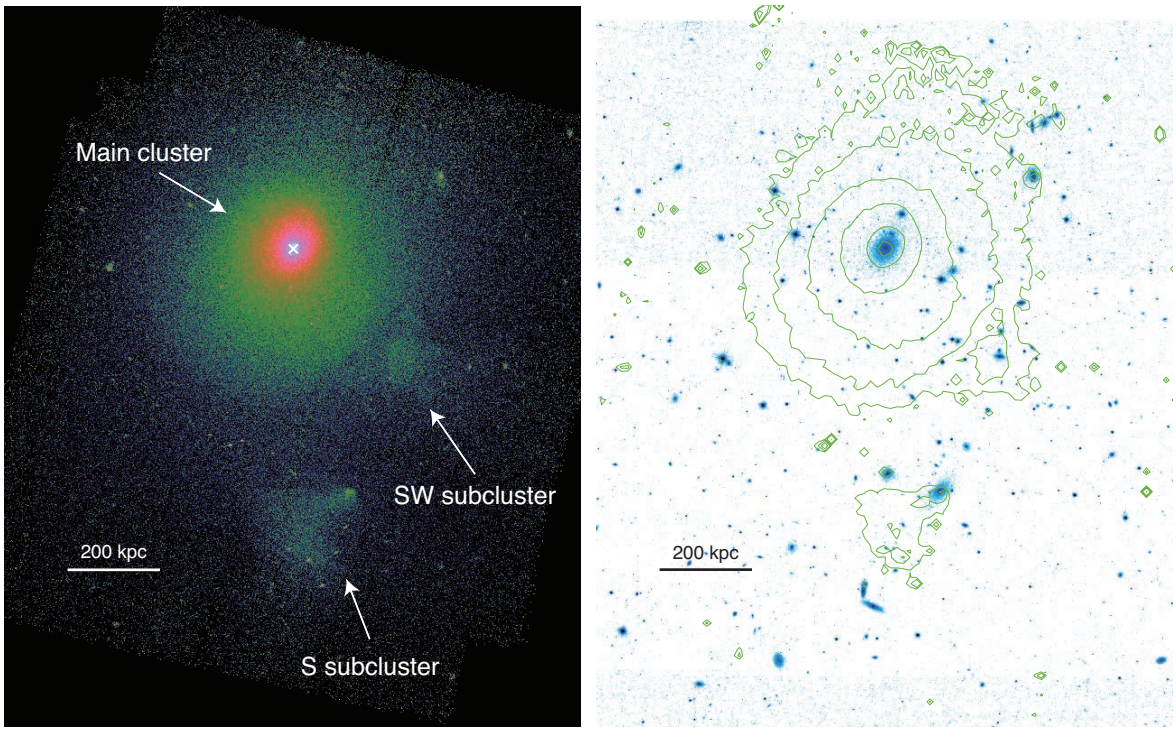

Figure 5.1 *Left*: $\sigma = 0.98$ arcsec Gaussian smoothed, exposure and vignetting corrected, background subtracted *Chandra* image of Abell 85 (0.6-7.5 keV). The cross represents the position of the central cD galaxy of the main cluster. *Right*: SDSS r-band optical image of the same sky region overlaid with *Chandra* X-ray contours.

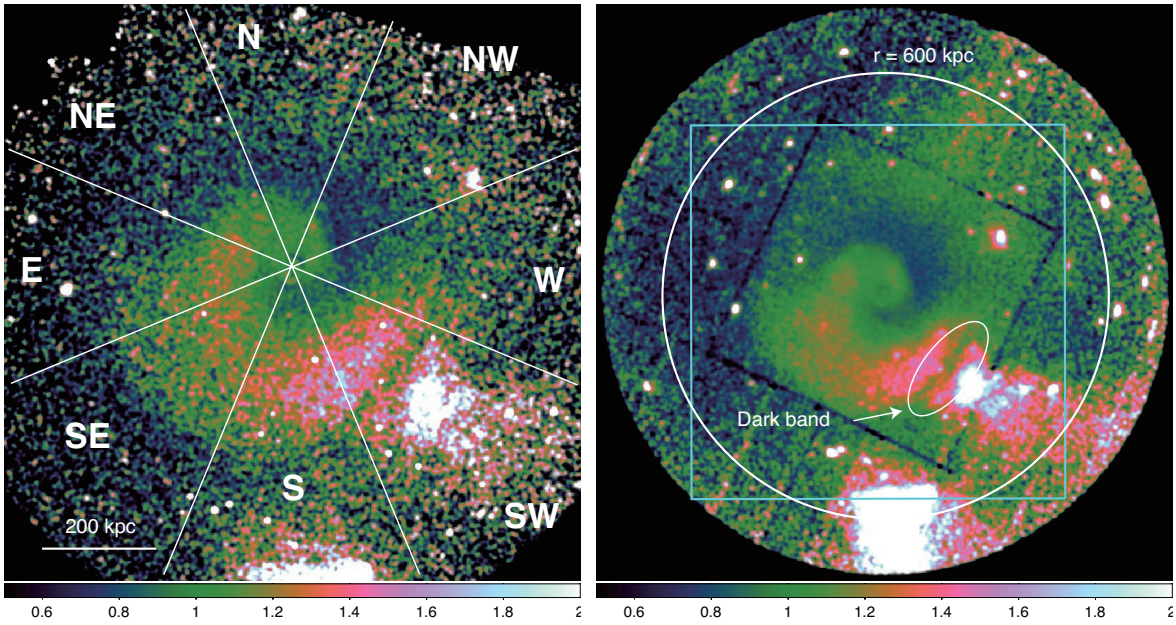

Figure 5.2 *Left*: $\sigma = 5.6$ arcsec Gaussian smoothed, *Chandra* relative deviation image with respect to the best-fitting 2D elliptical double beta model. We illustrate the eight directions for which projected radial profiles are extracted in Section 5.4.2 with the white lines. *Right*: $\sigma = 8.3$ arcsec Gaussian smoothed, *XMM-Newton* relative deviation image. The white circle denotes the radius of 600 kpc from the main cluster core, and the cyan square denotes the FOV of the *Chandra* relative deviation image. There is a dark narrow structure (Dark band) at the interface region of the main cluster and the SW subcluster.

the same field overlaid by *Chandra* X-ray contours (right, Eisenstein et al., 2011; Ahn et al., 2014).

To emphasize the small azimuthal asymmetries which cannot be clearly seen in the original images because of the overall surface brightness gradient, we created relative deviation images of the system with respect to the best-fitting 2D elliptical double beta model. We used SHERPA for fitting the sum of two 2D elliptical beta models: `beta2d+beta2d`. The centre positions (`xpos`, `ypos`), ellipticities (`ellip`) and roll angles (`theta`) were bound between the two beta models. Based on the *Chandra* image, the best fit ellipticity of the cluster is 0.17, and its long axis extends at 25 degrees clockwise from the north. After the best-fitting parameters were determined, we divided the original images by the best-fitting models. In Figure 5.2, we show the relative deviation images.

Thermodynamic mapping

We created the thermodynamic maps as described in Section 4.3.3. The assumed line-of-sight depth is $l = 1$ Mpc. The S/N ratio of each bin is about 33 (density) or 70 (temperature, pressure and entropy), corresponding to about 1100 counts/bin and 4900 counts/bin, respectively. The resulting thermodynamic maps are shown in Figure 5.3. The black ellipses are the point sources which were detected and excluded using the `wavdetect` tool in the CIAO software package with the scales of 1, 2, 4, 8, 16 pixels. We visually eliminated the false detections within 200 arcsec from the main cluster core and the S subcluster core.

In the spectral fitting, the redshift was fixed to 0.055 and the hydrogen column density was set to 2.8×10^{20} cm^{-2}, determined by the LAB (Leiden/Argentine/Bonn) radio HI survey (Kalberla et al., 2005). We obtain typical fitting errors of 5% for the density map, and 10% for the temperature, pressure and entropy maps[1]. Figure 5.5 shows the example fitting results for the region on the main cluster core and the highest temperature region.

In order to emphasize the small azimuthal variations of these quantities, we also created the trend-divided thermodynamic maps shown in Figure 5.4. The scatter plots of each physical quantity versus distance from the main cluster core were fitted with a function using the form $f(r) = A(1 + (r/B)^2)^{(-3C/2)}(1 + (r/D)^2)^{(-3E/2)}$, where A, B, C, D, E are free parameters, and r is the distance from the cluster centre. After the $f(r)$ was determined, the typical values of the respective physical quantities were calculated for every region taking r as the distance between the cluster centre and the geometrical centre of the region. Trend-divided maps were then created by dividing the original quantities by the typical value at the given radius.

5.2.2 *XMM-Newton* observations

Three out of the four Abell 85 observations with *XMM-Newton* (Jansen et al., 2001) were pointed at the cluster center and one observation was aimed ∼25 arcmin southeast of the core (Table 5.1), allowing us to look for extended emission in the south. The two deepest exposures were taken for the CHEERS[2] project (de Plaa & Cheers Collaboration in prep., Mernier et al., 2015; Pinto et al., 2015); the two older exposures were previously analysed

[1] Throughout this chapter we use C-statistic estimator for the fitting, which does not give concise goodness-of-fit values. We tried the spectral fitting using the same data with χ^2 estimator, and confirmed that we will obtain similar results, and that the typical reduced χ^2 is 0.99 for the typical NDF of 97.

[2] CHemical Evolution Rgs cluster Sample

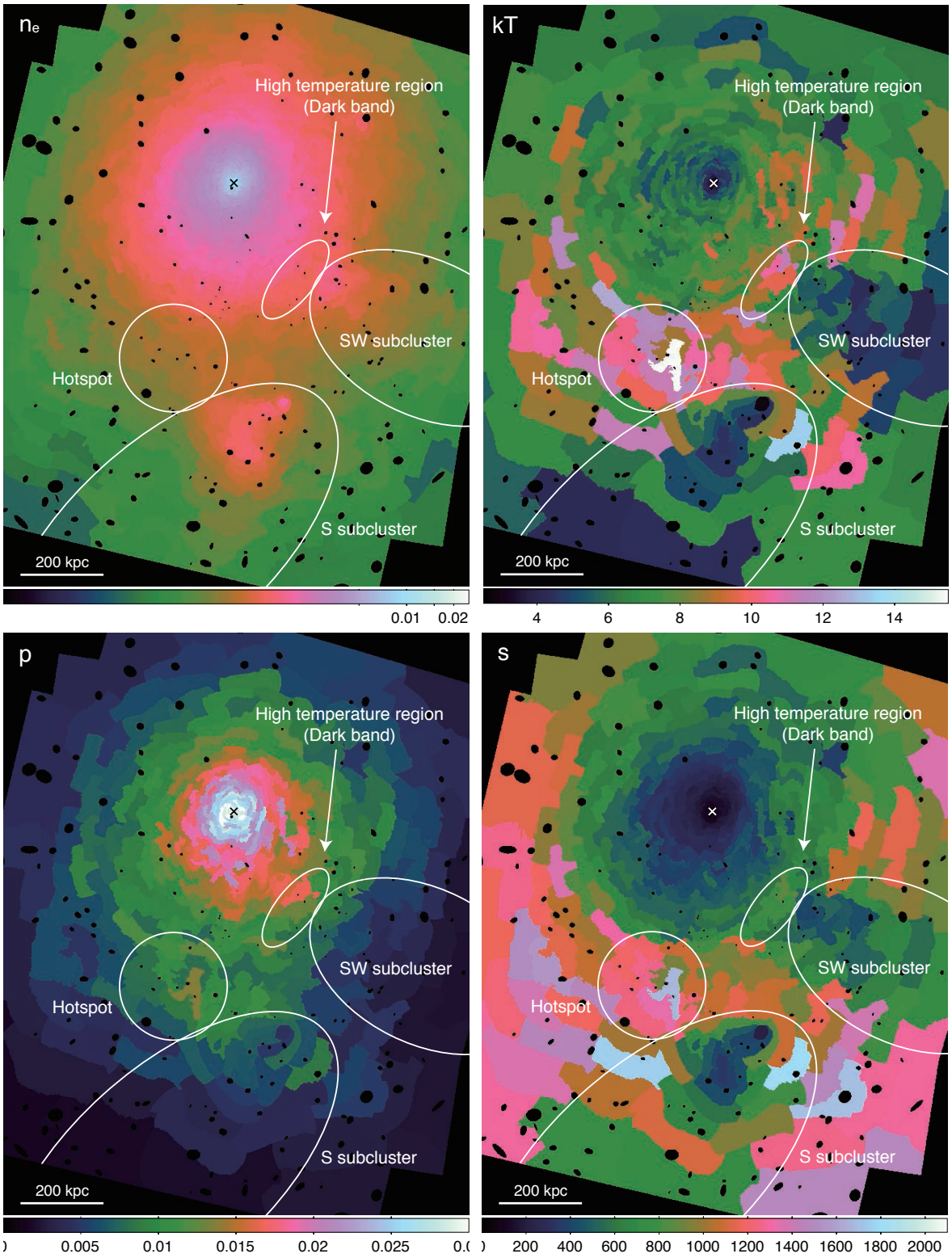

Figure 5.3 Projected thermodynamic maps of Abell 85. The S/N values used to create these images were 33 (around 1100 counts) for the density map and 70 (around 4900 counts) for others. Typical errors were 5% for density and 10% for other quantities. We assume a uniform line-of-sight depth of $l = 1$ Mpc over the entire field of view. The unit of density (left top), temperature (right top), pressure (bottom left) and entropy (bottom right) are $\mathrm{cm}^{-3} \times (l/1\ \mathrm{Mpc})^{-1/2}$, keV, $\mathrm{keVcm}^{-3} \times (l/1\ \mathrm{Mpc})^{-1/2}$ and $\mathrm{keVcm}^{2} \times (l/1\ \mathrm{Mpc})^{1/3}$, respectively. The cross denotes the central cD galaxy of the main cluster. Two subclusters (S subcluster and SW subcluster) and their tails are clealry seen. High-temperature regions (Hotspot and Dark band) are also observed.

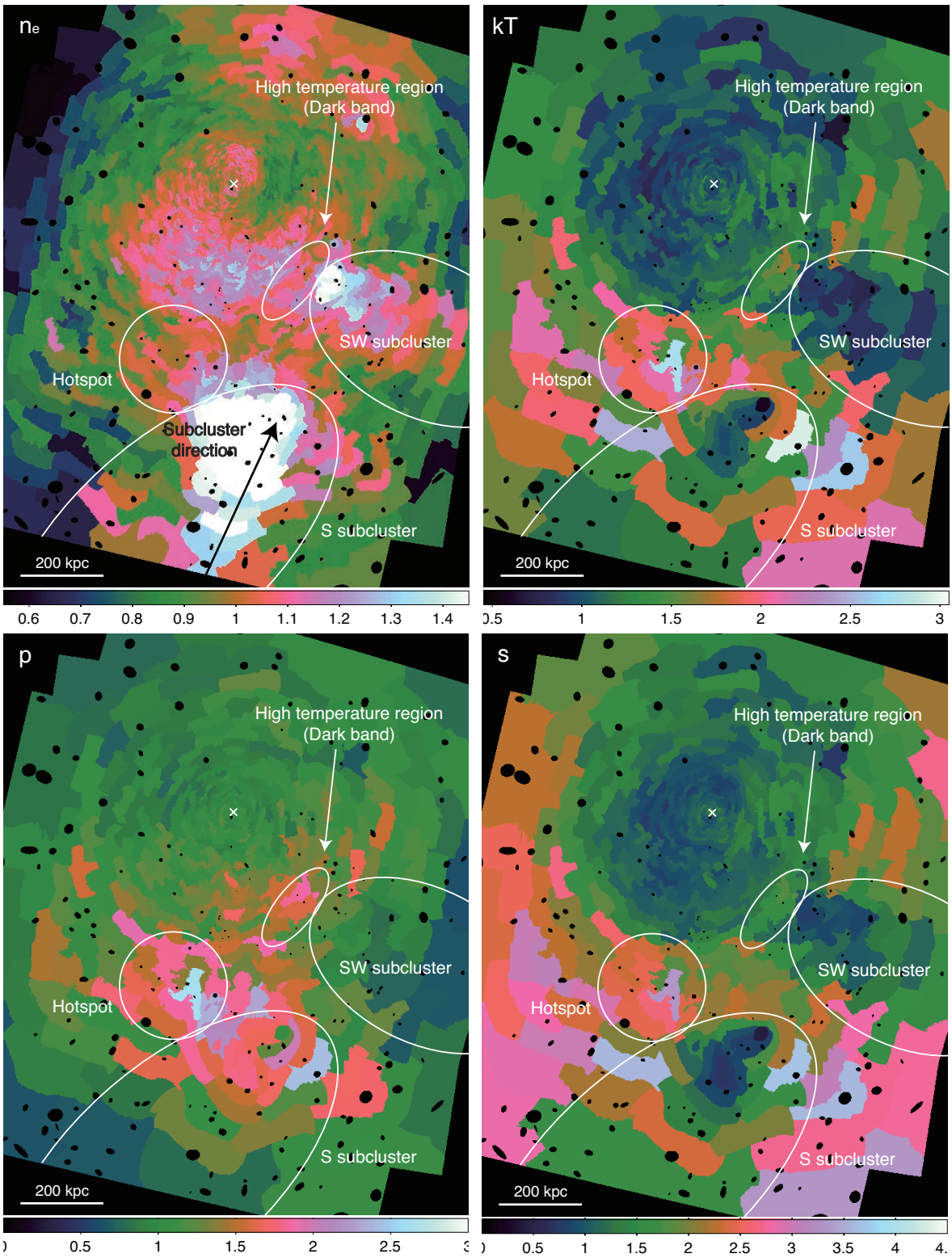

Figure 5.4 Trend-divided thermodynamic maps of Abell 85. The arrangement is same as Figure 5.3.

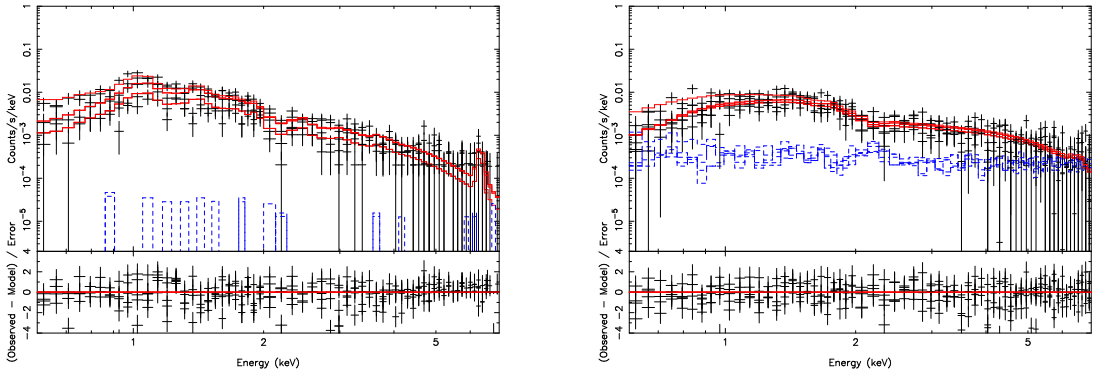

Figure 5.5 Examples of the spectral fitting. *Left:* the spectra extracted from the core of the cluster (just below the cross in Figure 5.3). *Right:* the spectra extracted from the highest temperature region (white region in the circle denoted as "Hotspot" in Figure 5.3 top right). The black crosses are the data, the red curves are the model, and the blue histograms are the background.

by Durret et al. (2003). In all the observations the EPIC instruments were operating in Full Frame mode, except in the two deepest exposures where pn was operating in Extended Full Frame mode.

The data were reduced using the *XMM-Newton* Science Analysis System (SAS) v13. The data reduction is adapted from Mernier et al. (2015). In summary, after having processed the data using the SAS tasks `emproc` and `epproc`, we filtered the event files to exclude the soft-proton flares by building 2-σ clipping Good Time Interval (GTI) files, both in the hard band (10-12 keV for MOS and 12-14 keV for pn) and the broad 0.3-10 keV band, because flares also occur in the soft band (De Luca & Molendi, 2004). We then created one image per instrument and per observation. The image extraction was restricted to the 400–1250 eV band, where the instrumental background is relatively low and uniform across the detectors. Using closed-filter observations, rescaled using the out-of-field-of-view count rates, we corrected each image for instrumental background. We combined the resulting images and corrected them for exposure and vignetting. The final image is shown in Figure 5.6.

The relative deviation image shown in the right panel of Figure 5.2 has been produced by dividing the final flat-fielded *XMM-Newton* image by the best-fit 2D elliptical double beta model using the SHERPA package. The best fit parameters of the model are consistent with the values obtained by fitting the *Chandra* image.

5.2.3 *Suzaku* observations

We reduced the data from three *Suzaku* observations of Abell 85: one pointing centred on the core of the cluster, and two additional pointings offset approximately 26 and 43 arcmin south of the cluster's X-ray peak. The data are summarized in Table 5.1 (see also Figure 5.6 for the pointing locations). Here, we concentrate on the data obtained with the X-ray Imaging Spectrometer (XIS) detectors 0, 1, and 3.

The data were reduced using the tools available in the HEAsoft package (version 6.16) to create a set of cleaned event lists with hot or flickering pixels removed. All standard

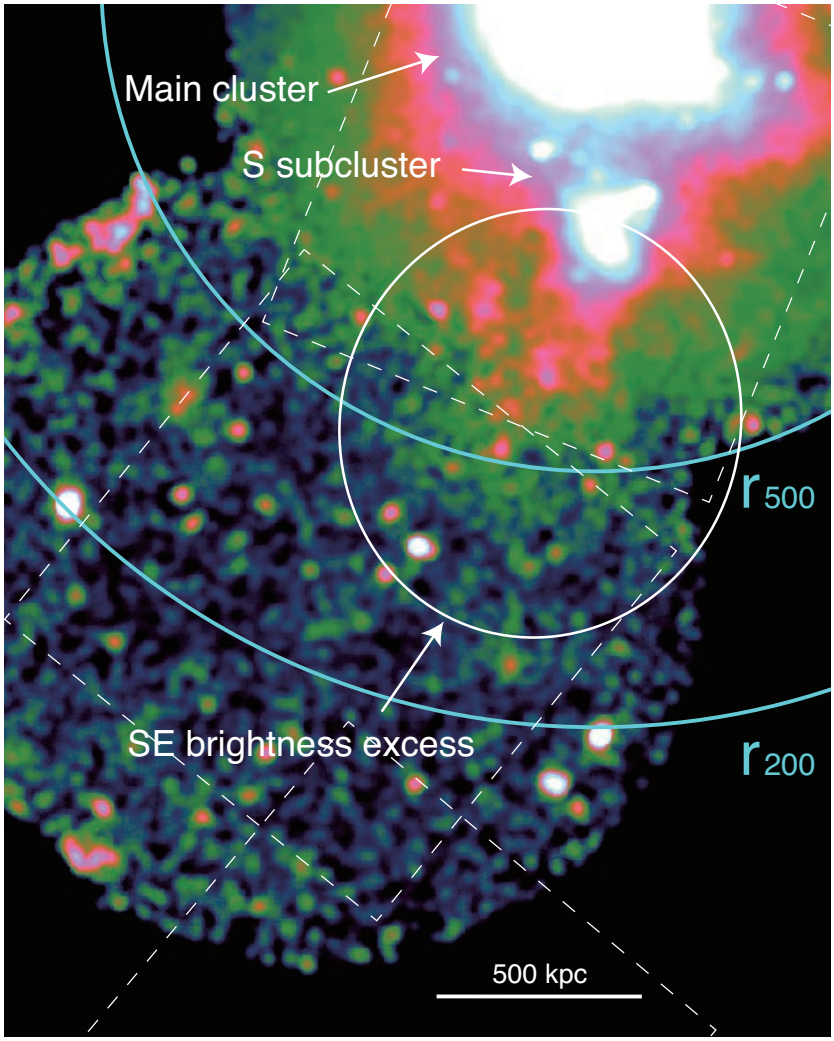

Figure 5.6 $\sigma = 25$ arcsec Gaussian smoothed, exposure map corrected *XMM-Newton* EPIC (MOS+pn) image of Abell 85. The four *XMM-Newton* datasets have been combined (Table 5.1). The overlaid white dashed squares represent the *Suzaku* pointings.

recommended screening criteria were applied[3]. We only included observation periods with the geomagnetic cut-off rigidity COR>6 GV. We used the latest calibration files that account for the modified non-X-ray background of the XIS1 detector following the increase in the charge injection level of 2011 June 1; in addition, for the XIS1 spectral analysis, we excluded two columns adjacent on each side of the charge-injected columns (the standard is to exclude one column on either side). We followed this methodology because the injected charge may leak into these additional columns and cause an increase in the instrumental background. We applied the contamination layer calibration from 2013 August 13.

We used the *Suzaku* mosaic to extract spectra from annuli centred on the cluster centre, $(\alpha, \delta) = (0 : 41 : 50.756, -9 : 18 : 03.49)$. Bright point sources were identified visually, cross-checked using the existing *XMM-Newton* mosaic, and removed from the analysis. The S subcluster seen in the *Chandra* image was removed as well. The projected and deprojected profiles of the thermodynamic properties were obtained with the XSPEC spectral fitting package (version 12.8.2; Arnaud, 1996). We used the `projct` model to deproject the data under the assumption of spherical symmetry. Sets of spectra extracted from concentric annuli were modelled simultaneously in the 0.7-7.0 keV band. We modelled each shell as a single-temperature thermal plasma in collisional ionization equilibrium using the `apec` code (Smith et al., 2001), with the temperature and spectrum normalization as free parameters. The *Suzaku* spectrum normalizations throughout this paper are normalised to an extraction area of $20^2\pi$ arcmin^2. Unless otherwise noted, the metallicity was set to 0.3 Solar (see Werner et al., 2013b). The Galactic absorption column density was fixed to the average value measured from the LAB survey (Kalberla et al., 2005).

The instrumental background was subtracted in the standard way, using the task `xisnxbgen` which constructs a background spectrum based on the latest Night Earth observation files. The cosmic X-ray background (CXB) model consisted of a power-law emission component that accounts for the unresolved population of point sources, one absorbed thermal plasma model for the Galactic halo (GH) emission, and an unabsorbed thermal plasma model for the Local Hot Bubble (LHB). The parameters of the power-law were fixed based on the best-fit results obtained by Simionescu et al. (2013), who analysed regions free of cluster emission in a large *Suzaku* mosaic centred around the Coma cluster. We note that similar values for the CXB power-law are also obtained by Urban et al. (2014) who analysed a *Suzaku* Key project mosaic centred on the Perseus cluster. The parameters for the LHB were fixed based on the all-sky average reported by Kuntz & Snowden (2000) using *ROSAT* data. Since the temperature of this component is only 0.08 keV, the signal that it contributes in the energy band 0.7-7.0 keV used for spectral fitting is negligible, therefore the best-fitting results are practically insensitive to large uncertainties on the normalization of this component. The temperature and normalization of the GH component were determined by fitting *Suzaku* spectra from an annulus free of cluster emission with inner and outer radii of 45 and 52 arcmin from the cluster core. The metallicity of the GH and LHB components were both assumed to be Solar.

The pointing in our mosaic located furthest from the centre of Abell 85 (the 46 arcmin offset), which was used to determine the best-fitting GH parameters, contains an X-ray bright star within the field of view that could be affecting the results. To mitigate this, we extracted a spectrum of this star and empirically modelled it with a power-law plus `apec` model; we

[3]Pottschmidt K., XIS Data Analysis, http://heasarc.gsfc.nasa.gov/docs/suzaku/analysis/abc/node9.html (2013).

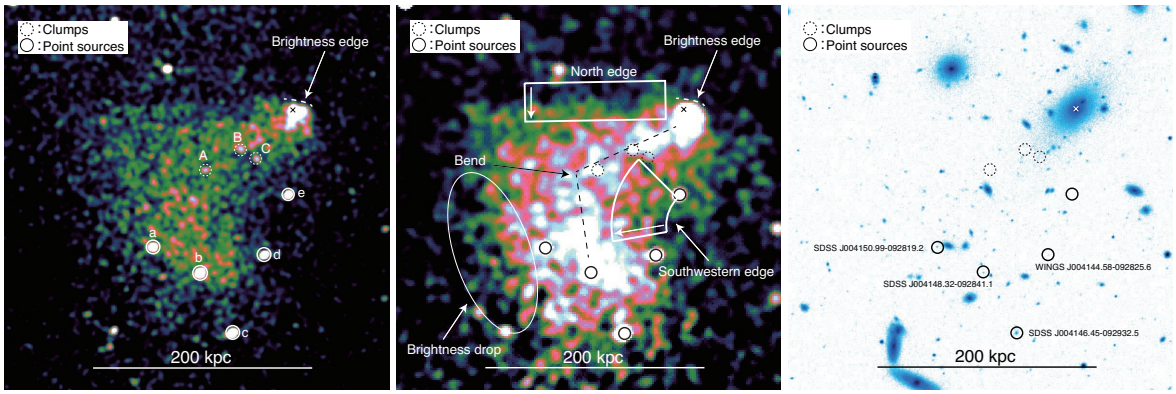

Figure 5.7 *Left*: Closeup *Chandra* image of the S subcluster (σ = 4.0 arcsec Gaussian smoothed). *Middle*: *Chandra* relative deviation image of the same sky region (σ = 6.8 arcsec Gaussian smoothed). *Right*: SDSS r-band optical image of the same sky region. The cross represents the position of the brightest central galaxy of this subcluster. The clumps in the subcluster tail and the nearby point sources are denoted with dashed and solid circles, respectively.

then ran ray-tracing simulations to estimate the level and spectrum of the scattered light from this source, and included this in our spectral fitting of the GH parameters. We find that the contribution of the stray light from the star amounts to only 5% of the total cosmic X-ray background flux in the 0.7-2.0 keV band. However, adding a cluster component above the CXB in the outer pointing in the mosaic in an annulus spanning 35-39 arcmin, we find that the contribution from the star can represent up to 30% of this additional signal. We thus do not report any measurements of the cluster thermodynamic properties based on the outermost pointing – only the centre and the 23 arcmin offset observations are used to derive the cluster properties.

5.3 Results

In the *Chandra* image and the thermodynamic maps (Figure 5.1 left, Figure 5.3, Figure 5.4), two subclusters are clearly seen in addition to the brightest main cluster (see also e.g. Durret et al., 2005a); one is ∼500 kpc south of the main cluster core (S subcluster) and the other is ∼350 kpc southwest of the core (SW subcluster).

5.3.1 The southern merger

S subcluster and a "hotspot"

Figure 5.7 shows a closeup view of the S subcluster. We see a contact discontinuity (brightness edge) at the north of its core. The X-ray brightness peak of the subcluster is spatially coincident with the position of its central dominant galaxy. The core appears extended to the south. From the core of the subcluster, a bright tail extends in the southeastern direction. The north edge of the tail extends from the core to the east for 200 kpc, and appears remarkably straight and smooth. In contrast, the southwestern edge appears blurred, indicating that the ICM transport properties are different along these two edges. About 150 kpc southeast of the

core, the tail appears bent (see also the thermodynamic maps in Figure 5.3). The tail shows an abrupt brightness drop at ∼200 kpc from the core.

The thermodynamic maps (see Figure 5.3 and Figure 5.4) show that the subcluster has a low-temperature, low-entropy core from which the broad low-entropy gas tail extends in the southeastern direction. The pressure of the S subcluster gas is higher than that of other regions at the same distances from the main cluster core. The radial change of the pressure along a line from the main cluster core to the S subcluster is gradual while the temperature, the density and the entropy profiles change abruptly at the brightness edge of the S subcluster.

Furthermore, a region of high-temperature and high-entropy gas, a "hotspot", is seen between the subcluster and the main cluster, to the northeast of the subcluster core (see also Tanaka et al., 2010).

Clumpy gas and the SE brightness excess

In the *Chandra* closeup image (Figure 5.7), we see three gas clump candidates – X-ray bright sources in the tail with no optical counterparts within a 3 arcsec radius. They have been detected with the `wavdetect` tool (along with the point sources, see Section 5.2.1) at a higher than 3σ significance.

Figure 5.8 top shows the surface brightness profiles (projected for 4 arcsec width) across the clump candidates. The projected profile of each clump candidate is well fitted with a Cauchy plus linear function. The FWHM of all three clump candidates calculated using the widths of the best-fitting functions are in the range of 2.1–2.8 arcsec for the Cauchy profile, which is about 1σ larger than the PSF model or the FWHM of the nearby point sources shown in Figure 5.7, except source 'd'. The luminosities of the clumps are ~ 1–2×10^{40} erg s^{-1}.

As seen in Figure 5.6, a surface brightness excess extends from the tail of the S subcluster all the way out to $\sim r_{500}$ (SE brightness excess). This brightness excess has been previously reported based on both *ROSAT* and *XMM-Newton* observations (Durret et al., 1998, 2003, 2005b).

Deprojected profile out to the outskirts

In Figures 5.9 and 5.10, we present the projected and deprojected thermodynamic profiles measured along the direction of the infall of the S subcluster using the *Suzaku* data. The low-entropy S subcluster has been excised from the *Suzaku* data analysis, otherwise, it would have dominated the ICM signal at those radii, and would have caused a severe departure from spherical symmetry making the deprojection analysis practically meaningless. The curves in the deprojected pressure and entropy profiles are the theoretically predicted profiles calculated following Nagai et al. (2007a) and Pratt et al. (2010), respectively. We fitted the pressure profile with the model leaving r_{500} as a free parameter, with other parameters fixed to the values presented in Planck Collaboration et al. (2014). M_{500} is expressed self-consistently as a cubic function of r_{500}, with the normalization of $M_{500}/{r_{500}}^3 = 7.2 \times 10^{14} \mathrm{M}_\odot/(1.33\ \mathrm{Mpc})^3$ (Mantz et al., 2010b,a). The best-fitting value of $r_{500} = 1.2 \pm 0.04$ Mpc and the corresponding M_{500} are also used in the entropy model.

As seen in both the projected and deprojected profiles, the temperature remains above ∼4 keV out to r_{200}. The deprojected density decreases monotonically to r_{200}, but flattens out in the outermost data point that lies beyond r_{200}. We note that we have used an extrapolation of the best-fitting beta model for the density (obtained ignoring the innermost two data points

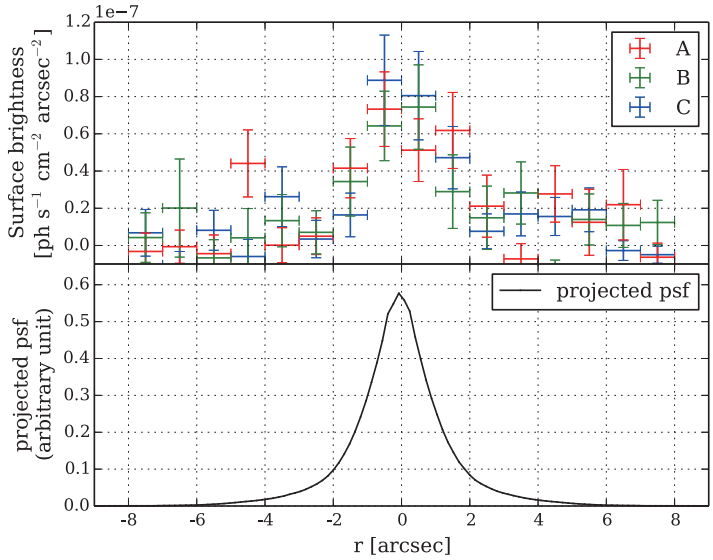

Figure 5.8 *Top*: Surface brightness profiles of the clumps shown in Figure 5.7. *Bottom*: Surface brightness profile (projected psf including multiple observations) of an arbitrary nearby X-ray point source calculated using the CIAO `psf` module.

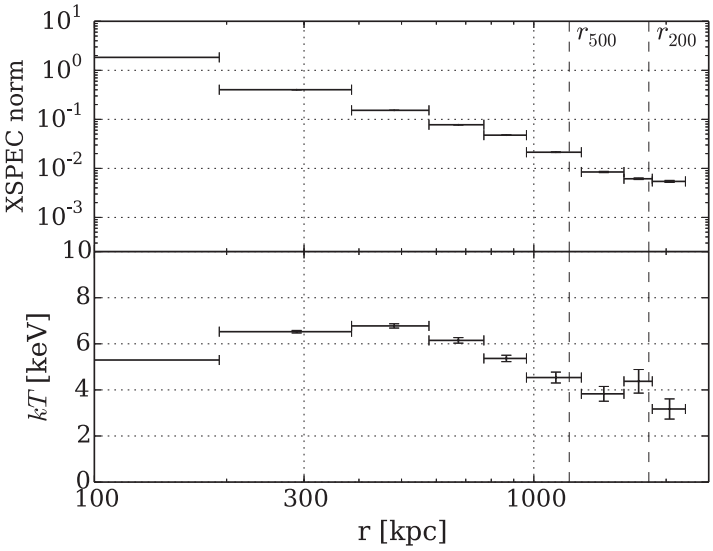

Figure 5.9 *Suzaku* projected radial profiles. The panels are XSPEC normalization per unit area and temperature from top to bottom.

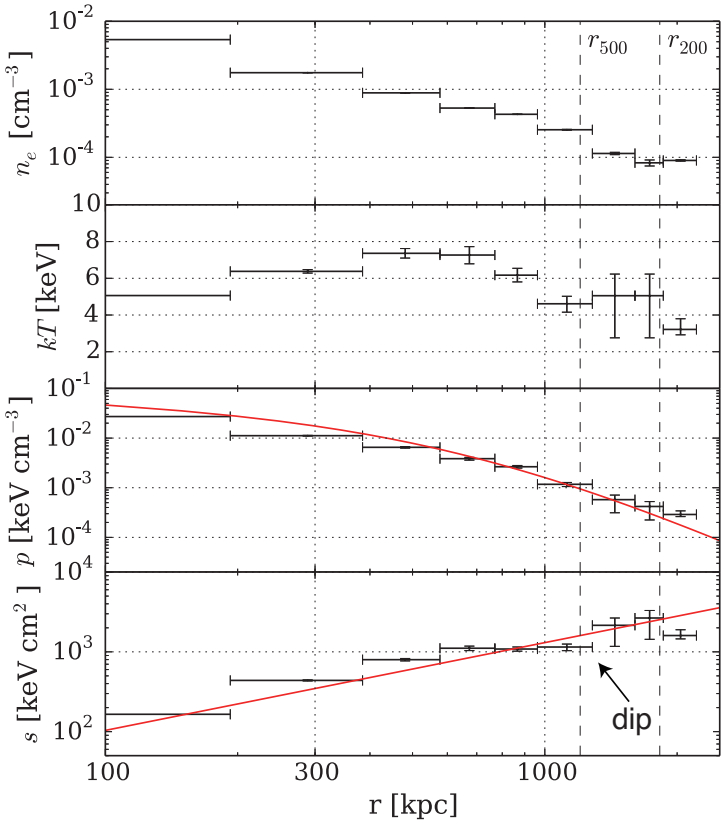

Figure 5.10 *Suzaku* deprojected radial thermodynamic profiles. The panels are density, temperature, pressure and entropy from top to bottom. The curve on the pressure profile is the best-fitting theoretical pressure profile (Nagai et al., 2007a), with the parameters estimated in Planck Collaboration et al. (2014). The line on the entropy profile is the theoretically predicted entropy profile (Pratt et al., 2010).

representing the cool core) in order to correct the density profile for the effect of projected emission from gas beyond the outer edge of the measurements.

The deprojected entropy profile shows an expected low-level excess above the expected power-law behaviour near the cluster core, which is attributable to additional heating due to the AGN feedback and ongoing mergers; at larger radii, the measured entropy agrees with the model out to r_{200}, with the exception of a dip found around 1.3 Mpc ($\sim r_{500}$) and which is probably associated with the low-surface brightness extension of the tail of the S subcluster.

Previous studies (e.g. Simionescu et al., 2011; Walker et al., 2013; Morandi & Cui, 2014; Urban et al., 2014) have revealed a flattening of the measured entropy profile in other clusters with respect to the expected model, starting at around $\sim 0.75 r_{200}$. In the case of Abell 85, by contrast, the deprojected entropy profile remains in good agreement with the model until r_{200} and turns over only beyond that radius. However, the large error bars on the last two data points inside r_{200} do not rule out a flattening of the entropy in Abell 85 in agreement with that observed in other systems. Moreover, the outermost data point in our profile shows an unusually high density (in most other systems, the density profile is monotonically decreasing even beyond r_{200}). If therefore the density in this outermost data point is biased high, either by the presence of an unresolved group or due to an unusually high clumping factor that is not azimuthally representative, the measured entropy immediately inside r_{200} could be biased high as a consequence.

5.3.2 Main cluster features

The main cluster has an asymmetric surface brightness morphology in which the core gas extends farther towards the northern direction whereas the outer gas extends south (Figure 5.1 left).

Large scale spiral

In the *Chandra* relative deviation image (Figure 5.2 left), we see an apparent brightness excess spiral, starting north of the core and extending counter-clockwise outward from the core. In the *XMM-Newton* relative deviation image (Figure 5.2 right), we can see that this spiral extends out to ∼600 kpc. This indicates ongoing gas sloshing, and the appearance of the spiral feature suggests that the interaction plane is close to the plane of the sky (Roediger et al., 2011). Sloshing motions extending to large radii have previously been seen in the Perseus cluster (Simionescu et al., 2012), Abell 2142 (Rossetti et al., 2013), Abell 2029 (Paterno-Mahler et al., 2013) and RXJ 2014.8-2430 (Walker et al., 2014).

In the trend-divided density map (Figure 5.4), an obvious counter-clockwise spiral feature of higher density gas can be seen around the main cluster core, corresponding to a sloshing spiral in the relative deviation images. Indications for this spiral structure are also seen in the temperature and entropy maps but cannot be seen in the pressure map. Instead of the spiral feature, the trend-divided pressure map displays an asymmetric morphology with a pressure excess in the southern and southeastern direction from the main cluster core.

Main cluster core

Closeup images (an X-ray image and a relative deviation image) of the main cluster core are shown in Figure 5.11. We see a surface-brightness cavity at 20 kpc south of the core. In

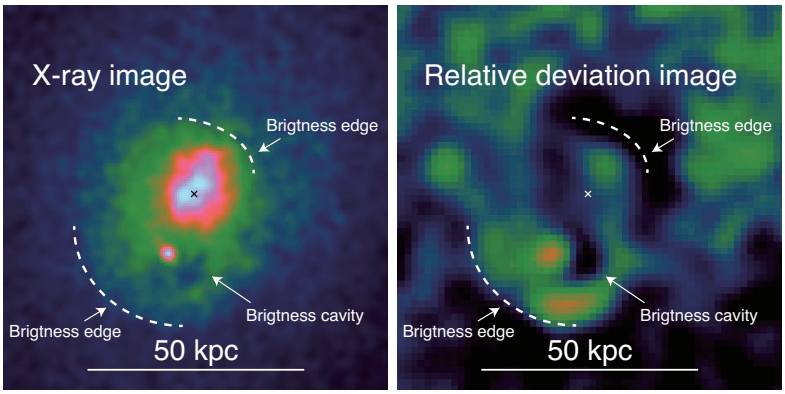

Figure 5.11 *Left*: Closeup image of the main cluster core($\sigma = 2.0$ arcsec Gaussian smoothed). *Right*: Relative deviation image of the same region (see also Figure 5.2). The cross corresponds to the central cD galaxy.

addition to the cavity, we see two arc-shaped brightness edges in the image. One is located northwest of the brightness peak, while the other is at $r = 35$ kpc to the south.

5.3.3 SW subcluster and the dark band

The temperature and entropy of the SW subcluster are relatively low, but it does not have a cool core (it has no surface brightness peak or an obvious central dominant galaxy). It has a diffuse, low-temperature and low-entropy tail extending to the west, and its pressure is consistent with that of the surrounding gas (Figure 5.3).

About 250 kpc southwest of the main cluster core, at the interface between the sloshing spiral and the SW subcluster, we see a straight, dark narrow structure (Dark band) with a width of ∼50 kpc and a length of ∼300 kpc which divides the SW subcluster from the sloshing gas of the main cluster (Figure 5.2). The part of the spiral adjacent to the Dark band is brighter than the other parts of the spiral. The regions corresponding to the Dark band have relatively high temperatures (Figure 5.3).

5.4 Discussion

5.4.1 The infall of the S subcluster

Dynamics of the S subcluster

In the temperature map (Figure 5.3 upper right), we see a high-temperature region (hotspot) in the northeast of the S subcluster. This hotspot has been first observed by *XMM-Newton* (Durret et al., 2005a). Tanaka et al. (2010), who conducted a subsequent *Suzaku* observation, proposed a scenario that the hot gas results from the merger of the S subcluster, colliding with the main cluster from the southwest.

In our thermodynamic maps (Figure 5.3), the low entropy tail of the subcluster extends to the southeast. It is thus more plausible that the subcluster is moving northwestward rather than northeastward as proposed in Tanaka et al. (2010). The tail is comprised of

two gas components of different entropy: higher entropy gas extending broadly (∼800 keV cm^2 × $(l/1$ Mpc$)^{1/3}$; green bins associated with the S subcluster in the bottom right panel of Figure 5.3), and lower entropy gas terminating at ∼200 kpc from the subcluster's core (∼400 keV cm^2 × $(l/1$ Mpc$)^{1/3}$; blue bins associated with the S subcluster in the bottom right panel of Figure 5.3), similar to what we see in the X-ray image (Figure 5.7). This indicates the scenario that, while the relatively higher entropy gas has been stripped from the outer X-ray halo of the S subcluster, the dense low-entropy gas is being stripped from its cool core remnant. The emissivity of the stripped higher entropy gas may be lower than that of the low entropy tail, resulting in an abrupt drop in surface brightness at the end of the tail.

Destruction of the cool core

Because the innermost low-entropy core of the subcluster along with its brightest central galaxy precedes the stripped tail, the cool core of the subcluster has likely been almost completely destroyed before reaching its current radius, $r \approx 500$ kpc of Abell 85. The possible gas clumps that we identified within the low entropy tail have no optical counterparts. Their luminosities of $L_{\rm X} = 1$–2×10^{40} erg s^{-1} are consistent with the luminosities of the coronae of late type galaxies (Sun et al., 2007), indicating that they might have been stripped off the member galaxies of the infalling group.

Excluding the immediate surrounding of the brightest central galaxy of the merging subcluster, its projected temperature is ∼4.5 keV. However, since this value is the emission weighted average of the ambient ICM and the stripped tail, the temperature is probably overestimated. To estimate the effect, we chose two bins representing the cluster ambient gas and the subcluster tail gas as shown in Figure 5.12, and fitted the spectra for the subcluster tail bin using the main cluster gas spectra as background. The spectrum of the main cluster gas bin was fitted with a single temperature plasma model. The temperature obtained for the main cluster gas bin was used as one of the temperature components of the two temperature plasma model with which we fitted the spectrum of the subcluster tail gas bin.

The best-fitting temperature of the tail changes from $kT = 4.5^{+0.4}_{-0.3}$ keV with the single temperature model to $kT = 2.7^{+0.5}_{-0.4}$ keV with the two temperature model. Under the assumption that the stripped tail gas did not mix with and did not get conductively heated by the ambient medium, we can use this temperature to estimate the mass of the infalling subcluster. For the 2.7 keV temperature, the mass-temperature scaling relation by Arnaud et al. (2005) predicts $M_{500} \approx 1.3 \times 10^{14} {\rm M}_\odot$. Mantz et al. (2010a) estimated the main cluster mass as $M_{500} \approx 7.2 \times 10^{14} {\rm M}_\odot$, which implies a merger mass ratio of ∼ 5.5.

Since this 2.7 keV temperature is extracted for the vicinity of the cool core region of the subcluster and this temperature is not necessarily representative of the subcluster as a whole, the mass of the subcluster may be underestimated. However, regardless of the exact mass ratio, this may demonstrate that cool cores can be effectively stripped during mergers.

Recently, observations of the Ophiuchus cluster have shown that sloshing induced by major late time mergers may even destroy the cool core of the main cluster (Million et al., 2010). These observations pose a challenge to simulations (e.g. Burns et al., 2008), which find that cool cores usually survive late major mergers. This indicates that the microphysical properties of the ICM is more complex than the simple ideal fluid approximation typically employed by these numerical models.

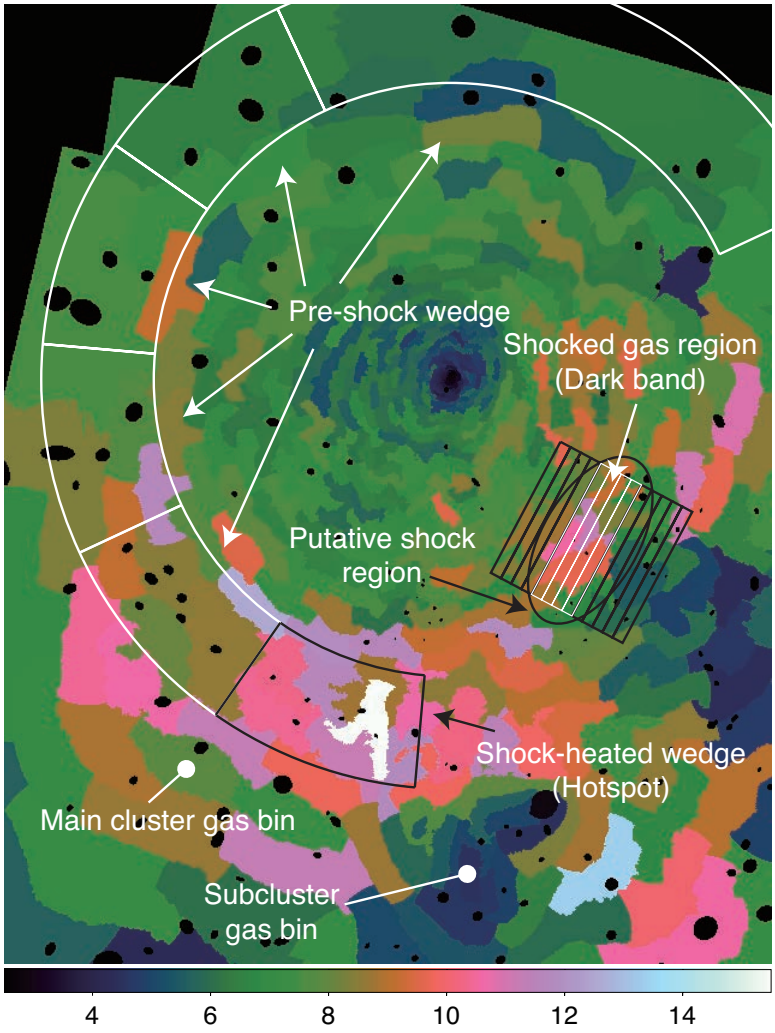

Figure 5.12 Closeup image of the temperature map. Two bins (Main cluster gas bin and Subcluster gas bin) are used to estimate the projection effect of the subcluster tail gas in Section 5.4.1. The bottommost black wedge (Shock-heated wedge) is used to extract the properties of the shock-heated gas and the white wedges (Pre-shock wedge) are used to evaluate the pre-shock gas properties in Section 5.4.3. The overlaid rectangular regions are used to extract the thermodynamic profiles in Section 5.4.3. The black ellipse denotes the putative shock region, and the white rectangles correspond to the Dark band.

Stripped tail and gas clumping

ROSAT and *XMM-Newton* images of Abell 85 (Durret et al., 1998, 2003, 2005b) have shown a large-scale brightness excess structure extending to the southeast of the S subcluster. Durret et al. (2003) estimated the temperature of this structure as ∼2 keV and proposed that it may be either due to the diffuse emission of a large scale structure filament connecting to the cluster, due to a chain of small groups of galaxies, or due to the stripped gas from the infalling S subcluster. Boué et al. (2008) conducted an optical study and concluded that the structure is consistent with groups falling into the main cluster.

However, the temperature profile measured by *Suzaku* shows $kT > 4$ keV out to r_{200}. This temperature is a factor of two higher than the previous measurement of ∼2 keV at the same radius. This discrepancy may be the result of the difference in the background treatment. While Durret et al. (2003) used blank-sky templates, we determined our local background using the outermost regions of the *Suzaku* observation. We find that the Galactic foreground component toward Abell 85 is a factor of three higher than the average value across the sky (Kuntz & Snowden, 2000). Using background templates will therefore underestimate the background and lead to a lower best-fitting temperature in the low surface brightness cluster outskirts.

If most of the excess emission were due to groups, we would expect $kT \approx 1$ keV for a typical group mass. The *Suzaku* spectra are inconsistent with such low temperature emission and they show that the temperature of the southern surface brightness excess is consistent with the projected temperature of the bright stripped tail of the S subcluster observed by *Chandra*. Thus, the SE brightness excess is probably also associated with the stripped gas of the infalling S subcluster.

Although the line-of-sight geometrical configuration is uncertain, this long tail may imply a long lifetime of the tail structure, indicating that strong turbulence or diffusion are suppressed. Also recently, long tails of stripped gas that survive within the ambient ICM for over 600 Myr have been detected in the outskirts of the cluster Abell 2142 (Eckert et al., 2014) and in the Coma cluster (Sanders et al., 2013).

This interpretation is also supported by the dip in the deprojected entropy profile. The location of this dip at r_{500} corresponds to the apparent termination of the SE brightness excess. The dip, therefore, may be caused by the projection of the low-entropy, bright tail gas against a background of high-entropy, faint main cluster gas. Note that this interpretation does not contradict the galaxy overdensity found in the southeast (Boué et al., 2008) because cluster mergers usually happen along large-scale filaments (in the cosmological sense), and we expect more galaxies along filaments than other directions.

The fact that the stripped tail of the infalling southern subcluster in Abell 85 is seen across a radial range of over 700 kpc, as well as the recent observations of the long trails of stripped gas in other systems (Sanders et al., 2013; Eckert et al., 2014), indicate that the stripping of infalling subclusters may seed gas inhomogeneities in the outskirts of clusters. The presence of gas clumping in cluster outskirts is seen in simulations (e.g. Roncarelli et al., 2006, 2013; Nagai & Lau, 2011; Vazza et al., 2013), and X-ray observations of clusters out to their virial radii have indirectly shown that clumping becomes significant at $r > 0.5r_{200}$ (Simionescu et al., 2011; Walker et al., 2013; Morandi & Cui, 2014; Urban et al., 2014). In the case of Abell 85, the deprojected entropy profile remains in good agreement with the expected power-law model until r_{200}, which would imply, at face value, that in this system clumping is not significant at radii $r_{500} < r < r_{200}$. However, this conclusion cannot be drawn robustly

because the large error bars on the last two data points inside r_{200} do not rule out a flattening of the entropy in Abell 85 in agreement with that observed in other systems. Moreover, this profile is extracted along the path of the S subcluster, which is clearly an unrelaxed direction. This may lead to the break of the assumption of the spherical symmetry in deprojection.

5.4.2 Gas motion and interaction

Gas sloshing in the main cluster

The images and thermodynamic maps of Abell 85 show spiral like features indicative of gas sloshing (see Figure 5.2 and Figure 5.4). For detailed simulations and discussion on gas sloshing, see e.g. Tittley & Henriksen (2005), Ascasibar & Markevitch (2006), Roediger et al. (2011), ZuHone et al. (2011).

Here we show an azimuthally resolved study of this sloshing spiral. In Figure 5.13, we display the projected radial profiles for the surface brightness and several thermodynamic quantities for the eight directions shown in Figure 5.2. For comparison, two profiles of an opposite direction pair (e.g. N and S) are drawn in each panel. The overlaid red/blue rectangles represent the radial intervals where the profile drawn in the corresponding color is brighter in the relative deviation images.

For most of the regions, the surface brightness profiles and the temperature profiles show an anticorrelation typical of sloshing phenomena, namely, alternating bright cooler regions and dim hotter regions (see e.g. Tittley & Henriksen, 2005). The resulting pressure profiles, each of which is a simple product of density and temperature in these regions, are consistent between the two opposite directions (see annotations in Figure 5.13). However, beyond ∼120 kpc of the NE-SW and the N-S directions (the blue rectangles in the NE-SW and N-S profiles), the surface brightness profiles corresponding to the outermost part of the spiral arm are brighter than those of the opposite directions, while the temperature profiles are either similar or the brighter part is hotter, resulting in a clear discrepancy in the pressure profiles between two opposite directions (see also Figure 5.4).

The high-pressure gas is most likely shock-heated and compressed by the infalling two subclusters. Both subclusters have associated putative shock-heated regions (see Section 5.4.3) and we can expect shock-heated gas anywhere around the region of interaction. The fact that these two subclusters are both located in the southwestern half of the main cluster is consistent with the higher pressure in the southwestern part of the spiral.

Gas sloshing and the morphology of the S subcluster

The bright stripped tail of the S subcluster shows a bent structure and has a 200 kpc long, relatively smooth and sharp northern edge, as described in Section 5.3.1. Figure 5.14 shows the surface brightness profiles across the northern and southwestern edges. While the brightness of the southwestern edge changes gradually, the profile across the north edge is steep, with a width of ∼10 kpc.

The typical temperature and density of the ambient ICM around the northern edge are ∼10 keV and $\sim 10^{-3}$ cm^{-3}, respectively, so the Coulomb mean free path is estimated as $\lambda \approx 30$ kpc. This value is larger than the width of the northern edge of ∼10 kpc, indicating suppression of transport processes.

Ordered flows of the ambient ICM from west to east, resulting from sloshing, can consistently explain both the smooth brightness edge and the bent morphology. It has been

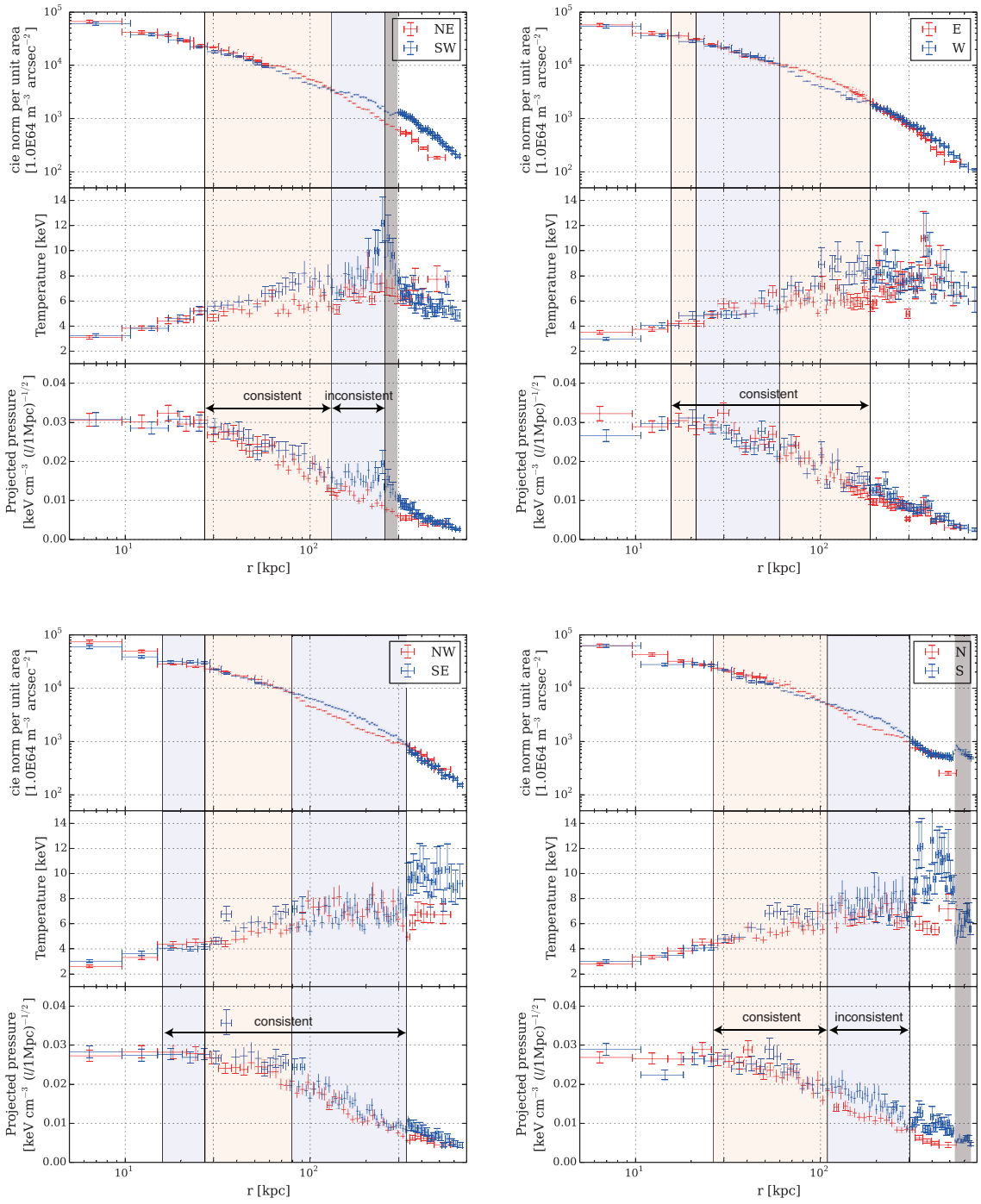

Figure 5.13 Radial projeced thermodynamic profiles for eight directions illustrated in Figure 5.2 left. Two profiles for an opposite direction pair are drawn in each panel. Individual panels are surface brightness (`cie` normalization per unit area), temperature and pressure, respectively from top to bottom. The black vertical lines represent the approximate locations of the spiral edges. The red and blue rectangles correspond to the spiral arm, whose colors correspond to the color of the brighter direction of the two directions in the relative deviation images (Figure 5.2). The grey rectangles in the upper left panel and bottom right panel represent the Dark band illustrated in Figure 5.2 right and the S subcluster, respectively.

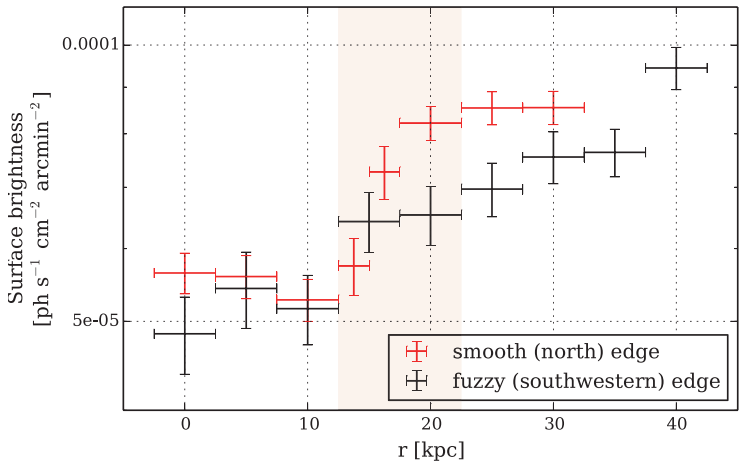

Figure 5.14 Surface brightness profiles across two edges shown in Figure 5.7. The red and black points correspond to the north edge and the southwestern edge respectively. The profiles are drawn with the directions shown by the arrows in Figure 5.7. The red rectangle denotes the north edge.

shown in simulations that sloshing causes ordered gas motion, and that magnetic fields are stretched and regulated by the velocity field (Ascasibar & Markevitch, 2006; Roediger et al., 2011; ZuHone et al., 2011, 2015). As the sloshing spiral in Abell 85 extends out to ∼600 kpc, there may be a non-negligible flow around the S subcluster, from west to east. The tail of the subcluster may be bent and blown eastward by this flow, which could have a radial gradient. In the same time, the ordered magnetic field lines, stretching from west-to-east could suppress conduction and thermodynamic instabilities, keeping the northern edge smooth.

VLA radio observations presented by Schenck et al. (2014) have revealed a bright radio galaxy between the S subcluster and the main cluster. This galaxy appears both in the X-ray and optical image, and a wide-angled radio tail extends to the east from the location of the galaxy. The tail is oriented parallel to the northern edge of the subcluster, which is compatible with the west-to-east velocity field and supports the above scenario.

The interaction between the sloshing gas and the tail of the subcluster can explain the overall properties of the system consistently and allow us to draw conclusions about the magnetic field geometry and its dynamical impact. Considering that galaxy clusters grow by accretion, we can expect that such a phenomenon is universal. However, to our knowledge, this is the first such interpretation because interactions between multiple X-ray substructures so far have been an overlooked point of view. Simulations of gas sloshing have so far mainly focused on binary mergers within relatively small radii. Future large scale sloshing simulations conducted out to large radii with magnetic fields, as well as multiple merger simulations focusing on the gas dynamics, will enable us to investigate the gas interaction quantitatively and will bring a deeper understanding as to how the gas evolves to a relaxed system.

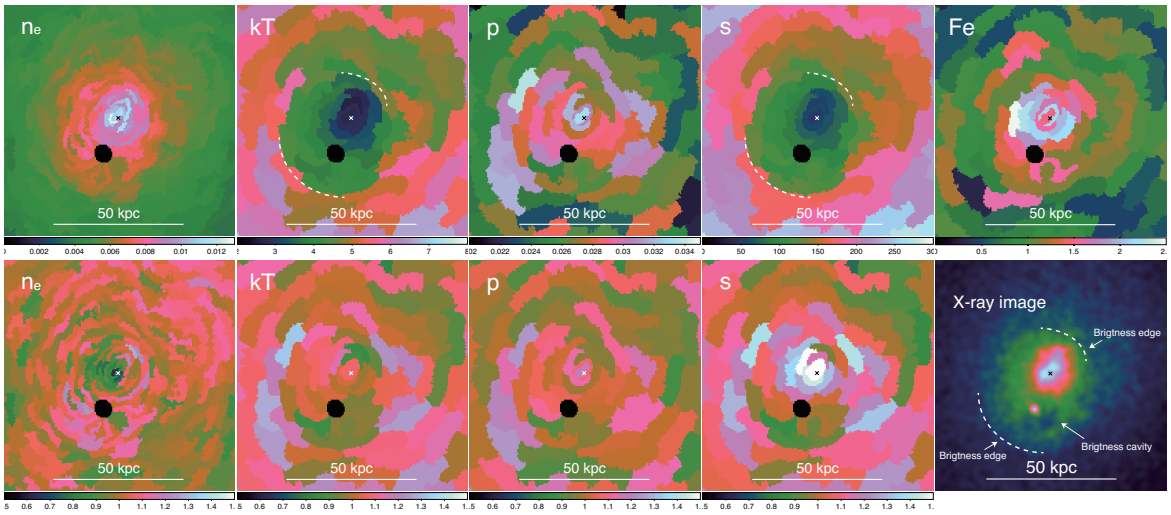

Figure 5.15 Projected thermodynamic maps around the main cluster core. Upper five maps are the original maps and lower four are the trend-divided ones. Panels are the maps of density ($\mathrm{cm}^{-3} \times (l/1\ \mathrm{Mpc})^{-1/2}$), temperature (keV), pressure ($\mathrm{keV\ cm}^{-3} \times (l/1\ \mathrm{Mpc})^{-1/2}$) , entropy ($\mathrm{keV\ cm}^{2} \times (l/1\ \mathrm{Mpc})^{1/3}$) and Fe abundance in the unit of solar value respectively from left to right. The rightmost panel of the lower row is the closeup X-ray image of the core (see also Figure 5.11). Typical errors are 5% for the density map, 20% for the Fe abundance map, and 10% for all other maps. The dashed curves represent the temperature and entropy edges.

Gas sloshing in the core of the main cluster

The thermodynamic maps of the same region as Figure 5.11 are shown in Figure 5.15. We see sharp edges at 15 kpc north and 35 kpc south of the main cluster core both in the temperature map and the entropy map, which correspond to the brightness edge in the image. They can be interpreted as cold fronts originating from the core gas sloshing, which is connected to the larger scale spiral out to several hundreds of kpc.

We detect a surface brightness cavity in the cluster core (Figure 5.11), which is also known to host diffuse radio emission (Schenck et al., 2014). The surface brightness of the cavity is $0.87\pm0.02\times10^{-6}$ ph s^{-1} cm^{-2} arcsec^{-2}, which is significantly (more than 5σ) fainter than the surrounding ambient gas whose surface brightness is $1.03\pm0.02\times10^{-6}$ ph s^{-1} cm^{-2} arcsec^{-2}. The cavity is probably due to a bubble blown by the AGN hosted by Holm 15A. The lack of a counterpart bubble may be due to the core gas sloshing which could hide the cavity.

5.4.3 Shock features

The origin of the hotspot

The only merging system that could have shock heated the gas to produce the "hotspot" is the infalling southern subcluster. Although the cool core remnant of this system is offset to the west of the hot spot, the dense low entropy gas associated with the tail seen in the Chandra image might be driving a shock as it is falling to the north.

If the hotspot (Figure 5.3, Section 5.3.1) is due to previous shock heating, the required Mach number of the shock $\mathscr{M}$ can be calculated using the Rankine-Hugoniot jump condition.

For $\gamma = 5/3$ gas, the ratio between the shock-heated gas temperature T_2 and the pre-shock gas temperature T_1 is determined through the equation

$$\frac{T_2}{T_1} = \frac{(\mathscr{M}^2 + 3)(5\mathscr{M}^2 - 1)}{16\mathscr{M}}, \tag{5.1}$$

where $\mathscr{M}$ is the Mach number of the shock. In Figure 5.12, we display the regions used to calculate the shock Mach number. The black wedge indicates the shock-heated region, and the white wedges are used to estimate the pre-shock gas temperature. The extracted temperatures are $kT_1 = 7.8 \pm 0.2$ keV and $kT_2 = 11.5^{+0.8}_{-0.7}$ keV, and the resulting Mach number is $\mathscr{M} = 1.5 \pm 0.1$, corresponding to a shock velocity of $\sim$2200 km s^{-1}.

Since this pre-shock region is arbitrary, we evaluated the systematic uncertainty by splitting the pre-shock region into five smaller wedges as shown in Figure 5.12. The obtained pre-shock temperature range of $kT_1 \approx$ 6–9 keV corresponds to a Mach number in the range of $\mathscr{M} \approx$ 1.3–1.8, which is consistent with previous studies (e.g. Tanaka et al., 2010; Schenck et al., 2014).

Although currently the hotspot appears displaced from the line of the S subcluster's motion, it is most likely due to the shock driven by the infall of the S subcluster. Gas sloshing (Section 5.4.2) can both redistribute the main cluster gas from an axisymmetric configuration and the associated ordered motion can displace the hotspot along the velocity field.

The mean line-of-sight velocity of Abell 85 is 16507±102 km s^{-1} (Oegerle & Hill, 2001), and the line-of-sight velocity of the brightest central galaxy of the S subcluster is 16886±35 km s^{-1} (Beers et al., 1991). The subcluster's relative line-of-sight velocity to the main cluster is thus estimated as 379±107 km s^{-1}. Assuming that the shock velocity of $\sim$2200 km s^{-1} represents the total velocity, the subcluster's motion is close to the plane of the sky.

The dark band and the SW subcluster

The fact that the gas associated with the dark band is hotter than the gas at other azimuths at the same radius (approximately as hot as the southern hotspot) suggests that it has been shock heated. To investigate the profiles across the "dark band", we chose rectangular regions parallel to the interface (rectangles in Figure 5.12), and extracted the thermodynamic profiles shown in Figure 5.16. In these profiles, the dark band is highlighted by a shaded grey rectangle. Figure 5.17 shows the example fitting results for the seventh and thirteenth (from the left) regions.

We see clear excess both in the temperature and the entropy of the Dark band, which suggests the presence of shock-heated gas. However, because this region is the interface between the sloshing gas and the subcluster, it is difficult to identify the pre-shock gas unambiguously.

Assuming the gas has been shock heated, we estimate the Mach number $\mathscr{M}$ in the same way presented in the Section 5.4.3. We combined the fifth, sixth, seventh and the eighth rectangular regions from left in Figure 5.12 and 5.16 as the shocked gas region and refitted the spectrum. The temperature derived for this region is $kT_2 = 9.1^{+0.5}_{-0.4}$ keV. As for the pre-shocked gas, we took a rectangular region which has the same shape and size as the shocked gas region, at the opposite position with respect to the central cD galaxy of the main cluster. The temperature of this region is $kT_1 = 6.5^{+0.4}_{-0.3}$ keV. The resulting Mach number is $\mathscr{M}$ =1.4±0.1.

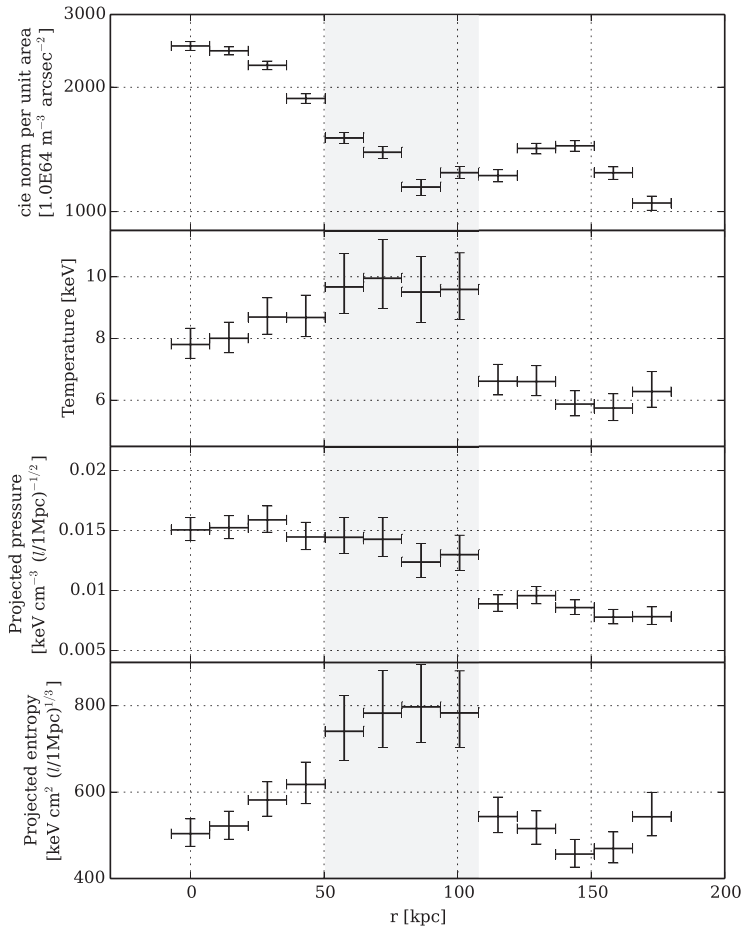

Figure 5.16 Thermodynamic profiles along the line perpendicular to the interface between the sloshing arm and the SW subcluster. Regions are visualized in Figure 5.12. The grey rectangle represents the Dark band.

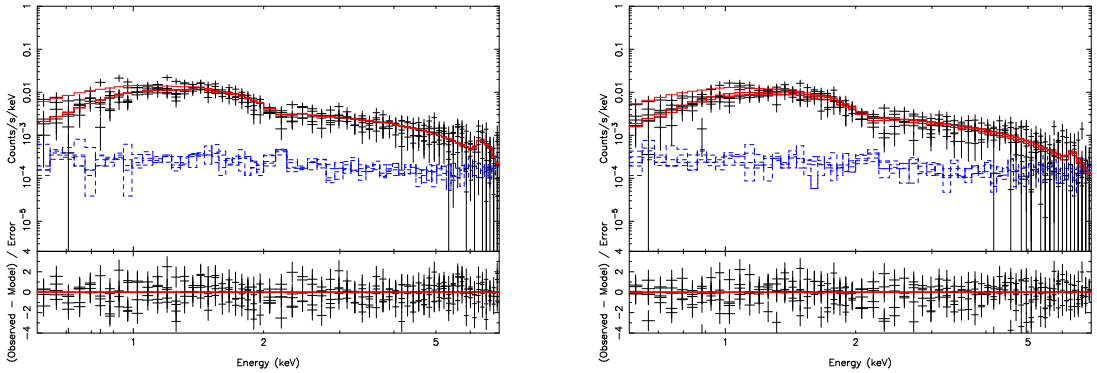

Figure 5.17 Examples of the spectral fitting. *Left:* the spectra extracted from the seventh region. *Right:* the spectra extracted from the thirteenth (from the left) region. The black crosses are the data, the red curves are the model, and the blue histograms are the background.

5.5 Summary

In this chapter, we investigate the galaxy cluster Abell 85 comprehensively. The main results of this work are summarized below.

1. We see a relatively large scale (∼600 kpc) brightness excess spiral in the system, which strongly indicates that the ICM is sloshing in the gravitational potential of the cluster. The sloshing was likely triggered by previous merger events, in addition to the two currently ongoing mergers.

2. The S subcluster has a peculiar morphology with a clear south-eastern tail that ends in an abrupt surface-brightness drop. One of the edges of the tail is smooth over 200 kpc, with the edge width of ∼10 kpc, which is narrower than the Coulomb mean free path of the electrons in the main cluster gas, while the other edge is blurred and bent.

3. We propose a scenario which explains the overall properties of the system consistently.

   (a) The sloshing was triggered several Gyrs ago, establishing ordered gas motions and ordered magnetic fields.

   (b) The outer gas of the subcluster has been stripped earlier, and the low-entropy core gas is currently being stripped.

   (c) The stripped gas is being blown and bent by the ordered velocity field induced by the sloshing. At the same time, the ordered magnetic field lines that are stretched and oriented along the spiral, are suppressing transport processes across the sharp edge.

4. We suggest that the S subcluster core is almost entirely stripped of the low-entropy gas, demonstrating a case of efficient destruction of a cool core during a merger. This observation poses a challenge to simulations, which find that cool cores usually survive late major mergers, and indicates that the microphysical properties of the ICM is more complex than the simple ideal fluid approximation typically employed by these numerical models.

5. The tail of the S subcluster hosts X-ray bright gas clump candidates that are not associated with galaxies. The tail appears to continue out to around r_{500} of the main cluster. The stripped tail of the infalling southern subcluster seems to continue across a radial range of over 700 kpc, which indicates that the stripping of infalling subclusters may seed gas inhomogeneities. The length of the tail may imply a long lifetime of the tail structure, indicating that strong turbulence or diffusion are suppressed.

6. Beyond the stripped tail, which extends to r_{500}, the deprojected entropy profile along the infall direction is consistent with the theoretical prediction out to r_{200}. However, due to the large errorbars we cannot rule out flattening as observed in other systems.

7. We confirm a previously known hotspot to the north-east of the S subcluster. The required Mach number to shock-heat the hotspot is in the range of $1.3 < \mathscr{M} < 1.8$, which is consistent with the previous observations.

8. The interface between the SW subcluster and the main cluster has a high temperature and high entropy and might have been shock-heated by the merger of the subcluster. The estimated merger Mach number of the SW subcluster is $\mathscr{M} = 1.4 \pm 0.1$.

9. We see cold fronts around the core of the main cluster where we see an X-ray faint cavity in the south which is probably due to an AGN blown bubble. The counterpart bubble may be hidden by the dense gas displaced by sloshing.

Chapter 6

"Feather"s and cold fronts in the Perseus cluster

6.1 Overview

The Perseus cluster is a nearby ($z = 0.0183$, Fabian et al., 2006), massive ($M_{200} = 6.65 \times 10^{14} M_{\odot}$, Simionescu et al., 2011), and the brightest cluster of galaxies in the X-ray sky (Edge et al., 1990). It had been known as one of the Abell catalogue clusters (Abell 426), and is one of the galaxy clusters from which extended X-ray emission was detected in the earliest period (Kellogg et al., 1971). Because of its proximity and X-ray brightness, it has been the most extensively studied galaxy cluster in the X-ray wavelength.

The Perseus cluster is a relatively relaxed, cool-core cluster, and its X-ray morphology is strongly centrally peaked on the position of its brightest cluster galaxy (BGC) NGC1275 (3C84, Fabian et al., 1981). NGC1275 is a giant elliptical galaxy, which is classified as a Seyfert Type 1.5 active galaxy (Yamazaki et al., 2013), and which hosts an X-ray and radio bright active galactic nucleus (AGN). It is also the brightest radio galaxy in GeV gamma-ray wavelength detected with Large Area Telescope onboard the *Fermi* Gamma-ray Telescope (Abdo et al., 2009; Atwood et al., 2009). NGC1275 is surrounded by filamentary Hα emission (Kent & Sargent, 1979; Fabian et al., 2011b), which are thought to be stabilized by magnetic fields (Fabian et al., 2008).

Many X-ray cavities have been observed around the core of the Perseus cluster. The innermost cavities are filled with radio lobes (Boehringer et al., 1993; Churazov et al., 2000; Fabian et al., 2000), suggesting that they are bubbles inflated by the jet from the central AGN, being filled with relativistic particles. This is one of the most critical observations regarding the AGN feedback mechanism as the heat source of the ICM to prevent the radiative cooling catastrophe (so-called "cooling flow problem"). The outer cavities are "ghost" cavities, which are not associated with radio emission peaks (Fabian et al., 2006, 2011a). The ghost cavities are though to be devoid of the relativistic particles, and thus related to the past activities of the central AGN.

A deep *Chandra* observation of the core of the Perseus cluster revealed the existence of weak shocks and ripples (Fabian et al., 2006). The ripples seem to be propagating outward, which are thus likely to be sound waves associated with the bubbles, transporting the energy input from the bubble to the ICM (Sanders & Fabian, 2007).

The X-ray morphology around the core is observed to be asymmetric, with a spiral-like arm

extending anticlockwise from the vicinity of the center (Churazov et al., 2000, 2003; Sanders & Fabian, 2007; Fabian et al., 2011a). The thermodynamic structures (Fabian et al., 2006) indicate that the spiral is a sloshing cold front (Ascasibar & Markevitch, 2006; Markevitch & Vikhlinin, 2007) due to a previous merger. *XMM-Newton* and *ROSAT* observations found that the X-ray morphology is asymmetric also in larger scales (Churazov et al., 2003; Simionescu et al., 2012), which is probably related to the innermost spiral pattern.

In addition to the apparent X-ray structures, there have been several indications for the internal/line-of-sight gas motions in the Perseus cluster. Churazov et al. (2004) suggested a lack of resonance scattering in the core of the Perseus cluster, which is intriguing because it implys gas motion in the core with the velocity of the order of half of the ICM sound speed. Tamura et al. (2014) hinted at gas bulk motion with a small radial velocity of 150-300 km s^{-1} at 2-4 arcmin west of the core. Zhuravleva et al. (2014) inferred the turbulent power spectra of ICM from the X-ray surface brightness fluctuations, and suggested that the turbulent heating can balance the ICM radiative cooling. All of the observations will probably be tested by the upcoming *ASTRO-H* satellite.

The observations of the outskirts of the Perseus cluster using *Suzaku* and *XMM-Newton* have provided one of the most detailed views of the ICM at large radii of galaxy cluster. The thermodynamic profiles out to the virial radii indicate that the ICM is inhomogeneous at large radii (Simionescu et al., 2011; Urban et al., 2014), which is one of the most actively discussed topics these days. Werner et al. (2013b) showed that the iron abundance is remarkably uniform from the center to the virial radii independent of the azimuthal directions with the value of $\sim$0.3 Solar. Matsushita et al. (2013) showed that both the iron-mass-to-light ratio (IMLR) and the silicon-mass-to-light ratio (SMLR) increase with radius. Both observations support the scenario that the ICM was enriched before the cluster formed.

Although a number of observations have been done and many features are investigated in detail from kpc scales to Mpc scales as mentioned above, there are a lot of features which still remain to be studied. Among such structures, we selected two structures which are relatively close to the core (within $<$100 kpc from the center), and both seem to be related to the above-mentioned sloshing cold front. Because of the brightness and the depth of observation, we think that the Perseus cluster is the best system to study thermodynamics (i.e. spectroscopic properties) of each substructure associated with cold fronts. Note that, the Virgo cluster, which is the third brightest, but the nearest galaxy cluster, is probably most suitable for studies of very small physical length scale structure, and actually has recently studied by Werner et al. (2016).

For the spectral fitting, we used XSPEC (version 12.8.2, Arnaud, 1996) to minimize χ^2. We used the chemical abundance table determined by Lodders (2003).

6.2 Observations and data reduction

The Perseus cluster has been observed many times with *Chandra*. The primary focal plane detector has been either the ACIS-S or the ACIS-I, and the aim points are significantly different between the ACIS-S coordinated observations and ACIS-I coordinated observations. Therefore we did not combine the data from the ACIS-S coordinated observations and the ACIS-I coordinated observations, but analyzed these two datasets of these coordinated observations separately.

For the ACIS-S coordinated observations, we selected fourteen ObsIDs (1513, 3209, 4289,

Table 6.1. Data

Satellite	Obs ID	Date	Detector	Net exposure time (ksec)[a]
Chandra	1513	2000-01-29	ACIS-S	24
Chandra	3209	2002-08-08	ACIS-S	96
Chandra	4289	2002-08-10	ACIS-S	95
Chandra	4946	2004-10-06	ACIS-S	24
Chandra	4947	2004-10-11	ACIS-S	30
Chandra	4948	2004-10-09	ACIS-S	119
Chandra	4949	2004-10-12	ACIS-S	29
Chandra	4950	2004-10-12	ACIS-S	88
Chandra	4951	2004-10-17	ACIS-S	96
Chandra	4952	2004-10-14	ACIS-S	164
Chandra	4953	2004-10-18	ACIS-S	30
Chandra	6139	2004-10-04	ACIS-S	56
Chandra	6145	2004-10-19	ACIS-S	85
Chandra	6146	2004-10-20	ACIS-S	47
Chandra	11713	2009-11-29	ACIS-I	112
Chandra	11714	2009-12-07	ACIS-I	92
Chandra	11715	2009-12-02	ACIS-I	73
Chandra	11716	2009-10-10	ACIS-I	40
Chandra	12025	2009-11-25	ACIS-I	18
Chandra	12033	2009-11-27	ACIS-I	19
Chandra	12036	2009-12-02	ACIS-I	48
Chandra	12037	2009-12-05	ACIS-I	85

Note. — (*a*) The net exposure time is after the data screening.

4946, 4947, 4948, 4949, 4950, 4951, 4952, 4953, 6139, 6145 and 6146) which have the satellite exposure time of above 10 ksec and are taken relatively long after the launch, in order to lessen the effect of the software/calibration uncertainty of the satellite initial-phase operation. For the ACIS-I coordinated observations, we selected eight ObsIDs (11713, 11714, 11715, 11716, 12025, 12033, 12036 and 12037) with similar criteria to the ACIS-S case. The details of the data reduction are shown in Section 4.2.1. The software versions were CIAO 4.7, and CALDB 4.6.5.

The net exposure times of each observation after the screenings are summarized in Table 6.1. The resulting total net exposure time is ∼1 Msec for the ACIS-S dataset and ∼500 ksec for the ACIS-I dataset. Since the Perseus cluster is the brightest cluster and the exposure times of the order of 500 ksec-1 Msec are longest-class exposure times, these data can be regarded as the highest-quality *Chandra* cluster data currently available.

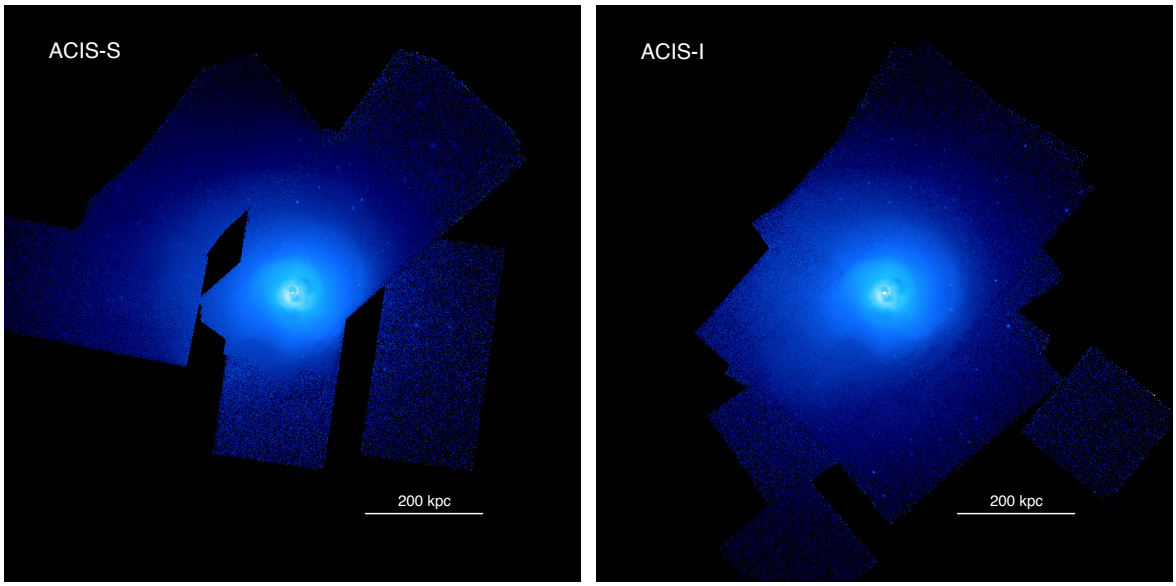

Figure 6.1 $\sigma = 0.98$ arcsec Gaussian smoothed, exposure and vignetting corrected, background subtracted *Chandra* images (0.6-7.5 keV) for the ACIS-S dataset (Left) and the ACIS-I dataset (Right).

6.3 Data analysis

6.3.1 Imaging analysis

We created the flat-fielded *Chandra* images of both the ACIS-S and the ACIS-I datasets as described in Section 4.3.1. The resulting images for both the ACIS-S and the ACIS-I datasets are shown in Figure 6.1 and 6.2. The on-axis directions of each of the observations are aligned within ∼10 arcsec from its BCG NGC1275 in the case of the ACIS-S datasets, whereas they are displaced at most ∼7 arcmin in the case of the ACIS-I datasets. Since the misalignment of the on-axis direction can cause worse angular resolutions (this effect can be easily seen in Figure 6.2), we decided to use only the ACIS-S datasets in the all subsequent analyses.

We created an unsharp-masked image with $\sigma_1 = 2$ pixel and $\sigma_2 = 20$ pixel (see Section 4.3.2). The unsharp-masked image is shown in Figure 6.3 left. Also, in order to emphasize the low-contrast azimuthal variations, we created a relative deviation image. The entire field of view was splitted into annuli with the width of 1 arcsec, which are concentered on the cluster center (position of NGC1275), and the average surface brightness value was calculated for each annulus. The value in each pixel in the flat-fielded image was divided by the corresponding average value, resulting in the relative deviation image shown in Figure 6.3 right.

6.3.2 Thermodynamic mapping

We created the thermodynamic maps as described in Section 4.3.3. The assumed line-of-sight depth is $l = 1$ Mpc. The S/N ratio of each bin is about 100, corresponding to about 10000 counts/bin. The resulting temperature, pressure and entropy maps are shown in Figure 6.4. The black circles are the positions of point sources which are visually identified and subtracted.

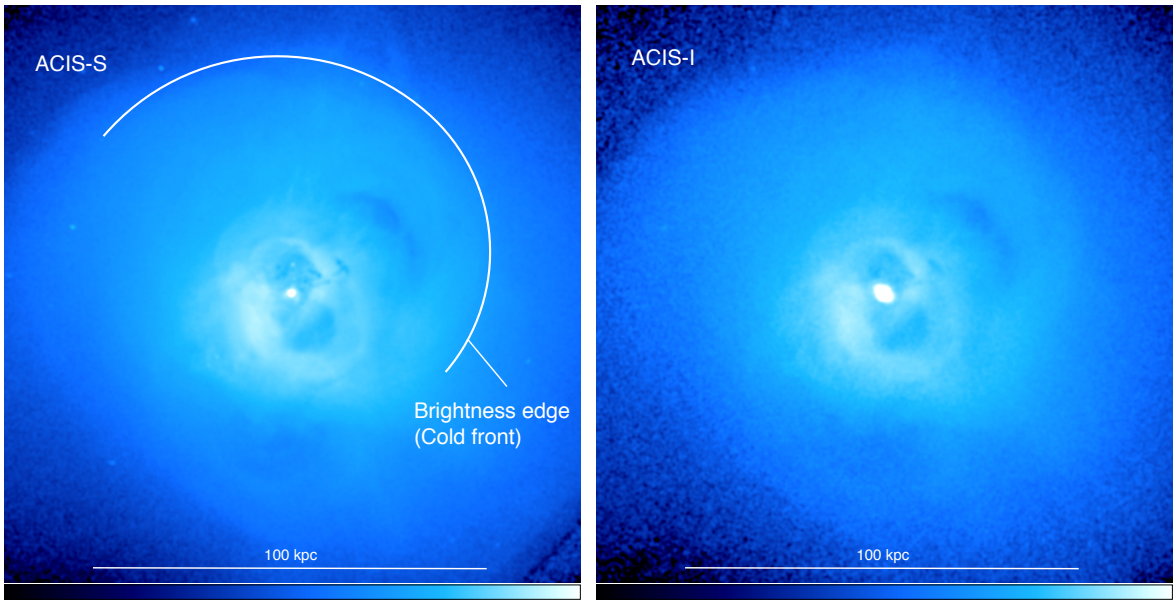

Figure 6.2 The zoom-in images of Figure 6.1. The arrangement is same as Figure 6.1.

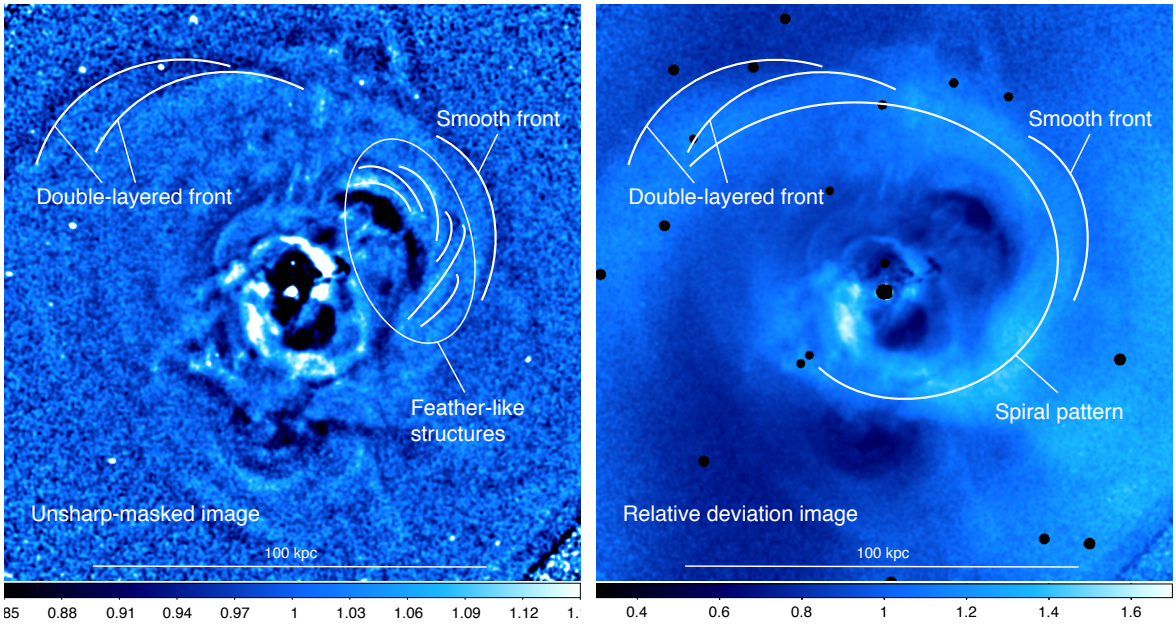

Figure 6.3 *Left:* unsharp-masked image created by dividing the $\sigma = 2$ pixel Gaussian smoothed image by the $\sigma = 20$ pixel Gaussian smoothed image. *Right:* $\sigma = 0.98$ arcsec Gaussian smoothed relative deviation image with respect to the radial average.

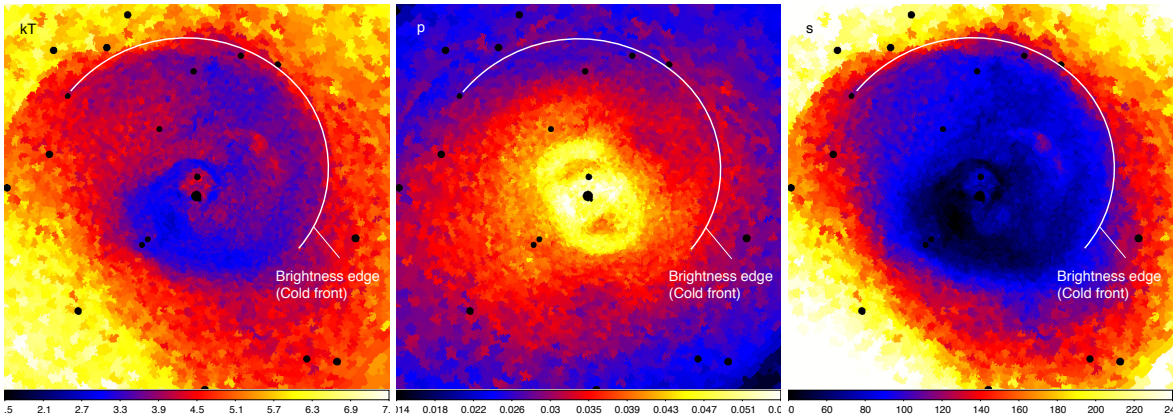

Figure 6.4 Projected thermodynamic maps assuming a uniform ICM line-of-sight depth of $l = 1$ Mpc. *Left:* projected temperature map in the unit of keV. *Middle:* projected pressure map in the unit of keVcm$^{-3} \times (l/1\ \mathrm{Mpc})^{-1/2}$. *Right:* projected entropy map in the unit of keVcm$^{2} \times (l/1\ \mathrm{Mpc})^{1/3}$.

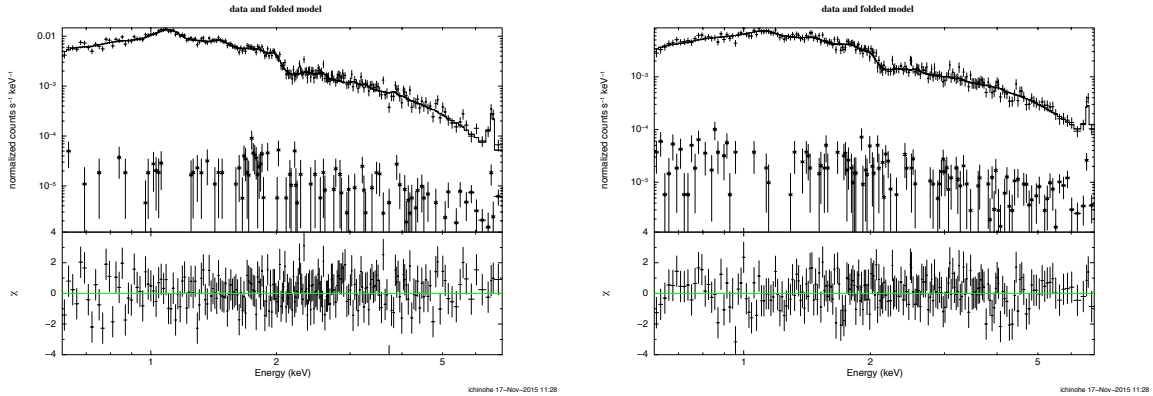

Figure 6.5 Examples of the spectral fitting. *Left:* the spectra extracted from below the northwestern cold front. *Right:* the spectra extracted from above the northwestern cold front. The + markers are the data, the curves are the model, and the × markers are the background.

In the spectral fitting, the redshift was fixed to 0.0183 and the hydrogen column density was set to 1.38×10^{21} cm^{-2}, determined by the LAB (Leiden/Argentine/Bonn) radio HI survey (Kalberla et al., 2005). We obtain typical fitting errors of 2% for the density map, and 4% for the temperature, pressure and entropy maps. The typical reduced χ^2 is 1.01, with the typical NDF of 210. Figure 6.5 shows the example fitting results for the regions which are marked with the green stars in Figure 6.11 left.

6.4 Results

6.4.1 Global morphological features

In the flat-fielded image (Figure 6.2), the unsharp-masked image (Figure 6.3 left) and the relative deviation image (Figure 6.3 right), we see plenty of structures. Since many of the features have already been mentioned and explored in the literature (e.g. Churazov et al., 2000, 2003; Fabian et al., 2006; Sanders & Fabian, 2007), here we point out the structures which have not been mentioned or are related to our subsequent detailed analyses.

In the relative deviation image (Figure 6.3 right), we see a clear spiral-like pattern which has been mentioned in the literature (e.g. Churazov et al., 2003; Fabian et al., 2006; Sanders & Fabian, 2007). Delineating the outer edge of the spiral, we see a brightness edge which starts about 50 kpc west of the core and extends anticlockwise to about 70 kpc north-east of the core in the flat-fielded image (Figure 6.2), which is more apparent in the unsharp-masked image (Figure 6.3 left).

This spiral-like structure and the edge are also apparent in the projected temperature and entropy maps (Figure 6.4). The fact that the gas beneath the edge is cooler and has lower-entropy than above the edge, as well as the fact that no clear pressure structure along the edge is seen, indicate that the edge is a cold front, originating from the sloshing motion of cool gas in the core (Ascasibar & Markevitch, 2006; Markevitch & Vikhlinin, 2007).

The west half of the front seems relatively smooth, while the east half of the front exhibits a more complex, double-layered structure, indicating the existence of developing instability which may be due to the sloshing motion of the ICM. We would like to point out the similarity between this cold front and the numerical simulation result by Roediger et al. (2013a) (Figure 6.6 middle). They attributed this phenomenon to the difference of mean shear at different azimuths of the front.

In the unsharp-masked image, underneath the west half of the front, we see feather-like structures, namely alternating bright and faint regions which have not been reported previously in the literature. Recently Werner et al. (2016) found similar structures just below the northwestern cold front in the Virgo cluster.

6.4.2 Double-layered structure of the eastern cold front

Figure 6.7 shows the close-up view of the eastern part of the cold front, where we see a peculiar double-layered structure. The overlaid partial annuli are adjusted so that their curvature matches the curvatures of the two fronts, and thermodynamic properties are extracted from these regions.

We extracted the surface brightness profile across these two fronts. Since the radius of the 90% enclosed-counts fraction aperture near the front is ~ 2 arcsec, we used 2 arcsec radial binning. The extracted surface brightness profile is shown in Figure 6.8 top left.

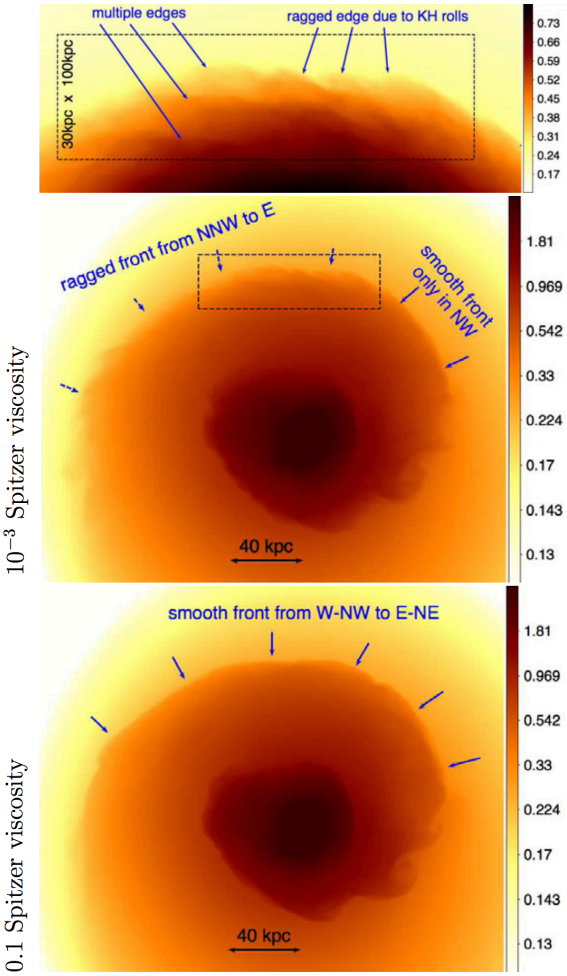

Figure 6.6 Synthetic X-ray images for the low- (middle panel) and high-viscosity (bottom panel) sloshing cold front, in arbitrary logarithmic scale. The top panel is the closeup view of the cold front denoted in the dashed rectangle in the middle panel. These figures are taken from Roediger et al. (2013a).

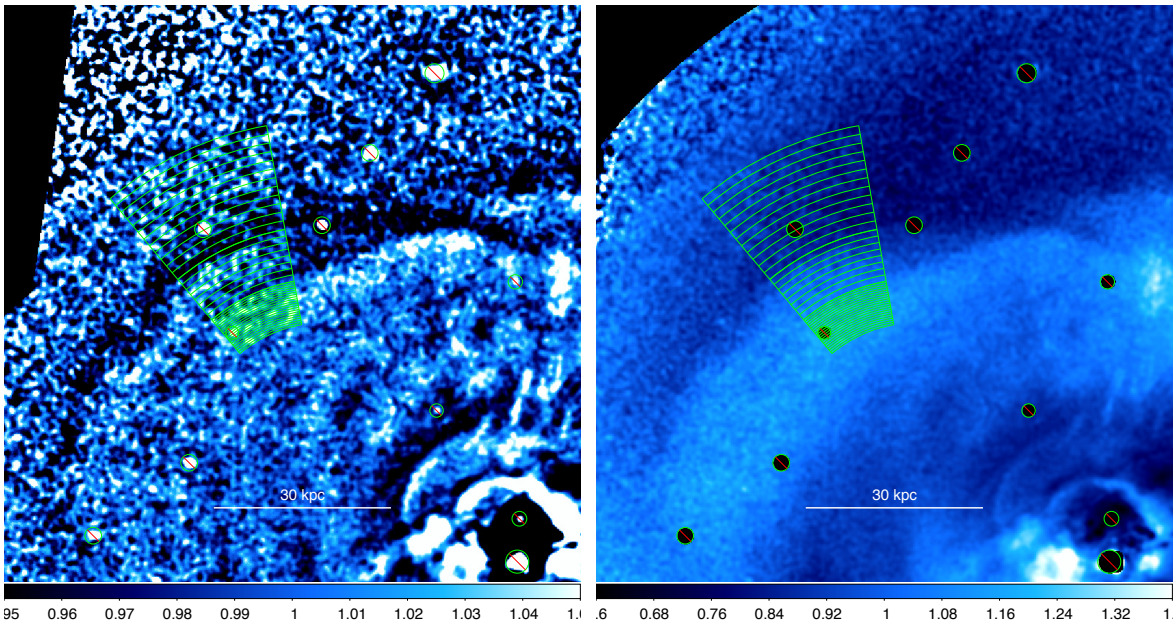

Figure 6.7 Same as Figure 6.3, zoomed in on the double-layered structure. Green partial annuli denote the regions from which spectra are extracted (see Figure 6.8.)

In order to estimate the positions of the breaks, we fitted the surface brightness profile using a projected double-broken power law model (see Chapter 7, Sections 7.4.2 and 7.5.3 for details). The center of the spherical symmetry is set to the concenter of the sectors. The model marginally describes the profile with $\chi^2/\mathrm{NDF} = 64.0/37$ and strongly prefers the double-broken power law model to the single-broken power law model by $\Delta\chi^2/\Delta\mathrm{NDF} = 79.4/3$. The positions of the two breaks are $r_{12} = 82.0 \pm 1.0$ arcsec and $r_{23} = 106.5 \pm 0.5$ arcsec respectively for the inner and outer breaks. These error ranges are overlaid in Figure 6.8 as the grey vertical bands.

For each region in Figure 6.7, we extracted spectra and fitted them using an absorbed single-temperature thermal plasma model; `phabs(apec)`. The hydrogen column density n_H is fixed to the average value of 0.196×10^{22} cm^2. We calculated the pseudo density $\tilde{n}$ from the best-fitting normalization of `apec` ϵ, using $\tilde{n} = \sqrt{\epsilon/A}$ where A is the area of the corresponding region. Using the pseudo density, the pseudo pressure and the pseudo entropy are also calculated using $\tilde{n}kT$ and $kT\tilde{n}^{-2/3}$. The resulting (pseudo) thermodynamic profiles are shown in Figure 6.7. The typical reduced χ^2 of the spectral fits is 1.01, with the typical NDF of 310. Figure 6.9 shows the example fitting results for the eleventh and twentieth regions from the innermost region in Figure 6.7.

The temperature profile are almost continuous at the first break and shows a rapid increase at the second break, while the Fe abundance is almost continuous over the entire radial change. Although almost continuous, we see some indications for the change in the temperature slopes and the existence of a mild jump around the first break. Although the pseudo pressure profile shows no rapid changes or jumps around the breaks, it is not monotonic. The pseudo entropy profile is qualitatively similar to the temperature profile.

We also plotted reference profiles in the temperature, the pressure and the entropy profiles, using the azimuthally averaged pseudo-temperature, pressure and entropy profiles. We

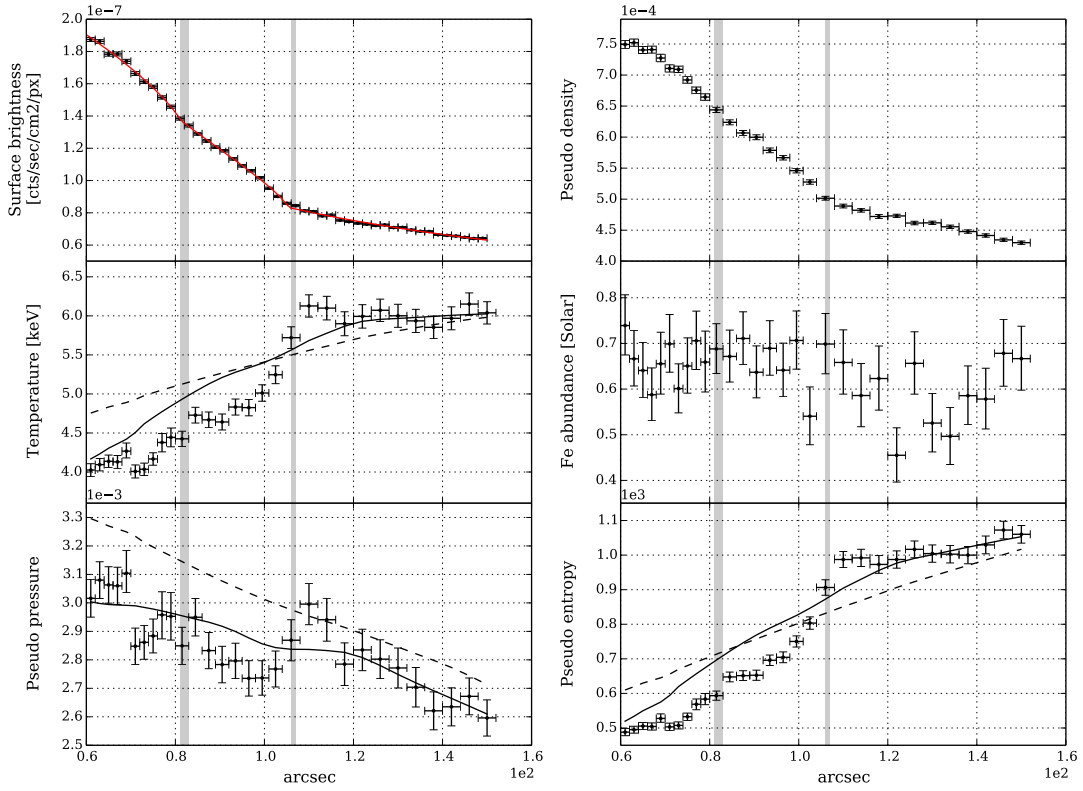

Figure 6.8 *Top left:* surface brightness profile extracted across the double-layered structure. The red curve is the best-fitting projected double-broken power-law model. *Top right:* pseudo-density profile. *Middle left:* projected temperature profile. *Middle right:* projected Fe abundance profile. *Bottom left:* pseudo-pressure profile. *Bottom right:* pseudo-entropy profile. The solid/dashed curves are reference profiles calculated using the azimuthally averaged profile over 60°-150°/the entire azimuths. The gray vertical bands denote the positions of the breaks in the surface brightness profile.

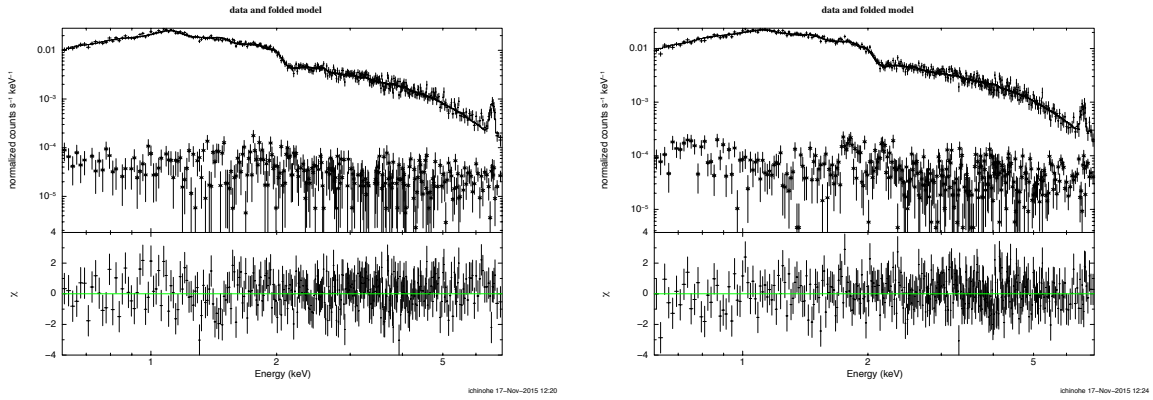

Figure 6.9 Examples of the spectral fitting. *Left:* the spectra extracted from the eleventh region. *Right:* the spectra extracted from the twentieth region. The + markers are the data, the curves are the model, and the × markers are the background.

splitted the entire field of view into annular grids, whose radial and azimuthal widths are 10 arcsec and 10° respectively, which are concentered on the cluster center. From each grid, we extracted spectra and analyzed them in the same way mentioned in the paragraphs above, resulting in thirty-six thermodynamic values per radial annulus. We averaged them to obtain the radial thermodynamic profiles. We calculated the thermodynamic values at the corresponding radius for each bin in the sectors from which the thermodynamic profiles are extracted (Figure 6.7), and averaged them in the sector to estimate the reference values. Since the projected pressure map shows a significant asymmetry as shown in Figure 6.4, we calculated the averaged thermodynamic profiles in two ways; (1) averaged over all the azimuths and (2) averaged over the azimuthal range of 60°-150°. The reference profiles based on the average over all the azimuths are plotted using the dashed curves and the ones using the azimuthal range of 60°-150° are plotted using the solid curves in Figure 6.8.

The overall pressure profile is lower than the 0°-360° reference profile (dashed line). In addition, we see a dip between the two breaks and a hump just outside the second break compared to the 60°-150° reference profile (solid line). The temperature and the entropy profiles are systematically lower than the reference profiles and seem to overtake the reference profiles around the second break.

6.4.3 Feather-like structures

Figure 6.10 shows the same images as Figure 6.3, zoomed-in to the vicinity of the feather-like structures, together with the SDSS r-band optical image (Eisenstein et al., 2011; Ahn et al., 2014). The alternating bright and faint regions are clearly seen in the unsharp-masked image (left panel). Among the structures which are apparent in the unsharp-masked image, the central faint region (brightness dip; denoted by the white rectangle) exhibits the most prominent contrast against the surrounding ICM, which even can be seen in the low-contrast relative deviation image (middle panel).

Figure 6.11 shows the closeup view of the projected thermodynamic maps (Figure 6.4). Northeast and south of the white rectangle, we see arms with low temperature and low entropy, which seem to correspond to the bright arms in the unsharp-masked image. We also

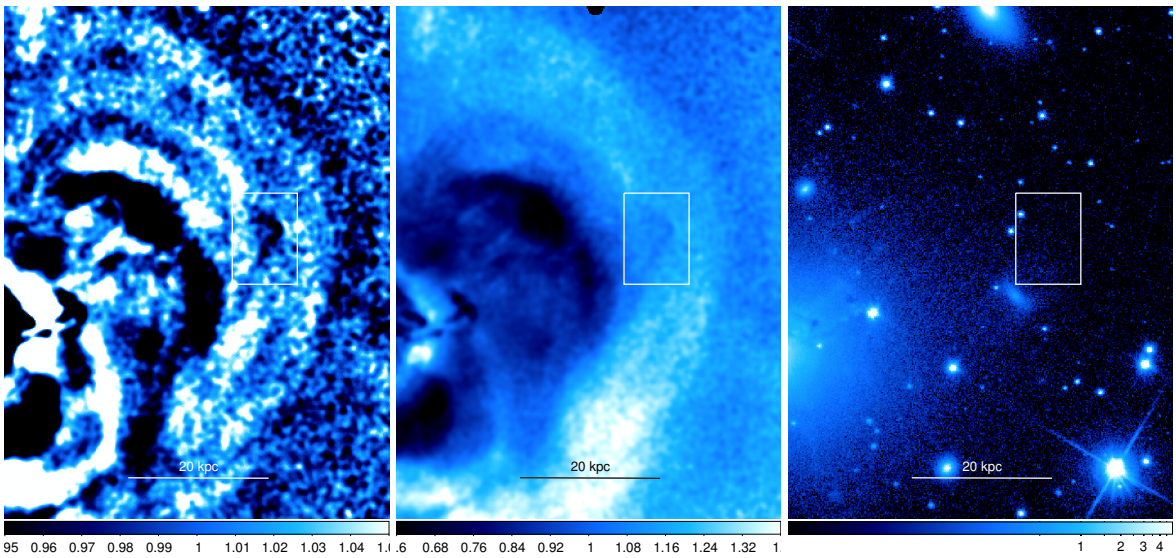

Figure 6.10 The closeup view of the unsharp-masked image (left), the relative deviation image (middle) and the SDSS r-band optical image of the corresponding sky region. The white rectangle in each image denotes the position of the brightness dip.

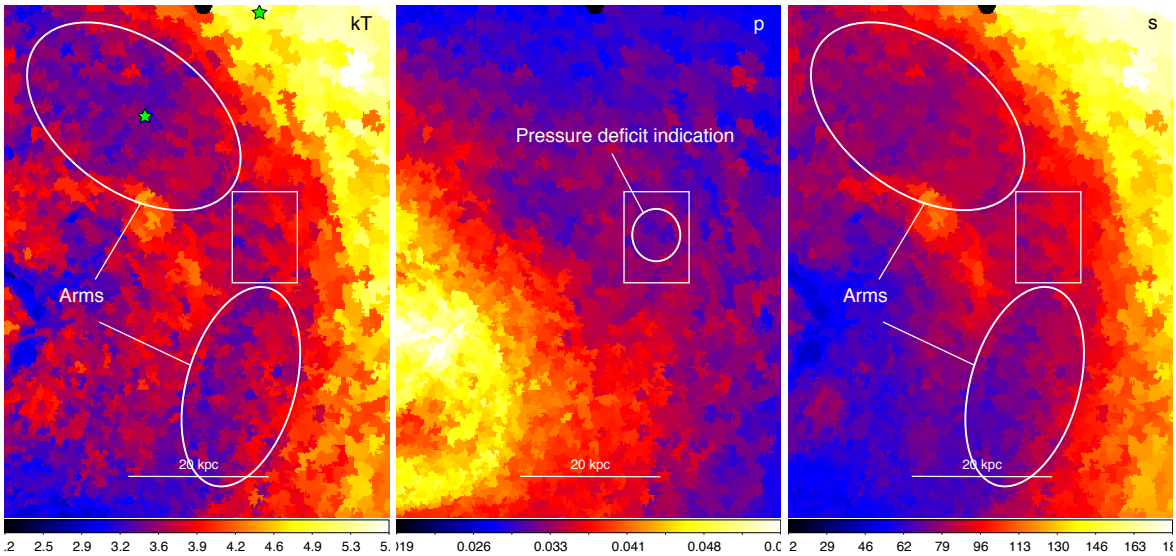

Figure 6.11 The closeup view of the projected temperature (left), pressure (middle) and entropy (left) maps (Figure 6.4). The white rectangle in each image denotes the position of the brightness dip. The green star markers denote the regions of which example spectra are shown in Figure 6.5.

see an indication of pressure deficit around the brightness dip in the pressure map.

To investigate the spectral properties of the feather-like structures, it is necessary to determine the regions from which the spectra are extracted. However, the shapes of the feather-like structures are not at all regular. In order to determine the regions for such complex structures, we prepared a grid of regions by slicing a sector centered on the cluster center. The region is sliced in intervals of 2 arcsec in the radial direction, and 1° in the azimuthal direction. This gridding method makes it relatively easy to take into account the effect of the overall radial gradient of the physical properties of the ICM if the cluster is symmetric.

Based on the unsharp-masked image, for each feather, we selected the grid elements which are located on the structure, and combined them to treat as a single region. Figure 6.12 shows the seven regions, created with the above procedure to follow the apparent structure. We number the regions from 0 to 6, from the north-eastern region to the southmost one.

For each region, we extracted spectra and fitted the data with an absorbed single-temperature thermal plasma model; `phabs(apec)`. We let all the parameters vary except for the redshift which is fixed to 0.0183. The typical reduced χ^2 is 1.24, with the typical NDF of 425.

Figure 6.13 shows the resulting (pseudo) thermodynamic properties of each feather region. In plotting them, the volume is calculated in two ways to check the systematic effect caused by the assumption of the geometrical setup of the ICM. In the first method, the volume is calculated assuming a unit uniform line-of-sight depth and the results based on this volume are shown in black in Figure 6.13. In the other method, it is calculated by summing up all the pseudo volume elements determined by each grid element. For each single grid element, which has a shape of partial annulus, the pseudo volume is calculated using $4\pi/3 \cdot (r_{\rm out}^2 - r_{\rm in}^2)^{3/2}/360$, where $r_{\rm out}$ and $r_{\rm in}$ are the outer and the inner radii of the grid element and 360 in the denominator represents the azimuthal fraction of each grid (1°). This pseudo volume corresponds to the volume of the spherical shell whose cross-sectional shape in the sky is the shape of the grid. The results based on this volume are shown in red in Figure 6.13. The volume calculation method only causes an overall shift in the normalization of the resulting thermodynamic properties but does not affect the relative trends.

Despite the apparent feathers in the unsharp-masked image, we find no strong fluctuations in any thermodynamic properties, except for the region 3 (the brightness dip) which shows a clear density drop as expected from the previous images, e.g. Figure 6.10 middle. The temperatures are consistent with each other. The pressure and the entropy show, respectively, a drop and a rise in region 3. We also see an indication of a temperature drop in the regions 2 and 4, which may represent the low-temperature arms previously mentioned in Section 6.4.3.

Generally, regions 0, 1 and 2 show similar thermodynamic properties to each other, as do regions 4, 5 and 6, while region 3 seems to exhibit anomalous thermodynamic properties. Thus, in the subsequent sections, we focus on the region 3 (the brightness dip) as the most prominent one of the feathers, and investigate it more in detail.

6.4.4 Brightness dip in detail

Thermodynamic properties in the dip

To investigate the ICM properties in the brightness dip (region 3) in detail, we rechose the regions based on the relative deviation image, because the unsharp-masked image is essentially an edge-enhanced image and thus is not suitable for considering the absolute brightness of the

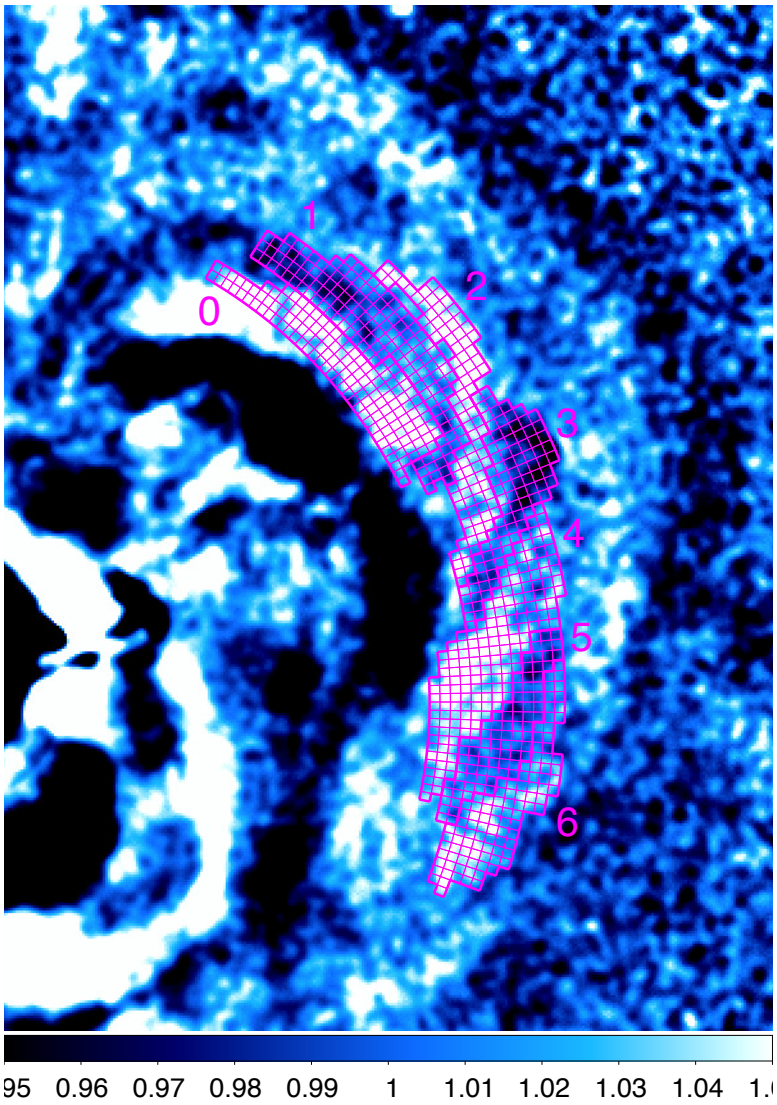

Figure 6.12 The regions for spectral extraction, overlaid on the unsharp-masked image. The regions are numbered from 0 to 6 from the north-eastern region to the southmost one.

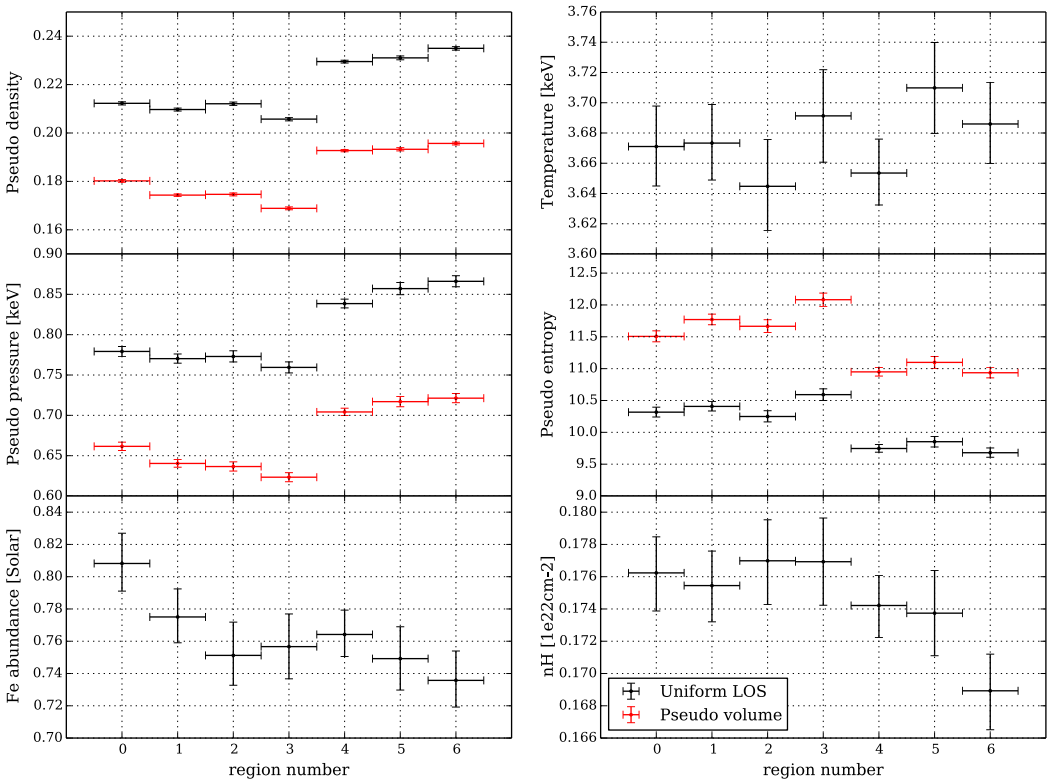

Figure 6.13 Pseudo/projected thermodynamic properties of the feather-like structures. *Top left:* pseudo density calculated using ϵ/V, where ϵ is the `apec` normalization and V is the volume of the ICM in the corresponding sky region, where a uniform line-of-sight depth is assumed (black) or the pseudo volumes are summed up (red). *Top right:* projected temperature, *Middle left:* pseudo pressure calculated using $\tilde{n}kT$, where kT is the projected temperature and $\tilde{n}$ is the pseudo density. *Middle right:* pseudo entropy calculated using $kT\tilde{n}^{-2/3}$, where kT is the projected temperature and $\tilde{n}$ is the pseudo density. *Bottom left:* Fe abundance. *Bottom right:* hydrogen column density. The units are keV, Solar and 1e22 cm^{-2} for the temperature, Fe abundance and hydrogen column density. The units of the pseudo density, pressure and entropy are arbitrary.

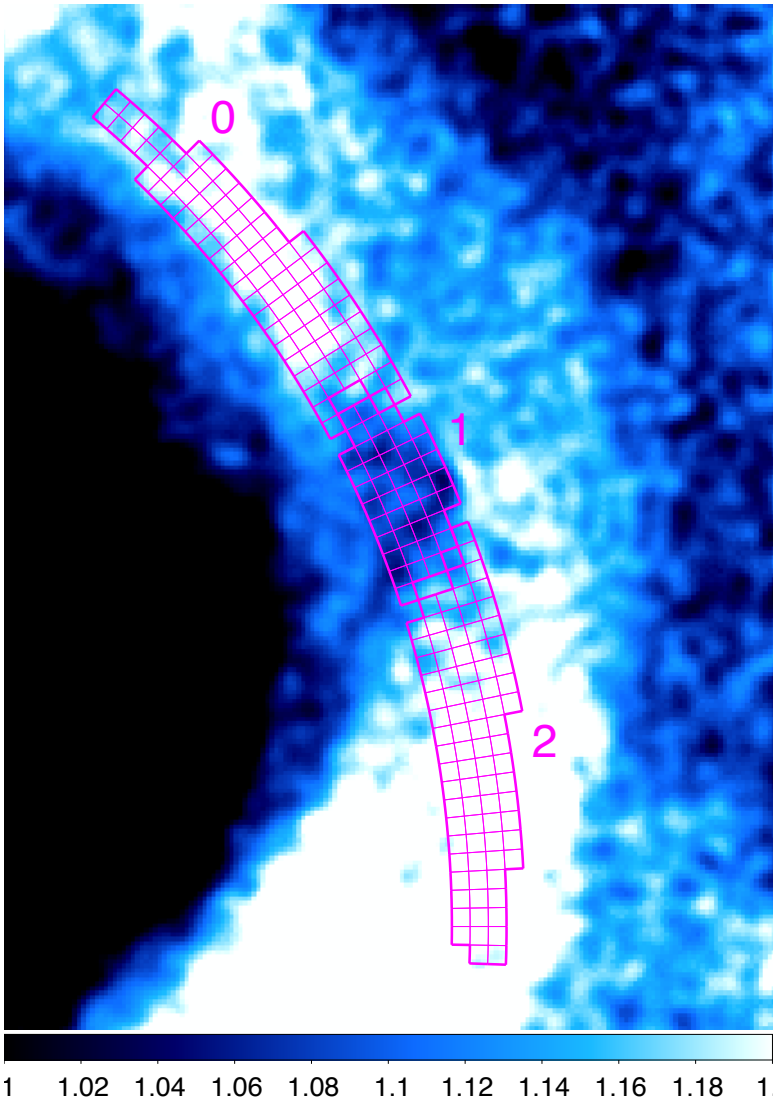

Figure 6.14 The regions employed in a detailed study of the brightness dip, overlaid on the relative deviation image. These regions are numbered from 0 to 2 from north to south.

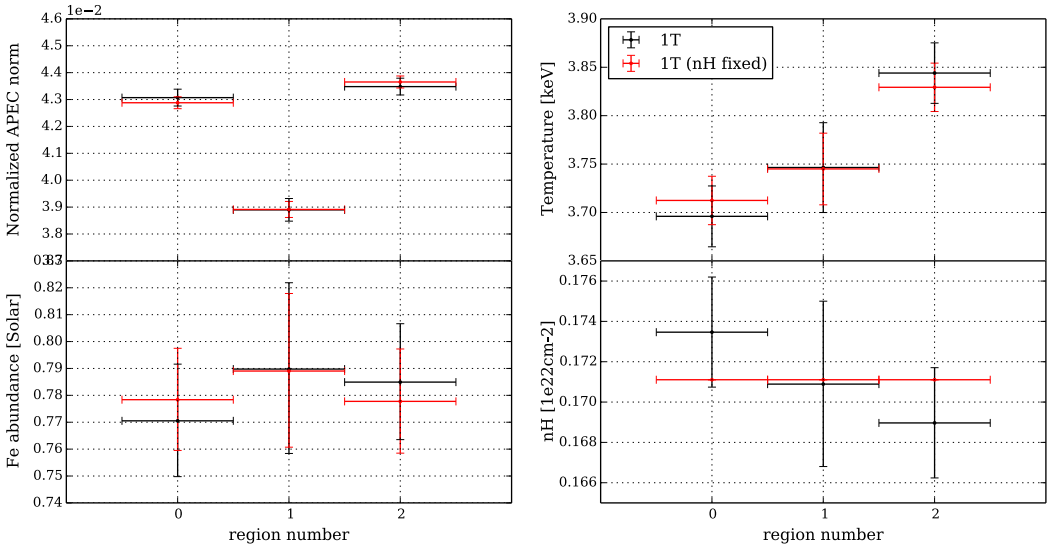

Figure 6.15 Best-fitting parameters of the single temperature model `phabs(apec)`. *Top left:* the `apec` normalization divided by the region area. *Top right:* the temperature. *Bottom left:* the Fe abundance. *Bottom right:* the hydrogen column density. *Black:* allowing all the parameters to vary except for the redshift (fixed to 0.0183). *Red:* allowing the temperature, the Fe abundance, and the normalization to vary. The hydrogen column density was fixed to the average value of the results shown in black.

structures. Figure 6.14 shows the regions employed for the detailed study. We number these regions from 0 to 2 from north to south. The areas of the regions 0 and 2 are double compared to that of the region 1 for each radius, lessening the uncertainty due to the difference of the radial dependency of the region shape between the regions. We used only the outer part of the brightness dip because at the inner radii, the strong azimuthal variation of the absolute brightness would probably make the detailed study complex.

For each region, we extracted spectra and fitted the data with an absorbed single-temperature thermal plasma model; `phabs(apec)`. We modeled each region independently with allowing all the parameters to vary except for the redshift. The resulting parameters are shown in Figure 6.15 in black. Although the normalization shows clear deficit from the trend in the brightness dip region (region 1), we do not see significant deviations of the other quantities.

For comparison, we modeled each region independently, allowing the temperature, the Fe abundance and the normalization to vary. The hydrogen column density was fixed to the average value of the results shown in black; $0.171\times10^{22}\mathrm{cm}^{-2}$. The results are shown in red in Figure 6.15.

The best-fitting normalization, Fe abundance and temperature agree within the error. Moreover, the χ^2 values shown in Table 6.2 indicate that allowing the hydrogen column density to vary does not significantly improve the fits. Further considering that it is unlikely that the hydrogen column density changes within this (<0.5 arcmin) length scale, we fix hydrogen column density to $0.171\times10^{22}\mathrm{cm}^{-2}$ in all the subsequent analyses.

Table 6.2. χ^2/NDF

Fitting condition	region 0	region 1	region 2	sum
1T	510.60/420	401.58/377	509.87/421	1422.05/1218
1T (nH fixed)	511.35/421	401.58/378	510.48/422	1423.41/1221
2T (nH fixed)	458.02/419	390.18/376	453.14/420	1301.34/1215

6.5 Discussion

6.5.1 Double-layered structure

As shown in Section 6.4.2, the projected double-broken power law model represents the surface brightness profile around the eastern part of the cold front (Figure 6.7) better than the single-broken power law model does. Although the best-fitting parameters other than the break radii are uncertain because the assumption of the spherical symmetry in the projection is probably inaccurate, it is very plausible that the underlying density profile also hosts a double-layered structure similar to the surface brightness profile or the images.

Kelvin-Helmholtz instability

Generally, at the shock front, when the density shows a drop, the temperature, the pressure and the entropy also show a drop because a shock front propagating through the ICM heats and compresses the gas behind it. In contrast, since cold fronts are merely the interface between a cold gas parcel and hot ambient medium, when the density exhibits a drop, the temperature and the entropy exhibit a jump, resulting in an almost continuous pressure profile across the front.

As shown in Figure 6.8, at the first break, we see no rapid changes in thermodynamic properties except for the changes in the slopes of the density and the temperature profiles. This means that, although it is possible that the underlying density structure might host not only a change in gradient but also a jump, the density structure is not strongly associated with either shock or cold fronts. On the other hand, at the second break, the temperature and the entropy show a clear increase and the pressure seems continuous, suggesting that the second break is a cold front.

Therefore, the gases below and above the first break probably have similar origins to each other, and have a different origin from the gas beyond the second break. Such a situation can be realized where Kelvin-Helmholtz instabilities (KHIs) are developing on top of the cold front: The first break was originally a cold front due to the sloshing motion of the gas induced by a previous merger event, which currently manifests itself with the spiral-shaped morphology. Due to the shearing motion of the gas, KHIs have been set off and are currently developing, where the second break represents the current maximum height of the KHI eddies. Since the KHIs mix the gas inside the front into the ambient gas, the thermodynamic properties inside and outside the first break are not discontinuous. The indications for the change in the temperature slopes at the first break may reflect that the gas between the first and the second breaks was dominated by the ambient gas before the onset of KHIs. This situation is

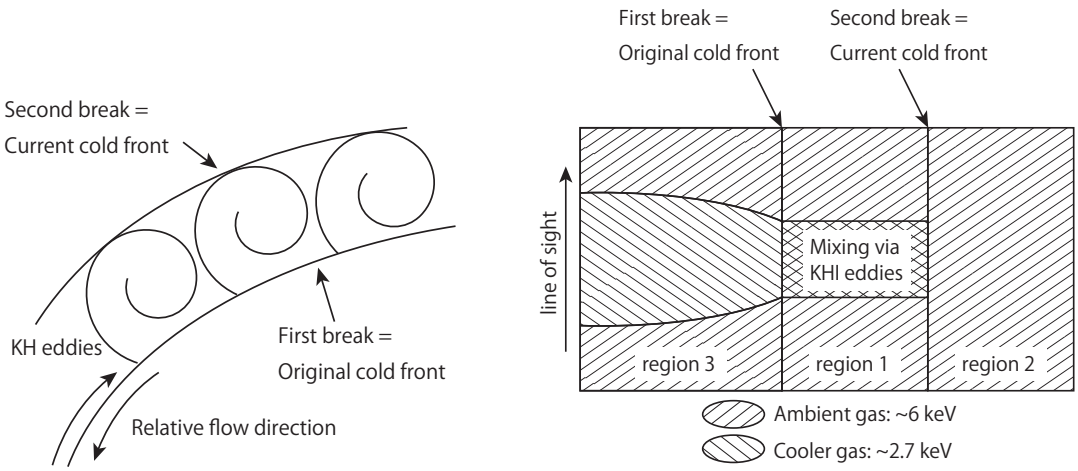

Figure 6.16 Schematic illustrations of the double-layered structure due to the developing KHIs on top of the sloshing cold front.

schematically drawn in Figure 6.16 left.

In order to test the scenario, we examined the multi-temperature property of the corresponding region. We combined together the sectors between the two breaks (region 1; see Figures 6.7 and 6.8). Also, we combined together the sectors beyond the outer breaks (region 2′; see Figures 6.7 and 6.8). Furthermore, we combined together the sectors below the first break (inner gas region, region 3; see Figures 6.7 and 6.8). These regions are shown in Figure 6.17. We extracted spectra using these regions and fitted them using single-temperature (1T; `phabs(apec)`) and two-temperature (2T; `phabs(apec+apec)`) models. Note that three-temperature modeling does not improve the fit ($\Delta\chi^2 < 1$), and thus we conclude that two-temperature modeling is necessary and sufficient to fit these datasets. Figure 6.18 shows the fitting results for the regions in Figure 6.17.

In addition to the above three regions, we defined a reference region (region 2), whose shape is identical to region 1 (pressure dip region), at 20° clockwise from region 1 with respect to the cluster center. This reference region is taken not to intersect the front, and thus expected to represent the ambient medium at similar radii.

Table 6.3 shows the fitting results. Both the spectra of regions 1 and 3 strongly prefer two-temperature modeling ($\Delta\chi^2/\Delta\mathrm{NDF} = 27.03/2$ and $44.87/2$), while those of regions 2 and 2′ do not very much ($\Delta\chi^2/\Delta\mathrm{NDF} = 9.24/2$ and $6.17/2$).

The best-fitting temperatures of the regions 2 and 2′ (1T modeling) are ~ 6 keV, which is consistent with the temperature of the outskirts of the cluster (5-7 keV; Simionescu et al., 2011). Considering that these regions do not significantly prefer 2T modeling, it is likely that both the regions represent the ambient hotter component. However, on the other hand, the best-fitting temperatures are inconsistent with each other. This discrepancy is likely due to the deviation from the simple two-temperature picture (outer hot gas and inner cool gas) assumed in the spectral modeling. The actual temperature profile of the ambient gas is expected to vary continuously, and therefore the ambient gas components which are projected along the line-of-sight should differ from radius to radius. This represents the systematic uncertainty originating from our geometrical assumption and region selections. As the uncertainty is smaller than the difference of the temperatures of the two components in the 2T fitting, we

Table 6.3. Summary of the two-temperature fitting results

Fitting condition	kT_1 (keV)	ϵ_1 $(10^{-3})^a$	kT_2 (keV)	ϵ_2 $(10^{-3})^a$
1T, region 1	4.93 ± 0.05	1.64 ± 0.01	N/A	N/A
1T, region 2	5.81 ± 0.08	1.29 ± 0.01	N/A	N/A
1T, region 2′	6.17 ± 0.05	2.80 ± 0.01	N/A	N/A
1T, region 3	4.25 ± 0.03	1.49 ± 0.01	N/A	N/A
2T, region 1	$5.91^{+0.36}_{-0.21}$	$1.31^{+0.07}_{-0.15}$	$2.74^{+0.36}_{-0.14}$	$0.33^{+0.15}_{-0.07}$
2T, region 2	$8.07^{+1.95}_{-0.75}$	$0.67^{+0.11}_{-0.27}$	$4.32^{+0.63}_{-0.24}$	$0.63^{+0.26}_{-0.15}$
2T, region 2′	$8.79^{+2.41}_{-1.06}$	$0.92^{+0.52}_{-0.41}$	$5.32^{+0.35}_{-0.37}$	$1.88^{+0.43}_{-0.51}$
2T, region 3	$5.66^{+0.56}_{-0.44}$	$1.02^{+0.16}_{-0.19}$	$2.65^{+0.36}_{-0.26}$	$0.48^{+0.17}_{-0.16}$
	Fe abundance (Solar)	n_H $(10^{22}$ cm$^2)$	χ^2/NDF	
1T, region 1	0.68 ± 0.02	0.195 ± 0.003	477.67/430	
1T, region 2	0.59 ± 0.03	0.193 ± 0.003	439.71/430	
1T, region 2′	0.61 ± 0.02	0.198 ± 0.002	438.03/433	
1T, region 3	0.68 ± 0.02	0.195 ± 0.003	501.43/426	
2T, region 1	0.67 ± 0.02	0.195 ± 0.003	450.64/428	
2T, region 2	0.61 ± 0.03	0.193 ± 0.003	430.47/428	
2T, region 2′	0.62 ± 0.02	0.197 ± 0.002	431.86/431	
2T, region 3	$0.65^{+0.03}_{-0.02}$	0.194 ± 0.003	456.56/424	

Note. — (*a*) `apec` normalization; $\epsilon = 10^{-14} \int n_e n_H dV / 4\pi[D_A(1+z)^2]$ where D_A is the angular diameter distance to the source (cm), n_e and n_H are the electron and hydrogen ion densities (cm^{-3})

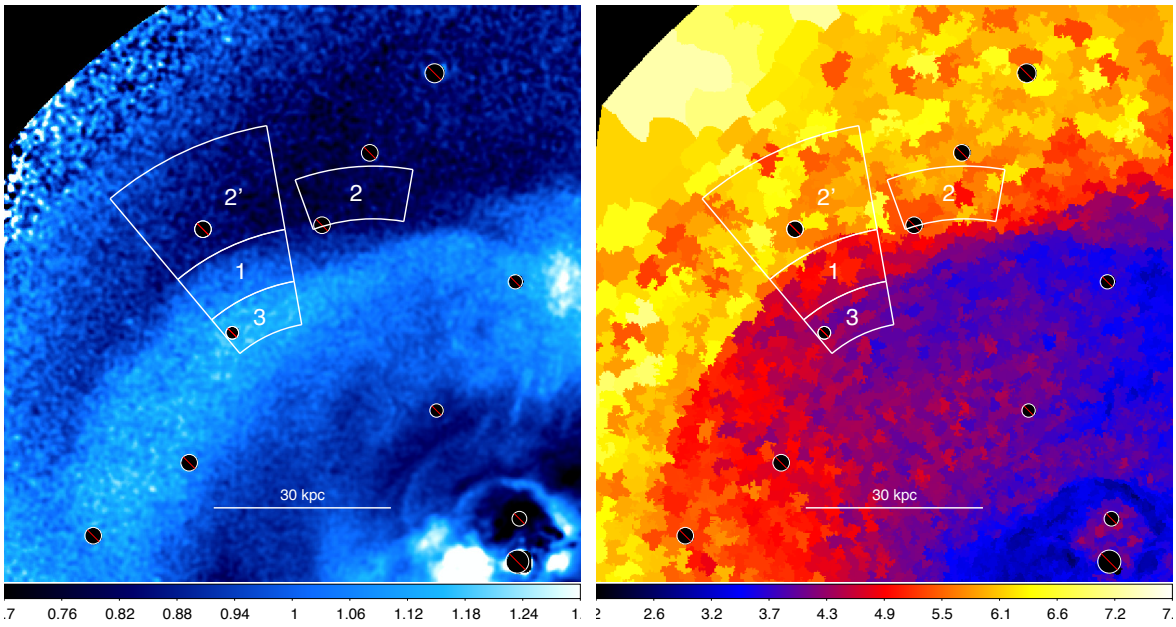

Figure 6.17 The regions used for examining the multi-temperature property of the double layered structure, overlaid on the relative deviation image (left) and the temperature map (right), (see also Figures 6.3 and 6.4).

expect that the systematic uncertainty does not significantly affect our subsequent arguments.

The best-fitting temperature and normalization of the hotter component for region 1 (2T modeling), are consistent with those for the 1T modeling in region 2 (reference region, scaled by the ratio of areas (0.98)), suggesting that the hotter component of region 1 represents the ambient medium at this radius. Furthermore, the temperatures of both the hotter and cooler components are consistent between regions 1 and 3, suggesting that the two temperature components which constitute each region are similar between the two regions. Given that the hotter components probably represent the ambient medium, it is likely that the cooler component of region 1 represents the gas originating from region 3 (inner gas region).

This supports the interpretation of the double-layered structure being a developing KHI, where the hotter component represents the ambient medium, while the cooler component represents the gas which is originally inside the cold front, being mixed into the ambient medium via the currently developing KHI, whichever situation (1T or 2T) the ambient medium is actually in. This picture is schematically drawn in Figure 6.16 right.

By numerical simulations, Roediger et al. (2013a) indeed showed that KHIs can be induced along the edge of the sloshing spiral under certain conditions, and that in such cases, the surface brightness profile hosts characteristic multiple edges, similarly to our case. It is also suggested by Roediger et al. (2013a,b) that the distance between the edges is about a fourth to a half of the scale length of the KH rolls. In our case, the distance between the two breaks is 25 ± 1 arcsec, corresponding to the actual distance of 9.1 ± 0.4 kpc, while the azimuthal extension of the double-layered structure is 30-40 kpc, which is consistent with the prediction from the simulation. Therefore, we suggest that this double-layered structure originates from the sloshing cold front accompanied by developing KHIs.

To our knowledge, this is the first observation in which the thermodynamic properties

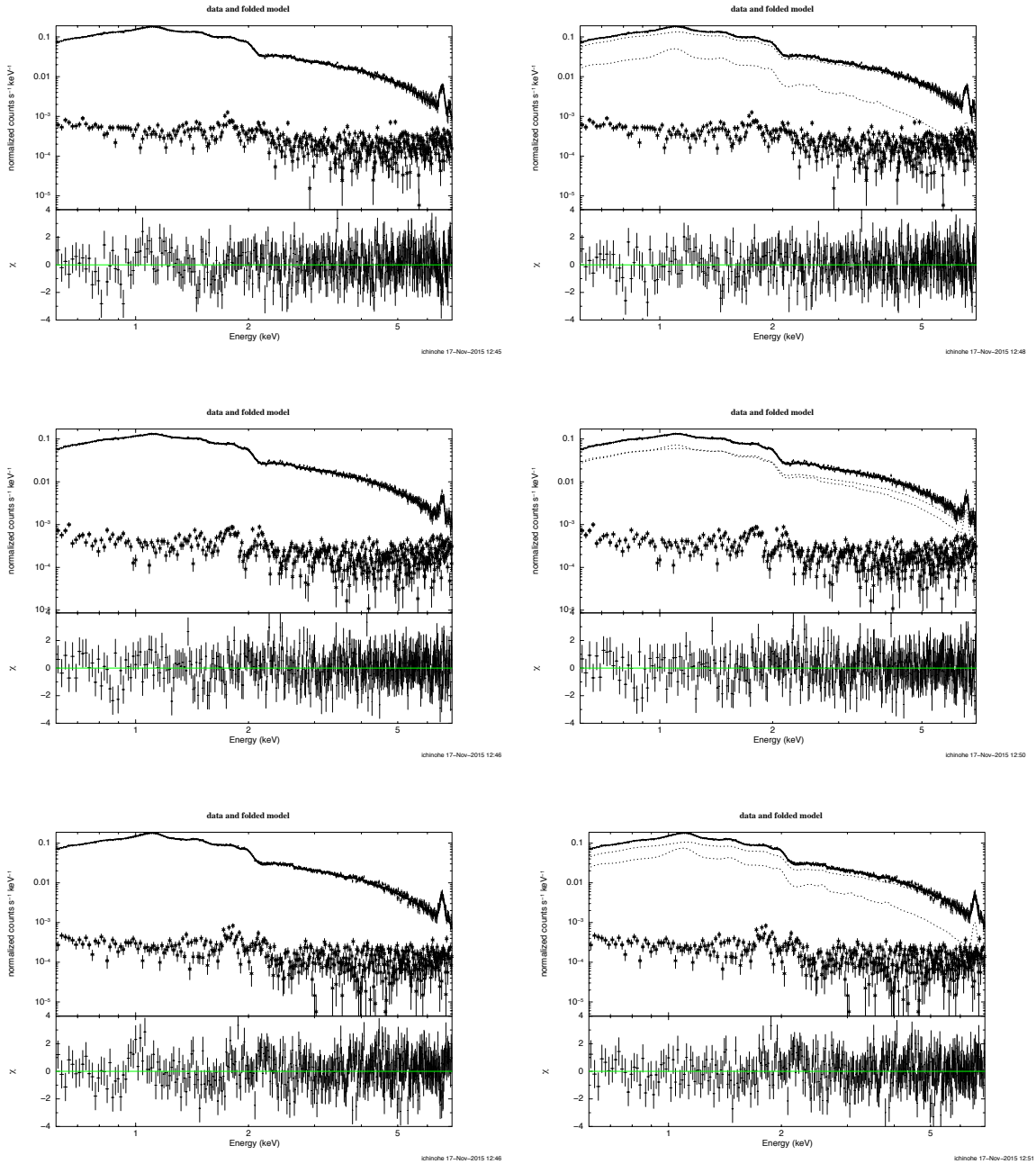

Figure 6.18 Examples of the spectral fitting. The panels correspond to the spectra extracted from the regions 1, 2 and 3 in Figure 6.17 from top to bottom. The left panels are the results of 1T fitting, while the right panels are the results of 2T fitting. The + markers are the data, the curves are the model, and the × markers are the background.

of the KHI layer candidate itself is investigated, resulting in a rather robust and consistent interpretation being drawn. Note that we found similar multiple-edge structures also in the surface brightness profile across the cold front in a merging cluster Abell 3667. See Chapter 7, Section 7.5.3 for details.

Pressure deficit and nonthermal pressure supports

Based on the KHI scenario, here we investigate the ICM microphysical properties. As shown in Figure 6.8, the pressure between the two breaks seems to be insufficient to balance the reference pressure. Assuming that the gas is uniform over the line-of-sight depth of L, the pseudo-density $\tilde{n}$ is translated to the physical density value of $n = 36\tilde{n}(L/67\ \mathrm{kpc})^{-1/2}\mathrm{cm}^{-3}$, where 67 kpc corresponds to the approximate distance of the structure from the cluster center ($\sim$3 arcmin). Similarly, the physical value of the pressure deficit Δp corresponding to the deficit of pseudo-pressure $\Delta\tilde{p} \sim 0.1 \times 10^{-3}$ is $\Delta p \sim 3.6 \times 10^{-3}$ keV cm$^{-3}(L/67\ \mathrm{kpc})^{-1/2}$.

In the case of the two-temperature modeling (see Table 6.3), assuming that the cooler component of the gas inside region 1 is uniform over the line-of-sight depth of L_1, the normalization of the `apec` ϵ_1 is translated to the physical density value of $n_1 = 9.7^{+1.2}_{-0.9} \times 10^{-3}(L_1/67\ \mathrm{kpc})^{-1/2}\mathrm{cm}^{-3}$. Similarly, that of the hotter component ϵ_2 is translated to $n_2 = 8.3^{+0.2}_{-0.5} \times 10^{-3}(L_2/350\ \mathrm{kpc})^{-1/2}\mathrm{cm}^{-3}$, where 350 kpc corresponds to the core radius $r_c = 15.85$ arcmin of the best-fitting β-model for the northeastern direction obtained by Urban et al. (2014). Accordingly, the pressure of each component is estimated at $p_1 = 2.6^{+0.5}_{-0.3} \times 10^{-2}(L_1/67\ \mathrm{kpc})^{-1/2}$keV cm^{-3} and $p_2 = 4.9 \pm 0.3 \times 10^{-2}(L_2/350\ \mathrm{kpc})^{-1/2}$keV cm^{-3}.

Although there are geometrical uncertainties, in both cases, the pressures seem to disagree with each other by a factor of order 10^{-2} keV cm^{-3}, with the gas between the two breaks or the cooler component having a lower pressure.

There are some candidates which can support the pressure deficit. The first one is magnetic pressure. In this case, assuming that the pressure deficit is fully supported by the magnetic pressure, $B^2/8\pi = \Delta p$ yields the magnetic field strength of $B = 10 - 40\ \mu$G, where $p = (n_e + n_i)kT$ is the pressure, assuming equal temperature between electrons and ions, and $n_e = 1.2n_i$.

As the sloshing induces gas motion, ram pressure can be another candidate. In this case, $\rho V^2 = \Delta p$ leads to the flow speed of $V \sim 400$ km/s, where the mass density $\rho = \mu m_p n_e$ with m_p being the proton mass and $\mu = 0.6$ being the mean particle weight.

KH eddies collapse into smaller-scale eddies and ultimately dissipate into heat, and the gas will be turbulent during the dissipation. Therefore, it is interesting to estimate whether or not the turbulent heating can balance the radiative cooling at this radius, assuming that the current size of the structure and the current flow speed represent the driving scales of turbulence. According to Zhuravleva et al. (2014), the turbulent heating rate Q_{turb} can be estimated using $Q_{\mathrm{turb}} = C_{\mathrm{Q}}\rho V_{\mathrm{1d}}^3/l$, where $C_Q \sim 5$ is a fiducial constant related to the Kolmogorov constant and may differ by a factor ~ 2, V_{1d} is the one-component velocity of the turbulence, and l is the corresponding spatial scale. Using $l = 30 - 40$ kpc and $V_{\mathrm{1d}} \sim 400$ km/s, the heat input rate can be estimated at $Q_{\mathrm{turb}} \sim 3 \times 10^{-26}$ erg/cm^3/s.

On the other hand, the cooling rate of the gas $Q_{\mathrm{cool}} = \Lambda n_e n_i$ is estimated at $\sim 1.4 \times 10^{-27}$erg/cm^3/s, where Λ is the normalized cooling function calculated in Sutherland & Dopita (1993), with the temperature of several keV and with approximating the ICM having a Solar metal abundance. Considering the uncertainties (e.g., geometry and the value of C_Q), we can only suggest that this cooling rate is comparable to $\lesssim Q_{\mathrm{turb}}$, meaning that the turbulent

heating is able to balance the radiative cooling.

The magnetic pressure support and the turbulent pressure support can coexist, and it is difficult to disentangle the two factors. However, it is worth pointing out that our estimated value of $Q_{\rm turb} \sim 3 \times 10^{-26}$ erg/cm^3/s agrees within an order of magnitude with the previous estimation of $Q_{\rm turb} \sim 10^{-26}$ erg/cm^3/s (Zhuravleva et al., 2014), although these two estimations are performed on the same target but in a completely different way: the previous estimation by Zhuravleva et al. (2014) has been done using the surface brightness fluctuations in a statistical manner, while we estimate it thermodynamically from a single distinct substructure. This may indicate the importance of turbulent heating regarding the cooling problem of cluster cores.

The density of the gas and the strength of shear flows are different from system to system, and the scale of the instability depends on the gas property at the corresponding position. Therefore, our arguments above are valid only for the double-layered structure in the Perseus cluster, and thus the estimated value itself is not necessarily expected to be universal. Instead, this result indicates that the turbulence triggered by sloshing-induced KHIs may have nonnegligible contributions to the ICM turbulence, which has not been considered extensively. It is possible that the gravitational energy injected by minor mergers supports the heat input into the ICM because gas sloshing is easily triggered by minor mergers that are constantly happening during the growth of galaxy clusters.

Convergent flows

Although the azimuthal average of the temperature and the entropy profiles (solid curves in Figure 6.8) increase monotonically toward the larger radii, our profiles do not seem to follow them. Instead, the temperature and the entropy profiles seem flat beyond the second break. At the same time, they may also indicate a signature of flattening between the first and the second break (80-100 arcsec).

These profiles indicate the existence of convergent gas flows at the second break, where the hot and high-entropy gas is moving inward from the outside and the cold and low-entropy gas is moving outward from the inside. Such convergent gas flows around sloshing cold fronts have been observationally suggested (Werner et al., 2016) and also actually indicated in the numerical simulations (e.g. Ascasibar & Markevitch, 2006; Roediger et al., 2011). Note that the reason of the flattening of the thermodynamic profiles inside the second break being not as clear as those outside the second break may be the complex gas flow due to the developing KHI eddies. The pressure enhancement above the second break may also be related to the convergent flow.

6.5.2 Feathers

Multi-temperature nature

In Section 6.4.4, we investigate the thermodynamic properties of the brightness dip by modeling the ICM simply as single-temperature plasma. However, the reduced χ^2 values shown in Table 6.2 indicate the insufficiency of the single-temperature modeling. Therefore, here we investigate the multi-temperature properties of the structures.

This method might also allow us to distinguish or restrict some of the possible scenarios for the origin of the brightness dip. For example,

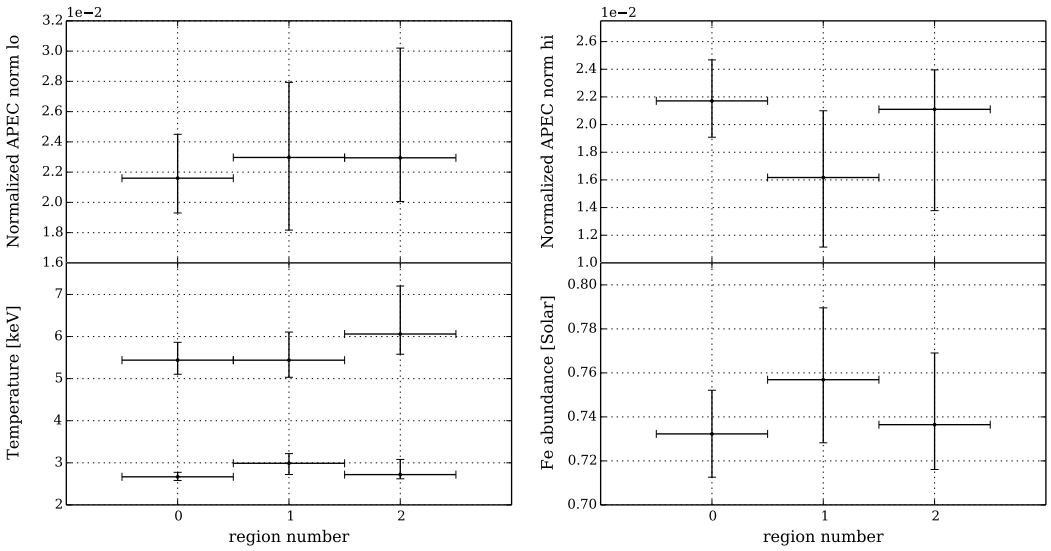

Figure 6.19 Best-fitting parameters of the two-temperature plasma model fitting. *Top left:* the normalized `apec` normalization of the low temperature component. *Top right:* the normalized `apec` normalization of the high temperature component. *Bottom left:* the temperatures of the two `apec` components. *Bottom right:* the Fe abundance of the two `apec` components.

1. if the brightness dip is caused by an additional, hot and tenuous gas layer, fitting the dip with an additional temperature component would be preferable compared with the surrounding gas.

2. if the brightness dip is caused by the depletion of the gas because of nonthermal pressure support by e.g. magnetic pressure or relativistic particles, the temperature structure is expected to be consistent across the structures, whereas the normalization is expected to be lower in the brightness dip.

3. if the brightness dip is caused by the gas rarefaction due to e.g. sound waves or shock waves, the temperature would show variations corresponding to the changes in density.

We note that previous studies, e.g. Fabian et al. (2006); Sanders & Fabian (2007), have suggested the multi-phase structure of the ICM, which supports our attempt on studying multi-temperature properties.

We modeled each dataset with a two-temperature plasma model; `phabs(apec+apec)`. In the fitting, we bound the Fe abundances of the two `apec` components. The best-fitting parameters are shown in Figure 6.19. For every region, the fits were indeed improved by $\gtrsim 3\sigma$ level with the two-temperature modeling ($\Delta\chi^2 = 53.33$, 11.40 and 57.34 for regions 0, 1 and 2 for ΔNDF=2), as shown in Table 6.2. We also tried three-temperature modeling using `apec(phabs+phabs+phabs)`, and found that this modeling does not improve the fit significantly ($\Delta\chi^2 < 2$ for all the regions). We conclude that two-temperature modeling is necessary and sufficient to fit these datasets. Figure 6.20 shows the fitting results for the regions in Figure 6.14.

The best-fitting temperatures agree within the error for both the hotter and cooler components. The normalization is also consistent across the regions for both the hotter and cooler

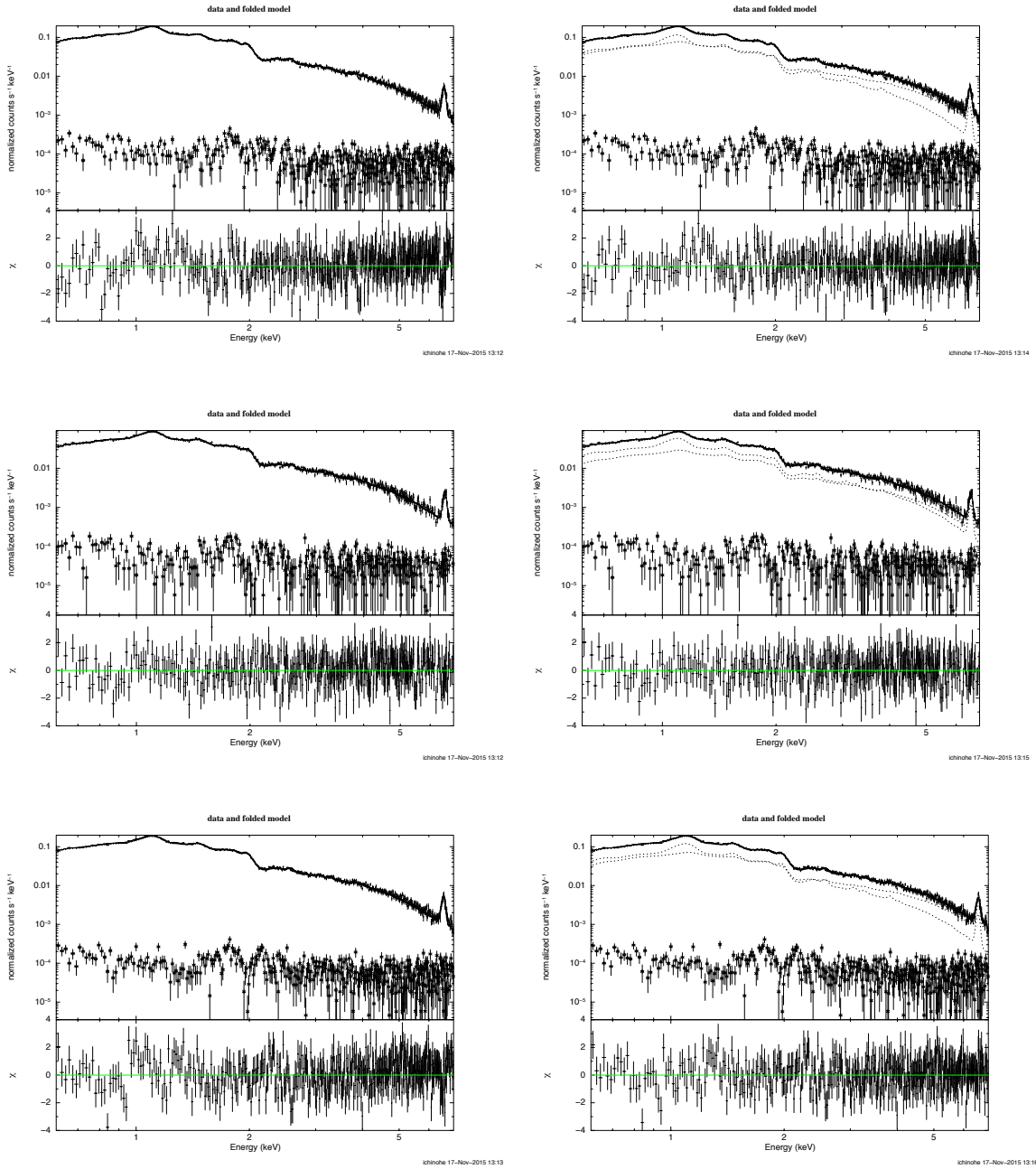

Figure 6.20 Examples of the spectral fitting. The panels correspond to the spectra extracted from the regions 0, 1 and 2 in Figure 6.14 from top to bottom. The left panels are the results of 1T fitting, while the right panels are the results of 2T fitting. The + markers are the data, the curves are the model, and the × markers are the background.

Table 6.4. Summary of the two-temperature fitting results

Parameter	region 0	region 1	region 2
Fe abundance	0.73 ± 0.02	0.76 ± 0.03	$0.74^{+0.03}_{-0.02}$
$kT_{\rm lo}$	$2.67^{+0.11}_{-0.09}$	$2.99^{+0.23}_{-0.27}$	$2.72^{+0.36}_{-0.10}$
$kT_{\rm hi}$	$5.44^{+0.42}_{-0.34}$	$5.44^{+0.67}_{-0.41}$	$6.06^{+1.14}_{-0.48}$
Normalized $\epsilon_{\rm lo}$ [a]	$2.16^{+0.29}_{-0.23} \times 10^{-2}$	$2.30^{+0.50}_{-0.48} \times 10^{-2}$	$2.30^{+0.73}_{-0.29} \times 10^{-2}$
Normalized $\epsilon_{\rm hi}$ [a]	$2.17^{+0.30}_{-0.27} \times 10^{-2}$	$1.62^{+0.48}_{-0.50} \times 10^{-2}$	$2.11^{+0.29}_{-0.73} \times 10^{-2}$

Note. — (*a*) `apec` normalization; $\epsilon = 10^{-14} \int n_e n_H dV / 4\pi [D_A(1+z)^2]$ where D_A is the angular diameter distance to the source (cm), n_e and n_H are the electron and hydrogen ion densities ($\rm cm^{-3}$), divided by the area of the region in $\rm arcmin^2$.

components. This seems at a first glance contradictory to the results of single-temperature modeling (Figure 6.15). However, based on the Figure 6.15, the difference of the `apec` normalization can be naively estimated at $\sim 0.4 \times 10^{-2}$, which is smaller than the fitting errors shown in Figure 6.19, which simply means the data quality is insufficient to resolve the deficit of the normalization in the two-temperature modeling.

Projected geometry and the origin of the brightness dip

As shown in the previous section, all of the three regions (dip and neighboring areas) are well described by a two-temperature plasma model. The temperature of the hotter component is $\sim$6 keV and that of the cooler component is $\sim$2.7 keV, being similar in all the regions. Moreover, these temperature values are consistent with the temperature values of the previously shown eastern double-layered structure (Section 6.5.1). Given that the feathers are below the western cold front, it is very likely that the cooler component represents the gas below the front, while the hotter component represents the ambient gas, similarly to the double-layered structure case.

As shown in the optical image in Figure 6.10, we do not see any corresponding optical structures around the brightness dip region, suggesting the brightness dip is purely an ICM substructure, i.e., not a structure generated by stars or galaxies, but simply due to the distribution of the diffuse gas. The temperatures of both the hotter and cooler components agree with each other between the three regions. This indicates that the brightness dip region is not associated with a temperature structure such as shock-heated or adiabatically compressed gas. We can also infer that the brightness dip is not a structure caused by the external gas component from a separate subcluster because it is likely that the external gas component has a different temperature, and in such a case, we could have detected its signatures, e.g. the three-temperature model improving the fit, or very different temperature values of both the hotter and cooler components.

The brightness dip is apparently dark, and single-temperature fitting results suggests that

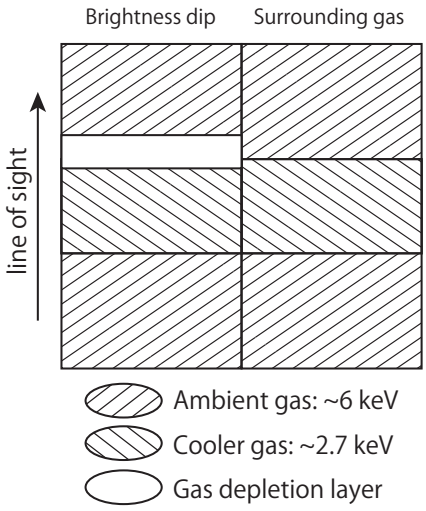

Figure 6.21 Schematic illustration of the possible geometrical situation in the brightness dip region.

the normalization at the dip is lower than the surroundings. Therefore, although the data quality is insufficient to resolve the normalization difference in the two-temperature fitting, we suggest that the brightness dip is most probably a region where the gas, whose properties are similar to the surroundings, is simply depleted in terms of the line-of-sight volume or the density. This situation is schematically shown in Figure 6.21.

Magnetic field strength

Based on the gas depletion scenario, here we investigate the microphysical properties of the ICM. As shown in Figure 6.3, the feather-like structures exist just beneath the western cold front. We would like to point out the similarity of these structures to the recent simulations of the gas sloshing of magnetized plasma (e.g. ZuHone et al., 2011, 2015; Werner et al., 2016). The simulations suggest that when a tangential flow due to the sloshing motion exists and the plasma is magnetized, the magnetic fields therein are stretched and amplified along the flow direction even if the magnetic fields were initially tangled. The stretched magnetic fields push out the gas around them with the amplified magnetic pressure, resulting in a fluctuation of the surface brightness which represents in projection the alignment of the magnetic fields inside the projected volume of the ICM.

Assuming that the ICM is uniform in each region and has a line-of-sight depth of L, the deficit of the `apec` normalization of $\sim 0.4 \times 10^{-2}$ shown in Figure 6.15 is translated to the deficit of the physical density of $\Delta n \sim 0.004$ cm$^{-3}(L/45$ kpc$)^{-1/2}$, where 45 kpc is the distance of the brightness dip from the cluster center ($\sim$2 arcmin). Given the temperature uniformity, the physical density deficit directly indicates the deficit of the physical pressure

$$\Delta p \sim 0.01 \text{ keV cm}^{-3}(L/45 \text{ kpc})^{-1/2}(kT/2.7 \text{ keV}), \tag{6.1}$$

where kT is the gas temperature, which should be supported by some other pressure component other than thermal pressure.

Considering the apparent similarity between the Perseus cluster (e.g. Figure 6.3) and the numerical simulation result by Werner et al. (2016) as well as other results of magnetized gas sloshing simulations in the literature (e.g. ZuHone et al., 2011, 2013), the most natural physical mechanism operating to support the gas pressure is magnetic pressure. The $\Delta p = B^2/8\pi$ relation immediately yields the magnetic field strength;

$$B \sim 30\ \mu\mathrm{G}(L/45\ \mathrm{kpc})^{-1/4}(kT/2.7\ \mathrm{keV})^{1/2}. \tag{6.2}$$

The estimated magnetic field strength (25-40 μG, depending on the temperature of the depleted gas) seems rather high, considering that the ambient magnetic field in the ICM has been estimated at around several μG (Carilli & Taylor, 2002; Bonafede et al., 2010, 2013). However, there have been observations which indicate ambient ICM magnetic field strengths of $\lesssim 40\mu$G (e.g. Taylor & Perley, 1993; Allen et al., 2001; Carilli & Taylor, 2002). Also, there have been observations which indicate ICM magnetic field strengths of $20 - 70\mu$G (e.g. Taylor et al., 2007; Fabian et al., 2008; Werner et al., 2013a) in association with Hα filaments. Furthermore, there have been simulations which suggest the ambient magnetic field can be enhanced by some factors from several μG, especially in the clusters which show dynamical activity such as gas sloshing (e.g. ZuHone et al., 2011, 2013, 2015).

Given that the Perseus cluster indeed shows many signs of dynamical activity, and that this kind of feather-like structures have not been seen ubiquitously (to our knowledge, Werner et al. (2016) is the only case; the feathers in Werner et al. (2016) are brighter than the surrounding medium, meaning a weaker magnetic field value, which is the opposite case to ours), it is very likely that we are indeed looking at an extreme situation, and thus we think this estimation is not implausible. Although there are several uncertainties (e.g., the gas depletion scenario, and the projected geometry), to our knowledge, this is the first example of measuring the ambient magnetic field strength of the ICM from the ICM substructure through thermodynamic properties.

Other candidates for the pressure support

The above scenario where the brightness dip is attributed to the magnetic fields amplified due to the gas motion is consistent with previous studies and simulations. However, other sources of pressure, such as non-thermal pressure support by relativistic particles or turbulent pressure support by gas motion, may also play a role. Importantly, we cannot reject some of these other scenarios, at least with the current observations.

One viable alternative scenario is that the brightness dip is a ghost bubble which represents a past activity of the central active galaxy, similarly to the other brightness cavities shown in Figures 6.2 and 6.3. Since such ghost cavities simply push out the gas, the resulting thermodynamic structure should be similar to the case of magnetic field amplification. However, given its relatively small size compared to the other bubbles, we do not think this is the case, because if the gas depletion were due to the ghost cavity, it would have had time to expand to the size similar to the other cavities, during its buoyant uplift.

Turbulence is another candidate, but it seems unlikely that turbulence is localized to within such a small and clearly confined region, and we do not think this is the case either. We can in principle test this scenario by measuring the width of the emission lines, which will become available after the *ASTRO-H* era.

6.6 Summary

In this chapter, we investigate the sloshing cold front around the core of the Perseus cluster, exploiting the highest-quality *Chandra* data currently available. The main results of this work are summarized below.

1. The western part of the front is relatively smooth, while the eastern part exhibits a double-layered structure. We point out the similarity of the appearance of the front to recent numerical simulation results for the first time. This observation indicates that the double-layered structure results from KHIs.

2. We find two significant edges in the surface brightness profile across the eastern fronts. The distance between the edges is about one fourth of the azimuthal extent of the structure, which is consistent with the prediction by numerical simulations of KHIs on cold fronts.

3. The emission from the KHI layer candidate is well described by a two-temperature plasma model, which is consistent with the prediction from the KHI scenario. This can be interpreted as the situation where the hotter component represents the ICM in the cluster outskirts and the cooler component represents the ICM originating from the core, and these are projected along the line-of-sight.

4. With the above supporting facts, we suggest that the double-layered structure results from KHIs developing on the sloshing cold front. This is the first thermodynamic study of the KHI layer candidate itself, resulting in a rather robust and consistent interpretation being drawn.

5. Based on the KHI scenario and assuming the projected geometry, we point out that the pressure in the KHI layer appears lower than the surrounding gas by $\sim 10^{-2}$ keV cm^{-3}. We proposed magnetic pressure and ram pressure as the physical mechanisms which support the pressure deficit. Currently, it is difficult to disentangle these two phenomena.

6. Based on the KHI scenario, we point out that the turbulent heating rate of 3×10^{26} erg/cm^3/s, estimated assuming that the KHIs eventually dissipate into heat, can balance the radiative cooling at this radius. The heating rate agrees within an order of magnitude with the previous estimation performed with a completely different method. This may indicate the importance of turbulent heating regarding the cooling problem of cluster cores and that the turbulence triggered by sloshing-induced KHIs may have nonnegligible contributions to the ICM turbulence, which has not been considered extensively.

7. We find feather-like structures below the western front. These features are qualitatively similar to the recent simulations of magnetized gas sloshing. Thermodynamic properties of the feathers support the scenario where the darkest feather is caused simply by gas depletion. Under this assumption, we estimated the ambient magnetic field strength at $\sim$30 μG. This is the first estimation of ambient magnetic field strength using such an X-ray substructure through thermodynamic properties.

Chapter 7

Cold front in Abell 3667

7.1 Overview

Abell 3667 is a nearby ($z = 0.055$, Sodre et al., 1992) non-cool-core cluster of galaxies, and the fifteenth brightest one in the X-ray sky (Edge et al., 1990). It is known for the various indications of its recent merger in a wide range of electromagnetic wavelengths: radio, optical and X-ray.

Early optical and X-ray observations of the system revealed an elongated and double-peaked X-ray morphology in the northwest-southeast direction, in which the locations of the two brightest galaxies coincide with the two X-ray peaks (Sodre et al., 1992). A more in depth optical study by Owers et al. (2009a) showed that the member galaxy distribution is significantly bimodal, and the offset of the peculiar velocities of the two galaxy distributions is $\sim$500 km/s.

In the radio band, its most prominent feature is the northwestern extended radio emission (Rottgering et al., 1997). This feature is classified as a radio relic, and is the brightest one among such features. The radio spectral index shows steepening from the outer edge toward the cluster center, indicating the aging of the non-thermal electrons (Hindson et al., 2014). At the opposite side of the radio relic with respect to the cluster center, less prominent radio relics are also observed (Rottgering et al., 1997). Roettiger et al. (1999) numerically studied the system and indicated that these relics are one of the consequences of merger activity. In addition to the relics, it has been suggested recently that Abell 3667 also hosts another type of diffuse radio emission, which connects these relics (radio bridge), and which may be associated with the ICM turbulence due to this merger (Carretti et al., 2013; Riseley et al., 2015). The overall radio structure is aligned well with the major axis of the X-ray emission and the axis of the galaxy bimodality.

The northwestern radio relic is extensively studied also in the X-ray band. Finoguenov et al. (2010); Sarazin et al. (2013) investigated the thermodynamic structure around the relic using *XMM-Newton*, and observed a sharp drop of the temperature and the surface brightness, indicating that the origin of the relic is a merger shock with the Mach number of $M \sim 2$. Subsequent *Suzaku* observations also confirmed the result (Akamatsu et al., 2012a; Akamatsu & Kawahara, 2013), further indicating that the plasma may be out of thermal equilibrium in this region. Its non-thermal nature has also been extensively explored, but the problem of whether the X-ray emission associated with the relic is thermal or non-thermal is still to be resolved (Fusco-Femiano et al., 2001; Rephaeli & Gruber, 2004; Nakazawa et al., 2009;

Finoguenov et al., 2010; Akamatsu et al., 2012a).

Initially, the X-ray brightness edge opposite to the northwestern relic was thought to be also a shock front (Markevitch et al., 1999). The *Chandra* observation of the brightness drop surprisingly revealed that this is not the case, but instead, the edge is a "cold front" which is the interface between a cool, dense gas volume and the hot, tenuous ambient medium (Vikhlinin et al., 2001a). Abell 3667 is one of the first clusters in which a cold front was observed while, to date, it is known that cold fronts are more ubiquitous than shock fronts (Markevitch & Vikhlinin, 2007; Owers et al., 2009b).

The thinness of the cold front, which cannot be resolved even with the *Chandra* angular resolution, has been offering us a wealth of indications regarding ICM microphysics. Vikhlinin et al. (2001a) first suggested that transport processes are heavily suppressed across the interface, and also pointed out the absence of hydrodynamic instabilities at the front. Vikhlinin et al. (2001b) estimated the magnetic field strength required to keep the front hydrodynamically stable. Vikhlinin & Markevitch (2002) considered the role of gravity for the stability, while Churazov & Inogamov (2004) suggested the intrinsic width of the interface can also stabilize the front. Mazzotta et al. (2002) pointed out a signature of a possible very-large-scale developing instability.

The cold front is also studied numerically by e.g., Heinz et al. (2003), and the predictions are confirmed by deeper data: the thermodynamic maps based on the *XMM-Newton* and *Chandra* observations revealed that cold, low-entropy and high-metallicity gas is uplifted toward the tip of the front (Briel et al., 2004; Lovisari et al., 2009; Datta et al., 2014), while the shape of the front itself was observed to be mushroom-like (Owers et al., 2009b).

Because of its prominence and proximity, this cold front is a rather well studied one, as mentioned above. However, the data still seem to be insufficiently studied. The main reason is that the studies done so far have been neglecting the azimuthal information of the front. Since hydrodynamic instabilities occur on the interface, the azimuthal variation should contain a lot of information about the microphysical properties of the ICM, in the similar way as the radial information does. Abell 3667 is relatively nearby, and the front is very prominent, with a large opening angle, which make it the ideal target for such a study regarding the azimuthal variation.

For the spectral fitting, we used XSPEC (version 12.8.2) (Arnaud, 1996) to minimize χ^2. We used the chemical abundance table determined by Lodders (2003).

7.2 Observations and data reduction

Abell 3667 has been observed nine times in total using the *Chandra* ACIS-I detectors. We selected eight ObsIDs (513, 889, 5751, 5752, 5753, 6292 and 6295) which have the satellite exposure time of above 10 ksec. The details of the data reduction are shown in Section 4.2.1. The software versions were CIAO 4.7, and CALDB 4.6.5. The net exposure times of each observation after screening are summarized in Table 7.1. The resulting total net exposure time is $\sim$500 ksec.

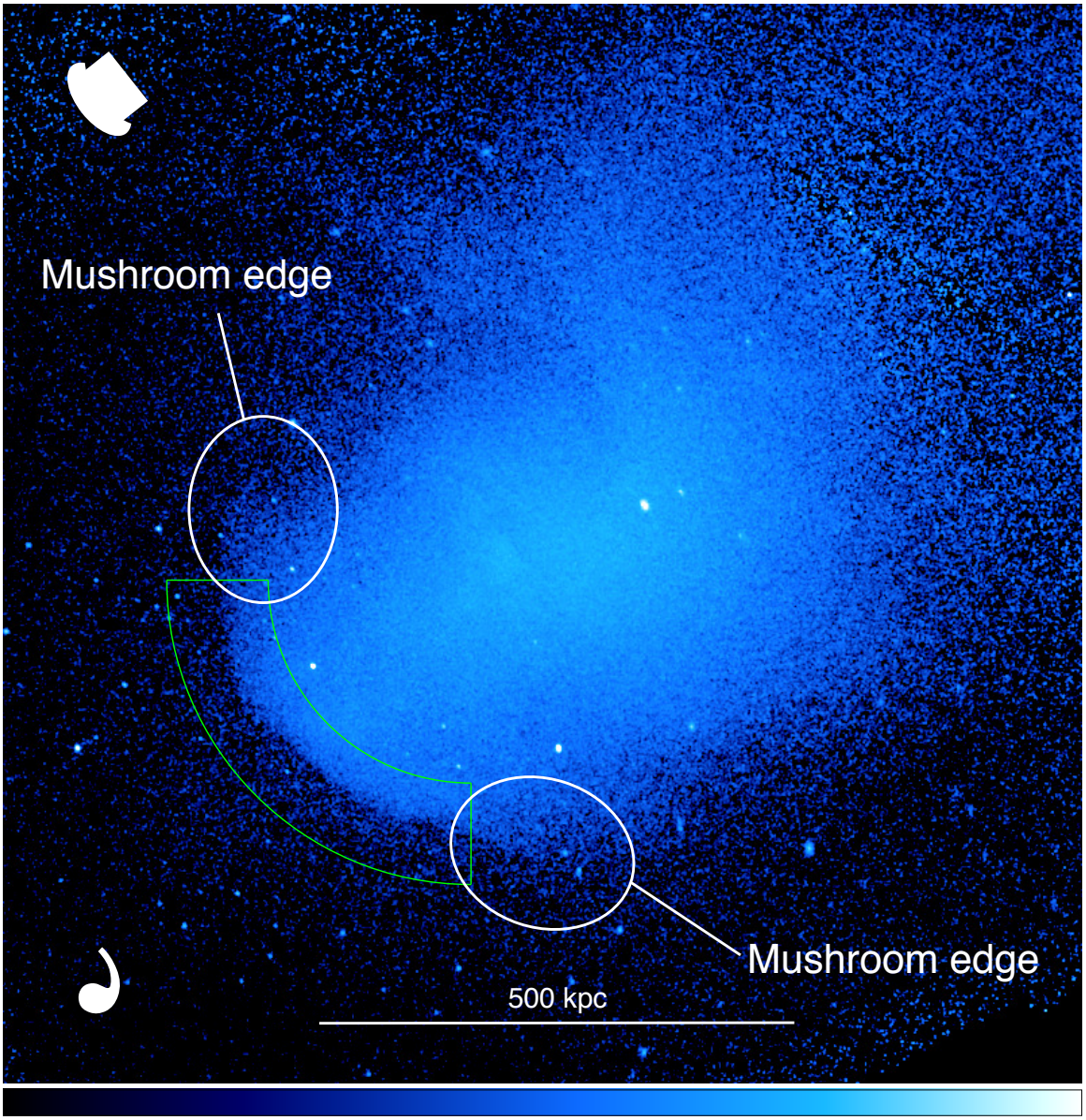

Figure 7.1 $\sigma = 0.98$ arcsec Gaussian smoothed, exposure and vignetting corrected, background subtracted *Chandra* image (0.6-7.5 keV) of Abell 3667. The location of the cold front is denoted in green. The overall morphology is comma-shaped (see the white rotated comma). The cold front is mushroom-shaped (see the white rotated mushroom shape and also the fourth panel in Figure 2.4 top).

Table 7.1. Data

Satellite	Obs ID	Date	Detector	Net exposure time (ksec)[a]
Chandra	513	2000-11-03	ACIS-I	43
Chandra	889	2001-09-22	ACIS-I	50
Chandra	5751	2006-06-21	ACIS-I	126
Chandra	5752	2006-06-21	ACIS-I	59
Chandra	5753	2006-06-21	ACIS-I	74
Chandra	6292	2006-06-21	ACIS-I	45
Chandra	6295	2006-06-21	ACIS-I	47
Chandra	6296	2006-06-21	ACIS-I	49

Note. — (*a*) The net exposure time is after the data screening.

7.3 Data analysis

7.3.1 Imaging analysis

We created the flat-fielded *Chandra* image as described in Section 4.3.1. The resulting image is shown in Figure 7.1.

We created an unsharp-masked image with $\sigma_1 = 5$ pixel and $\sigma_2 = 50$ pixel (see Section 4.3.2). The unsharp-masked image is shown in Figure 7.2 left. Also, in order to emphasize the low-contrast azimuthal variations, we created a relative deviation image by dividing the flat-fielded image by the best-fitting two-dimensional elliptical beta model. We used CIAO's modeling and fitting package SHERPA to fit the model `beta2d` to the observed flat-fielded image. The resulting relative deviation image is shown in Figure 7.2 right.

7.3.2 Thermodynamic mapping

We created the thermodynamic maps as described in Section 4.3.3. The assumed line-of-sight depth is $l = 1$ Mpc. The S/N ratio of each bin is about 150, corresponding to about 23000 counts/bin. The resulting temperature, Fe abundance, pressure and entropy maps are shown in Figure 7.3. The black ellipses are the positions of point sources which are detected using the `wavdetect` tool in the CIAO software package with the scales of 1, 2, 4, 8, 16 pixels.

In the spectral fitting, the redshift was fixed to 0.055 and the hydrogen column density was set to 4.5×10^{20} cm^{-2}, determined by the LAB (Leiden/Argentine/Bonn) radio HI survey (Kalberla et al., 2005). We obtain typical fitting errors of 4% for the temperature, pressure and entropy maps, and 20% for the Fe abundance map. The typical reduced χ^2 is 1.07, with the typical NDF of 350. Figure 7.4 shows the example fitting results for the regions which are marked with the green stars in Figure 7.3 top left.

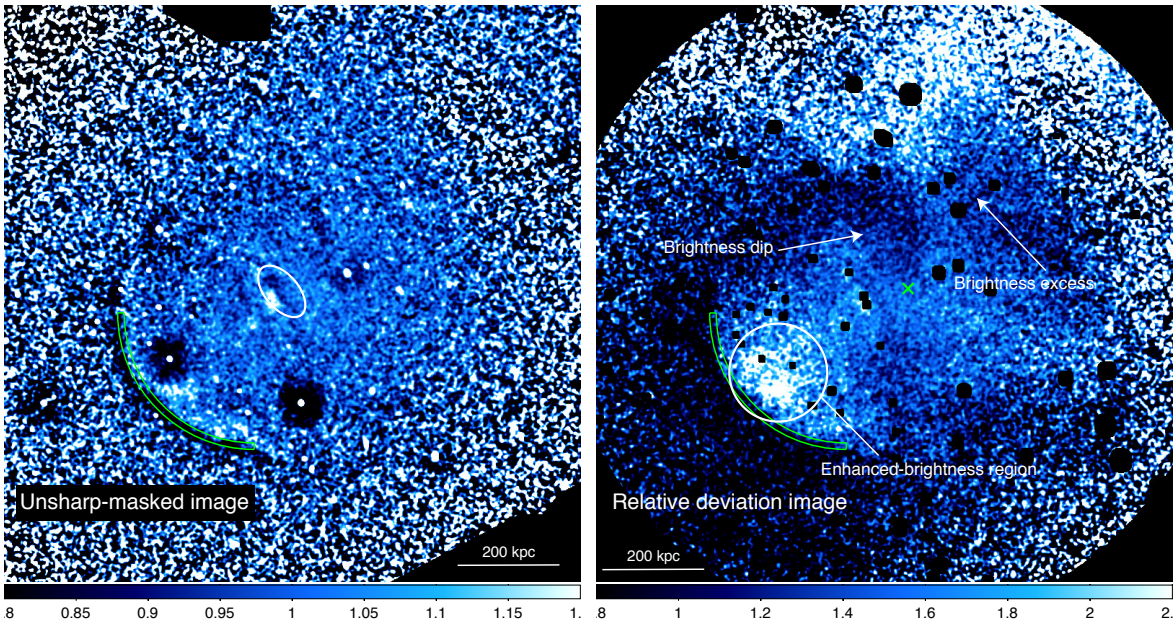

Figure 7.2 *Left:* unsharp-masked image created by dividing the $\sigma = 5$ pixel Gaussian smoothed image by the $\sigma = 50$ pixel Gaussian smoothed image. *Right:* $\sigma = 0.98$ arcsec Gaussian smoothed relative deviation image with respect to the best-fitting 2D elliptical beta profile. The location of the cold front is denoted in green. The white ellipse in the left-hand panel denotes the brightness dip mentioned in Section 7.4.1. The green cross in the right-hand panel is the peak of the best-fitting 2D elliptical beta profile.

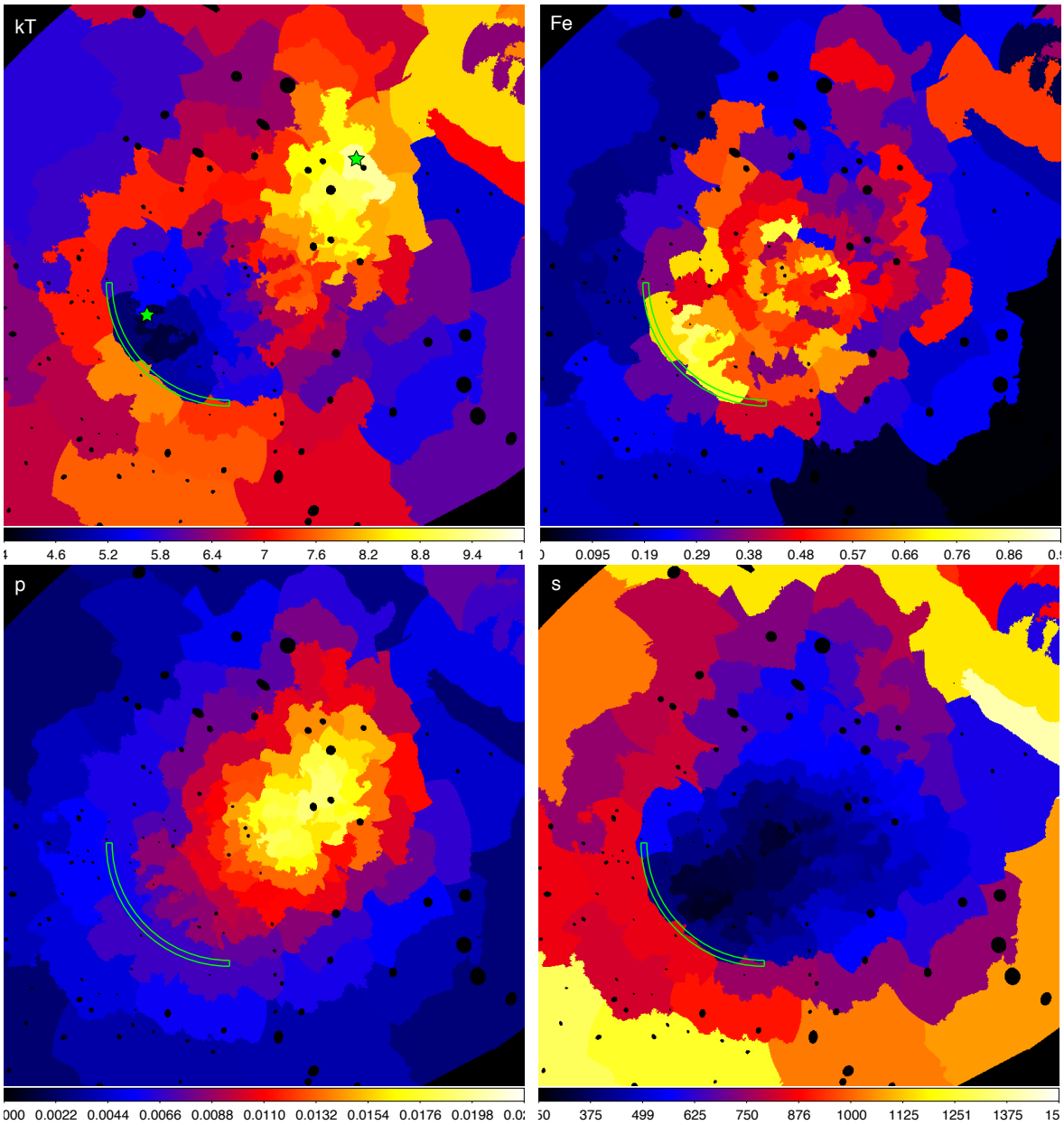

Figure 7.3 Projected thermodynamic maps assuming a uniform ICM line-of-sight depth of $l = 1$ Mpc. *Top left:* projected temperature map in the unit of keV. *Top right:* projected Fe abundance map with respect to the solar abundance by Lodders (2003). *Bottom left:* projected pressure map in the unit of keVcm$^{-3} \times (l/1\ \mathrm{Mpc})^{-1/2}$. *Bottom right:* projected entropy map in the unit of keVcm$^2 \times (l/1\ \mathrm{Mpc})^{1/3}$. The location of the cold front is denoted in green. The green star markers denote the regions of which example spectra are shown in Figure 7.4.

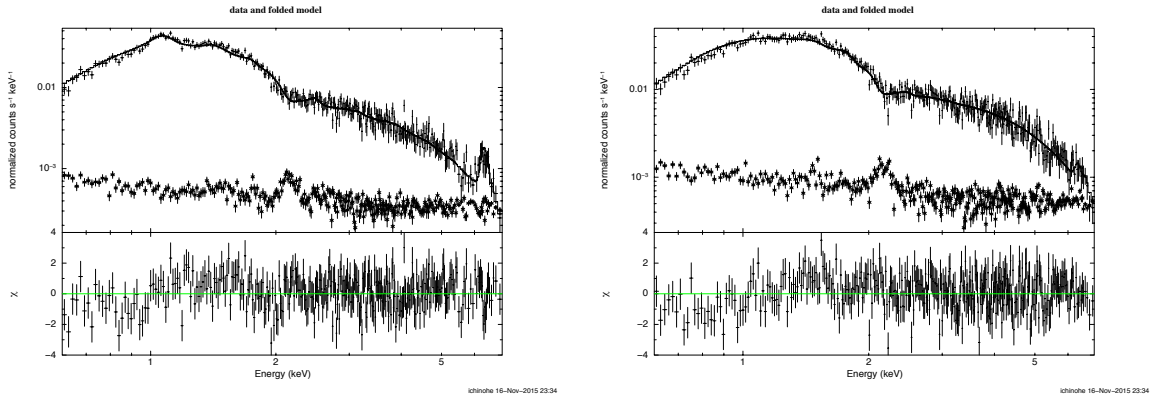

Figure 7.4 Examples of the spectral fitting. *Left:* the spectra extracted from below the cold front. *Right:* the spectra extracted from near the cluster center. The + markers are the data, the curves are the model, and the × markers are the background.

7.4 Results

7.4.1 Global morphological features

In every image (i.e. Figure 7.1 and 7.2), the abrupt surface brightness drop, which azimuthally extends for ∼500 kpc, is clearly visible on the southeastern part of the cluster (see the green sectors in the images). This brightness edge is also clearly visible in the projected temperature, metallicity and entropy maps (Figure 7.3 top left, top right and bottom right). The absence of the corresponding feature in the pressure map (Figure 7.3 bottom left) shows that the pressure is almost continuous at the interface. All of these features are typical of cold fronts (Markevitch & Vikhlinin, 2007).

The interface appears abrupt in terms of the drop of the surface brightness. On the other hand, it seems to have an azimuthal variation in terms of the radii or the curvature radius, which has not been explicitly pointed out previously. The surface-brightness contrast across the interface is strong towards southeast, but gradually weakened to the north and south along the front, forming a mushroom-like shape (see the white rotated mushroom shape in Figure 7.1 and also the fourth panel in Figure 2.4 top). The mushroom-like shape is also clear in the relative deviation image (Figure 7.2 right). We also see in the relative deviation image a region of the enhanced brightness just beneath the interface.

Overall shape of the cluster is comma-shaped, where a brightness dip exists to the north of the cluster's brightness peak, and a brightness excess, which seems to extend anti-clockwise from the brightness peak, exists further out (see the white rotated comma in Figure 7.1). These dip and excess are more visible in the relative deviation image (see the annotations in Figure 7.2 right). This feature was first mentioned in Mazzotta et al. (2002) who suggested that this shape is due to the development of hydrodynamic instability.

On the brightness peak, there is a surface brightness dip extending from the northeast to the southwest, which is clearly visible as a dark region just at the northwest of the brightness peak in the unsharp-masked image (see the white ellipse in Figure 7.2 left), and has not been mentioned in the literature. Note that this is not a spurious feature due to e.g., chip gaps or dead strips. We confirmed this feature in the raw count image of the ObsID 889 dataset, in

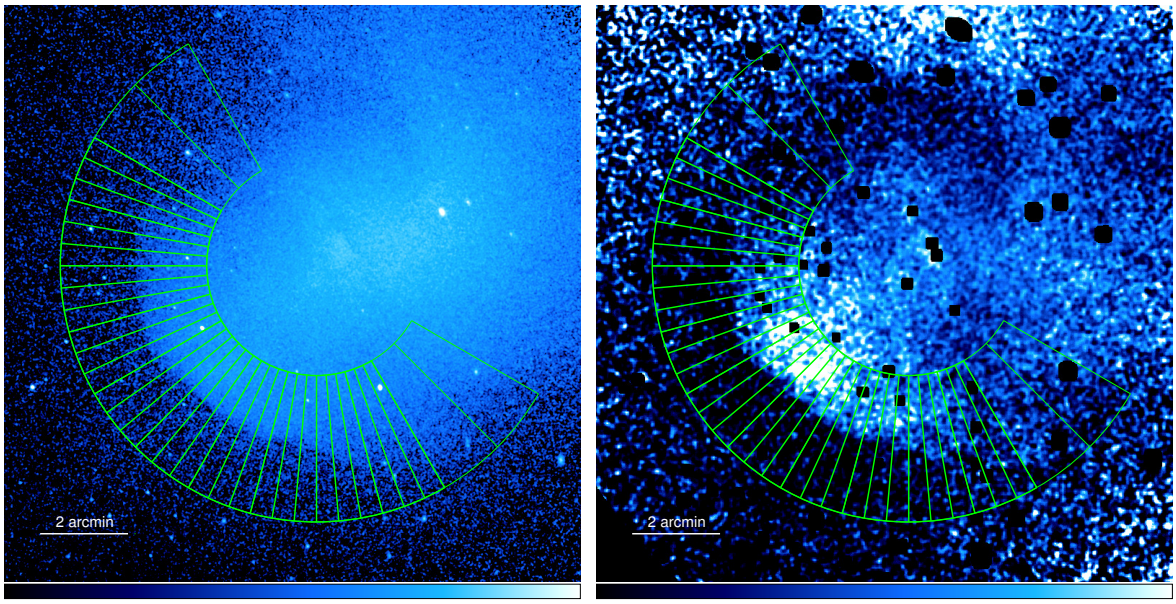

Figure 7.5 Same as Figure 7.2. The overlaid green sectors denote the regions from which the surface brightness profiles are extracted (see also Figures 7.6 and 7.7)

which the feature is almost entirely on the active surface of the CCD chip.

In the temperature map, we see relatively cool gas extending broadly from near the cold front towards the west, and also see hot gas residing to the northwest (see around the green star markers in Figure 7.3 top left). Despite these relatively clearly separated two temperature components, we do not see such bimodalities in the entropy and the metallicity maps (Figure 7.3 bottom right and top right). The relatively regular and centrally-peaked shape of the overall pressure morphology (see Figure 7.3 bottom left) suggests that the ICM motions are subsonic in the dark matter potential well within this length scale, while the pressure distribution is highly elliptical with the major axis almost perpendicular to the cold front. We also see the lowest-temperature/entropy, highest-metallicity gas concentrating just beneath the front, enhancing the thermodynamic contrast across the interface. These morphological thermodynamic structures are consistent with previous observations using *XMM-Newton* (Briel et al., 2004; Lovisari et al., 2009) or *Chandra* data with different datasets or methods (Mazzotta et al., 2002; Datta et al., 2014).

7.4.2 Surface brightness properties

Surface brightness profile

We see above that the interface is very smooth but seems to show azimuthal variations. In order to investigate the cold front, we extracted surface brightness profiles across the front. The partial-annulus-shaped regions used to extract surface brightness profiles are shown in Figure 7.5. We determined the center of these partial annuli so that their radial directions are roughly perpendicular to the cold front. The narrower sectors have an opening angle of 5° and the wider sectors are 15° wide, corresponding to 22 kpc and 67 kpc at the radius of the front.

To model the shape of the surface brightness profiles quantitatively, we assumed that

the underlying radial density profile $n(r)$ is expressed as a broken power law with a jump of normalization at the break;

$$n(r) = \begin{cases} j_{12} n_0 \left(\dfrac{r}{r_{12}}\right)^{-\alpha_1} & (r \leq r_{12}) \\ n_0 \left(\dfrac{r}{r_{12}}\right)^{-\alpha_2} & (r_{12} < r) \end{cases}, \tag{7.1}$$

where r_{12} and j_{12} are the radius of the break and the amplitude of the jump there, n_0 is the overall normalization, and α_1 and α_2 are the power-law slopes of the density profile inside and outside the front.

Ignoring line emission, the emissivity of the ICM is described using the emissivity of thermal bremsstrahlung radiation $\epsilon = \xi(T, Z)n^2$, where n is the density and $\xi(T, Z)$ is a coefficient which weakly depends on temperature and metallicity. Assuming spherical symmetry and approximating ξ to be constant, the surface brightness profile $S(x)$ can be obtained by integrating the density profile along the line-of-sight direction y;

$$S(x) = 2A \int_0^\infty n^2(r) dy = 4A \int_0^\infty \frac{x(1+s^2) n(x(1+s^2))}{\sqrt{s^2+2}} ds, \tag{7.2}$$

where x is the coordinate along which the surface brightness profile is extracted, A is a constant which includes both the effect of ξ and the effect of $\propto r^{-2}$ decrement of the intensity and s is a transformed variable using $r = \sqrt{x^2+y^2} = x(1+s^2)$. We fitted this model to the extracted profiles using the Minuit2 fitting library integrated in the ROOT data analysis framework to minimize χ^2.

The surface brightness profiles extracted for wider sectors and their best-fitting projected broken power-law models are shown in Figure 7.6. The profiles and the shapes of their best-fitting model show azimuthal variations. The surface brightness drop is very steep especially in the azimuthal range of 195°-270°, which was already apparent in the images (see e.g. Figure 7.5 right).

Azimuthal variations

Figure 7.7 shows the azimuthal variations of the best-fitting parameters of our assumed density model (Equation 7.1). The black/red and the gray/magenta points represent the best-fitting parameters for the surface brightness profile extracted for the wider (15°) sectors and the narrower (5°) sectors.

All of the parameters show significant azimuthal variations. The azimuthal profile of the jump j_{12} is clearly peaked at around 210°-240°, and has a relatively symmetric shape. The overall trend is the same in the profile of finer azimuthal resolution (5°, grey), but there seem to be a systematic hump and a systematic dip of the jump amplitude around 220°-225° and 235°-250°, respectively.

Although the profile of the break r_{12} is more or less constant at azimuths of 170°-300°, it shows an indication of a downward-convex shape, which may or may not be attributed to the misalignment between the sectors and the cold front. On top of the convex shape, it shows azimuthal variations of relatively large length scale, about 15°-25°. Figure 7.8 shows the DCT (Discrete Cosine Transform) power spectrum of the break radii calculated using the data points in the azimuthal range of 165°-270°, where the jump j_{12} is $\gtrsim 2$. We see significant

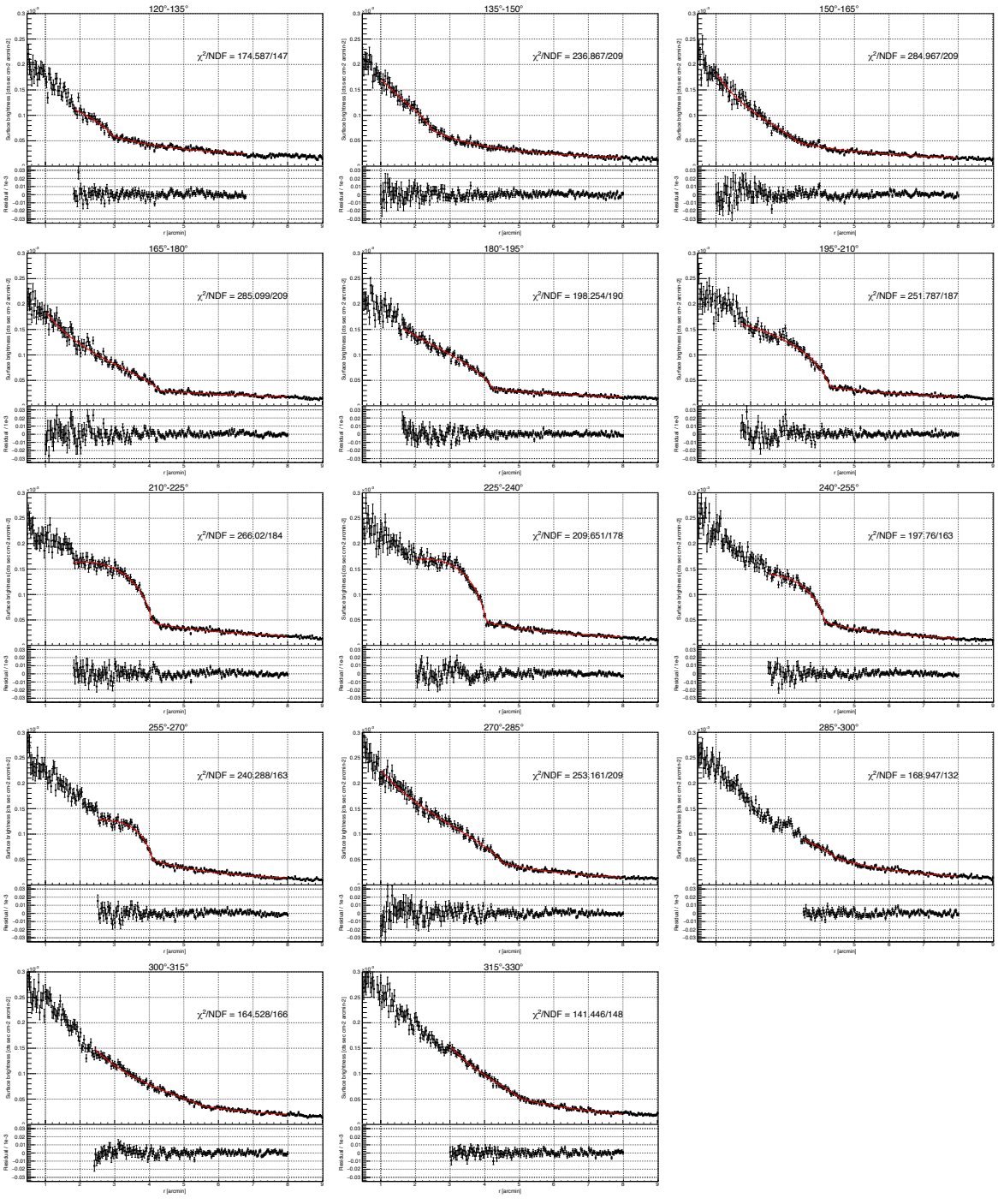

Figure 7.6 The surface brightness profiles extracted using 15° sectors. The red curves are the best-fitting projected broken power law models.

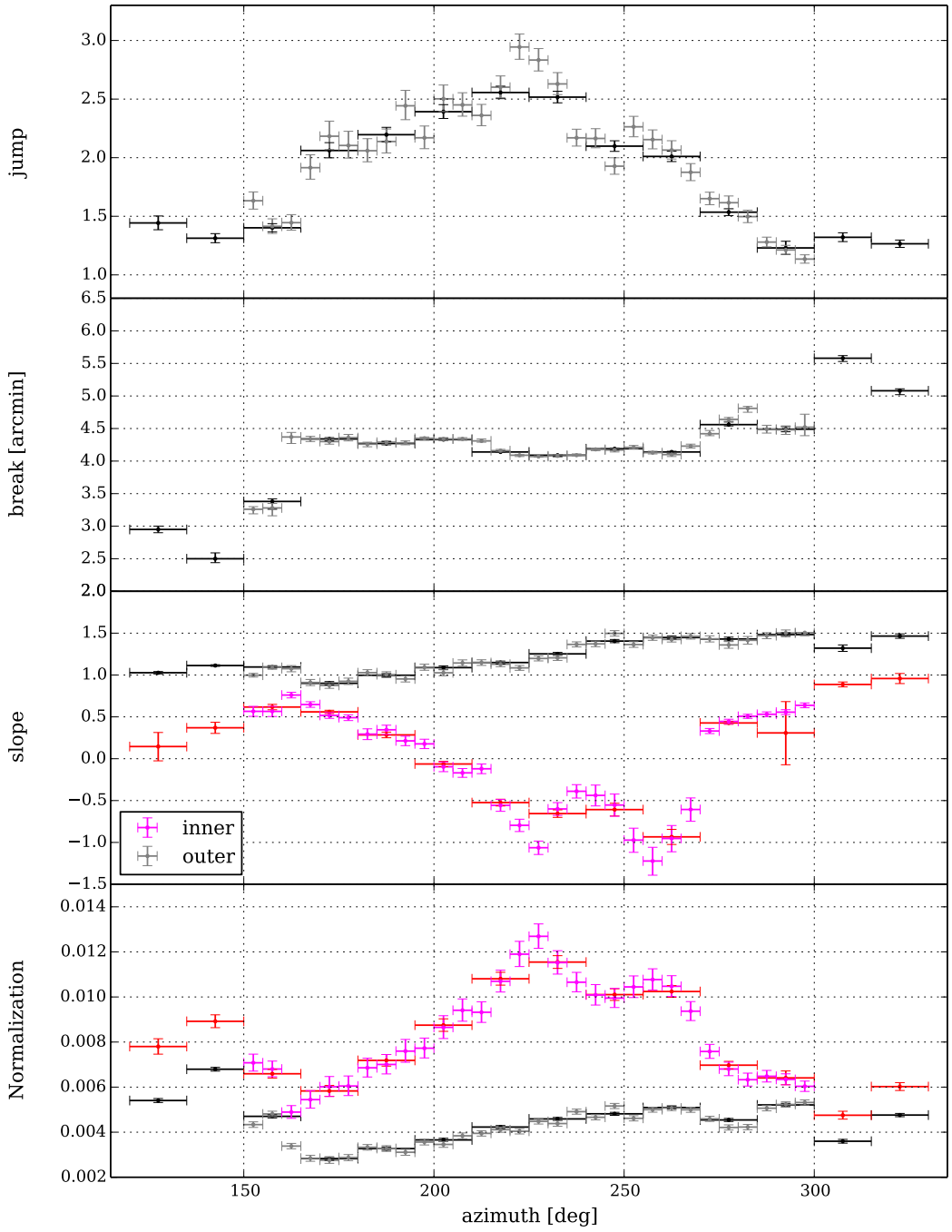

Figure 7.7 The azimuthal variations of the best-fitting parameters of the projected broken power law models. *Top row:* the jump j_{12} in density at the break, *Second row:* the radius of the break r_{12}, *Third row:* the slope inside/outside the interface (α_1, α_2). *Bottom row:* the normalization inside/outside the interface ($j_{12}n_0$, n_0). In the bottom two panels, the red/magenta points represent the values inside the break, where the black/gray points represent the values outside the break. The difference between black and gray or between red and magenta is the opening angle of the sectors (15° and 5°).

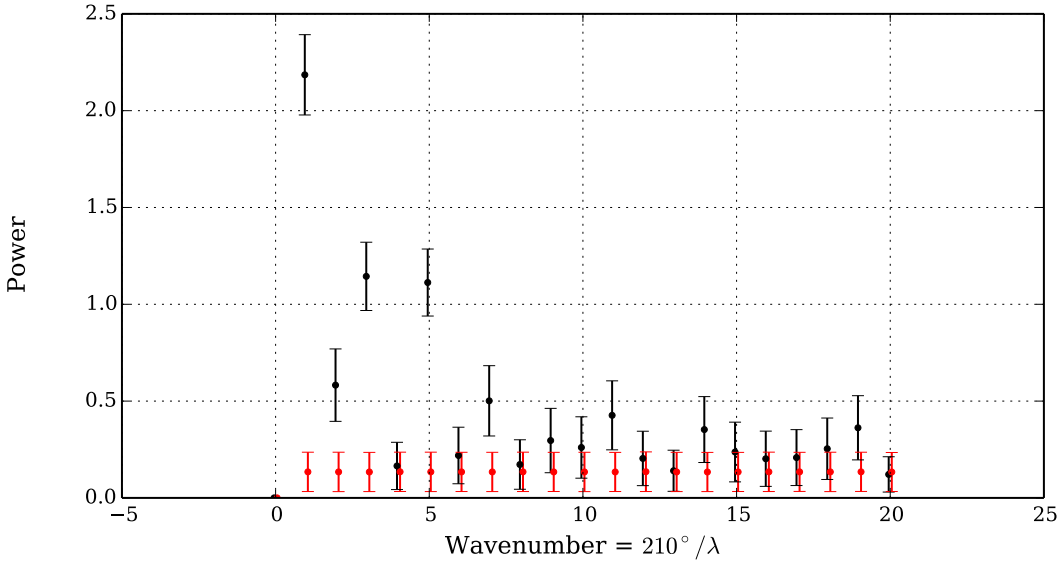

Figure 7.8 DCT (Discrete Cosine Transform) power spectrum of the break radii in the azimuthal range of 165°-270°. The black points are the power spectrum derived from the current data. The red points are the power spectrum derived from a mock dataset, which does not fluctuate with the average value and the average error.

excesses which are inconsistent with the power spectrum representing the model that does not fluctuate (red). This means that the break radii actually fluctuate with position angle.

The profile of the outer power-law slope α_1 shows moderate changes, whereas that of the inner power-law slope α_2 shows an asymmetric, two-peaked shape. The inner power-law slopes become even positive around the highest contrast part of the front, implying the density increases toward the front, as indicated in the relative deviation image (enhanced-brightness region in Figure 7.2 right).

7.4.3 Thermodynamic properties

Thanks to the high-quality deep observation of ∼500 ksec, we are able to investigate the deprojected thermodynamic properties with an azimuthal resolution of 15° for a single cold front (see Section 4.4.1 for the concept of deprojection). Figure 7.9 shows the 10 directions from each of which we extracted a deprojected thermodynamic profile. We used the model `projct` to incorporate the effect of the projection of outer gas volumes, under the assumption of spherical symmetry. We fixed the metallicity to the values obtained from the projected thermodynamic profiles. In the spectral fitting, the typical reduced χ^2 is 1.02, with the typical NDF of 1500. Figure 7.10 shows the example fitting results for the deprojection analysis.

Figures 7.11 and 7.12 show the deprojected thermodynamic profiles, where 0 arcsec in the x axes corresponds to the location of the interface. Figure 7.13 shows the azimuthal variations of the thermodynamic quantities just under and above the interface, together with the ratio of the inner quantity to the outer quantity.

Generally, at the high-contrast parts of the front (195°-270°), clearly both the density and the temperature show a jump by a factor of ∼2-3. Since the jumps of the density and the temperature are in the opposite sense, the entropy also exhibits a huge jump and

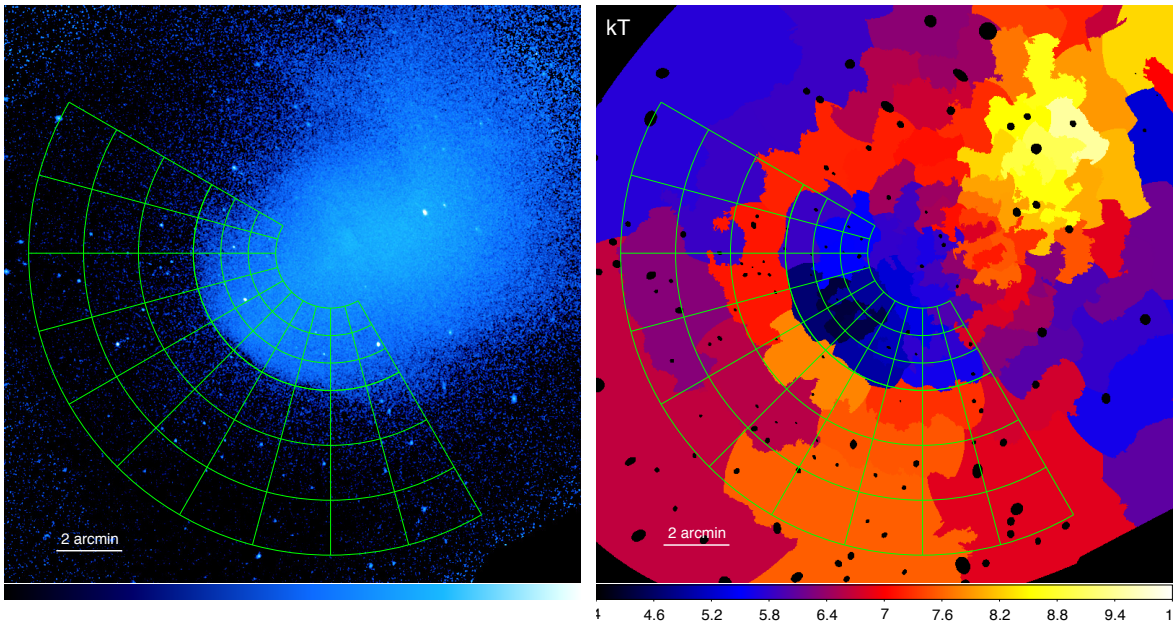

Figure 7.9 The flat-fielded image (left) and the projected temperature map (see also Figures 7.1 and 7.3). The overlaid green sectors denote the regions from which the deprojected thermodynamic profiles are extracted (see also Figures 7.11, 7.12 and 7.13)

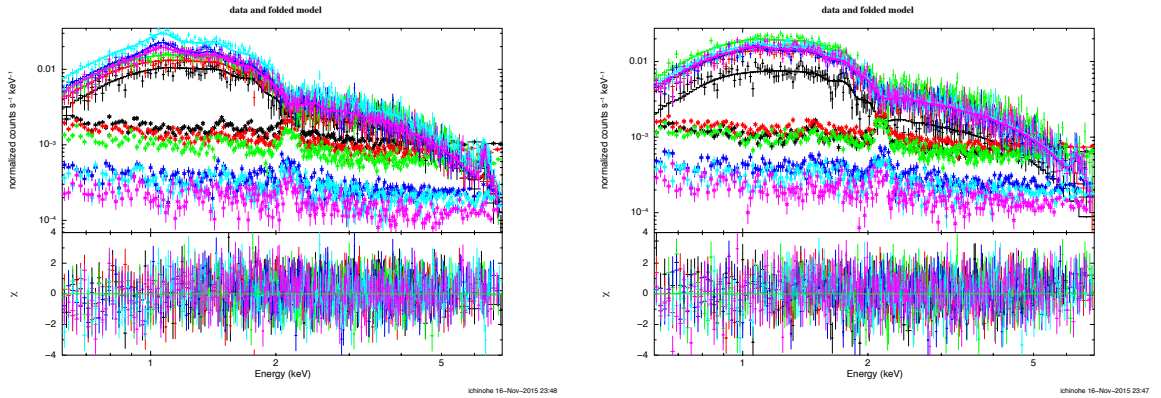

Figure 7.10 Examples of the deprojection analysis. *Left:* the spectra extracted from the 225°-240° azimuth. *Right:* the spectra extracted from the 285°-300° azimuth. The + markers are the data, the curves are the model, and the × markers are the background. Different colors correspond to different radial ranges (black, red, green, blue, cyan and magenta from outermost to innermost).

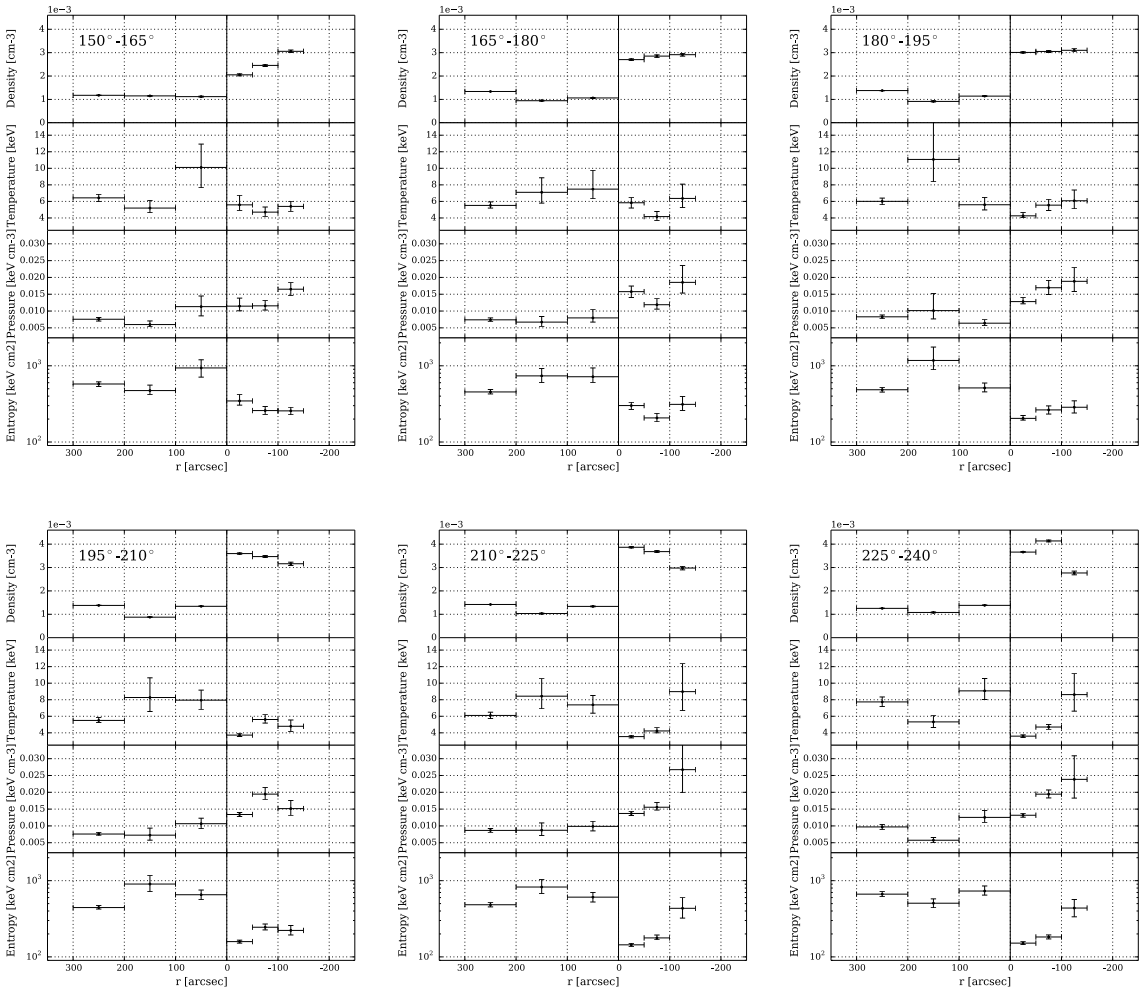

Figure 7.11 The deprojected thermodynamic profiles. In each panel, the subpanels show the density, the temperature, the pressure and the entropy from top to bottom.

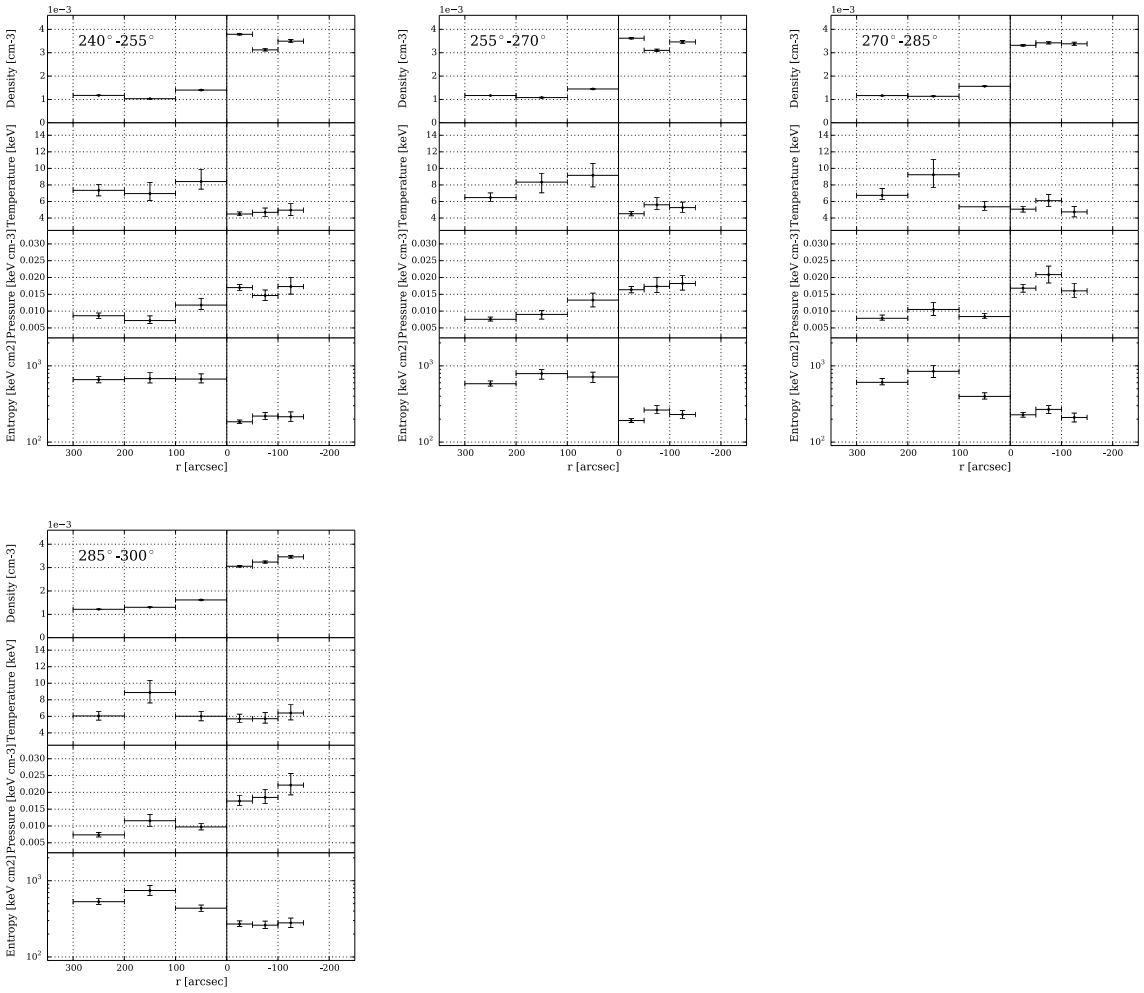

Figure 7.12 Figure 7.11, continued.

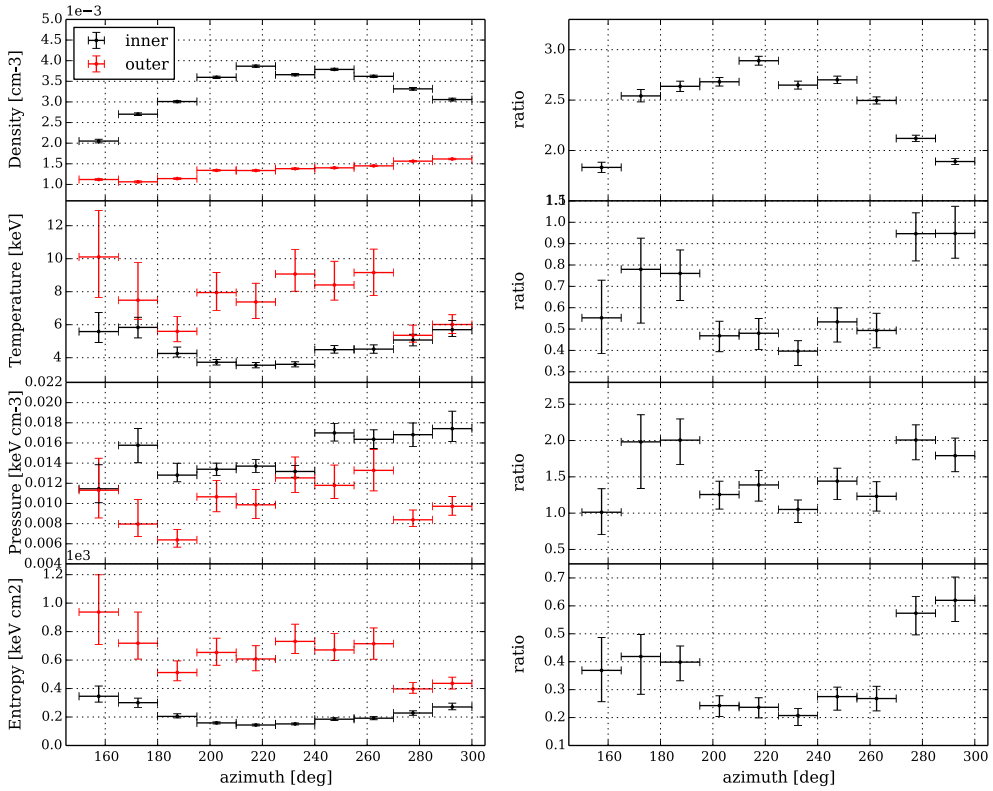

Figure 7.13 The azimuthal variations of the thermodynamic quantities just inside (black) and outside (red) the front. The left panels show the azimuthal variations of the density, the temperature, the pressure and the entropy from top to bottom. The right panels show the ratio of the inner value to the outer value for the corresponding quantities.

the pressure shows an almost continuous profile. Underneath the front, the entropy and the temperature profiles seem to show downtrends toward the interface, while the density profiles show uptrends. On the other hand, at the low-contrast part of the front ($195^\circ <$ and $<270^\circ$) the temperatures show milder jumps, resulting in relatively bigger/smaller jumps in the pressure/entropy profiles. These ratios are consistent with the results by Owers et al. (2009b) who examined the front focusing only on the highest-contrast part (about 210°-240°).

7.5 Discussion

7.5.1 Origin of the cold front

When a volume of gas, stratified in its gravitational potential well, is subjected to ambient flow, a very sharp cold front will quickly form (Markevitch & Vikhlinin, 2007). It is because the denser part of the gas feels smaller deceleration by ram pressure than the more diffuse part of the gas, and thus the denser part will be uplifted relatively to the more rarefied ambient part toward the interface (see also Figure 2.4 top panels).

It has also been shown in a number of numerical simulations that, in such a situation, the shape of the front will be mushroom-like when it is seen from a direction perpendicular to the flow direction (Heinz et al., 2003; Roediger et al., 2015a,b). This is because the flow velocity along the interface increases toward the large angles, and as a result, the hydrodynamic instability quickly develops at the larger angles.

In addition to the mushroom-shape of the surface brightness profile, the front also shows a characteristic thermodynamic structure. That is, the dense core gas with low-entropy and high-metallicity is gradually uplifted during the motion, and finally reaches the leading edge of the front. This leads to the thermodynamic structure where the lowest-entropy/temperature and highest-metallicity gas is just below the front.

In our case, as seen in Figures 7.1 and 7.2, the shape of the front is clearly mushroom-shaped, and the edges of the front seem to be dissolved into the ambient medium. The deprojected thermodynamic profiles (Figures 7.11, 7.12 and 7.13) as well as the projected ones (Figure 7.3) clearly display the thermodynamic structure typical of uplifted core gas. In addition, the pressure map which is highly elongated in the northwest-southeast direction, and also a number of observational indications, e.g. the galaxy distribution which is well aligned along the major axis (Proust et al., 1988; Owers et al., 2009a) and the radio relics located to northwest and southeast (Rottgering et al., 1997), suggest that the cold front is forming because of a merger very close to the sky plane.

We would also like to point out the striking similarity of our X-ray image (Figure 7.1) to the numerical simulation by Roediger et al. (2015b) who modeled the inviscid stripping of an initially extended atmosphere subjected to the ambient flow during the initial relaxation phase (Figure 7.14). The cold front in Abell 3667 is especially similar to the inviscid simulation result at ∼780 Myr (Figure 7.14 top row, third column) in two perspectives; (1) the opening of the front or the angle where the stripping starts, and more importantly, (2) the variations of the front radii whose length scale is smaller than the opening angle of the entire cold front (sub-opening-angle scale variation).

It is also shown in the numerical simulations by Roediger et al. (2015b) that the impact of the inclination angle of the line-of-sight direction with respect to the direction perpendicular to the merger plane is relatively strong above $\sim 30^\circ$, for which case the interface becomes less pronounced and the sub-opening-angle scale variations are no longer clearly visible.

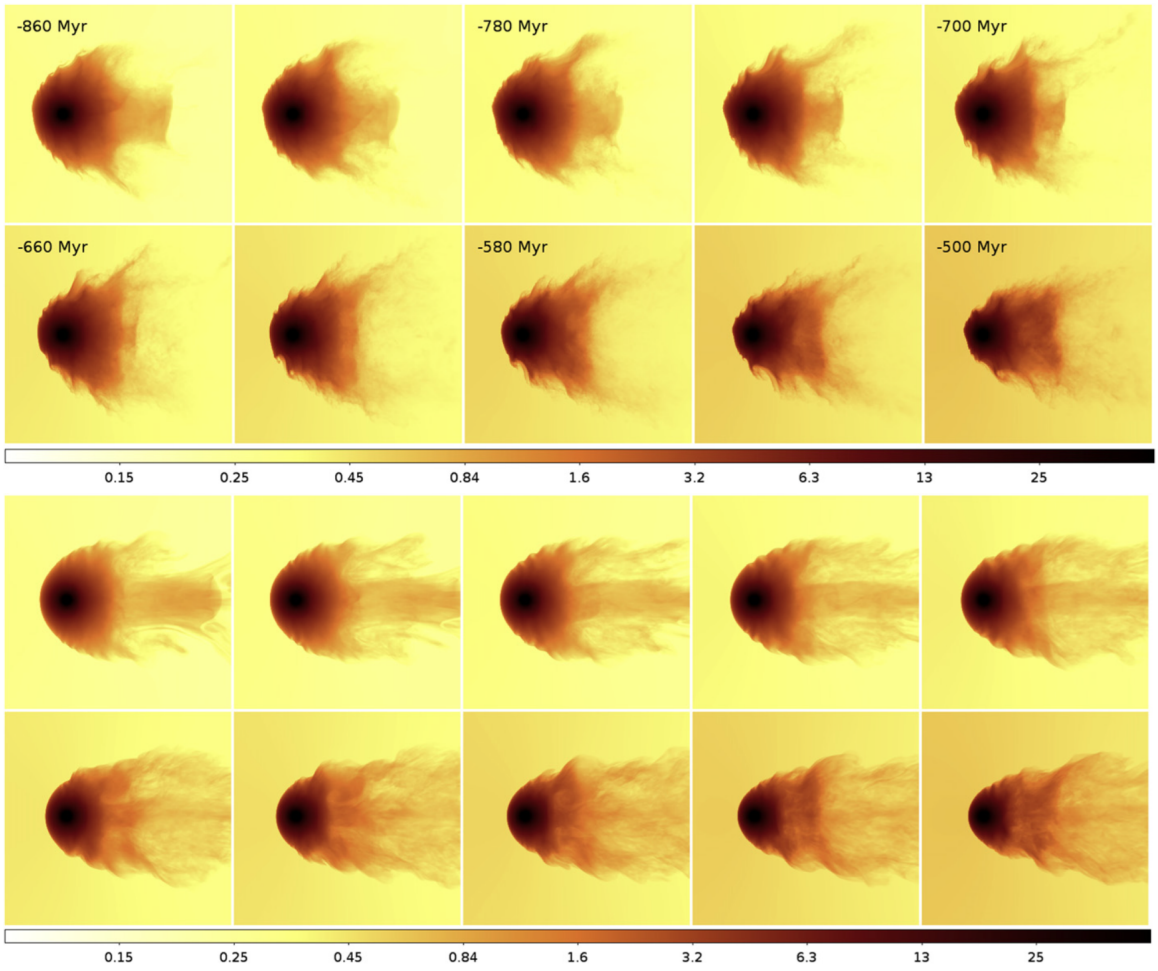

Figure 7.14 X-ray images (0.7-1.1 keV) of simulated gas-stripped galaxy taken from Roediger et al. (2015b). The upper/lower panels are for the inviscid/viscous (Re=46 at pericenter, 0.1 Spitzer viscosity) atmosphere.

Given all the arguments above, we suggest that the front is formed via a merger event taking place nearly in the sky plane. Note that gas sloshing parallel to the line of sight direction is another possible interpretation (Kitayama et al., 2014). To test these different scenarios, the best way is to measure the line-of-sight velocity inside and outside the interface by Doppler shift measurements. It is not possible with current X-ray spectroscopy using CCD, but the Soft X-ray Spectrometer (SXS) onboard the *ASTRO-H* satellite may allow them to be measured (Kitayama et al., 2014). The sloshing interpretation is also challenged to be able to reproduce all the observed signatures which are remarkably consistent with the merger scenario.

7.5.2 Gas dynamics

From the thermodynamic information, we can estimate the velocity of the cool gas relative to the ambient medium (Vikhlinin et al., 2001a; Landau & Lifshitz, 1959). By approximating the cool gas as a blunt body subjected to an ambient flow, and neglecting the change in the gravitational potential along the streamline, the ratio of the pressure of the flow at the stagnation point p_0 (i.e. next to the tip of the front) to the pressure of the flow in the free streaming region p_1 (i.e. far above the front) is a function of the cloud velocity v;

$$\frac{p_0}{p_1} = \begin{cases} \left(1 + \dfrac{\gamma-1}{2}{M_1}^2\right)^{\gamma/(\gamma-1)} & (M_1 \leq 1) \\ \left(\dfrac{\gamma+1}{2}\right)^{(\gamma+1)/(\gamma-1)} {M_1}^2 \left(\gamma - \dfrac{\gamma-1}{2{M_1}^2}\right)^{-1/(\gamma-1)} & (M_1 > 1) \end{cases}, \tag{7.3}$$

where $\gamma = 5/3$ is the adiabatic index of the monoatomic gas and $M_1 = v/c_s$ is the Mach number of the free stream, with c_s being the free-stream sound speed.

It is difficult to measure p_0 because the stagnation point is physically small, but assuming pressure balance between the inner and the outer gas, we can infer p_0 from the pressure inside the front. One caveat is that, since the ICM is a plasma, the effect of the magnetic draping layer at the interface may contribute to the pressure balance. However, it is highly unlikely that the magnetic pressure overwhelms the gas pressure, so this effect should be small.

Assuming that the azimuthal range of 210°-240° represents the tip of the front and using $p_0 \sim 0.0134 \pm 0.0004$ keV cm^{-3} (average of the bins just below the front) and $p_1 \sim 0.0092^{+0.0005}_{-0.0004}$ keV cm^{-3} (average of the outermost bins) from the deprojected thermodynamic profiles (Figures 7.11, 7.12 and 7.13), the Mach number of the free stream is calculated at $M_1 = 0.70 \pm 0.06$. This value is consistent with the previous estimation by Datta et al. (2014) but smaller than the previous estimation of 1.0±0.2 by Vikhlinin et al. (2001a); this discrepancy may be due to the indirect measurement of n_e by Vikhlinin et al. (2001a), who inferred the density assuming that the surface brightness profile follows a β model.

The sound speed c_{s1} in the free stream is calculated using $c_{s1} = \sqrt{\gamma k T_1/\mu m_p}$, where kT_1 is the temperature of the free stream, and $\mu = 0.6$ is the mean particle weight with respect to the proton mass m_p. Using $kT_1 = 6.9^{+0.4}_{-0.3}$ keV and $M_1 = v/c_{s1}$, the velocity of the cool gas is estimated at $v = 950 \pm 80$ km s^{-1}.

Owers et al. (2009a) have shown from optical observations that the member galaxy distribution of Abell 3667 shows a significant bimodality. The difference of the peculiar velocities between the two components is about 500 km s^{-1}. Assuming that the merger which induced the cold front is between two gas components which correspond to the two galaxy populations, and that the galaxy peculiar velocity difference is same as the ICM peculiar velocity

difference, the inclination angle θ of the trajectory of the cool gas against the sky plane is estimated at $\theta \sim \tan^{-1}(500/\sqrt{950^2 - 500^2}) \sim 30°$, which is relatively large but is marginally consistent with the inclination angle allowed for the sub-opening-angle scale variations to be visible (see also Section 7.5.1).

Comments on the previously suggested bow shock

Vikhlinin et al. (2001a) measured the cold gas to be transonic with the Mach number of $M = 1.0 \pm 0.2$, and indicated the existence of a possible bow shock. The position of the bow shock corresponds to $r \sim 200$ arcsec and $\theta \sim 225° - 285°$ (i.e., between the first and the second bins in the last panel of Figure 7.11 and the panels of the top row of Figure 7.12). We do not find corresponding systematic thermodynamic structures associated with the bow shock candidate, which is consistent with our subsonic Mach number measurement.

7.5.3 Kelvin-Helmholtz instability

Sub-opening-angle scale variations

What makes the front in Abell 3667 apparently different from other cold fronts are its variations on azimuthal scales smaller than the opening angle of the entire front (sub-opening-angle scale variation). This variation may have been missed in other cold fronts because the studies of cold fronts done so far have been focusing mainly only on the width of the front, simply neglecting the azimuthal information by extracting the surface brightness profile from much wider sectors (e.g. Owers et al., 2009b; Ghizzardi et al., 2010; Datta et al., 2014).

As we pointed out in Section 7.4.2, the radii of the front show azimuthal variations, and the variation is similar to the inviscid simulation results (Figure 7.14 upper panels). Actually, high-viscosity (Re=46 at pericenter, 0.1 Spitzer viscosity) simulation results are qualitatively inconsistent with our observations because they predict much smoother interfaces (Figure 7.14 lower panels). This suggests that the Reynolds number of the ICM is much higher in Abell 3667.

Roediger et al. (2015b) suggests that, in the inviscid stripping, the momentum transfer between two gas phases occurs via Kelvin-Helmholtz instabilities (KHIs), while in the viscous case, it does via viscosity. The simulation results (Figure 7.14 upper panels) clearly show KHIs occurring close to the tip of the front and developing toward the edge, strongly suggesting that our azimuthal variations of the interface are the signatures of the onset of developing KHIs.

However, what is intriguing is that although the interface does show these azimuthal variations, it does not seem to show variations below the length scale of $\sim 10°$, or equivalently $\sim$45 kpc, dissimilar to the inviscid simulation results, where we see the onset of KHIs for very small scales. This discrepancy indicates that the ICM is indeed viscous to some extent and the growth of KHIs on smaller scales is suppressed by the viscosity.

Multiple edges

Although fitting the surface brightness profiles with a projected broken power law model (Equation 7.1) yields reasonable fits as shown in Figure 7.6, we see some systematic residuals in the sectors of 210°-225° and 225°-240°. Indeed, each fit improves by $> 3\sigma$ level when the

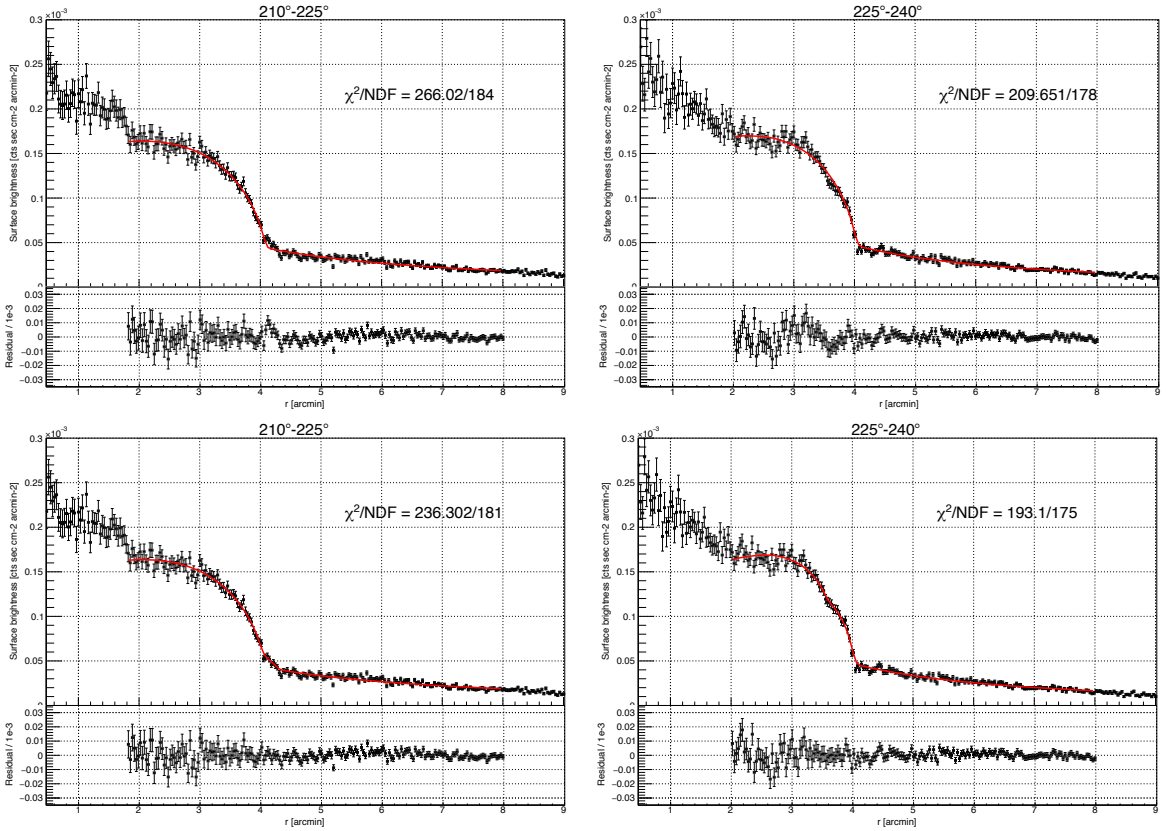

Figure 7.15 The top two panels are the same as shown in Figure 7.6. In the bottom two panels, the best-fitting projected double-broken power law models are overlaid instead of the best-fitting projected single-broken power law.

surface brightness profiles are fitted with a projected double-broken power law model using the radial density profile of

$$n(r) = \begin{cases} j_{12} j_{23} n_0 \left(\dfrac{r_{12}}{r_{23}}\right)^{-\alpha_2} \left(\dfrac{r}{r_{12}}\right)^{-\alpha_1} & (r \leq r_{12}) \\ j_{23} n_0 \left(\dfrac{r}{r_{23}}\right)^{-\alpha_2} & (r_{12} < r \leq r_{23}) \\ n_0 \left(\dfrac{r}{r_{23}}\right)^{-\alpha_3} & (r_{23} < r) \end{cases} , \tag{7.4}$$

where r_{12}/r_{23} are the radii of the inner/outer breaks, j_{12}/j_{23} are the jumps at the inner/outer breaks, n_0 is the normalization and $\alpha_1/\alpha_2/\alpha_3$ are the innermost/middle/outermost power-law slopes ($\Delta\chi^2 = 29.7$ and 16.6 for ΔNDF$= 3$ respectively for the sectors 210°-225° and 225°-240°, compared to the single-broken power law model).

Figure 7.15 shows the fitting results using the projected double-broken power law model. Clearly the residuals are mitigated. The density jumps are significant; $j_{12} = 1.68^{+0.31}_{-0.23}$ and $j_{23} = 1.65^{-0.23}_{-0.22}$ for the 210°-225° sector and $j_{12} = 1.21 \pm 0.07$ and $j_{23} = 2.59 \pm 0.10$ for the 225°-240° sector.

Recently it has been suggested by Roediger et al. (2013a) that, when there are developing

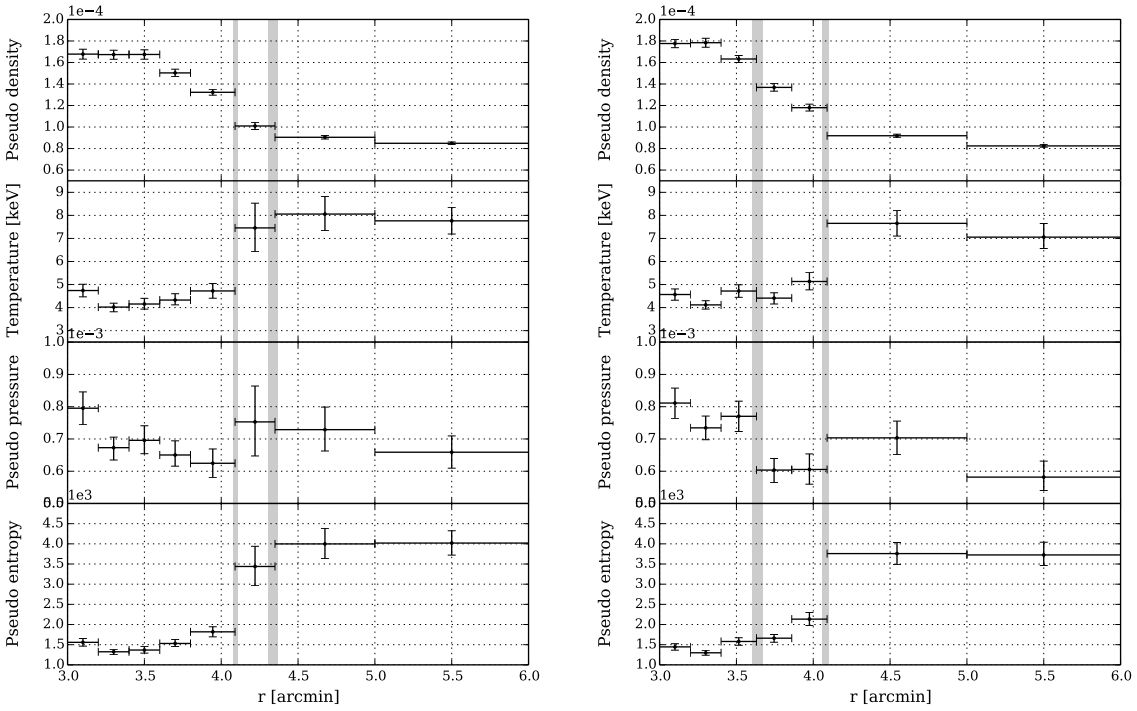

Figure 7.16 Thermodynamic profiles in the two directions where we see multiple edges in the corresponding surface brightness profiles (*Left:* 210°-225° and *Right:* 225°-240°). The panels are the pseudo density, the temperature, the pseudo pressure and the pseudo entropy from top to bottom. The vertical gray bands denote the edges in the surface brightness profiles. See also Figure 6.8 and the corresponding text.

KHIs at a cold front, the surface brightness profile across the front exhibits multiple edges, similarly to our case. The differences in radii between the breaks are $\Delta r_{\rm break} \equiv r_{23} - r_{12} = 0.26^{+0.02}_{-0.04}$ arcmin and $\Delta r_{\rm break} = 0.46^{+0.03}_{-0.05}$ arcmin respectively for the sectors 210°-225° and 225°-240°, which correspond to the actual lengths of $\Delta r_{\rm break} = 17^{+1}_{-3}$ kpc and $\Delta r_{\rm break} = 30^{+2}_{-3}$ kpc.

Roediger et al. (2013a,b) further suggested that the separation between the edges corresponds to about a fourth to a half of the scale length of the KH rolls. From $\Delta r_{\rm break}$ values, the scale length of the KH rolls is thus estimated at around 30-120 kpc, which is consistent with the sub-opening-angle scale variation of the interface.

Figure 7.16 shows the thermodynamic profiles for the corresponding sectors. In the profiles extracted for the sector 210°-225° (Figure 7.16 left), we see a jump of the temperature and entropy at the inner edge while they are continuous at the outer edge, which means that the thermodynamic properties between the edges are similar to those of the outer ambient gas. Given that the break radii are different between the sectors 210°-215° and 215°-225° as shown in Figure 7.7, it is likely that the multiple edges in this direction are caused by the fluctuation of the break radii and the thermodynamic properties between the edges are dominated by the outer ambient gas.

In contrast, in the profiles extracted for the sector 225°-240° (Figure 7.16 right), we see a

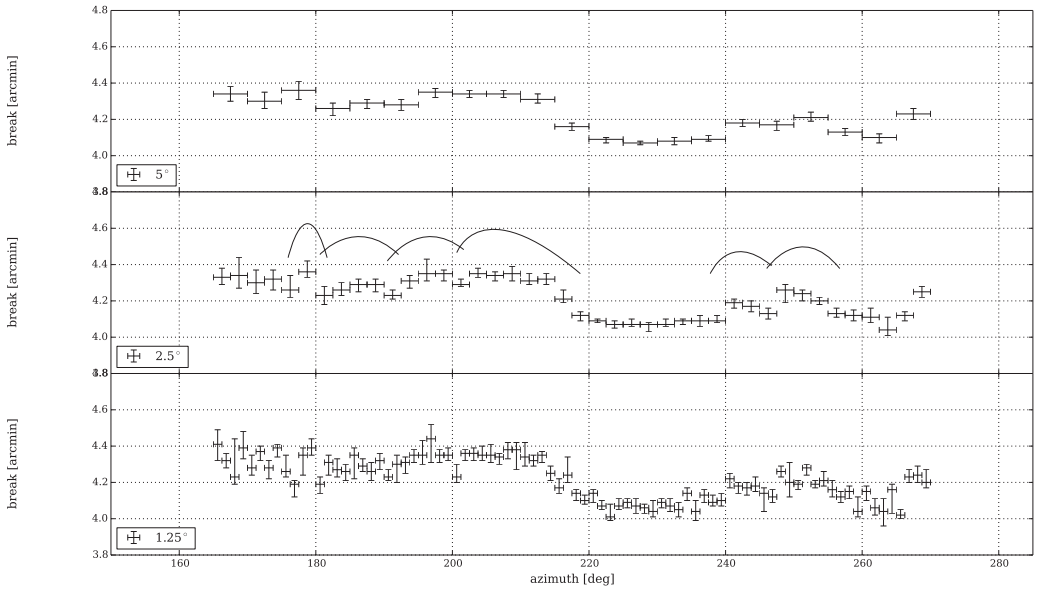

Figure 7.17 The break radii shown in different azimuthal resolution. 5°, 2.5° and 1.25° from top to bottom. The black curves denote the "sequential humps" (see the text below).

jump of the temperature and entropy at the outer edge while they are continuous at the inner edge. Moreover, the pressure profile seems to exhibit a deficit between the edges. We would like to point out the qualitative similarity of the surface brightness and the thermodynamic structures between this interface and the double-layered structure in the Perseus cluster (see Section 6.4.2). As shown in Figure 7.7, the break radius measured in the 15° resolution are consistent with the break radii measured in the 5° resolution. This means that both the multiple edges and the thermodynamic structure in this direction are not attributable to the simple azimuthal resolution effect unlike the case of the 210°-225° sector (previous paragraph), strongly indicating the existence of a projected KHI layer.

All these measurements are consistent with the scenario that KHIs are developing on the interface. To our knowledge, this is the first observational indication of KHIs along a merger cold front (not at the edges).

Detailed view of the fluctuation of break radii

The length scales of the fluctuation of the break radii appear to be limited in the range of 10°-25° when we look at the azimuthal profile in the 5° resolution (see gray points in Figure 7.7). Here we investigate the properties of the fluctuation by examining the azimuthal profile with finer angular resolutions.

Figure 7.17 shows the azimuthal profile of the break radii (165°-270°) extracted in 5°, 2.5°, and 1.25° resolutions (see also the second panel of Figure 7.7 for the 5° and 15° profiles). We find that the overall shapes of the profiles are similar to each other. However, in the finer resolution profiles, we find substructures which are missed even in the 5° profile.

In the 2.5° resolution profile, we find sequential hump-like structures, which are missed in the 5° profile (see the curves in Figure 7.17). The widths of the humps seem to be smaller in

the outer azimuths.

In the 1.25° profile, we also see the similar sequential hump-like structures, although they are less prominent due to the larger errorbars. The fact that the humps are less prominent in this resolution indicates that the data quality is insufficient for $\lesssim 1.25°$ resolutions. Therefore, although it is likely that the humps are actually present, we cannot infer either low-level existence or nonexistence of the smaller scale structures.

ICM effective viscosity

Assuming that KHIs are actually developing on the interface and that the scales of the fluctuations (sequential humps) represent the length scales of the KHI eddies, we can extract implications for the effective viscosity of the ICM.

In general, finite shear flow induces exponentially developing KHIs. If the gas were inviscid and incompressible, KHIs would develop on all length scales. However, the growth of the perturbation is suppressed when the Reynolds number Re of the ICM in the hot layer (outside the interface) is below the critical value

$$\mathrm{Re} = \frac{\rho \lambda V}{\mu} < \mathrm{Re}_{\mathrm{crit}} \sim 64\sqrt{\Delta}, \tag{7.5}$$

where ρ is the density, λ is the length scale, V is the shear strength, μ is the viscosity, ρ_1 and ρ_2 are the densities of the two gas phases on the two sides of the interface, and $\Delta = (\rho_1 + \rho_2)^2/\rho_1\rho_2$ (Roediger et al., 2013b; Chandrasekhar, 1961)[1].

This relation means that for a fixed viscosity, the difference of the shear strengths results in the difference of the length scales of the KHI modes which can develop. In other words, when a value of the effective viscosity μ is given, the perturbation of length-scale λ is suppressed if $\lambda < \lambda_{\mathrm{crit}} = \mu \mathrm{Re}_{\mathrm{crit}}/\rho V$.

When a sphere is subjected to incompressible ideal flow, the speed of the fluid on the sphere $v(\theta)$ is expressed using $v(\theta) = 3V \sin\theta/2$, where V is the speed of the flow and θ is the angle between the flow and the direction of the radius vector of a given position on the sphere. Therefore, assuming that the interface is spherical, we can calculate the flow speed at each azimuth.

Figure 7.18 shows the λ_{crit} values at each azimuth for various viscosity values. In plotting them, we assumed that the axis of symmetry with respect to the ambient flow is at 225°. For the density values, we used the deprojected ones (see Section 7.4.3). The black crosses roughly represent the sequential humps that we pointed out in the previous section.

The instabilities whose length scales are $< \lambda_{\mathrm{crit}}$ must be suppressed. However, we indeed see several instability candidates (humps; the black crosses in Figure 7.4.3). Therefore, the viscosity above $\sim$ 200 g/cm/s is unlikely because we would not find the sequential humps with such high viscosity values. Consequently, we obtain a conservative upper limit of the ICM viscosity at $\sim$ 200 g/cm/s.

As shown in the previous section, the length scales of sequential humps seem to be smaller in the outer azimuths. This may indicate that the smaller humps are actually not present in the inner azimuths because they are stable under the corresponding shear at that azimuth, although we cannot rule out the possibility that the smaller humps that we are not able to

[1] Roediger et al. (2013b) estimated the value of 64 with a simple analytic argument. They offered some more conservative estimations of $\mathrm{Re}_{\mathrm{crit}} = 10\sqrt{\Delta}$ or $16\sqrt{\Delta}$, but given that we do not see developing KHIs in Figure 7.14 bottom rows (Re = 46), we think these critical Reynolds numbers are too conservative.

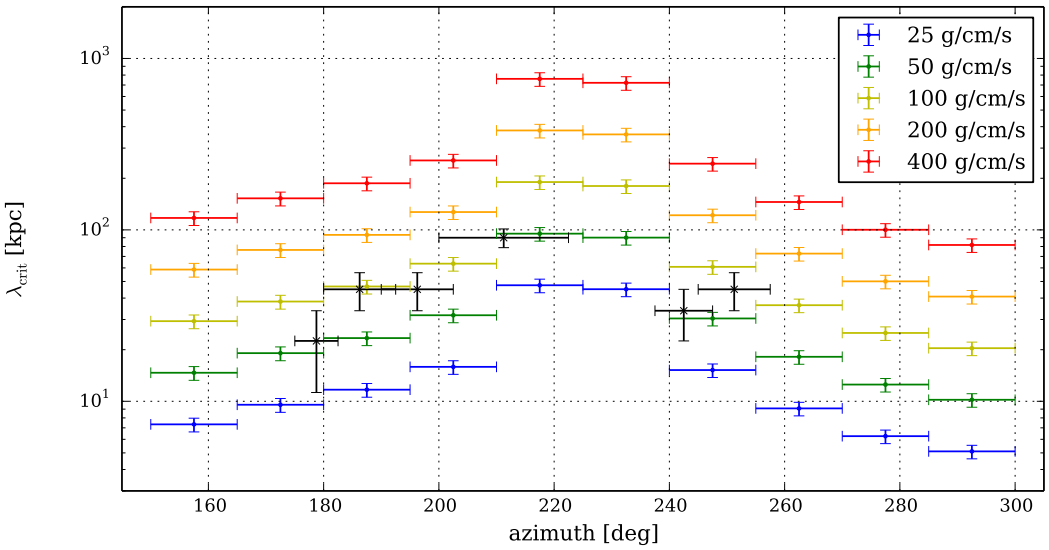

Figure 7.18 λ_{crit} values at each azimuth for various viscosity values. The instabilities whose length scales are λ_{crit} must be suppressed. The black crosses represent the sequential humps that we pointed out in the previous section.

detect or resolve exist on top of a larger hump. In this case, the viscosity below ~ 25 g/cm/s is not preferred because we might see humps with the scales smaller than actually observed. Combining this with the above upper limit, we can naively limit the ICM effective viscosity within the range of $25 - 200$ g/cm/s.

On one hand, the estimated viscosity depends on the numerous assumptions that we made (e.g., geometry, KHI scenario and existence and scales of the humps). In addition, it is difficult to break it down into the many kinds of physical processes which may affect the effective value. For example, the perturbations on smaller scales are suppressed not only by viscosity, but also by e.g. the surface tension at the interface or the finite width of the interface (Landau & Lifshitz, 1959; Churazov & Inogamov, 2004; Roediger et al., 2013b). The instabilities at larger scales can be suppressed by e.g. the compressibility of the fluid or the gravity (Vikhlinin & Markevitch, 2002; Churazov & Inogamov, 2004; Roediger et al., 2013b). The magnetic field which inevitably exists also plays a role; it might be acting as a surface tension term, or the effect of anisotropy of the viscosity (Braginskii viscosity) may be nonnegligible (ZuHone et al., 2015).

On the other hand, however, to our knowledge, this is the first case where the ICM viscosity is presented in a limited range. Previous studies have focused only on the existence/nonexistence of a physical phenomenon (e.g., KHI) and have not looked into the properties of the phenomenon itself (e.g., the scales of KHI), resulting in presenting only one of the lower or upper limits. We think that this difference clearly shows the importance of our new perspective of higher-order substructure.

To interpret our estimated effective viscosity of the ICM, we compare the estimated viscosity of ~ 100 g/cm/s to the fiducial viscosity of plasma, expressed as the isotropic Spitzer-like

temperature-dependent viscosity (Spitzer, 1965; Sarazin, 1986; Roediger et al., 2013a)

$$\mu = 5200 \text{ g/cm/s} \left(\frac{kT}{8.4 \text{ keV}} \right)^{5/2}, \tag{7.6}$$

where 8.4 keV is the typical temperature just outside the interface and the Coulomb logarithm $\ln \Lambda = 40$ is assumed. Our estimated value is suppressed by between one and two orders of magnitude compared to the isotropic Spitzer-like temperature-dependent viscosity. This suppression is likely due to the magnetic field lines parallel to the interface which freeze in the ambient flow along the interface. Because of the small gyroradii, momentum transfer across the field lines should be reduced. Note that, the existence of such a layer of magnetic field lines is consistent with the widths of the interface that are thinner than the Coulomb mean free paths (see Section 7.5.4).

Generally, the ICM viscosity should depend on other physical parameters such as the gas temperature and the strength and configuration of the magnetic field. Therefore, it is not necessarily expected that the estimated value is universal. On the other hand, the suppression of the effective viscosity from the Spitzer value at the interface of cold fronts (previous paragraph) has indeed been suggested by several observations and numerical simulations (e.g. Werner et al., 2016; Roediger et al., 2013a,b). Moreover, interestingly, the corresponding dynamic viscosity $\nu = \mu/\rho \sim 7 \times 10^{28}$ cm^2/s is consistent with the previous upper limit $\nu < 3 \times 10^{29}$ cm^2/s (Coma cluster, Schuecker et al., 2004) and the lower limit $\nu > 4 \times 10^{27}$ cm^2/s (Perseus cluster, Fabian et al., 2003), which are estimated for different targets and in different methods. These facts may imply the universality of the effective viscosity of the ICM, and if this is the case, our work provides the first observational estimation of the ICM effective viscosity which has been one of the fundamental but unknown microphysical parameters of the ICM.

Possible Karman vortex

We point out the comma-like shape of the main cluster in Section 7.4.1 (Figure 7.1). This makes us imagine the similarity to the Karman vortex. Using the viscosity value obtained in the previous section $\mu \sim 100$ g/cm/s, the Reynolds number corresponding the comma-shape whose spatial scale is ~ 500 kpc and assuming a speed of 950 km/s is estimated at Re ~ 2100. In the case of a sphere, the Karman vortex street is established if $\sim 300 <$ Re $< 3.7 \times 10^5$, and if $650 <$ Re the vortex street becomes turbulent (Kiya et al., 2001). Thus, it is possible that the Karman vortex has been established in this system.

The vortex shedding frequency $f = SV/\lambda$, where S is the Strouhal number and $S \sim 0.2$ for the Karman vortex regime, is calculated at $f \sim 0.4$ Gyr^{-1}. Since the typical dynamical timescale of galaxy clusters is of order Gyr, there must not be multiple Karman vortices, which is consistent with our observation. Note that, if we use the Spitzer viscosity in the calculation above, it does not yield the Reynolds number within the Karman vortex regime (Re ~ 40).

7.5.4 Thickness of the front

Cold fronts have been of interest because of their thinness (e.g. Markevitch & Vikhlinin, 2007). Indeed, as shown in Figure 7.6, some of the profiles show a remarkable brightness drop especially in the azimuthal range of 195°-270°.

Table 7.2. χ^2/NDF for the Gaussian-convoluted projected broken power-law fitting

σ (arcsec)	195°-210°	210°-225°	225°-240°	240°-255°	255°-270°
0 (no convolution)	251.787/187	266.02/184	209.651/178	197.76/163	240.288/163
2	252.832/187	261.966/184	212.302/178	200.339/163	240.143/163
4	254.801/187	253.79/184	218.817/178	202.895/163	241.004/163
6	257.796/187	247.713/184	228.228/178	207.243/163	243.735/163
8	262.325/187	245.204/184	238.627/178	213.562/163	248.385/163

One mechanism which should take place and contribute to the smearing of the interface is Coulomb diffusion across the interface. The Coulomb mean free path of electrons (λ for each side and $\lambda_{\rm a\rightarrow b}$ across the interface from side a to side b) can be calculated using

$$\begin{cases} \lambda = 15 \text{ kpc} \left(\dfrac{kT}{7 \text{ keV}}\right)^2 \left(\dfrac{n_e}{10^{-3} \text{ cm}^{-3}}\right)^{-1} \\ \lambda_{\rm a\rightarrow b} = \lambda_{\rm b} \dfrac{T_{\rm a}}{T_{\rm b}} \dfrac{G(1)}{G(\sqrt{T_{\rm a}/T_{\rm b}})} \end{cases}, \tag{7.7}$$

where $G(x) = (\mathrm{erf}(x) - x\mathrm{erf}'(x))/2x^2$ and $\mathrm{erf}(x)$ is the error function (Spitzer, 1965; Markevitch & Vikhlinin, 2007).

Since usually $\lambda_{\rm in\rightarrow out}$ is longer than $\lambda_{\rm out\rightarrow in}$ at cold fronts, here we consider $\lambda_{\rm in\rightarrow out}$ as the typical length scale for Coulomb collision for smearing the front, because the diffusion across the interface should contribute to the smearing most. Using the observed values (see Figures 7.11, 7.12 and 7.13), $\lambda_{\rm in\rightarrow out,195^\circ-210^\circ} \sim 7.4$ kpc, $\lambda_{\rm in\rightarrow out,210^\circ-225^\circ} \sim 6.5$ kpc, $\lambda_{\rm in\rightarrow out,225^\circ-240^\circ} \sim 8.2$ kpc, $\lambda_{\rm in\rightarrow out,240^\circ-255^\circ} \sim 8.7$ kpc and $\lambda_{\rm in\rightarrow out,255^\circ-270^\circ} \sim 9.4$ kpc. These length scale values are generally similar to the previous estimates (e.g. Vikhlinin et al., 2001a; Markevitch & Vikhlinin, 2007).

Assuming the Maxwellian distribution of electrons, the typical velocity of the electrons is calculated using

$$\bar{v}_{\rm rms} = \sqrt{\langle v^2 \rangle} = \sqrt{3kT/m_e} = 50 \text{ kpc/Myr} \left(\frac{kT}{4.0 \text{ keV}}\right)^{1/2}. \tag{7.8}$$

Therefore the collisional time is $\lambda/\bar{v}_{\rm rms} \sim 0.2$ Myr, which is far shorter than the dynamical timescale of ~Gyr, implying that the front width should be at least several times $\lambda_{\rm in\rightarrow out}$ if the Coulomb diffusion is not suppressed.

In order to test the necessity of the smearing of the model profiles, we fitted a Gaussian-convoluted, projected broken power law[2], with the width of the Gaussian fixed to certain values, to the same profiles shown in Figure 7.6. The selected widths of the Gaussian are

[2] A "Gaussian-smeared, projected density profile" and a "projected, Gaussian-smeared density profile" are formally different. However, the width derived using the former model is at least larger than the one using the latter model. This means our upper limit of the width of the interface derived using the former model is the most conservative upper limit. Therefore the actual interface may be thinner, strengthening our argument for the suppression of the Coulomb diffusion.

$\sigma = 2, 4, 6, 8$ arcsec. The best-fitting parameters are similar to the fitting that does not include Gaussian convolution (Section 7.4.2), and the resulting χ^2/NDF values are shown in Table 7.2.

Except for the 210°-225° sector, which is one of the two sectors where we see the multiple edge structure, we can roughly estimate the upper limits of the Gaussian width required on the model at $\lesssim 4$ arcsec. These upper limits are smaller than the Coulomb mean free path of $\gtrsim 7$ arcsec, which indicates a strong suppression of the Coulomb diffusion for each single azimuth. This argument is consistent with the previous arguments where the thickness of the front is examined using wider sectors (e.g. Vikhlinin et al., 2001a; Vikhlinin & Markevitch, 2002; Datta et al., 2014).

One mechanism which can suppress the diffusion across the interface is the magnetic field. At the interface where strong shear flows take place, we can expect the magnetic field lines, which are frozen in the flow, extending along the flow, to be parallel to the interface. Such magnetic field lines can easily suppress the diffusion even if the magnetic field is very weak and dynamically negligible, because the typical gyroradius r_g of the thermal electrons is very short;

$$r_g = \frac{\sqrt{3 m_e kT}}{|q|B} c_0 = 10^{-10}\ \mathrm{kpc} \left(\frac{kT}{4.0\ \mathrm{keV}}\right)^{1/2} \left(\frac{B}{\mathrm{nG}}\right)^{-1} \ll \mathrm{kpc}, \tag{7.9}$$

where q is the elementary charge, c_0 is the speed of light, and B is the magnetic field strength. Thus, it is very likely that the Coulomb diffusion is (almost) completely suppressed across the interface.

Note that the radius of the 90% enclosed-counts fraction aperture near the front is $\sim$ 2 arcsec, roughly corresponding to the Gaussian σ of 1.2 arcsec, marginally comparable with the apparent broadening of the interface ($\sigma \lesssim 4$ arcsec). Therefore it is more plausible that the apparent finite width of the interface, if any, is due to the PSF effect as well as the projection effect. The observed KHIs developing on the front (Section 7.5.3) might also contribute to the possible broadening of the interface.

7.5.5 Gas mixing at the mushroom edge

As shown in Figure 7.13, the temperature and the entropy jumps are relatively moderate at the edge of the front (i.e. 165°-195°, 270°-300°) compared with the tip of the front (i.e. 195°-270°). Given that these edge azimuths correspond to the edge of the mushroom-shape in the image (see Figures 7.1 and 7.9), this difference is probably due to the mixing of the gas induced by the fully developed, turbulent KHIs.

7.6 Summary

In this chapter, we investigate the merger cold front in the galaxy cluster Abell 3667, from a new point of view, focusing on the azimuthal variation. The main results of this work are summarized below.

1. We point out the striking similarity of the cold front in Abell 3667 to the recent numerical simulation of inviscid gas-stripping for the first time. This indicates that the front is formed by a merger which takes place nearly in the sky plane, and also the effective viscosity of the ICM is suppressed to some extent.

2. By extracting the azimuthally resolved surface brightness profile, we find that the radii of the interface fluctuate with position angle. This fact has never been considered so far.

3. We find multiple edges in the surface brightness profiles of some of the azimuths. The ratio of the distance of the edges to the typical scale of the fluctuation in the azimuthal direction is consistent with the prediction from the numerical simulation results of the KHIs on cold fronts. In one direction, we find that the surface brightness profile and the corresponding thermodynamic structure are qualitatively similar to those of the double-layered interface found in the Perseus cluster, which we interpret as a KHI layer.

4. With the above supporting facts, we propose the scenario that KHIs are developing on the cold front in Abell 3667. This is the first observational indication of developing KHIs on a merger cold front.

5. Based on the assumption that KHIs are actually developing on the interface and that the apparent length scales of the sequential humps represent the minimum allowed length scales of the instability at the corresponding azimuths, we estimated the effective viscosity of the ICM at $\nu \sim 7 \times 10^{28}$ cm^2/s. This is the first case where the value of the ICM effective viscosity is observationally presented in a limited range (not a single upper/lower limit).

6. Our estimated viscosity value is suppressed by between one and two orders of magnitude compared to the fiducial Spitzer viscosity, as indicated in previous observations and simulations, probably because of the magnetic field lines. The estimated value is consistent with the previous lower and upper limits. These facts may indicate the intriguing universality of the effective viscosity of the ICM, which need not be universal.

7. We propose a scenario that the comma-shaped morphology of the cluster is due to Karman vortex.

8. We find that the Coulomb diffusion is probably suppressed for each single azimuth. This may be attributed to magnetic fields parallel to the front, which can suppress the Coulomb diffusion almost completely.

9. We find that the temperature and the entropy jumps are moderate at the edges of the front. This is likely due to the mixing of the gas via fully developed turbulent KHIs.

Chapter 8

Conclusion

In this thesis, we investigate X-ray substructure in galaxy clusters in order to infer the microphysical properties of the ICM. We mainly focus on "cold front"s, which are the interface between a lower temperature, denser gas parcel and a more rarefied, hotter ambient medium, extending the point of view to both "higher-order" and "lower-order" structure. Our main achievements are listed up below:

- In Abell 85, we find a smooth edge in one of the two subclusters currently falling in, which is smooth over 200 kpc. The width of the edge is ∼10 kpc, which is narrower than the electron Coulomb mean free path at this position (∼30 kpc). We suggest that this results from the ordered magnetic field lines induced by the main cluster large-scale (∼600 kpc) gas sloshing, demonstrating the interaction between multiple X-ray substructures for the first time, so far an overlooked point of view. Given that clusters grow via mergers, such a phenomenon should be universal, and thus it indicates the importance of such substructure-substructure interactions in the context of cluster hierarchical evolution.

- We suggest that the subcluster gas is almost completely stripped during its infall in Abell 85. This poses a challenge to recent simulations which find the core usually survives major mergers, indicating that the microphysical properties of the ICM is more complex than the simple ideal fluid approximation typically employed by these numerical models. The stripped tail seems to extend over ∼700 kpc out to r_{500}, which may imply a long lifetime of the tail, and thus the suppression of strong turbulence and diffusion.

- In the Perseus cluster, we find a significant double-layered interface. From thermodynamic studies, we find that the double-layered interface is consistent with being a KHI layer on the sloshing cold front. This is the first case where a KHI layer candidate itself is examined thermodynamically, resulting in stronger evidence for the existence of such an instability layer. We find pressure deficit of the order of $\sim 10^{-2}$ keV cm^{-3} in the KHI layer with respect to the ambient medium, which could be supported by magnetic fields or ram pressure. Based on the KHI scenario, we estimate the turbulent heating rate resulting from the collapse of the KHI at 3×10^{-26} erg/cm^3/s, and find that it may balance radiative cooling. We also find the estimated turbulent heating rate agrees within an order of magnitude with the previous estimate performed on the same system with a completely different method. This indicates the importance of the turbulent heating

in the context of the cooling problem in the cores of galaxy clusters, and also that the turbulence triggered by sloshing-induced KHIs have nonnegligible contributions to the ICM turbulence, which has not been considered extensively.

- In the Perseus cluster, we find feather-like structures below the sloshing cold front. From thermodynamic studies, we find that the structure is consistent with being due simply to gas depletion, which originates from magnetic field amplification associated with the sloshing motion of the ICM, which has been indicated in the literature. Based on this scenario, we for the first time estimated the ambient magnetic field strength at ~ 30 μG using such an X-ray substructure through thermodynamic properties.
- In Abell 3667, we for the first time point out that the radii of the cold front fluctuate with position angle. Observational results are consistent with the scenario that KHIs are developing on the cold front. This is the first observational indication of developing KHIs on a merger cold front. Based on the assumption that KHIs are actually developing on the interface and that the apparent length scales of the fluctuations represent the minimum allowed length scales of the instability at the corresponding azimuth, we estimated the physical value of the effective viscosity at $\nu \sim 7 \times 10^{28}$ cm^2/s. This is the first case where the value of the ICM viscosity is observationally presented in a limited range. The viscosity value is suppressed by between one and two orders of magnitude compared to the fiducial Spitzer viscosity, as indicated in previous observations and simulations, probably because of the magnetic field lines. The estimated viscosity is consistent with the previous observational upper and lower limits, possibly indicating the intriguing universality of the ICM effective viscosity, which need not be universal.

Although all of the new insights regarding the ICM microphysics obtained here appear to be independent from each other, all of them can be discussed from one underlying aspect, i.e., the insufficiency of the simple hydro*static* description of the ICM. Indeed, the aim of the data analysis performed in this work was to highlight the hydro*dynamic* behavior of the ICM.

Until now, most of the ICM studies have focused on the thermodynamic properties and the elemental composition, treating the plasma as an ideal fluid and largely lacking information about the associated gas motions. Our studies by comparison have offered some of the first quantitative estimates of its fundamental microphysical properties, e.g., the viscosity, turbulence, and magnetic field strength, stressing the necessity for a hydro*dynamic*, or *magnetohydrodynamic* treatment of the ICM.

As our observed phenomena and estimated quantities are some of the first examples and currently it is difficult to draw conclusions about their generality or universality. However, by actually observing them and estimating the physical parameters, we think we have introduced new plausible observational points of view (higher-order and lower-order substructure) with which we might be able to estimate the ICM microphysical parameters even in other targets under the condition of sufficiently good data. Numerical simulations are recent major tools and are also important, but usually they are qualitative. We think it is observations with these points of view that are essential for the quantitative understanding of the most dominant baryons in our Universe.

Future prospects

The ICM microphysics plays a key role in the fields of astrophysics and cosmology. On one hand, from the astrophysical point of view, cluster mergers are the most energetic events in

the Universe, which release tremendous gravitational energy that is channeled into other forms of energy, such as heat, turbulence, or particle acceleration. However, the problem of how the energy is transported and dissipated in the ICM highly depends on the ICM microphysics and still remains uncertain. On the other hand, from the cosmological point of view, the cluster mass function constructed from X-ray mass estimates is one of the most important cosmological probes. However, the biases caused by the microphysical properties of the ICM, such as electron-ion nonequilibrium, non-thermal pressure, or gas inhomogeneity, make the X-ray mass estimates uncertain.

Therefore, our work has impacts not only on the problem of understanding the physics of the most dominant baryon in the Universe, but also on solving other important problems in the fields of astrophysics and cosmology.

Although we unveil a variety of unknown aspects of the ICM, significant further progress is expected with the dynamical information of the ICM, which is available after the launch of *ASTRO-H*. The Soft X-ray Spectrometer (SXS) installed onboard *ASTRO-H* allows high-resolution spectroscopy of galaxy clusters, and enables the Doppler shift, as well as the width of spectral lines to be measured.

The measurement of the Doppler shift of spectral lines offers information regarding the relative line-of-sight velocity of different ICM components in the same system. For example, by measuring the line-of-sight velocity of the S subcluster with respect to the main cluster, we can infer the angle of motion with respect to the sky plane and from this infer the actual length of the smooth northern edge and the stripped tail in Abell 85. Although Abell 85 is a complex system, this may lead to quantitative estimates of the lifetime of these structures, and thus quantitative constraints on the turbulence and diffusion efficiency of the ICM. Also, by measuring the line-of-sight velocity of the gas just below and above the cold front in Abell 3667, we can test our interpretation of the cold gas volume moving mostly in the sky plane. The competing scenario of gas sloshing parallel to the line-of-sight can also be tested.

On the other hand, the measurement of the width of spectral lines provides information about turbulent motion, which has not been accessible so far. For example, by measuring the turbulent strength at the stripped tail in Abell 85, we could check the hypothesis of the turbulence being weak. However, in most cases, the angular resolution of SXS (1.3 arcmin HPD) is insufficient to resolve the substructures we studied in this work, and thus the direct measurement of the turbulence would still be difficult. Instead, the information about the turbulent strength obtained for other parts of the cluster or other targets complements the information on the ICM microphysical properties drawn with studies of X-ray substructure, and may help us to draw a comprehensive view of the ICM microphysics. Direct studies of turbulence and ICM motion in small-scale structures will be available after the launch of *Athena*, which will offer the microcalorimeter energy resolution with a good angular resolution of a few arcsec.

Bibliography

Abdo, A. A., Ackermann, M., Ajello, M., Asano, K., Baldini, L., Ballet, J., Barbiellini, G., Bastieri, D., Baughman, B. M., Bechtol, K., Bellazzini, R., Blandford, R. D., Bloom, E. D., Bonamente, E., Borgland, A. W., Bregeon, J., Brez, A., Brigida, M., Bruel, P., Burnett, T. H., Caliandro, G. A., Cameron, R. A., Caraveo, P. A., Casandjian, J. M., Cavazzuti, E., Cecchi, C., Celotti, A., Chekhtman, A., Cheung, C. C., Chiang, J., Ciprini, S., Claus, R., Cohen-Tanugi, J., Colafrancesco, S., Cominsky, L. R., Conrad, J., Costamante, L., Dermer, C. D., de Angelis, A., de Palma, F., Digel, S. W., Donato, D., do Couto e Silva, E., Drell, P. S., Dubois, R., Dumora, D., Farnier, C., Favuzzi, C., Finke, J., Focke, W. B., Frailis, M., Fukazawa, Y., Funk, S., Fusco, P., Gargano, F., Georganopoulos, M., Germani, S., Giebels, B., Giglietto, N., Giordano, F., Glanzman, T., Grenier, I. A., Grondin, M.-H., Grove, J. E., Guillemot, L., Guiriec, S., Hanabata, Y., Harding, A. K., Hartman, R. C., Hayashida, M., Hays, E., Hughes, R. E., Jóhannesson, G., Johnson, A. S., Johnson, R. P., Johnson, W. N., Kadler, M., Kamae, T., Kanai, Y., Katagiri, H., Kataoka, J., Kawai, N., Kerr, M., Knödlseder, J., Kuehn, F., Kuss, M., Latronico, L., Lemoine-Goumard, M., Longo, F., Loparco, F., Lott, B., Lovellette, M. N., Lubrano, P., Madejski, G. M., Makeev, A., Mazziotta, M. N., McEnery, J. E., Meurer, C., Michelson, P. F., Mitthumsiri, W., Mizuno, T., Moiseev, A. A., Monte, C., Monzani, M. E., Morselli, A., Moskalenko, I. V., Murgia, S., Nakamori, T., Nolan, P. L., Norris, J. P., Nuss, E., Ohsugi, T., Omodei, N., Orlando, E., Ormes, J. F., Paneque, D., Panetta, J. H., Parent, D., Pepe, M., Pesce-Rollins, M., Piron, F., Porter, T. A., Rainò, S., Razzano, M., Reimer, A., Reimer, O., Reposeur, T., Ritz, S., Rodriguez, A. Y., Romani, R. W., Ryde, F., Sadrozinski, H. F.-W., Sambruna, R., Sanchez, D., Sander, A., Sato, R., Parkinson, P. M. S., Sgrò, C., Smith, D. A., Smith, P. D., Spandre, G., Spinelli, P., Starck, J.-L., Strickman, M. S., Strong, A. W., Suson, D. J., Tajima, H., Takahashi, H., Takahashi, T., Tanaka, T., Taylor, G. B., Thayer, J. G., Thompson, D. J., Torres, D. F., Tosti, G., Uchiyama, Y., Usher, T. L., Vilchez, N., Vitale, V., Waite, A. P., Wood, K. S., Ylinen, T., Ziegler, M., Aller, H. D., Aller, M. F., Kellermann, K. I., Kovalev, Y. Y., Kovalev, Y. A., Lister, M. L., & Pushkarev, A. B. 2009, ApJ, 699, 31

Abell, G. O. 1958, ApJS, 3, 211

Ahn, C. P., Alexandroff, R., Allende Prieto, C., Anders, F., Anderson, S. F., Anderton, T., Andrews, B. H., Aubourg, É., Bailey, S., Bastien, F. A., & et al. 2014, ApJS, 211, 17

Akamatsu, H., de Plaa, J., Kaastra, J., Ishisaki, Y., Ohashi, T., Kawaharada, M., & Nakazawa, K. 2012a, PASJ, 64, 49

Akamatsu, H. & Kawahara, H. 2013, PASJ, 65, 16

Akamatsu, H., Takizawa, M., Nakazawa, K., Fukazawa, Y., Ishisaki, Y., & Ohashi, T. 2012b, PASJ, 64, 67

Allen, S. W., Evrard, A. E., & Mantz, A. B. 2011, ARA&A, 49, 409

Allen, S. W., Taylor, G. B., Nulsen, P. E. J., Johnstone, R. M., David, L. P., Ettori, S., Fabian, A. C., Forman, W., Jones, C., & McNamara, B. 2001, MNRAS, 324, 842

Arnaud, K. A. 1996, in Astronomical Society of the Pacific Conference Series, Vol. 101, Astronomical Data Analysis Software and Systems V, ed. G. H. Jacoby & J. Barnes, 17

Arnaud, K. A., Smith, R. K., Siemiginowska, A., Edgar, R. J., Grant, C. E., Kuntz, K. D., & Schwartz, D. A. 2011, in AAS/High Energy Astrophysics Division, Vol. 12, AAS/High Energy Astrophysics Division

Arnaud, M., Pointecouteau, E., & Pratt, G. W. 2005, A&A, 441, 893

Ascasibar, Y. & Markevitch, M. 2006, ApJ, 650, 102

Aschenbach, B. 1985, Reports on Progress in Physics, 48, 579

Aschenbach, B. 2002, in Society of Photo-Optical Instrumentation Engineers (SPIE) Conference Series, Vol. 4496, X-Ray Optics for Astronomy: Telescopes, Multilayers, Spectrometers, and Missions, ed. P. Gorenstein & R. B. Hoover, 8–22

Aschenbach, B., Braeuninger, H., Briel, U., Brinkmann, W., Fink, H., Heinecke, N., Hippmann, H., Kettenring, G., Metzner, G., & Ondrusch, A. 1981, Space Sci. Rev., 30, 569

Atwood, W. B., Abdo, A. A., Ackermann, M., Althouse, W., Anderson, B., Axelsson, M., Baldini, L., Ballet, J., Band, D. L., Barbiellini, G., & et al. 2009, ApJ, 697, 1071

Barcons, X., Nandra, K., Barret, D., den Herder, J.-W., Fabian, A. C., Piro, L., Watson, M. G., & the Athena Team. 2015, Journal of Physics Conference Series, 610, 012008

Beers, T. C., Gebhardt, K., Forman, W., Huchra, J. P., & Jones, C. 1991, AJ, 102, 1581

Begeman, K. G., Broeils, A. H., & Sanders, R. H. 1991, MNRAS, 249, 523

Boehringer, H., Voges, W., Fabian, A. C., Edge, A. C., & Neumann, D. M. 1993, MNRAS, 264, L25

Böhringer, H. & Werner, N. 2010, A&A Rev., 18, 127

Bonafede, A., Feretti, L., Murgia, M., Govoni, F., Giovannini, G., Dallacasa, D., Dolag, K., & Taylor, G. B. 2010, A&A, 513, A30

Bonafede, A., Vazza, F., Brüggen, M., Murgia, M., Govoni, F., Feretti, L., Giovannini, G., & Ogrean, G. 2013, MNRAS, 433, 3208

Boué, G., Durret, F., Adami, C., Mamon, G. A., Ilbert, O., & Cayatte, V. 2008, A&A, 489, 11

Bradt, H. V. D., Ohashi, T., & Pounds, K. A. 1992, ARA&A, 30, 391

Braginskii, S. I. 1958, Soviet Journal of Experimental and Theoretical Physics, 6, 494

Brandenburg, A. & Nordlund, Å. 2011, Reports on Progress in Physics, 74, 046901

Brecher, K. & Burbidge, G. R. 1972, Nature, 237, 440

Briel, U. G., Finoguenov, A., & Henry, J. P. 2004, A&A, 426, 1

Brinkman, A. C., Gunsing, C. J. T., Kaastra, J. S., van der Meer, R. L. J., Mewe, R., Paerels, F., Raassen, A. J. J., van Rooijen, J. J., Bräuninger, H., Burkert, W., Burwitz, V., Hartner, G., Predehl, P., Ness, J.-U., Schmitt, J. H. M. M., Drake, J. J., Johnson, O., Juda, M., Kashyap, V., Murray, S. S., Pease, D., Ratzlaff, P., & Wargelin, B. J. 2000, ApJ, 530, L111

Brüggen, M. & Kaiser, C. R. 2002, Nature, 418, 301

Brüggen, M. & Vazza, F. 2015, in Astrophysics and Space Science Library, Vol. 407, Astrophysics and Space Science Library, ed. A. Lazarian, E. M. de Gouveia Dal Pino, & C. Melioli, 599

Brunetti, G., Setti, G., Feretti, L., & Giovannini, G. 2001, MNRAS, 320, 365

Burenin, R. A., Vikhlinin, A., Hornstrup, A., Ebeling, H., Quintana, H., & Mescheryakov, A. 2007, ApJS, 172, 561

Burns, J. O., Hallman, E. J., Gantner, B., Motl, P. M., & Norman, M. L. 2008, ApJ, 675, 1125

Byram, E. T., Chubb, T. A., & Friedman, H. 1966, Science, 152, 66

Canizares, C. R., Davis, J. E., Dewey, D., Flanagan, K. A., Galton, E. B., Huenemoerder, D. P., Ishibashi, K., Markert, T. H., Marshall, H. L., McGuirk, M., Schattenburg, M. L., Schulz, N. S., Smith, H. I., & Wise, M. 2005, PASP, 117, 1144

Carilli, C. L. & Taylor, G. B. 2002, ARA&A, 40, 319

Carretti, E., Brown, S., Staveley-Smith, L., Malarecki, J. M., Bernardi, G., Gaensler, B. M., Haverkorn, M., Kesteven, M. J., & Poppi, S. 2013, MNRAS, 430, 1414

Cash, W. 1979, ApJ, 228, 939

Cavaliere, A. G., Gursky, H., & Tucker, W. H. 1971, Nature, 231, 437

Chandrasekhar, S. 1961, Hydrodynamic and hydromagnetic stability (Oxford University Press)

Churazov, E., Brüggen, M., Kaiser, C. R., Böhringer, H., & Forman, W. 2001, ApJ, 554, 261

Churazov, E., Forman, W., Jones, C., & Böhringer, H. 2000, A&A, 356, 788

—. 2003, ApJ, 590, 225

Churazov, E., Forman, W., Jones, C., Sunyaev, R., & Böhringer, H. 2004, MNRAS, 347, 29

Churazov, E., Forman, W., Vikhlinin, A., Tremaine, S., Gerhard, O., & Jones, C. 2008, MNRAS, 388, 1062

Churazov, E., Gilfanov, M., Forman, W., & Jones, C. 1999, ApJ, 520, 105

Churazov, E. & Inogamov, N. 2004, MNRAS, 350, L52

Clarke, T. E. 2004, Journal of Korean Astronomical Society, 37, 337

Clowe, D., Bradač, M., Gonzalez, A. H., Markevitch, M., Randall, S. W., Jones, C., & Zaritsky, D. 2006, ApJ, 648, L109

Cowan, G. 1997, Statistical data analysis (Oxford University Press)

Cowie, L. L. & McKee, C. F. 1977, ApJ, 211, 135

Datta, A., Schenck, D. E., Burns, J. O., Skillman, S. W., & Hallman, E. J. 2014, ApJ, 793, 80

De Luca, A. & Molendi, S. 2004, A&A, 419, 837

de Plaa, J., Zhuravleva, I., Werner, N., Kaastra, J. S., Churazov, E., Smith, R. K., Raassen, A. J. J., & Grange, Y. G. 2012, A&A, 539, A34

den Herder, J. W., Brinkman, A. C., Kahn, S. M., Branduardi-Raymont, G., Thomsen, K., Aarts, H., Audard, M., Bixler, J. V., den Boggende, A. J., Cottam, J., Decker, T., Dubbeldam, L., Erd, C., Goulooze, H., Güdel, M., Guttridge, P., Hailey, C. J., Janabi, K. A., Kaastra, J. S., de Korte, P. A. J., van Leeuwen, B. J., Mauche, C., McCalden, A. J., Mewe, R., Naber, A., Paerels, F. B., Peterson, J. R., Rasmussen, A. P., Rees, K., Sakelliou, I., Sako, M., Spodek, J., Stern, M., Tamura, T., Tandy, J., de Vries, C. P., Welch, S., & Zehnder, A. 2001, A&A, 365, L7

Dreher, J. W., Carilli, C. L., & Perley, R. A. 1987, ApJ, 316, 611

Durret, F., Felenbok, P., Lobo, C., & Slezak, E. 1998, A&AS, 129, 281

Durret, F., Lima Neto, G. B., & Forman, W. 2005a, A&A, 432, 809

—. 2005b, Advances in Space Research, 36, 618

Durret, F., Lima Neto, G. B., Forman, W., & Churazov, E. 2003, A&A, 403, L29

Eckert, D., Molendi, S., Owers, M., Gaspari, M., Venturi, T., Rudnick, L., Ettori, S., Paltani, S., Gastaldello, F., & Rossetti, M. 2014, A&A, 570, A119

Edge, A. C. 2001, MNRAS, 328, 762

Edge, A. C., Stewart, G. C., Fabian, A. C., & Arnaud, K. A. 1990, MNRAS, 245, 559

Eisenstein, D. J., Weinberg, D. H., Agol, E., Aihara, H., Allende Prieto, C., Anderson, S. F., Arns, J. A., Aubourg, É., Bailey, S., Balbinot, E., & et al. 2011, AJ, 142, 72

Ettori, S. & Fabian, A. C. 2000, MNRAS, 317, L57

Evrard, A. E. 1990, ApJ, 363, 349

Fabian, A. C. 1994, ARA&A, 32, 277

Fabian, A. C., Hu, E. M., Cowie, L. L., & Grindlay, J. 1981, ApJ, 248, 47

Fabian, A. C., Johnstone, R. M., Sanders, J. S., Conselice, C. J., Crawford, C. S., Gallagher, III, J. S., & Zweibel, E. 2008, Nature, 454, 968

Fabian, A. C. & Nulsen, P. E. J. 1977, MNRAS, 180, 479

Fabian, A. C., Sanders, J. S., Allen, S. W., Canning, R. E. A., Churazov, E., Crawford, C. S., Forman, W., Gabany, J., Hlavacek-Larrondo, J., Johnstone, R. M., Russell, H. R., Reynolds, C. S., Salomé, P., Taylor, G. B., & Young, A. J. 2011a, MNRAS, 418, 2154

Fabian, A. C., Sanders, J. S., Crawford, C. S., Conselice, C. J., Gallagher, J. S., & Wyse, R. F. G. 2003, MNRAS, 344, L48

Fabian, A. C., Sanders, J. S., Ettori, S., Taylor, G. B., Allen, S. W., Crawford, C. S., Iwasawa, K., Johnstone, R. M., & Ogle, P. M. 2000, MNRAS, 318, L65

Fabian, A. C., Sanders, J. S., Taylor, G. B., Allen, S. W., Crawford, C. S., Johnstone, R. M., & Iwasawa, K. 2006, MNRAS, 366, 417

Fabian, A. C., Sanders, J. S., Williams, R. J. R., Lazarian, A., Ferland, G. J., & Johnstone, R. M. 2011b, MNRAS, 417, 172

Faltenbacher, A., Kravtsov, A. V., Nagai, D., & Gottlöber, S. 2005, MNRAS, 358, 139

Finoguenov, A., Sarazin, C. L., Nakazawa, K., Wik, D. R., & Clarke, T. E. 2010, ApJ, 715, 1143

Forman, W. & Jones, C. 1982, ARA&A, 20, 547

Forman, W., Jones, C., Churazov, E., Markevitch, M., Nulsen, P., Vikhlinin, A., Begelman, M., Böhringer, H., Eilek, J., Heinz, S., Kraft, R., Owen, F., & Pahre, M. 2007, ApJ, 665, 1057

Forman, W., Jones, C., Cominsky, L., Julien, P., Murray, S., Peters, G., Tananbaum, H., & Giacconi, R. 1978, ApJS, 38, 357

Forman, W., Nulsen, P., Heinz, S., Owen, F., Eilek, J., Vikhlinin, A., Markevitch, M., Kraft, R., Churazov, E., & Jones, C. 2005, ApJ, 635, 894

Fujita, Y., Matsumoto, T., & Wada, K. 2004, Journal of Korean Astronomical Society, 37, 571

Fukazawa, Y., Makishima, K., Tamura, T., Ezawa, H., Xu, H., Ikebe, Y., Kikuchi, K., & Ohashi, T. 1998, PASJ, 50, 187

Fusco-Femiano, R., Dal Fiume, D., Orlandini, M., Brunetti, G., Feretti, L., & Giovannini, G. 2001, ApJ, 552, L97

Garmire, G. P., Bautz, M. W., Ford, P. G., Nousek, J. A., & Ricker, Jr., G. R. 2003, in Society of Photo-Optical Instrumentation Engineers (SPIE) Conference Series, Vol. 4851, X-Ray and Gamma-Ray Telescopes and Instruments for Astronomy., ed. J. E. Truemper & H. D. Tananbaum, 28–44

Garrett, K. & Dūda, G. 2011, Advances in Astronomy, 2011, 8

Gastaldello, F., Wik, D. R., Molendi, S., Westergaard, N. J., Hornstrup, A., Madejski, G., Ferreira, D. D. M., Boggs, S. E., Christensen, F. E., Craig, W. W., Grefenstette, B. W., Hailey, C. J., Harrison, F. A., Madsen, K. K., Stern, D., & Zhang, W. W. 2015, ApJ, 800, 139

George, M. R., Fabian, A. C., Sanders, J. S., Young, A. J., & Russell, H. R. 2009, MNRAS, 395, 657

Ghizzardi, S., Rossetti, M., & Molendi, S. 2010, A&A, 516, A32

Giacconi, R., Branduardi, G., Briel, U., Epstein, A., Fabricant, D., Feigelson, E., Forman, W., Gorenstein, P., Grindlay, J., Gursky, H., Harnden, F. R., Henry, J. P., Jones, C., Kellogg, E., Koch, D., Murray, S., Schreier, E., Seward, F., Tananbaum, H., Topka, K., Van Speybroeck, L., Holt, S. S., Becker, R. H., Boldt, E. A., Serlemitsos, P. J., Clark, G., Canizares, C., Markert, T., Novick, R., Helfand, D., & Long, K. 1979, ApJ, 230, 540

Grevesse, N. & Sauval, A. J. 1998, Space Sci. Rev., 85, 161

Heinz, S., Churazov, E., Forman, W., Jones, C., & Briel, U. G. 2003, MNRAS, 346, 13

Helfand, D. J., Ku, W. H.-M., & Abramopoulos, F. 1980, Highlights of Astronomy, 5, 747

Henriksen, M. J. & Markevitch, M. L. 1996, ApJ, 466, L79

Hindson, L., Johnston-Hollitt, M., Hurley-Walker, N., Buckley, K., Morgan, J., Carretti, E., Dwarakanath, K. S., Bell, M., Bernardi, G., Bhat, N. D. R., Bowman, J. D., Briggs, F., Cappallo, R. J., Corey, B. E., Deshpande, A. A., Emrich, D., Ewall-Wice, A., Feng, L., Gaensler, B. M., Goeke, R., Greenhill, L. J., Hazelton, B. J., Jacobs, D., Kaplan, D. L., Kasper, J. C., Kratzenberg, E., Kudryavtseva, N., Lenc, E., Lonsdale, C. J., Lynch, M. J., McWhirter, S. R., McKinley, B., Mitchell, D. A., Morales, M. F., Morgan, E., Oberoi, D., Ord, S. M., Pindor, B., Prabu, T., Procopio, P., Offringa, A. R., Riding, J., Rogers, A. E. E., Roshi, A., Shankar, N. U., Srivani, K. S., Subrahmanyan, R., Tingay, S. J., Waterson, M., Wayth, R. B., Webster, R. L., Whitney, A. R., Williams, A., & Williams, C. L. 2014, MNRAS, 445, 330

Hoshino, A. 2012, in American Institute of Physics Conference Series, Vol. 1427, American Institute of Physics Conference Series, ed. R. Petre, K. Mitsuda, & L. Angelini, 336–337

Huang, Z. & Sarazin, C. L. 1996, ApJ, 461, 622

Hunt, R. 1971, MNRAS, 154, 141

Ichinohe, Y., Uchida, Y., Watanabe, S., Edahiro, I., Hayashi, K., Kawano, T., Ohno, M., Ohta, M., Takeda, S., Fukazawa, Y., Katsuragawa, M., Nakazawa, K., Odaka, H., Tajima, H., Takahashi, H., Takahashi, T., & Yuasa, T. 2016, Nuclear Instruments and Methods in Physics Research Section A: Accelerators, Spectrometers, Detectors and Associated Equipment, 806, 5

Ichinohe, Y., Werner, N., Simionescu, A., Allen, S. W., Canning, R. E. A., Ehlert, S., Mernier, F., & Takahashi, T. 2015, Monthly Notices of the Royal Astronomical Society, 448, 2971

Chandra IPI Teams. 2014, The *Chandra* Proposers' Observatory Guide, Version 17.0

Jansen, F., Lumb, D., Altieri, B., Clavel, J., Ehle, M., Erd, C., Gabriel, C., Guainazzi, M., Gondoin, P., Much, R., Munoz, R., Santos, M., Schartel, N., Texier, D., & Vacanti, G. 2001, A&A, 365, L1

Jenkins, A., Frenk, C. S., Pearce, F. R., Thomas, P. A., Colberg, J. M., White, S. D. M., Couchman, H. M. P., Peacock, J. A., Efstathiou, G., & Nelson, A. H. 1998, ApJ, 499, 20

Kaastra, J. S., Mewe, R., & Nieuwenhuijzen, H. 1996, in UV and X-ray Spectroscopy of Astrophysical and Laboratory Plasmas, ed. K. Yamashita & T. Watanabe, 411–414

Kalberla, P. M. W., Burton, W. B., Hartmann, D., Arnal, E. M., Bajaja, E., Morras, R., & Pöppel, W. G. L. 2005, A&A, 440, 775

Kawaharada, M., Okabe, N., Umetsu, K., Takizawa, M., Matsushita, K., Fukazawa, Y., Hamana, T., Miyazaki, S., Nakazawa, K., & Ohashi, T. 2010, ApJ, 714, 423

Kelley, R. L., Mitsuda, K., Allen, C. A., Arsenovic, P., Audley, M. D., Bialas, T. G., Boyce, K. R., Boyle, R. F., Breon, S. R., Brown, G. V., Cottam, J., Dipirro, M. J., Fujimoto, R., Furusho, T., Gendreau, K. C., Gochar, G. G., Gonzalez, O., Hirabayashi, M., Holt, S. S., Inoue, H., Ishida, M., Ishisaki, Y., Jones, C. S., Keski-Kuha, R., Kilbourne, C. A., McCammon, D., Morita, U., Moseley, S. H., Mott, B., Narasaki, K., Ogawara, Y., Ohashi, T., Ota, N., Panek, J. S., Porter, F. S., Serlemitsos, A., Shirron, P. J., Sneiderman, G. A., Szymkowiak, A. E., Takei, Y., Tveekrem, J. L., Volz, S. M., Yamamoto, M., & Yamasaki, N. Y. 2007, PASJ, 59, 77

Kellogg, E., Murray, S., Giacconi, R., Tananbaum, T., & Gursky, H. 1973, ApJ, 185, L13

Kellogg, E., Murray, S., Tananbaum, H., Gursky, H., Giacconi, R., & Forman, W. 1971, in Bulletin of the American Astronomical Society, Vol. 3, Bulletin of the American Astronomical Society, 477

Kempner, J. C., Sarazin, C. L., & Ricker, P. M. 2002, ApJ, 579, 236

Kent, S. M. & Sargent, W. L. W. 1979, ApJ, 230, 667

King, I. 1962, AJ, 67, 471

Kitayama, T., Bautz, M., Markevitch, M., Matsushita, K., Allen, S., Kawaharada, M., McNamara, B., Ota, N., Akamatsu, H., de Plaa, J., Galeazzi, M., Madejski, G., Main, R., Miller, E., Nakazawa, K., Russell, H., Sato, K., Sekiya, N., Simionescu, A., Tamura, T., Uchida, Y., Ursino, E., Werner, N., Zhuravleva, I., ZuHone, J., & on behalf of the ASTRO-H Science Working Group. 2014, ArXiv e-prints

Kiya, M., Ishikawa, H., & Sakamoto, H. 2001, Journal of Wind Engineering and Industrial Aerodynamics, 89, 1219 , bluff Body Aerodynamics and Applications

Kokubun, M., Nakazawa, K., Enoto, T., Fukazawa, Y., Gilmore, K., Kataoka, J., Kawaharada, M., Laurent, P., Lebrun, F., Limousin, O., Makishima, K., Mizuno, T., Mori, K., Nakamori, T., Ohno, M., Ohta, M., Sato, G., Tajima, H., Takahashi, H., Takahashi, T.,

Tanaka, T., Terada, Y., Uchiyama, H., Uchiyama, Y., Watanabe, S., Yatsu, Y., & Yamaoka, K. 2010, in Society of Photo-Optical Instrumentation Engineers (SPIE) Conference Series, Vol. 7732, Society of Photo-Optical Instrumentation Engineers (SPIE) Conference Series, 15

Komatsu, E., Smith, K. M., Dunkley, J., Bennett, C. L., Gold, B., Hinshaw, G., Jarosik, N., Larson, D., Nolta, M. R., Page, L., Spergel, D. N., Halpern, M., Hill, R. S., Kogut, A., Limon, M., Meyer, S. S., Odegard, N., Tucker, G. S., Weiland, J. L., Wollack, E., & Wright, E. L. 2011, ApJS, 192, 18

Koyama, K., Tsunemi, H., Dotani, T., Bautz, M. W., Hayashida, K., Tsuru, T. G., Matsumoto, H., Ogawara, Y., Ricker, G. R., Doty, J., Kissel, S. E., Foster, R., Nakajima, H., Yamaguchi, H., Mori, H., Sakano, M., Hamaguchi, K., Nishiuchi, M., Miyata, E., Torii, K., Namiki, M., Katsuda, S., Matsuura, D., Miyauchi, T., Anabuki, N., Tawa, N., Ozaki, M., Murakami, H., Maeda, Y., Ichikawa, Y., Prigozhin, G. Y., Boughan, E. A., Lamarr, B., Miller, E. D., Burke, B. E., Gregory, J. A., Pillsbury, A., Bamba, A., Hiraga, J. S., Senda, A., Katayama, H., Kitamoto, S., Tsujimoto, M., Kohmura, T., Tsuboi, Y., & Awaki, H. 2007, PASJ, 59, 23

Kuntz, K. D. & Snowden, S. L. 2000, ApJ, 543, 195

Laganá, T. F., Andrade-Santos, F., & Lima Neto, G. B. 2010, A&A, 511, A15

Landau, L. D. & Lifshitz, E. M. 1959, Fluid mechanics (Oxford: Pergamon Press)

Lau, E. T., Kravtsov, A. V., & Nagai, D. 2009, ApJ, 705, 1129

Lienhard, J. H. 1966, (Published by the Technical Extension Service, Washington State University)

Lodders, K. 2003, ApJ, 591, 1220

López-Cruz, O., Añorve, C., Birkinshaw, M., Worrall, D. M., Ibarra-Medel, H. J., Barkhouse, W. A., Torres-Papaqui, J. P., & Motta, V. 2014, ApJ, 795, L31

Lovisari, L., Kapferer, W., Schindler, S., & Ferrari, C. 2009, A&A, 508, 191

Macario, G., Markevitch, M., Giacintucci, S., Brunetti, G., Venturi, T., & Murray, S. S. 2011, ApJ, 728, 82

Machacek, M., Jones, C., Forman, W. R., & Nulsen, P. 2006, ApJ, 644, 155

Makishima, K., Ezawa, H., Fukuzawa, Y., Honda, H., Ikebe, Y., Kamae, T., Kikuchi, K., Matsushita, K., Nakazawa, K., Ohashi, T., Takahashi, T., Tamura, T., & Xu, H. 2001, PASJ, 53, 401

Mantz, A., Allen, S. W., Ebeling, H., Rapetti, D., & Drlica-Wagner, A. 2010a, MNRAS, 406, 1773

Mantz, A., Allen, S. W., Rapetti, D., & Ebeling, H. 2010b, MNRAS, 406, 1759

Markevitch, M. 2006, in ESA Special Publication, Vol. 604, The X-ray Universe 2005, ed. A. Wilson, 723

Markevitch, M., Forman, W. R., Sarazin, C. L., & Vikhlinin, A. 1998, ApJ, 503, 77

Markevitch, M., Gonzalez, A. H., Clowe, D., Vikhlinin, A., Forman, W., Jones, C., Murray, S., & Tucker, W. 2004, ApJ, 606, 819

Markevitch, M., Gonzalez, A. H., David, L., Vikhlinin, A., Murray, S., Forman, W., Jones, C., & Tucker, W. 2002, ApJ, 567, L27

Markevitch, M., Govoni, F., Brunetti, G., & Jerius, D. 2005, ApJ, 627, 733

Markevitch, M., Ponman, T. J., Nulsen, P. E. J., Bautz, M. W., Burke, D. J., David, L. P., Davis, D., Donnelly, R. H., Forman, W. R., Jones, C., Kaastra, J., Kellogg, E., Kim, D.-W., Kolodziejczak, J., Mazzotta, P., Pagliaro, A., Patel, S., Van Speybroeck, L., Vikhlinin, A., Vrtilek, J., Wise, M., & Zhao, P. 2000, ApJ, 541, 542

Markevitch, M., Sarazin, C. L., & Vikhlinin, A. 1999, ApJ, 521, 526

Markevitch, M. & Vikhlinin, A. 2007, Phys. Rep., 443, 1

Markevitch, M., Vikhlinin, A., & Mazzotta, P. 2001, ApJ, 562, L153

Mason, K. O., Breeveld, A., Much, R., Carter, M., Cordova, F. A., Cropper, M. S., Fordham, J., Huckle, H., Ho, C., Kawakami, H., Kennea, J., Kennedy, T., Mittaz, J., Pandel, D., Priedhorsky, W. C., Sasseen, T., Shirey, R., Smith, P., & Vreux, J.-M. 2001, A&A, 365, L36

Matsushita, K., Sakuma, E., Sasaki, T., Sato, K., & Simionescu, A. 2013, ApJ, 764, 147

Mazzotta, P., Fusco-Femiano, R., & Vikhlinin, A. 2002, ApJ, 569, L31

Mazzotta, P., Markevitch, M., Vikhlinin, A., Forman, W. R., David, L. P., & van Speybroeck, L. 2001, ApJ, 555, 205

McNamara, B. R. & Nulsen, P. E. J. 2007, ARA&A, 45, 117

Mernier, F., de Plaa, J., Lovisari, L., Pinto, C., Zhang, Y.-Y., Kaastra, J. S., Werner, N., & Simionescu, A. 2015, A&A, 575, A37

Million, E. T., Allen, S. W., Werner, N., & Taylor, G. B. 2010, MNRAS, 405, 1624

Mitchell, R. J., Culhane, J. L., Davison, P. J. N., & Ives, J. C. 1976, MNRAS, 175, 29P

Mitsuda, K., Bautz, M., Inoue, H., Kelley, R. L., Koyama, K., Kunieda, H., Makishima, K., Ogawara, Y., Petre, R., Takahashi, T., Tsunemi, H., White, N. E., Anabuki, N., Angelini, L., Arnaud, K., Awaki, H., Bamba, A., Boyce, K., Brown, G. V., Chan, K.-W., Cottam, J., Dotani, T., Doty, J., Ebisawa, K., Ezoe, Y., Fabian, A. C., Figueroa, E., Fujimoto, R., Fukazawa, Y., Furusho, T., Furuzawa, A., Gendreau, K., Griffiths, R. E., Haba, Y., Hamaguchi, K., Harrus, I., Hasinger, G., Hatsukade, I., Hayashida, K., Henry, P. J., Hiraga, J. S., Holt, S. S., Hornschemeier, A., Hughes, J. P., Hwang, U., Ishida, M., Ishisaki, Y., Isobe, N., Itoh, M., Iyomoto, N., Kahn, S. M., Kamae, T., Katagiri, H., Kataoka, J., Katayama, H., Kawai, N., Kilbourne, C., Kinugasa, K., Kissel, S., Kitamoto, S., Kohama, M., Kohmura, T., Kokubun, M., Kotani, T., Kotoku, J., Kubota, A., Madejski,

G. M., Maeda, Y., Makino, F., Markowitz, A., Matsumoto, C., Matsumoto, H., Matsuoka, M., Matsushita, K., McCammon, D., Mihara, T., Misaki, K., Miyata, E., Mizuno, T., Mori, K., Mori, H., Morii, M., Moseley, H., Mukai, K., Murakami, H., Murakami, T., Mushotzky, R., Nagase, F., Namiki, M., Negoro, H., Nakazawa, K., Nousek, J. A., Okajima, T., Ogasaka, Y., Ohashi, T., Oshima, T., Ota, N., Ozaki, M., Ozawa, H., Parmar, A. N., Pence, W. D., Porter, F. S., Reeves, J. N., Ricker, G. R., Sakurai, I., Sanders, W. T., Senda, A., Serlemitsos, P., Shibata, R., Soong, Y., Smith, R., Suzuki, M., Szymkowiak, A. E., Takahashi, H., Tamagawa, T., Tamura, K., Tamura, T., Tanaka, Y., Tashiro, M., Tawara, Y., Terada, Y., Terashima, Y., Tomida, H., Torii, K., Tsuboi, Y., Tsujimoto, M., Tsuru, T. G., Turner, M. J. L. ., Ueda, Y., Ueno, S., Ueno, M., Uno, S., Urata, Y., Watanabe, S., Yamamoto, N., Yamaoka, K., Yamasaki, N. Y., Yamashita, K., Yamauchi, M., Yamauchi, S., Yaqoob, T., Yonetoku, D., & Yoshida, A. 2007, PASJ, 59, 1

Mitsuda, K., Kelley, R. L., Boyce, K. R., Brown, G. V., Costantini, E., Dipirro, M. J., Ezoe, Y., Fujimoto, R., Gendreau, K. C., den Herder, J.-W., Hoshino, A., Ishisaki, Y., Kilbourne, C. A., Kitamoto, S., McCammon, D., Murakami, M., Murakami, H., Ogawa, M., Ohashi, T., Okamoto, A., Paltani, S., Pohl, M., Porter, F. S., Sato, Y., Shinozaki, K., Shirron, P. J., Sneiderman, G. A., Sugita, H., Szymkowiak, A., Takei, Y., Tamagawa, T., Tashiro, M., Terada, Y., Tsujimoto, M., de Vries, C., Yamaguchi, H., & Yamasaki, N. Y. 2010, in Society of Photo-Optical Instrumentation Engineers (SPIE) Conference Series, Vol. 7732, Society of Photo-Optical Instrumentation Engineers (SPIE) Conference Series, 11

Morandi, A. & Cui, W. 2014, MNRAS, 437, 1909

Murray, S. S. 1980, Highlights of Astronomy, 5, 727

Murray, S. S., Austin, G. K., Chappell, J. H., Gomes, J. J., Kenter, A. T., Kraft, R. P., Meehan, G. R., Zombeck, M. V., Fraser, G. W., & Serio, S. 2000, in Society of Photo-Optical Instrumentation Engineers (SPIE) Conference Series, Vol. 4012, X-Ray Optics, Instruments, and Missions III, ed. J. E. Truemper & B. Aschenbach, 68–80

Nagai, D., Kravtsov, A. V., & Vikhlinin, A. 2007a, ApJ, 668, 1

Nagai, D. & Lau, E. T. 2011, ApJ, 731, L10

Nagai, D., Vikhlinin, A., & Kravtsov, A. V. 2007b, ApJ, 655, 98

Nakazawa, K., Sarazin, C. L., Kawaharada, M., Kitaguchi, T., Okuyama, S., Makishima, K., Kawano, N., Fukazawa, Y., Inoue, S., Takizawa, M., Wik, D. R., Finoguenov, A., & Clarke, T. E. 2009, PASJ, 61, 339

Nousek, J. A. & Shue, D. R. 1989, ApJ, 342, 1207

Oegerle, W. R. & Hill, J. M. 2001, AJ, 122, 2858

Owers, M. S., Couch, W. J., & Nulsen, P. E. J. 2009a, ApJ, 693, 901

Owers, M. S., Nulsen, P. E. J., Couch, W. J., & Markevitch, M. 2009b, ApJ, 704, 1349

Parrish, I. J., McCourt, M., Quataert, E., & Sharma, P. 2012, MNRAS, 422, 704

Parrish, I. J., Quataert, E., & Sharma, P. 2009, ApJ, 703, 96

Paterno-Mahler, R., Blanton, E. L., Randall, S. W., & Clarke, T. E. 2013, ApJ, 773, 114

Peterson, J. R., Kahn, S. M., Paerels, F. B. S., Kaastra, J. S., Tamura, T., Bleeker, J. A. M., Ferrigno, C., & Jernigan, J. G. 2003, ApJ, 590, 207

Peterson, L. E. 1975, ARA&A, 13, 423

Petrosian, V., Bykov, A., & Rephaeli, Y. 2008, Space Sci. Rev., 134, 191

Pinto, C., Fabian, A. C., Werner, N., Kosec, P., Ahoranta, J., de Plaa, J., Kaastra, J. S., Sanders, J. S., Zhang, Y.-Y., & Finoguenov, A. 2014, A&A, 572, L8

Pinto, C., Sanders, J. S., Werner, N., de Plaa, J., Fabian, A. C., Zhang, Y.-Y., Kaastra, J. S., Finoguenov, A., & Ahoranta, J. 2015, A&A, 575, A38

Planck Collaboration, Ade, P. A. R., Aghanim, N., Armitage-Caplan, C., Arnaud, M., Ashdown, M., Atrio-Barandela, F., Aumont, J., Baccigalupi, C., Banday, A. J., & et al. 2014, A&A, 571, A16

Planck Collaboration, Ade, P. A. R., Aghanim, N., Arnaud, M., Ashdown, M., Atrio-Barandela, F., Aumont, J., Baccigalupi, C., Balbi, A., Banday, A. J., & et al. 2013, A&A, 550, A131

Pottschmidt, K., ISAS/JAXA, & the X-ray Astrophysics Laboratory, NASA/Goddard Space Flight Center. 2015, The *Suzaku* Technical Description, Version: January, 2015

Pratt, G. W., Arnaud, M., Piffaretti, R., Böhringer, H., Ponman, T. J., Croston, J. H., Voit, G. M., Borgani, S., & Bower, R. G. 2010, A&A, 511, A85

Predehl, P., Andritschke, R., Becker, W., Bornemann, W., Bräuninger, H., Brunner, H., Boller, T., Burwitz, V., Burkert, W., Clerc, N., Churazov, E., Coutinho, D., Dennerl, K., Eder, J., Emberger, V., Eraerds, T., Freyberg, M. J., Friedrich, P., Fürmetz, M., Georgakakis, A., Grossberger, C., Haberl, F., Hälker, O., Hartner, G., Hasinger, G., Hoelzl, J., Huber, H., von Kienlin, A., Kink, W., Kreykenbohm, I., Lamer, G., Lomakin, I., Lapchov, I., Lovisari, L., Meidinger, N., Merloni, A., Mican, B., Mohr, J., Müller, S., Nandra, K., Pacaud, F., Pavlinsky, M. N., Perinati, E., Pfeffermann, E., Pietschner, D., Reiffers, J., Reiprich, T., Robrade, J., Salvato, M., Santangelo, A. E., Sasaki, M., Scheuerle, H., Schmid, C., Schmitt, J., Schwope, A. D., Sunyaev, R., Tenzer, C., Tiedemann, L., Xu, W., Yaroshenko, V., Walther, S., Wille, M., Wilms, J., & Zhang, Y.-Y. 2014, in Society of Photo-Optical Instrumentation Engineers (SPIE) Conference Series, Vol. 9144, Society of Photo-Optical Instrumentation Engineers (SPIE) Conference Series, 1

Proust, D., Mazure, A., Sodre, L., Capelato, H., & Lund, G. 1988, A&AS, 72, 415

Randall, S., Nulsen, P., Forman, W. R., Jones, C., Machacek, M., Murray, S. S., & Maughan, B. 2008, ApJ, 688, 208

Randall, S. W., Nulsen, P. E. J., Jones, C., Forman, W. R., Bulbul, E., Clarke, T. E., Kraft, R., Blanton, E. L., David, L., Werner, N., Sun, M., Donahue, M., Giacintucci, S., & Simionescu, A. 2015, ApJ, 805, 112

Rasia, E., Tormen, G., & Moscardini, L. 2004, MNRAS, 351, 237

Reiprich, T. H., Basu, K., Ettori, S., Israel, H., Lovisari, L., Molendi, S., Pointecouteau, E., & Roncarelli, M. 2013, Space Sci. Rev., 177, 195

Reiprich, T. H., Hudson, D. S., Zhang, Y.-Y., Sato, K., Ishisaki, Y., Hoshino, A., Ohashi, T., Ota, N., & Fujita, Y. 2009, A&A, 501, 899

Rephaeli, Y. & Gruber, D. 2004, ApJ, 606, 825

Reynolds, C. S., McKernan, B., Fabian, A. C., Stone, J. M., & Vernaleo, J. C. 2005, MNRAS, 357, 242

Riseley, C. J., Scaife, A. M. M., Oozeer, N., Magnus, L., & Wise, M. W. 2015, MNRAS, 447, 1895

Roediger, E., Brüggen, M., Simionescu, A., Böhringer, H., Churazov, E., & Forman, W. R. 2011, MNRAS, 413, 2057

Roediger, E. & Hensler, G. 2005, A&A, 433, 875

Roediger, E., Kraft, R. P., Forman, W. R., Nulsen, P. E. J., & Churazov, E. 2013a, ApJ, 764, 60

Roediger, E., Kraft, R. P., Machacek, M. E., Forman, W. R., Nulsen, P. E. J., Jones, C., & Murray, S. S. 2012, ApJ, 754, 147

Roediger, E., Kraft, R. P., Nulsen, P., Churazov, E., Forman, W., Brüggen, M., & Kokotanekova, R. 2013b, MNRAS, 436, 1721

Roediger, E., Kraft, R. P., Nulsen, P. E. J., Forman, W. R., Machacek, M., Randall, S., Jones, C., Churazov, E., & Kokotanekova, R. 2015a, ApJ, 806, 103

—. 2015b, ApJ, 806, 104

Roettiger, K., Burns, J. O., & Stone, J. M. 1999, ApJ, 518, 603

Roncarelli, M., Ettori, S., Borgani, S., Dolag, K., Fabjan, D., & Moscardini, L. 2013, MNRAS, 432, 3030

Roncarelli, M., Ettori, S., Dolag, K., Moscardini, L., Borgani, S., & Murante, G. 2006, MNRAS, 373, 1339

Rossetti, M., Eckert, D., De Grandi, S., Gastaldello, F., Ghizzardi, S., Roediger, E., & Molendi, S. 2013, A&A, 556, A44

Rottgering, H. J. A., Wieringa, M. H., Hunstead, R. W., & Ekers, R. D. 1997, MNRAS, 290, 577

Russell, H. R., Sanders, J. S., Fabian, A. C., Baum, S. A., Donahue, M., Edge, A. C., McNamara, B. R., & O'Dea, C. P. 2010, MNRAS, 406, 1721

Rybicki, G. B. & Lightman, A. P. 1979, Radiative processes in astrophysics (New York, Wiley-Interscience, 1979. 393 p.)

Sanders, J. S. 2006, MNRAS, 371, 829

Sanders, J. S. & Fabian, A. C. 2007, MNRAS, 381, 1381

Sanders, J. S., Fabian, A. C., Churazov, E., Schekochihin, A. A., Simionescu, A., Walker, S. A., & Werner, N. 2013, Science, 341, 1365

Sanders, J. S., Fabian, A. C., Smith, R. K., & Peterson, J. R. 2010, MNRAS, 402, L11

Sanders, J. S., Fabian, A. C., & Taylor, G. B. 2005, MNRAS, 356, 1022

Sarazin, C. L. 1986, Reviews of Modern Physics, 58, 1

Sarazin, C. L. 2002, in Astrophysics and Space Science Library, Vol. 272, Merging Processes in Galaxy Clusters, ed. L. Feretti, I. M. Gioia, & G. Giovannini, 1–38

Sarazin, C. L. 2011, Basic Properties of Clusters of Galaxies and The Physics of the Intracluster Gas

Sarazin, C. L., Finoguenov, A., & Wik, D. R. 2013, Astronomische Nachrichten, 334, 346

Sasaki, T., Matsushita, K., & Sato, K. 2014, ApJ, 781, 36

Schekochihin, A. A., Cowley, S. C., Dorland, W., Hammett, G. W., Howes, G. G., Quataert, E., & Tatsuno, T. 2009, ApJS, 182, 310

Schenck, D. E., Datta, A., Burns, J. O., & Skillman, S. 2014, AJ, 148, 23

Schuecker, P., Finoguenov, A., Miniati, F., Böhringer, H., & Briel, U. G. 2004, A&A, 426, 387

Serlemitsos, P. J., Soong, Y., Chan, K.-W., Okajima, T., Lehan, J. P., Maeda, Y., Itoh, K., Mori, H., Iizuka, R., Itoh, A., Inoue, H., Okada, S., Yokoyama, Y., Itoh, Y., Ebara, M., Nakamura, R., Suzuki, K., Ishida, M., Hayakawa, A., Inoue, C., Okuma, S., Kubota, R., Suzuki, M., Osawa, T., Yamashita, K., Kunieda, H., Tawara, Y., Ogasaka, Y., Furuzawa, A., Tamura, K., Shibata, R., Haba, Y., Naitou, M., & Misaki, K. 2007, PASJ, 59, 9

Shin, M.-S. & Ruszkowski, M. 2014, MNRAS, 445, 1997

Sijacki, D. & Springel, V. 2006, MNRAS, 371, 1025

Simionescu, A., Allen, S. W., Mantz, A., Werner, N., Takei, Y., Morris, R. G., Fabian, A. C., Sanders, J. S., Nulsen, P. E. J., George, M. R., & Taylor, G. B. 2011, Science, 331, 1576

Simionescu, A., Werner, N., Urban, O., Allen, S. W., Fabian, A. C., Mantz, A., Matsushita, K., Nulsen, P. E. J., Sanders, J. S., Sasaki, T., Sato, T., Takei, Y., & Walker, S. A. 2013, ApJ, 775, 4

Simionescu, A., Werner, N., Urban, O., Allen, S. W., Fabian, A. C., Sanders, J. S., Mantz, A., Nulsen, P. E. J., & Takei, Y. 2012, ApJ, 757, 182

Simionescu, A., Werner, N., Urban, O., Allen, S. W., Ichinohe, Y., & Zhuravleva, I. 2015, ApJ, 811, L25

Slee, O. B., Roy, A. L., Murgia, M., Andernach, H., & Ehle, M. 2001, AJ, 122, 1172

Smith, R. K., Brickhouse, N. S., Liedahl, D. A., & Raymond, J. C. 2001, ApJ, 556, L91

Sodre, Jr., L., Capelato, H. V., Steiner, J. E., Proust, D., & Mazure, A. 1992, MNRAS, 259, 233

Spitzer, L. 1965, Physics of fully ionized gases (New York: Interscience Publication)

Springel, V. & Farrar, G. R. 2007, MNRAS, 380, 911

Strüder, L., Briel, U., Dennerl, K., Hartmann, R., Kendziorra, E., Meidinger, N., Pfeffermann, E., Reppin, C., Aschenbach, B., Bornemann, W., Bräuninger, H., Burkert, W., Elender, M., Freyberg, M., Haberl, F., Hartner, G., Heuschmann, F., Hippmann, H., Kastelic, E., Kemmer, S., Kettenring, G., Kink, W., Krause, N., Müller, S., Oppitz, A., Pietsch, W., Popp, M., Predehl, P., Read, A., Stephan, K. H., Stötter, D., Trümper, J., Holl, P., Kemmer, J., Soltau, H., Stötter, R., Weber, U., Weichert, U., von Zanthier, C., Carathanassis, D., Lutz, G., Richter, R. H., Solc, P., Böttcher, H., Kuster, M., Staubert, R., Abbey, A., Holland, A., Turner, M., Balasini, M., Bignami, G. F., La Palombara, N., Villa, G., Buttler, W., Gianini, F., Lainé, R., Lumb, D., & Dhez, P. 2001, A&A, 365, L18

Sun, M., Donahue, M., Roediger, E., Nulsen, P. E. J., Voit, G. M., Sarazin, C., Forman, W., & Jones, C. 2010, ApJ, 708, 946

Sun, M., Jones, C., Forman, W., Vikhlinin, A., Donahue, M., & Voit, M. 2007, ApJ, 657, 197

Sutherland, R. S. & Dopita, M. A. 1993, ApJS, 88, 253

Tajima, H., Blandford, R., Enoto, T., Fukazawa, Y., Gilmore, K., Kamae, T., Kataoka, J., Kawaharada, M., Kokubun, M., Laurent, P., Lebrun, F., Limousin, O., Madejski, G., Makishima, K., Mizuno, T., Nakazawa, K., Ohno, M., Ohta, M., Sato, G., Sato, R., Takahashi, H., Takahashi, T., Tanaka, T., Tashiro, M., Terada, Y., Uchiyama, Y., Watanabe, S., Yamaoka, K., & Yonetoku, D. 2010, in Society of Photo-Optical Instrumentation Engineers (SPIE) Conference Series, Vol. 7732, Society of Photo-Optical Instrumentation Engineers (SPIE) Conference Series, 16

Takahara, M. & Takahara, F. 1981, Progress of Theoretical Physics, 65, 369

Takahashi, T., Abe, K., Endo, M., Endo, Y., Ezoe, Y., Fukazawa, Y., Hamaya, M., Hirakuri, S., Hong, S., Horii, M., Inoue, H., Isobe, N., Itoh, T., Iyomoto, N., Kamae, T., Kasama, D., Kataoka, J., Kato, H., Kawaharada, M., Kawano, N., Kawashima, K., Kawasoe, S., Kishishita, T., Kitaguchi, T., Kobayashi, Y., Kokubun, M., Kotoku, J., Kouda, M., Kubota, A., Kuroda, Y., Madejski, G., Makishima, K., Masukawa, K., Matsumoto, Y., Mitani, T., Miyawaki, R., Mizuno, T., Mori, K., Mori, M., Murashima, M., Murakami, T., Nakazawa, K., Niko, H., Nomachi, M., Okada, Y., Ohno, M., Oonuki, K., Ota, N., Ozawa, H., Sato, G., Shinoda, S., Sugiho, M., Suzuki, M., Taguchi, K., Takahashi, H., Takahashi, I., Takeda, S., Tamura, K.-I., Tamura, T., Tanaka, T., Tanihata, C., Tashiro, M., Terada, Y., Tominaga, S., Uchiyama, Y., Watanabe, S., Yamaoka, K., Yanagida, T., & Yonetoku, D. 2007, PASJ, 59, 35

Takahashi, T., Mitsuda, K., Kelley, R., Aharonian, F., Akamatsu, H., Akimoto, F., Allen, S., Anabuki, N., Angelini, L., Arnaud, K., & et al. 2014, in Society of Photo-Optical Instrumentation Engineers (SPIE) Conference Series, Vol. 9144, Society of Photo-Optical Instrumentation Engineers (SPIE) Conference Series, 25

Tamura, T., Yamasaki, N. Y., Iizuka, R., Fukazawa, Y., Hayashida, K., Ueda, S., Matsushita, K., Sato, K., Nakazawa, K., Ota, N., & Takizawa, M. 2014, ApJ, 782, 38

Tanaka, N., Furuzawa, A., Miyoshi, S. J., Tamura, T., & Takata, T. 2010, PASJ, 62, 743

Tanaka, Y., Inoue, H., & Holt, S. S. 1994, PASJ, 46, L37

Taylor, G. B., Fabian, A. C., Gentile, G., Allen, S. W., Crawford, C., & Sanders, J. S. 2007, MNRAS, 382, 67

Taylor, G. B. & Perley, R. A. 1993, ApJ, 416, 554

Tittley, E. R. & Henriksen, M. 2005, ApJ, 618, 227

Totani, T. 2004, Physical Review Letters, 92, 191301

Tsunemi, H., Hayashida, K., Tsuru, T. G., Dotani, T., Hiraga, J. S., Anabuki, N., Bamba, A., Hatsukade, I., Kohmura, T., Mori, K., Murakami, H., Nakajima, H., Ozaki, M., Uchida, H., & Yamauchi, M. 2010, in Society of Photo-Optical Instrumentation Engineers (SPIE) Conference Series, Vol. 7732, Society of Photo-Optical Instrumentation Engineers (SPIE) Conference Series, 10

Tucker, W. H. & Rosner, R. 1983, ApJ, 267, 547

Turner, M. J. L., Abbey, A., Arnaud, M., Balasini, M., Barbera, M., Belsole, E., Bennie, P. J., Bernard, J. P., Bignami, G. F., Boer, M., Briel, U., Butler, I., Cara, C., Chabaud, C., Cole, R., Collura, A., Conte, M., Cros, A., Denby, M., Dhez, P., Di Coco, G., Dowson, J., Ferrando, P., Ghizzardi, S., Gianotti, F., Goodall, C. V., Gretton, L., Griffiths, R. G., Hainaut, O., Hochedez, J. F., Holland, A. D., Jourdain, E., Kendziorra, E., Lagostina, A., Laine, R., La Palombara, N., Lortholary, M., Lumb, D., Marty, P., Molendi, S., Pigot, C., Poindron, E., Pounds, K. A., Reeves, J. N., Reppin, C., Rothenflug, R., Salvetat, P., Sauvageot, J. L., Schmitt, D., Sembay, S., Short, A. D. T., Spragg, J., Stephen, J., Strüder, L., Tiengo, A., Trifoglio, M., Trümper, J., Vercellone, S., Vigroux, L., Villa, G., Ward, M. J., Whitehead, S., & Zonca, E. 2001, A&A, 365, L27

Urban, O., Simionescu, A., Werner, N., Allen, S. W., Ehlert, S., Zhuravleva, I., Morris, R. G., Fabian, A. C., Mantz, A., Nulsen, P. E. J., Sanders, J. S., & Takei, Y. 2014, MNRAS, 437, 3939

van Speybroeck, L. P., Jerius, D., Edgar, R. J., Gaetz, T. J., Zhao, P., & Reid, P. B. 1997, in Society of Photo-Optical Instrumentation Engineers (SPIE) Conference Series, Vol. 3113, Grazing Incidence and Multilayer X-Ray Optical Systems, ed. R. B. Hoover & A. B. Walker, 89–104

Vazza, F., Eckert, D., Simionescu, A., Brüggen, M., & Ettori, S. 2013, MNRAS, 429, 799

Vikhlinin, A., Burenin, R. A., Ebeling, H., Forman, W. R., Hornstrup, A., Jones, C., Kravtsov, A. V., Murray, S. S., Nagai, D., Quintana, H., & Voevodkin, A. 2009a, ApJ, 692, 1033

Vikhlinin, A., Kravtsov, A. V., Burenin, R. A., Ebeling, H., Forman, W. R., Hornstrup, A., Jones, C., Murray, S. S., Nagai, D., Quintana, H., & Voevodkin, A. 2009b, ApJ, 692, 1060

Vikhlinin, A., Markevitch, M., & Murray, S. S. 2001a, ApJ, 551, 160

—. 2001b, ApJ, 549, L47

Vikhlinin, A. A. & Markevitch, M. L. 2002, Astronomy Letters, 28, 495

Walker, S. A., Fabian, A. C., & Sanders, J. S. 2014, MNRAS, 441, L31

Walker, S. A., Fabian, A. C., Sanders, J. S., Simionescu, A., & Tawara, Y. 2013, MNRAS, 432, 554

Weisskopf, M. C., Tananbaum, H. D., Van Speybroeck, L. P., & O'Dell, S. L. 2000, in Society of Photo-Optical Instrumentation Engineers (SPIE) Conference Series, Vol. 4012, X-Ray Optics, Instruments, and Missions III, ed. J. E. Truemper & B. Aschenbach, 2–16

Werner, N., Finoguenov, A., Kaastra, J. S., Simionescu, A., Dietrich, J. P., Vink, J., & Böhringer, H. 2008, A&A, 482, L29

Werner, N., Oonk, J. B. R., Canning, R. E. A., Allen, S. W., Simionescu, A., Kos, J., van Weeren, R. J., Edge, A. C., Fabian, A. C., von der Linden, A., Nulsen, P. E. J., Reynolds, C. S., & Ruszkowski, M. 2013a, ApJ, 767, 153

Werner, N., Urban, O., Simionescu, A., & Allen, S. W. 2013b, Nature, 502, 656

Werner, N., Zhuravleva, I., Churazov, E., Simionescu, A., Allen, S. W., Forman, W., Jones, C., & Kaastra, J. S. 2009, MNRAS, 398, 23

Werner, N., ZuHone, J. A., Zhuravleva, I., Ichinohe, Y., Simionescu, A., Allen, S. W., Markevitch, M., Fabian, A. C., Keshet, U., Roediger, E., Ruszkowski, M., & Sanders, J. S. 2016, MNRAS, 455, 846

White, S. D. M., Navarro, J. F., Evrard, A. E., & Frenk, C. S. 1993, Nature, 366, 429

Wik, D. R., Hornstrup, A., Molendi, S., Madejski, G., Harrison, F. A., Zoglauer, A., Grefenstette, B. W., Gastaldello, F., Madsen, K. K., Westergaard, N. J., Ferreira, D. D. M., Kitaguchi, T., Pedersen, K., Boggs, S. E., Christensen, F. E., Craig, W. W., Hailey, C. J., Stern, D., & Zhang, W. W. 2014, ApJ, 792, 48

Wik, D. R., Sarazin, C. L., Finoguenov, A., Matsushita, K., Nakazawa, K., & Clarke, T. E. 2009, ApJ, 696, 1700

Xiang, F., Churazov, E., Dolag, K., Springel, V., & Vikhlinin, A. 2007, MNRAS, 379, 1325

XMM-Newton Community Support Team & XMM-Newton Science Operations Centre Team. 2014, XMM-Newton Users Handbook, Issue 2.12

Yamazaki, S., Fukazawa, Y., Sasada, M., Itoh, R., Nishino, S., Takahashi, H., Takaki, K., Kawabata, K. S., Yoshida, M., & Uemura, M. 2013, PASJ, 65, 30

Zhuravleva, I., Churazov, E., Schekochihin, A. A., Allen, S. W., Arévalo, P., Fabian, A. C., Forman, W. R., Sanders, J. S., Simionescu, A., Sunyaev, R., Vikhlinin, A., & Werner, N. 2014, Nature, 515, 85

Zhuravleva, I., Churazov, E., Sunyaev, R., Sazonov, S., Allen, S. W., Werner, N., Simionescu, A., Konami, S., & Ohashi, T. 2013, MNRAS, 435, 3111

ZuHone, J. A., Kunz, M. W., Markevitch, M., Stone, J. M., & Biffi, V. 2015, ApJ, 798, 90

ZuHone, J. A., Markevitch, M., & Lee, D. 2011, ApJ, 743, 16

ZuHone, J. A., Markevitch, M., Ruszkowski, M., & Lee, D. 2013, ApJ, 762, 69

Zwicky, F. 1937, ApJ, 86, 217

Acknowledgements

First of all, I would really like to express my best gratitude to my supervisor Prof. Tadayuki Takahashi for his continuous supports and encouragements. You have offered me a number of exciting opportunities that I would not be able to experience in any other place. I am also deeply grateful to Dr. Norbert Werner and Dr. Aurora Simionescu for their kind and thorough help in my science projects. You have led me to the spectacular world of galaxy cluster physics through the countless stimulating discussions.

My sincere thanks also go to Dr. Greg Madejski, Prof. Steve Allen, Mr. Ondrej Urban, Dr. Becky Canning, and Dr. Irina Zhuravleva for the friendly atmosphere at Stanford/SLAC. The stay has been one of the best experience in my research life. I would like to thank also to Prof. Andy Fabian, Dr. Stephen Walker and Dr. Helen Russell for the helps, advice and discussions during my stay in Cambridge.

I would like to deeply thank to Dr. Hirokazu Odaka, Dr. Yasuyuki Tanaka, Dr. Yoshiyuki Inoue, Dr. Hiroki Akamatsu, Dr. Shin'ichiro Takeda, Dr. Atsushi Harayama, Dr. Shin Watanabe and Prof. Ryugo Hayano for their encouragements and inspiring opinions, and also to Dr. Steven Ehlert, Mr. François Mernier and Dr. Maxim Markevitch for their helpful comments and advice.

I am indebted to Kumiko Hoshikawa, Yoko Ohta, Hisako Ito, Kuniko Kono, and the secretaries and coordinators in the Department of Physics, ALPS, KIPAC, SLAC, and IoA, for assisting me with my student life.

I also thank Keiko Takahashi and the doctor at Stiftung Spital Interlaken for the trouble in the happening at Mürren. My wrist is cured! I thank Saito-san, Tarou-shi, Tamotsu, Ogino-sensei, Duke, Ucchie, Katchan, Komeda, Tomaru, Yamamoto, Nagayoshi, Iwai, and all the previous and current colleagues for making me feel relaxed and happy. I thank Robin, who accommodated me with a wonderful room at Menlo Park, and Hiwi and Micky, who cheerfully entertained me during my stay there. I thank Masato, Hishinuma, Y. Shibata, Otaka, Hayakawa, Takimoto, Shino, Tachibana, Yoshiki, Otomura, K. Shibata, D. Shibata, Gen-san and Daigo for spicing up my life.

Last but not least, I thank Megumi Tsuno and my family for taking my dreams seriously and being always encouraging. I owe what I am today to your supports.

Thank you very much and arigatou gozaimashita!